CRANFIELD INSTITUTE OF TECHNOLOGY

SILSOE COLLEGE

Ph.D. Thesis

Academic Year 1988/1989

Abdullah Ali Al-Ghazal

An investigation into the mechanics of agricultural discs

Supervisor: Professor Dr. R.J.Godwin

July, 1989

This thesis is submitted for the degree of Doctor of Phisosophy
in Agricultural Machinery Engineering

To my Parents

To my Wife

To my Children

A B S T R A C T

A prediction model based upon Mohr-Coulomb soil mechanics theory has been developed to predict the interaction between the soil and agricultural discs of different geometries and operating angles to both vertical and tilted discs. The model is based on two forms of soil failure. The magnitude of each form of failure is dependent upon a passive reaction on the concave side of the disc and a vertical bearing reaction on the convex side of the disc. The predicted results are in close agreement with the results of the experimental studies.

Disc geometry is one of the most important factors to be considered in evaluating the soil reaction acting upon a disc tool. A theoretical analysis of the disc geometry was therefore carried out. The analysis of the disc geometry makes it possible to determine the factors required for the predicted forces acting on a disc tool.

The experimental studies were conducted in a sandy loam soil at a moisture content in the friable range, under controlled soil bin conditions. The work was carried out at full-scale with 3 dimensional force measuring apparatus developed primarily for this investigation. The discs studied had a range of disc angles between 15^{o} and 60^{o} and a range of tilt angles between 0^{o} and 35^{o}. The

depth of cut ranged from 80 mm to 140 mm and at speeds between 0.75 m/s and 1.5 m/s.

The disturbance area of the soil caused by the rotating soil cutting disc is calculated to define the disturbed area for any combination of disc angle, disc diameter, gang spacing and depth of work in order to accurately calculate specific resistance.

Disturbance and soil inversion were investigated using transparent discs and soil tracers,with a variety of disc and tilt angles in order to quantify inversion and mixing.

ACKNOWLEDGEMENTS

The author is sincerely grateful for the encouragement and personal involvement of Professor Dr. R.J. Godwin during the course of this study.

A very special thanks to Mr. Tony Reynolds for his assistance, suggestions and many hours spent in the preparation of the soil and recording of the experimental data.

Gratitude is expressed to Professor R.W. Radley and to Mr. Mike Hann, as members of the research committee, and for helping in completion of this work at various stages.

Many thanks are due to Mr. Bryan Morgan for his proof-reading of the draft copy of this thesis and to Dr. M.J. O'Dogherty for his assistance in checking data, and also to Mrs. Woodland for typing the thesis.

I thank, too, all other members of staff of Silsoe College who have contributed to the development of the project.

LIST OF CONTENTS

Contents (Cont'd)

Contents (Cont'd)

Contents (Cont'd)

Contents (Cont'd) Page

Contents (Cont'd)

LIST OF FIGURES

Figures (Cont'd)

Figures (Cont'd)

Figures (Cont'd)

Figures (Cont'd) Page

Figures (Cont'd) Page

Figures (Cont'd) Page

LIST OF TABLES

CHAPTER 1

1. Introduction

1.1. Introduction

The earliest attempts at ploughing involved attaching a forked stick to an animal and using it for turning over or loosening the soil (Ingersoll, 1926). The earliest application for a revolving soil penetrating disc was the sward cutter which was patented in England in 1788. Scarifier discs with a number of thin spaced discs were used in France and England in 1840. In the United States, a patent for what might be termed the first disc plough was recorded in 1847. George Page developed a revolving moldboard for a plough which retained a regular share, landside and coulter. A patent for the first pure disc plough was recorded in 1867 but this plough may never have been built. In 1875, the first disc plough with two discs and adjustable axles was developed. Following the original patent, many designs have evolved resulting in the modern disc as used today. The objectives of tillage are to manipulate the soil for any purpose and to provide optimum environmental condition for crops.

The design of tillage tools is still largely an art rather than a science. The design factors for control or

manipulation of the soil are implement shape, initial soil condition and the manner of soil movement caused by the tool. The designer has only developed and refined the tool shape and most tillage implement shapes have been achieved by cut-and-try methods. The first research into the fundamental principles of soil reactions on tillage implements was conducted by Nichols (1930 and 1931) and Baver (1932) in which they measured the dynamic properties of soil and related them to the design of tillage tool performance. Clyde (1936 and 1937) reported the soil reaction forces on plough discs, plough bodies and coulters. Spoor (1969) studied the implement shape requirements for a number of soil manipulation processes to identify the basic design features of soil engaging implements.

The disc plough has been used as the implement for primary preparation for many years. The disc plough is the major implement for both primary and secondary tillage in the developing countries of the tropics. The disc plough can be used in nearly every sort of soil condition such as wet, sticky, extremely hard, stony and dry soil where it is difficult for the moldboard plough to operate. Disc harrows are used mostly in the temperate region for secondary preparation. Sometimes, heavy disc harrows are used for primary tillage. With the growing problem of straw incorporation in farming, the use of the disc plough for primary tillage is increasing.

1.2. Objectives

The objectives of this project are:

1. To develop an understanding of the soil mechanics/ physics of soil cutting, compressive failure on the convex side and flow over the disc surfaces.

2. To investigate the effects of disc geometry and the factors discussed in (1) on the magnitude and direction of the resultant forces on the discs.

3. To develop techniques to predict the soil forces acting on discs of varying geometric configuration.

1.3. Experimental approach

The fundamental studies were conducted under controlled soil bin conditions to determine:

1. The soil cutting, compressive failure on the convex side and flow over the disc.

2. The magnitude and direction of the resultant forces.

3. Techniques for predicting the soil forces acting on a disc.

4. The specific resistance and how 1, 2, 3 above are affected by the geometry of the disc.

1.4. Theoretical approach

The general approach was to develop a model based on Mohr-Coulomb soil mechanics to predict the force reaction on the disc from a knowledge of the type of soil failure involved.

CHAPTER 2

2. Literature review

2.1. Introduction

Discs are important implements used at present for primary and secondary tillage. They are considered to be good implements for a wide range of soil types and preparations. The disc blade has been discussed by many workers. Most of the published papers consider discs with horizontal axles (Clyde, 1939), with relatively few studies on discs with their axle inclined to the horizontal. This chapter reviews and discusses the most relevant research.

2.2. The work of Clyde

Clyde (1954) discussed and gave examples of the problems in studying the science of mechanics relating to tractor and implements. He suggested that to avoid major mistakes it is advisable to construct a force diagram with all important forces and then use the laws of mechanics. These techniques have been used by Clyde and Tanquary (1957) to determine the force analysis in three various cases. Clyde (1936) studied the line of action of the useful soil force by dynamometer methods. He pointed out that the

position, direction and magnitude of the useful soil force on a tillage tool is important. Clyde (1937) studied the useful soil force on mouldboard ploughs and disc ploughs in terms of two non-intersecting forces or a resultant force and a couple, see Figure 2.1. Clyde (1939) studied a series of field tests in a silt loam soil for five disc blades at an average speed of 3 mph to study the effect of size, attitude angles, loading, depth of cut and soil conditions on the design and operation of disc tools. He reported that the reaction of the soil on tillage tools is the sum of infinitely small forces distributed over the contact area and it can be represented by either (i) a single resultant force and a couple, or (ii) two non-intersecting forces. He analysed the results of the 18 in (460 mm) and the 22 in (560 mm) disc sizes and he indicated that the draught L and the side force S are a function of the vertical force V, which is numerically equal to, but opposite in direction to the net weight carried by the discs at equilibrium. He assumed that this is because the disc harrows operate at a constant net weight. Clyde (1939) used the tillage dynamometer for measuring the soil forces on the discs mentioned above and reported the effect of the disc angles on L and S at various magnitude of V. Clyde (1939) observed that a small change in the soil conditions was very effective in changing the magnitude of S at small disc angles of 15^{o} and 19^{o}. He reported that as the depth of work of a disc increases in the soil, a point is reached

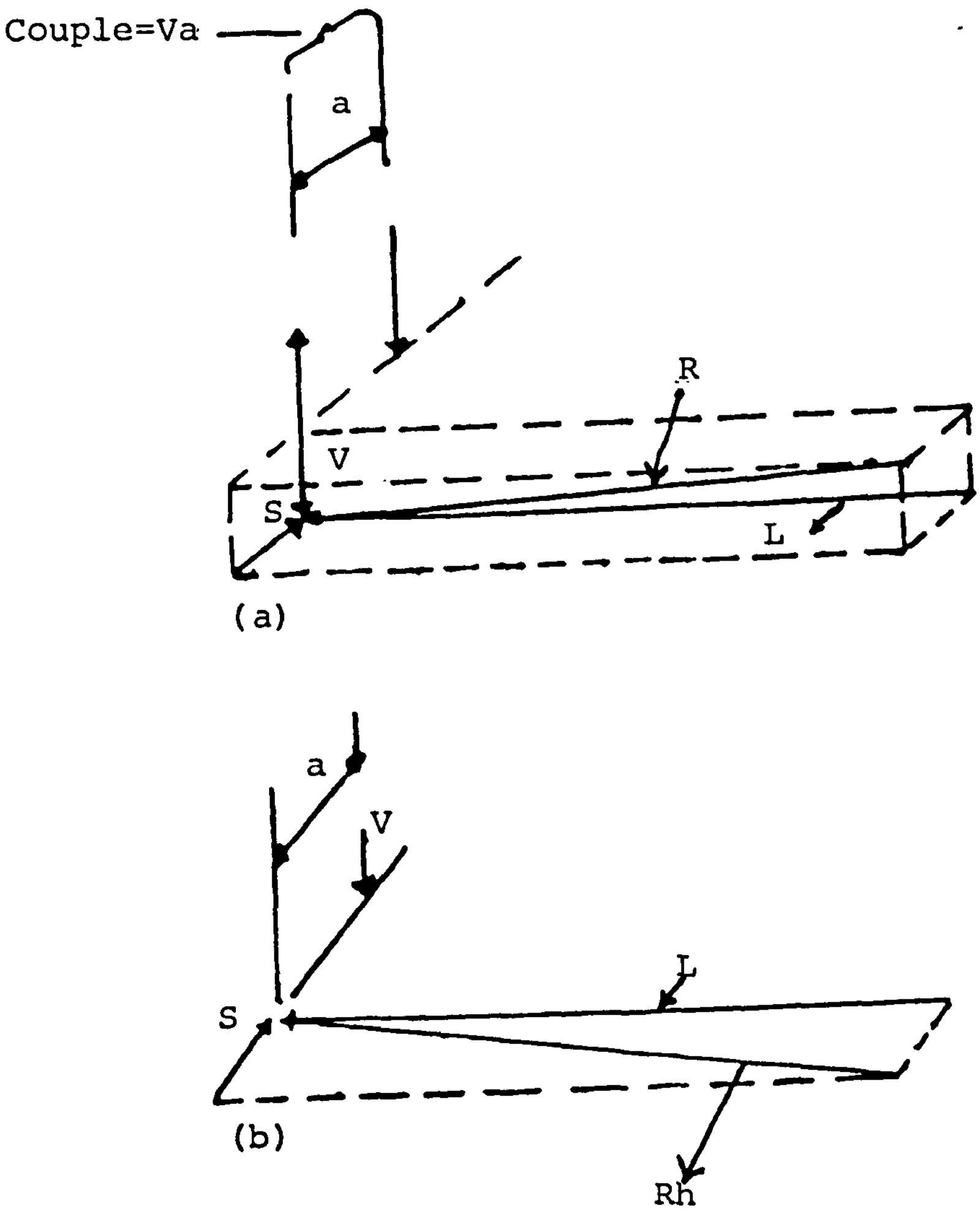

Figure 2.1. Two methods of measurement of the total soil reaction on a tillage tool (Clyde, 1944)
(a) one force and a couple Va
(b) two non-intersecting forces Rh and V

where the disc starts to present an appreciable bearing surface on its back which opposes penetration. He pointed out that this point is reached sooner if the disc is sharpened on the back of the disc.

Clyde (1939) measured the values of the critical depth for 18 in (460 mm) and 22 in (560 mm) discs sharpened on the back as shown in Table 2.1. below.

Disc angle degrees	Critical depth (in)	
	Disc dia. 18 in	Disc dia. 22 in
15	1 3/16	1 1/4
17	2	1 1/2
19	2 9/16	2
21	3 3/8	2 3/8
23	3 13/16	3

Table 2.1. Critical depth for 18 in and 22 in discs (Clyde, 1939)

2.3. The work of McCreery and Nichols

McCreery and Nichols (1956) studied the geometry of the disc and related it to the soil reaction. They pointed out the importance of considering the inherent features of disc shape to an understanding of the relationship between

disc designs and soil reactions. Most workers study this important fact and use it in their work either explicitly or implicitly. McCreery and Nichols (1956) investigated and studied disc geometry as a first step to understanding the soil reaction. They indicated that the common disc geometry is a section of a sphere cut off by a plane as shown in the shaded area in Fig. 2.2. The radius of the sphere is the radius of curvature R of the disc from which the disc is cut. The edge of the disc is therefore a circle and the diameter and depth of concavity of the disc is based on the distance of the cutting plane from the centre O of the sphere and the radius of the sphere. The packing and compacting of the soil by a disc is based on how much area on the back of the disc is engaged. McCreery and Nichols (1956) called this area the bearing area and it operates in the vertical plane normal to the direction of motion as shown in Fig. 2.3.

To explain, if the convex side of the disc is engaged in the soil, they defined a critical value of Θ disc angle. McCreery and Nichols (1956) reported that if the critical value Θ which is the angle in a horizontal plane at the soil surface between the tangent to the cutting edge and the plane P as shown in Fig. 2.3. is greater than or equal to $\emptyset$, which is the disc angle, between the line of travel and the plane P, there will be no bearing area on the convex back side of the disc. If the angle $\emptyset$ is smaller than Θ, the convex back

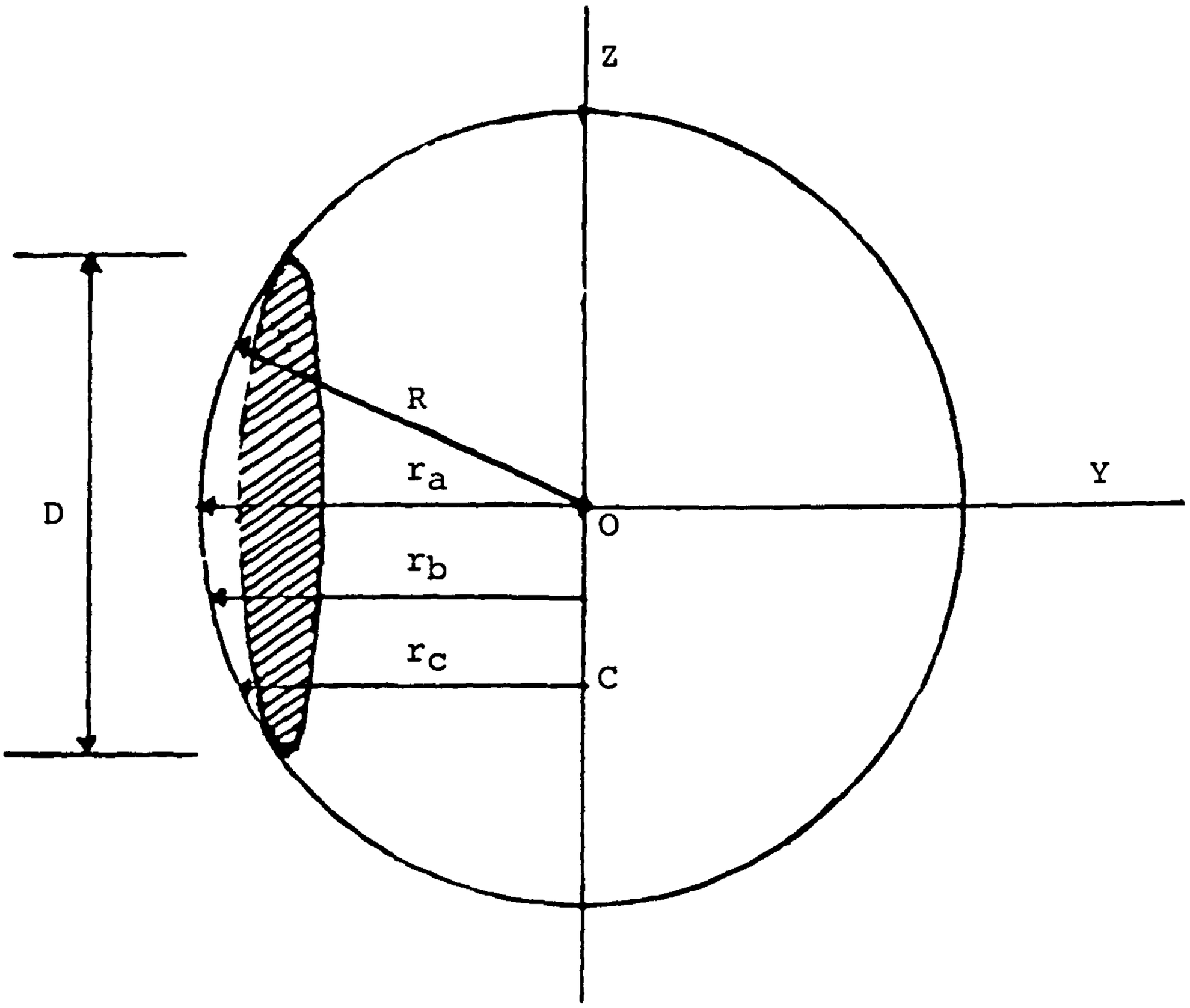

Figure 2.2. Geometry of the disc showing the disc as a section of a sphere (McCreery and Nichols 1956)

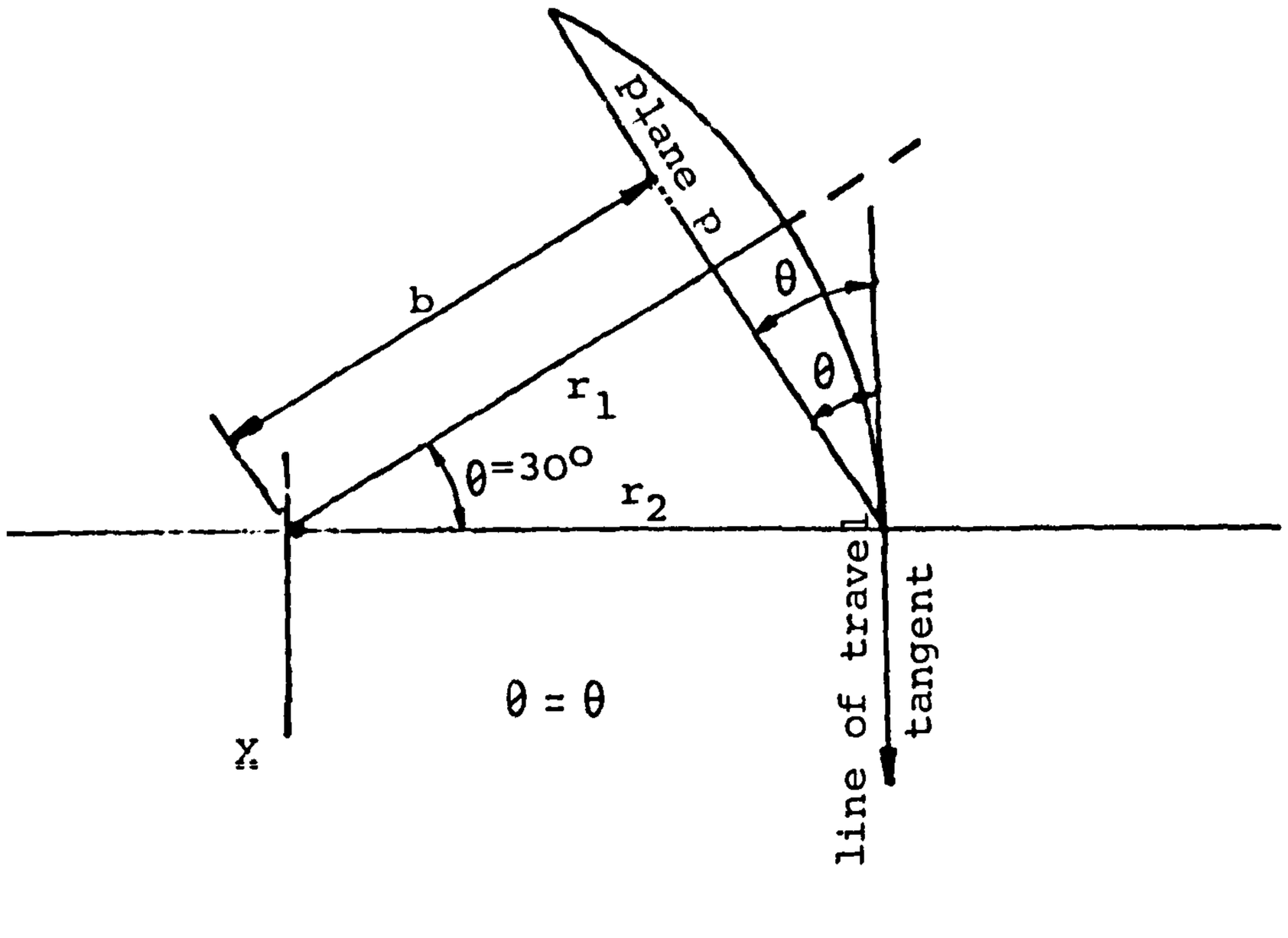

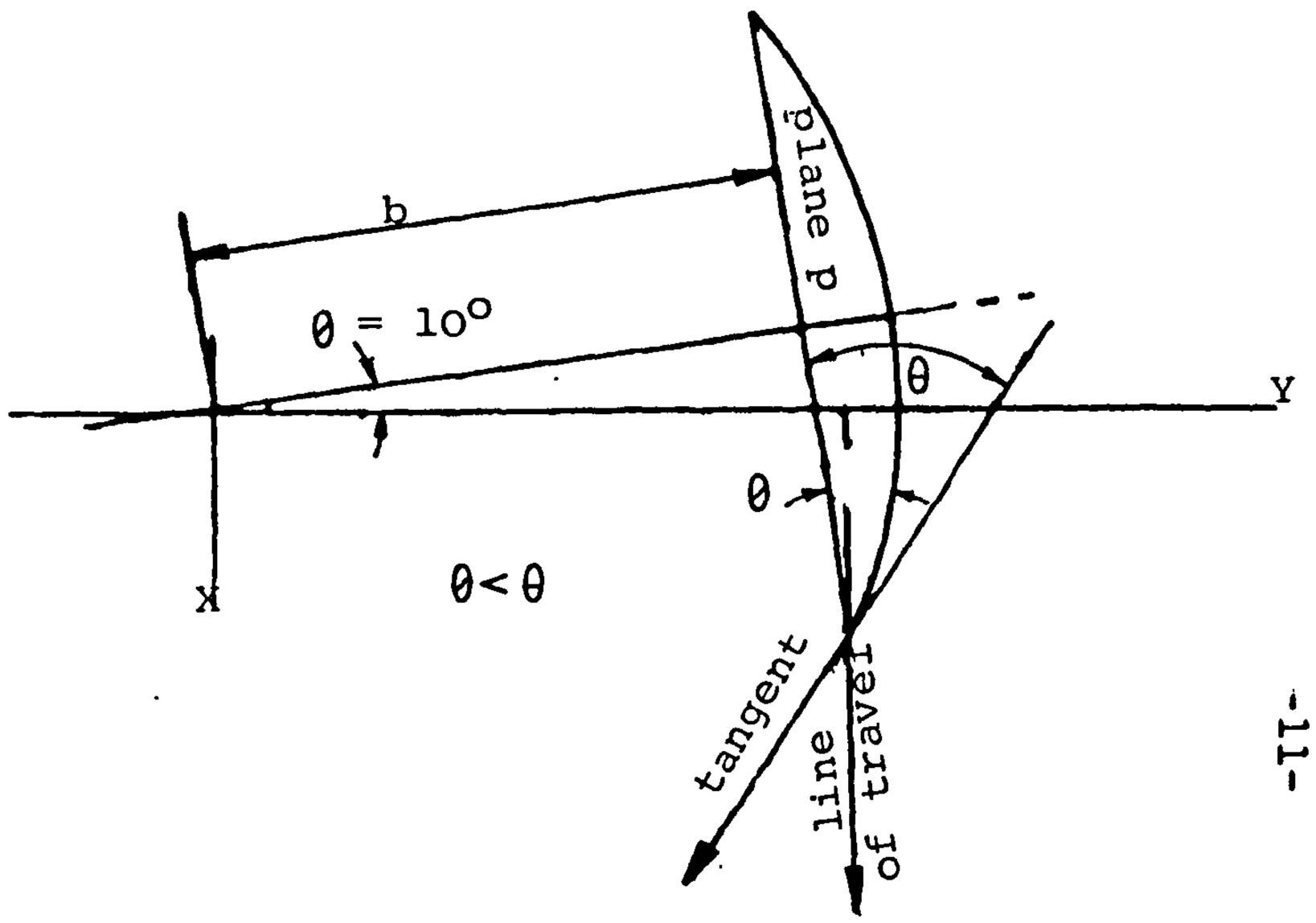

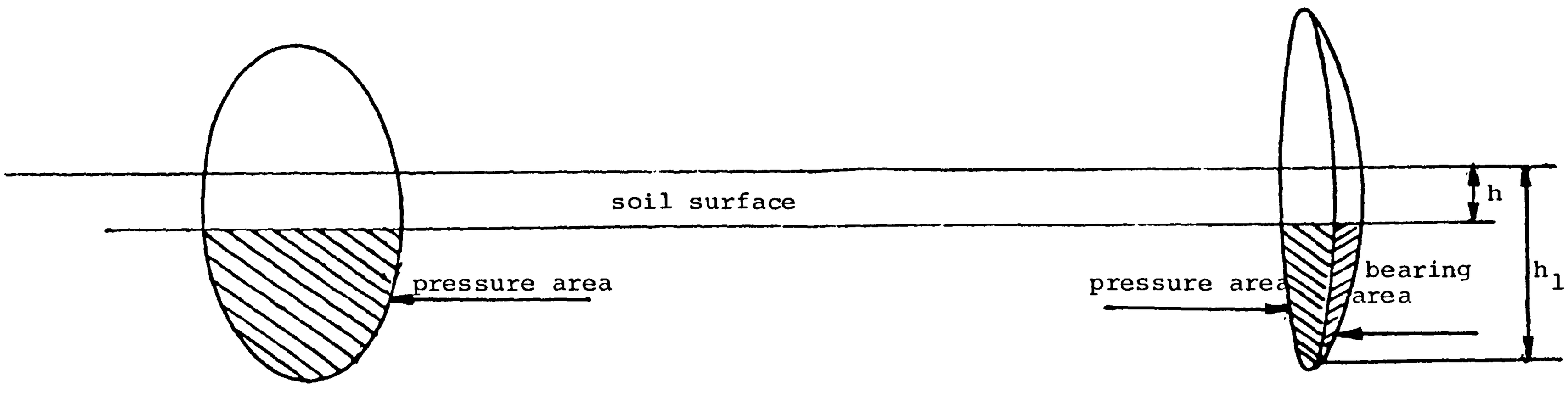

Figure 2.3. Vertical bearing area and vertical pressure area at two disc angles (McCreery and Nichols, 1956)

of the disc will be engaged on the soil. McCreery and Nichols (1956) determined the values of critical disc angles θ graphically and they used the fact that when θ is equal to the angle of Ø, the angle θ is the same as the angle at the centre of the arc between r1 and r2 as shown in Fig. 2.3. However, the graphical determination of these critical values is inflexible and is not an algebraical determination. They studied the pressure area on the front of the disc and the bearing area on the back of the disc at angles of 30^{o} and 10^{o} with respect to the line of travel as shown in Fig. 2.3. McCreery and Nichols (1956) calculated and tabulated these areas for four common 24 in (600 mm) discs having different curvatures when they were set at various angles. McCreery and Nichols (1956) did not show how these areas were calculated but they did conduct a mathematical analysis for these values which they omitted from the paper because of the complexity of the formula used in their calculations. They reported that the bearing area on the edge of the disc is affected by the sharpening technique of the disc. They also indicated that if the sharpening is on the convex back of the disc, the bearing area increases by an amount based on the thickness of the disc. They mentioned that if the sharpening is on the concave face of the disc the bearing area decreases for a disc at any given angle. For the rotation of the disc, they developed an equation in terms of forward speed, rotation of the disc and disc angles and they found out that the relationship of

forward speed to rotation of the disc is a function of disc angle as shown below:

$$T = \frac{C}{\cos \phi} \qquad \text{.....(2.1.)}$$

where

T = Forward travel in revolutions

C = One revolution or circumference

Ø = Disc angle

2.4. The work of Barnes et al.

Barnes et al (1960) used the Buckingham Pi theorem as described by Murphy (1950) to predict the draught components of the soil reaction on a prototype disc tool by studying the component of a model disc implement. They determined the Pi terms needed to express the relation from two groups of variables. Each group of variables was based on the way in which the soil description was given. The first soil description used the soil physical properties of bulk density, moisture content, clay content and angle of soil-metal friction suggested by Nichols (1931). In the second soil description, they studied the soil mechanical properties of bulk density , apparent cohesion, angle of shearing resistance, angle of soil-metal friction and apparent adhesion suggested by Payne (1956). Each system of soil variables

was studied in conjunction with disc variables of the disc diameter, another pertinent length such as the radius of curvature or the curvature of the disc, the disc angle and the tilt angle,forward speed and the acceleration due to gravity. The independent variable was the draught force or the horizontal component of the soil reaction force on the disc. Barnes et al (1960) concluded that the distorted model approach using shear properties of soil shows a more precise prediction than the approach depending on the mechanical analysis of the soil. Barnes et al (1960) observed that the prediction of the minimum-disc angle for minimum draught force depended on a better understanding of the disc geometry and soil-disc interface properties.

2.5. The work of Johnston and Birtwistle

Johnston and Birtwistle (1963) determined the effect of the tilt angle, disc angle, velocity of operation, disc diameter, disc concavity, width and depth of furrow on the soil forces. The purpose of their study was to determine some of the required disc tool force information to ensure the best power economy. They studied the resultant forces of draught, vertical and side components as a force per unit area of furrow. They reported that the minimum rearward draught force occurred over a wide range of values of disc angle. They also pointed out that the angle of minimum draught was a function of a number of other variables

such as the manner of edge sharpening, the furrow width and soil type.

It should be mentioned here that Gordon (1941) studied each force component as a whole and not per unit area of furrow cross section as showed by Johnston and Birtwistle (1963). This may be one of the reasons that the results of the forces varied between their works. They reported that the diameter of the disc and concavity, the depth and furrow width were found non-significant on the draught force. They observed that the side force per unit area of furrow cross section increases with disc diameter and disc angle while the effect of depth was negligible with disc 23½ in and negative with a disc 20 in. Johnston and Birtwistle (1963) indicated that the minimum vertical force per unit area of furrow cross section occurred at a disc angle of 50^{o} and a tilt angle of 10^{o}.

2.6. The work of Taylor

Taylor (1967) studied the effect of tilt and disc angle, width of cut and speed of operation on three components of soil force reaction of soil on wheatland plough discs. It may be mentioned here that the study was for tilt axis discs although Kepner et al (1978) defined these discs as vertical discs. Taylor (1967) measured the forces

by using a trailed rig. The tests were carried out in two soils of silt clay and sandy clay loam at a depth of 3½ in and 5 in respectively. Taylor (1967) analysed the resultant forces statistically. He determined polynomial regression equations between each soil force component and the variables mentioned above taking the effect of their interaction into account. He reported that as the disc angle increases, the draught increases. The total width of cut increases as the disc angle increases and the draught is minimized at maximum width of cut by using the smallest possible angle. Taylor (1967) reported that the side force is at a minimum at high tilt angles, possibly combined with small disc angles. He explained this behaviour as resulting from increasing interference on the back of the disc. He also indicated that the side force increases with speed and increases more than proportionally to width of cut. He determined that the vertical force was increased as the disc angle was decreased and increased sharply at the small values of disc angle. The width and speed had little effect on V.

2.7. The work of Gill et al.

Gill et al (1976) studied the irregularity of soil disturbance depth by circular and rotating soil-cutting tools: disc harrows, disc ploughs and rotary tillers. They determined methods for assessing the nature of the irregularities

of the bottom of the tilled layer of the soil. They indicated that the areas of the furrow bottom which remain undisturbed have the shape of cusps and the net effect is ridging of the bottom of the furrow. Gill et al (1976) pointed out that when the ridging is small the depth of operation is nearly uniform. In disc ploughs, they noticed that the disc tilt creates ridges that are not symmetrical on each side of the cusp. Gill et al (1981 a) studied the depth of operation and width of cut which they used to influence forces on nine test discs. They used various widths and depths of cut for three shapes and three sizes of discs operating at a constant disc angle of 21.8^{o} (0.38 rad) and a constant velocity at 1.3 m/s in two different soils.

Gill et al (1981 a) measured the critical disc angles at selected depths by using two straight edges horizontally at the leading edge of the vertical mounted disc, one through the plane of the disc and the other tangent to the back surface of the disc, using a protractor to measure the critical angles between the two lines. They used this practical method because the discs they used did not have completely regular shapes. The critical disc angle may be calculated by the method reported by Harrison and Thivavarnvongs (1976) if the discs are part of a true sphere or cone. It should be indicated that Harrison and Thivavarnvongs (1976) suggested a graphical method to

determine the critical disc angle which it is better than the practical method used by Gill et al (1981 a) when there is no convenient equation to determine the critical disc angle for double concavity discs. They reported that the draught, side and vertical forces are influenced by the width of cut. They also pointed out that the minimum specific draught occurred when the width of cut is equal to the projected width of the disc. Gill et al (1980 a) concluded that both disc angle and disc shape influence on the forces on a large disc.

Gill et al (1980 b) showed that the ground-driven rotation of discs with a small bearing area on the convex side of the disc is greater than that of comparable spherical discs with higher pressure on the back of the disc operating in the same soil and operational conditions. Gill et al (1981 b) indicated that increasing the disc radius of curvature reduces the value of the vertical forces when the disc angle is between 11.46 - 17.18^{o} (0.2 - 0.3 rad). They also pointed out a quantitative relationship between radius of curvature, speed, disc angle, and the magnitude of the vertical force, when the disc was kept at a constant depth of cut. They showed that increasing the radius of curvature of the disc and/ or increasing the disc angle in a range of 0.2 - 0.3 rad resulted in a reduced force on the back of the disc and a reduction on the magnitude of vertical and draught forces.

Gill et al (1982) showed that increasing the weight on discs increased the penetration at all disc angles. They also indicated that decreasing the radius of curvature with large disc angle resulted in deeper penetration than occurs with larger radius of curvature of the disc because the increase of the curvature on the front face of the disc provides an increase in downward force component on the soil.

2.8. The work of Abo El Eas and Wills

Abo El Eas and Wills (1986) studied the geometry of a disc with a horizontal axis and related it to the soil interraction in terms of projected areas and volumes both on the face and back of the disc. Their work was similar to the pioneering work of McCreery and Nichols (1956) but they went further into investigating and studying the geometry of the disc and relate it to an understanding of soil reaction. Abo El Eas and Wills (1986) defined the disc geometry mathematically and relate it to the soil-disc interface by knowing the radius of curvature, the disc diameter and the depth of cut. They determined mathematically the critical disc angle and the critical depth in terms of the chord and the radius of the disc. The equations that were developed determine the projected bearing areas on the back of the disc on the horizontal and vertical planes perpendicular to the direction of

travel and the soil volume disturbance on the convex back side of the disc. They also analysed mathematically the vertical pressure area on the face of the disc on both the vertical and horizontal planes normal to the direction of motion and the weight of the soil on the concave side of the disc.

2.9. The work of Godwin et al.

Godwin et al (1987) developed a model based on Mohr-Coulomb theory to predict the forces acting on vertical discs. Their model was developed based upon (i) the passive soil cutting solution derived by Hettiaratchi et al (1966 and 1974) to determine the passive reaction on the face of the disc and (ii) the bearing capacity solution developed by Meyerhof (1961) to determine the scrubbing forces on the back of the disc. Godwin et al (1987) reported that their model (i) adequately reflected the effect of changing the depth of cut, the radius of curvature of the disc and disc angle, and (ii) that the model proved satisfactory for new disc design when used with stress analysis techniques. This model is the first attempt to predict disc forces using Mohr-Coulomb theory.

With regard to the magnitudes of forces, the authors showed that the draught and vertical passive force components

decrease with decreasing disc angle, and the side force increases to a maximum at a disc angle of 45^{o} and then decreases. On the other hand, they observed that the values of the draught, vertical and side force components on the scrubbing reaction were maximum at disc angle of 0^{o} and reduced to zero when the disc was rotated until the angle reached the critical disc angle. This study was used for both spherical and conical discs working at 0.1 m and 0.04 m depth with disc angles from 0^{o} to 90^{o}.

Godwin et al (1987) pointed out that there is no soil surcharge on the back of the disc and the weight effects on the scrubbing reaction can be ignored as the depth of cut is relatively shallow. These factors will be taken into account by the author when a model is developed based on Mohr-Coulomb theory to predict the forces acting on the tilt discs.

2.10. Conclusions

Considerable research has been conducted into the effects of the primary geometric variables upon the soil forces acting upon agricultural discs. Little work, however, has been conducted upon the effect of these variables on soil flow and degree of inversion or the effect of different sharpening methods upon disc activity. Although soil forces have been calculated using Mohr-Coulomb soil mechanics

for discs with horizontal axes,(Godwin et al, 1987), no attempt has been made to link this to the geometric characteristics of discs whose axes are inclined to the vertical. It is the intention of the author to rectify these shortcomings in the following chapters.

CHAPTER 3

3. Materials and method of investigations

3.1. Introduction

The investigations described in this chapter were carried out in the laboratory soil bin developed at the College. The soil bin was used because the standardised soil treatment would produce a homogeneous and repeatable media, whilst field tests would reduce the effectiveness of any comparison due to the poor homogeneity of the soil and changeability of the weather. The review of the literature reported in Chapter 2 reveals that most previous work has been concerned with vertical discs and apparently little consideration has been given to the outside sharpening bevel with its limitation of tilt angles. Therefore, it was considered important to investigate the mechanics of tilt disc blades with a view to develop a suitable prediction model based on the Mohr-Coulomb soil mechanics and blade parameters.

3.2. Plan of investigation

In order to determine the mechanics of the disc it was decided to use the variables listed below to measure the draught, vertical and side forces.

1. A range of disc angles between 15^{o} and 60^{o}.

2. A range of tilt angles between 0^{o} and 35^{o}.

3. A range of depth of cut between 80 and 140 mm.

4. A range of speed between .75 and 1.5 m/sec.

5. Two disc concavities with varying sharpening techniques (outside and inside). Three series of tests were carried out:

(i) In the first series of tests nine disc angles of 15^{o}, 20^{o}, 25^{o}, 30^{o}, 35^{o}, 40^{o}, 45^{o}, 55^{o}, and 60^{o} and four tilt angles of 0^{o}, 20^{o}, 30^{o}, and 35^{o} were studied. The depth of cut, 140 mm, and speed, 0.386 m/sec, were held constant. Two discs of shallow concavity each with inside concave face sharpening and outside convex face sharpening were used. A full factorial experimental design was used which included combining all factors at all levels. In this study, however, with nine disc angles, four tilt angles and two shallow discs with three replications, this required two hundred and sixteen test runs. The same factorial design was repeated for the two deep discs with outside convex face sharpening and inside concave face sharpening.

For the deep disc with inside sharpening, five disc angles of 35°, 40°, 45°, 55°, and 60°, three tilt angles of 0°, 20°, and 30° and three replications were used. The deep disc with outside sharpening was operated at four disc angles of 40°, 45°, 55°, and 60°, and three tilt angles of 0°, 20°, and 30° with three replications. The total of test runs for these experiments were two hundred and ninety seven for the two disc concavities each with outside and inside sharpening. The randomization of the four disc concavities was used to give confidence in the soil preparations of the soil bin.

For every tilt angle change, a precut was made to create the correct shape of furrow wall for the following main cut disc pass. The gang spacing between the main cuts was based upon the disc angles, radius of the disc, and the depth of operation. It was decided to use 120 mm, 130 mm, 140 mm, 160 mm, 180 mm, 190 mm, 200 mm, 220 mm, and 240 mm between the main cut for the disc angle of 15°, 20°, 25°, 30°, 35°, 40°, 45°, 55°, and 60° respectively. For every tilt angle change, the carrier height was adjusted to maintain the depth of operation at 140 mm.

(ii) The second series of tests was designed to evaluate the influence of depth of operation on the

forces produced by a range of disc and tilt angles. Three different depths of 80 mm, 100 mm and 140 mm were used. The forward speed of 0.386 m/sec was held constant. The same two disc concavities each with inside concave sharpening and outside convex sharpening were used. A full factorial design would be considered for these experiments.

In this study, to complete the programme, with three replications, the total test would have required eight hundred and ninety one runs, which would consume a great deal of time. The alternative was to use an experimental programme based upon response surface analysis, as designed by Box and Wilson (1951), to reduce the number of individual runs. The number of test runs needed to cover the same range of disc and tilt angles as above was reduced to one hundred and sixty two runs for both disc concavities each with inside and outside sharpening. Five combinations of disc (15^{o}, 30^{o}, and 60^{o}) and tilt angles (0^{o}, 20^{o}, and 35^{o}) were studied, selected from the first series of test runs for the shallow concavity inside and outside sharpening. The other two deep concavity discs with inside and outside sharpening were operated at four combinations of disc (35^{o}, 40^{o}, and 60^{o}) and tilt angles of 0^{o}, 20^{o}, and 30^{o}, selected from the first series of tests.

At depth of 80 mm, the gang spacings between the main cuts of soil were 100 mm, 120 mm, 130 mm, 135 mm and 180 mm for disc angles of 15^{o}, 30^{o}, 35^{o}, 40^{o}, and 60^{o} respectively. The gang spacings for depth of 100 mm were 110 mm, 130 mm, 140 mm, 150 mm and 200 mm for the same disc angles used respectively as above. All other procedures were maintained as in the first series of tests.

(iii) In the third series of tests the objective was to evaluate the effects of different forward velocities on the forces produced by a varying range of disc and tilt angles. In this study, the same disc and tilt angle combinations as in the second series of tests for both disc concavities with inside and outside bevels were studied. The depth of cut of 140 mm was held constant. Three different velocities of 0.75 m/sec, 1 m/sec, and 1.5 m/sec were used. At the higher speeds of 1.5 m/sec and medium speed of 1 m/sec, the bridge outputs were recorded for one and two sections of the bin respectively due to the shorter time available for the analyser to record the next point. At low speed of 0.75 m/sec, the analyser sampled three sections of the soil bin run which were used as sub-samples of each replicate. This procedure was maintained throughout all low speed tests.

3.3. General description of the new soil bin

A soil bin designed and developed by Godwin et al (1980) was used extensively over a period of 16 years in the College. However, because of a number of severe limitations of this bin, a replacement soil bin was designed and developed in 1986 as shown in Fig. 3.1. The new bin uses a similar principle for soil handling as the old, albeit with mechanical assistance at each stage. The main characteristics of the soil bin and related equipment are described below:

i. The effective length of the bin is approximately 20 m. The width and the depth of the bin are 1.7 m and 1.0 m respectively. The maximum depth of soil is 0.8 m. The bin is sunk into the floor of a heated and well-lit clear-span building with 4 m x 4 m vehicular access doors.

ii. A diesel engine of 75 kW with a variable speed hydraulic transmission was selected to operate the soil processor, which runs on steel rails at the edge of the bin and is winched along in either direction by two endless steel cables.

iii. The soil processor contains a grab bucket, scraper blades, roller and a reciprocating set of tines for all soil preparation. A 6 kW electric motor, which

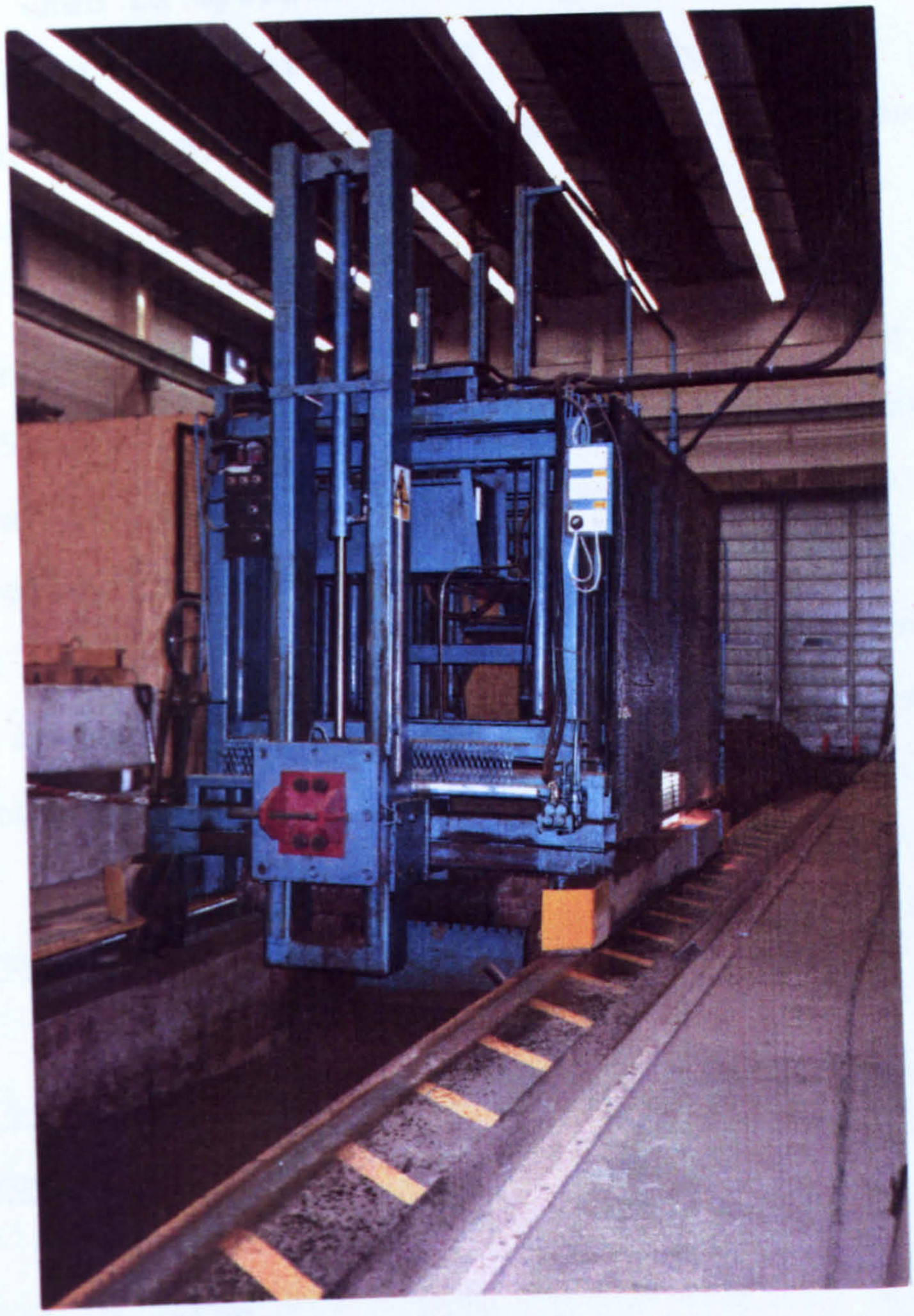

Figure 3.1. General view of soil implement research laboratory

is supplied from three phase cables on a sliding rail is used to operate various hydraulic controls. An overhead gantry crane of 2 tonnes capacity is used for mounting the implements or the experimental apparatus.

iv. The forward speed of the soil processing trolley is up to 5 m/sec. It was possible to carry out six preparations and tests in an 8 hour working day. The trolley is normally under the complete control of the operator seated on board. In an emergency, there are limit switches in the bin and manual shut-down controls in the adjacent data processing room.

3.4. Instrumentation

3.4.1. An octagonal ring transducer for three dimensional force measurements

3.4.1.1. Introduction

During asymmetrical tillage tool/soil interaction studies, a knowledge of the three forces components and moments are important. A literature review indicates that different techniques have been used to determine the information needed to make such an assessment. Some researchers obtained information on all three force compon-

ents and moments about the three force principal axes, but others did not. Clyde (1937) attached the tillage tool to a triangular subframe which was held in a main frame by six hydraulic transducers to measure the direction and magnitude of the resultant force. Rogers (1955) and Morling (1963) used the same frame but they used six strain gauge ring type transducers. Payne (1956) and Tanner (1960) suspended the tillage tool from a series of single dynamometers for measuring the horizontal and vertical forces. Hendrick and Buchele (1963) used a dynamometer with attached strain gauges to measure horizontal force, vertical force and bending moment. Siemens (1963) used the octagonal transducer to determine the force on model blades. Siemens et al (1965) and Godwin (1975) used an extended octagonal ring transducer to measure the horizontal and vertical force components and the resulting moment. An extended octagonal ring transducer was also used by Boyd and Neelezny (1967) to measure the forces on vibrating telephone cable laying tines. Chisholm (1970) used a dynamometer to determine more complete information on force and moment. Seig (1982) mounted a cantilever beam onto an extended octagonal ring transducer to measure the side force.

3.4.1.2. Transducer design

The transducer based upon the extended ring principle was designed using the design data of Cook and Rabinowicz

(1963) and Godwin (1975). The details of this design are given in Appendix 2. It was designed to measure the horizontal, the vertical, the side force and the moments in the plane of each of these three forces. The extended octagonal transducer included two rings and a torque tube as shown in Figure 3.2. and Figure 3.3. First ring was developed to measure the horizontal force Fx1, the vertical force Fz, and the resulting moment Mdv. The second ring was perpendicular to the first ring and included the horizontal force Fx2, the side force Fs and the moment Mds. The torque tube was mounted perpendicular to both rings to measure the moments Msv1 and Msv2.

The strain gauges were mounted on the transducer rings and the tube and wired into Wheatstone bridge circuits as shown in Figure 3.4. The strain gauges should be bonded at angles of $\theta = 50^{o}$ and 90^{o} after the recommendation of Siemens (1963) in accordance with the photoelastic determination by Cook and Rabinowicz (1963) for the octagonal ring transducer. At these angles which located the stress nodes, the gauges were mounted to measure the vertical and horizontal forces respectively where the resulting moments from the eccentric horizontal and vertical forces respectively are equal to zero. Siemens (1963) reported that cross-sensitivity was no greater than 2% at these locations.

The position of the stress node was dependent on the

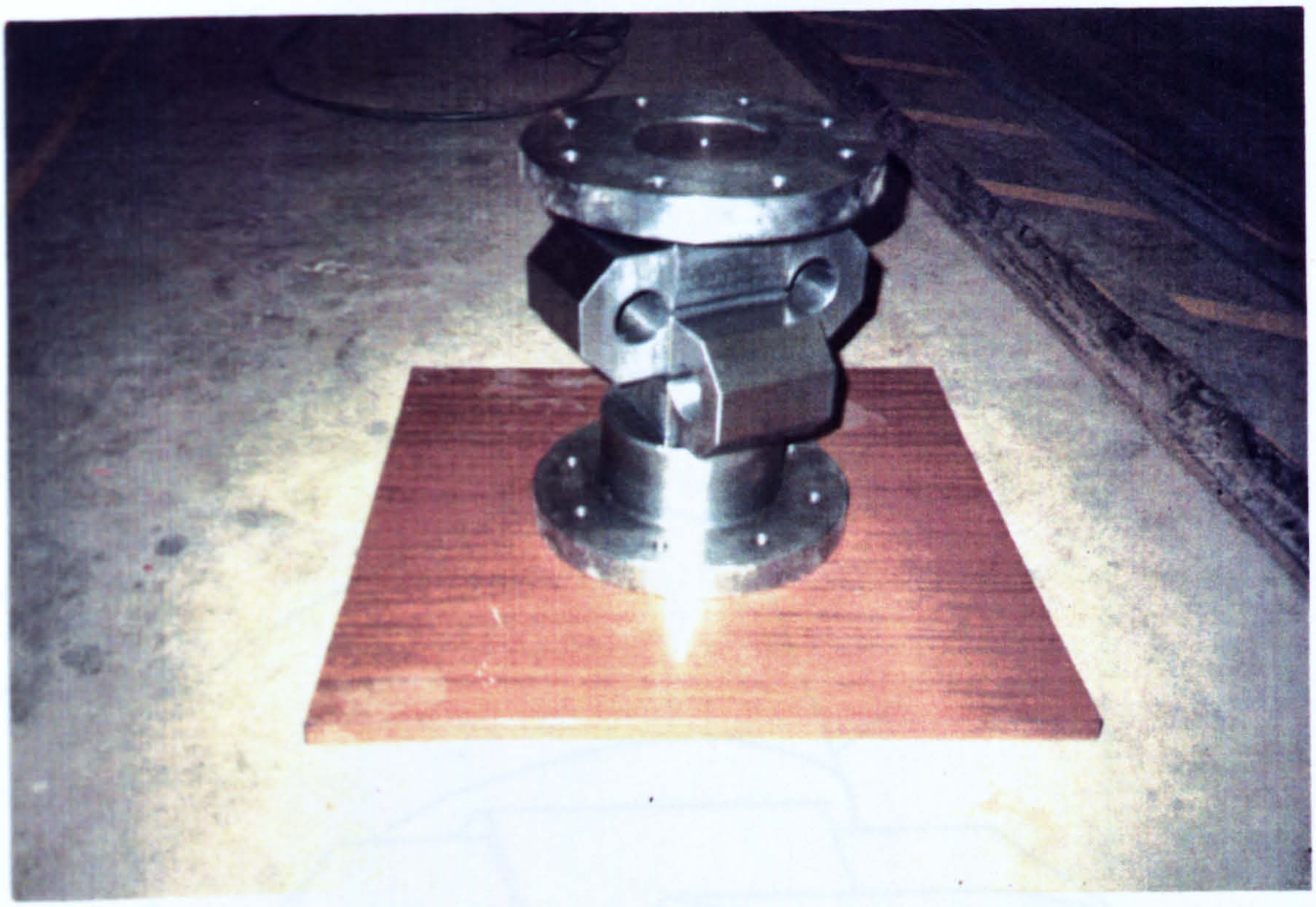

Figure 3.2. The transducer

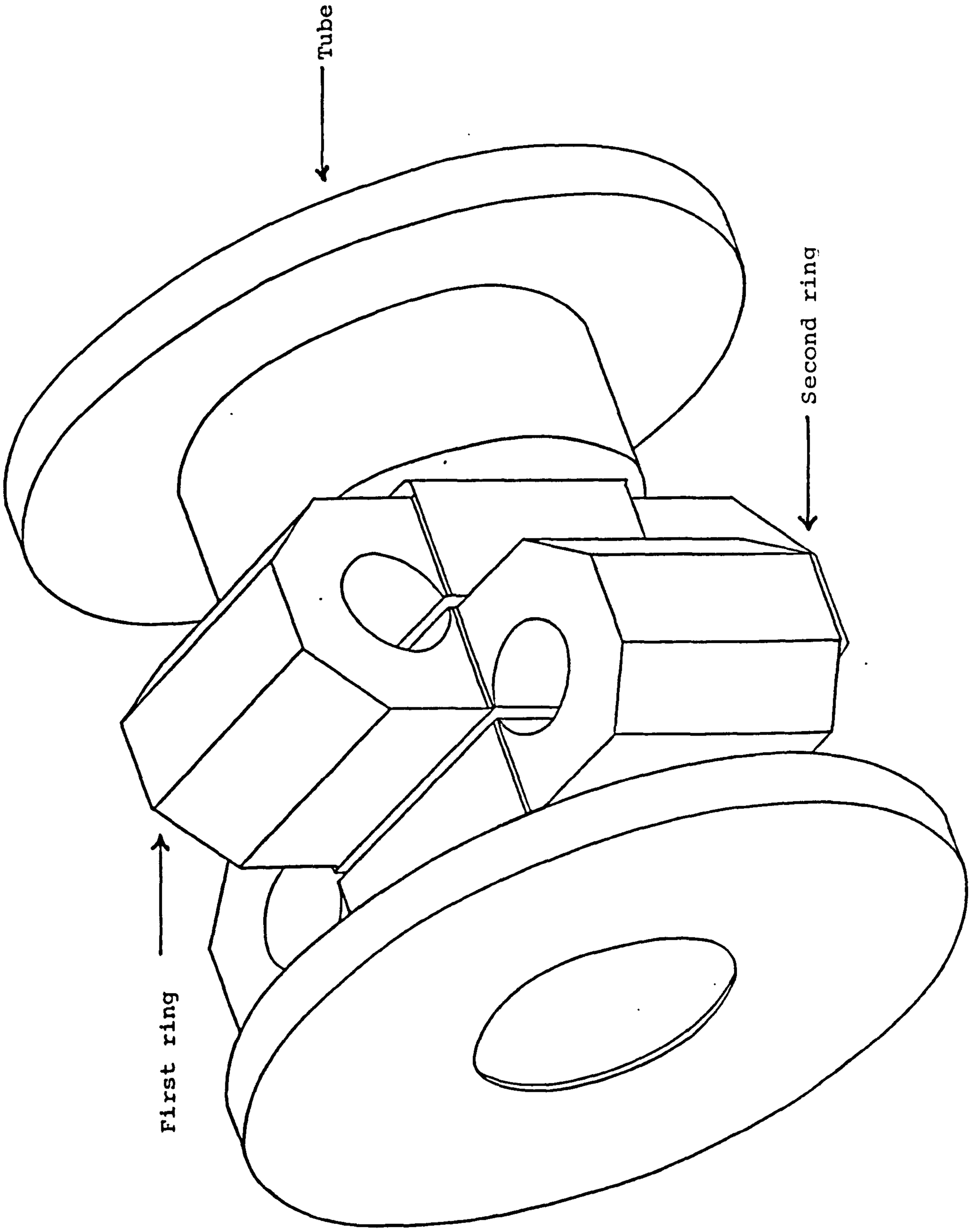

Figure 3.3. Asymmetric view of the transducer

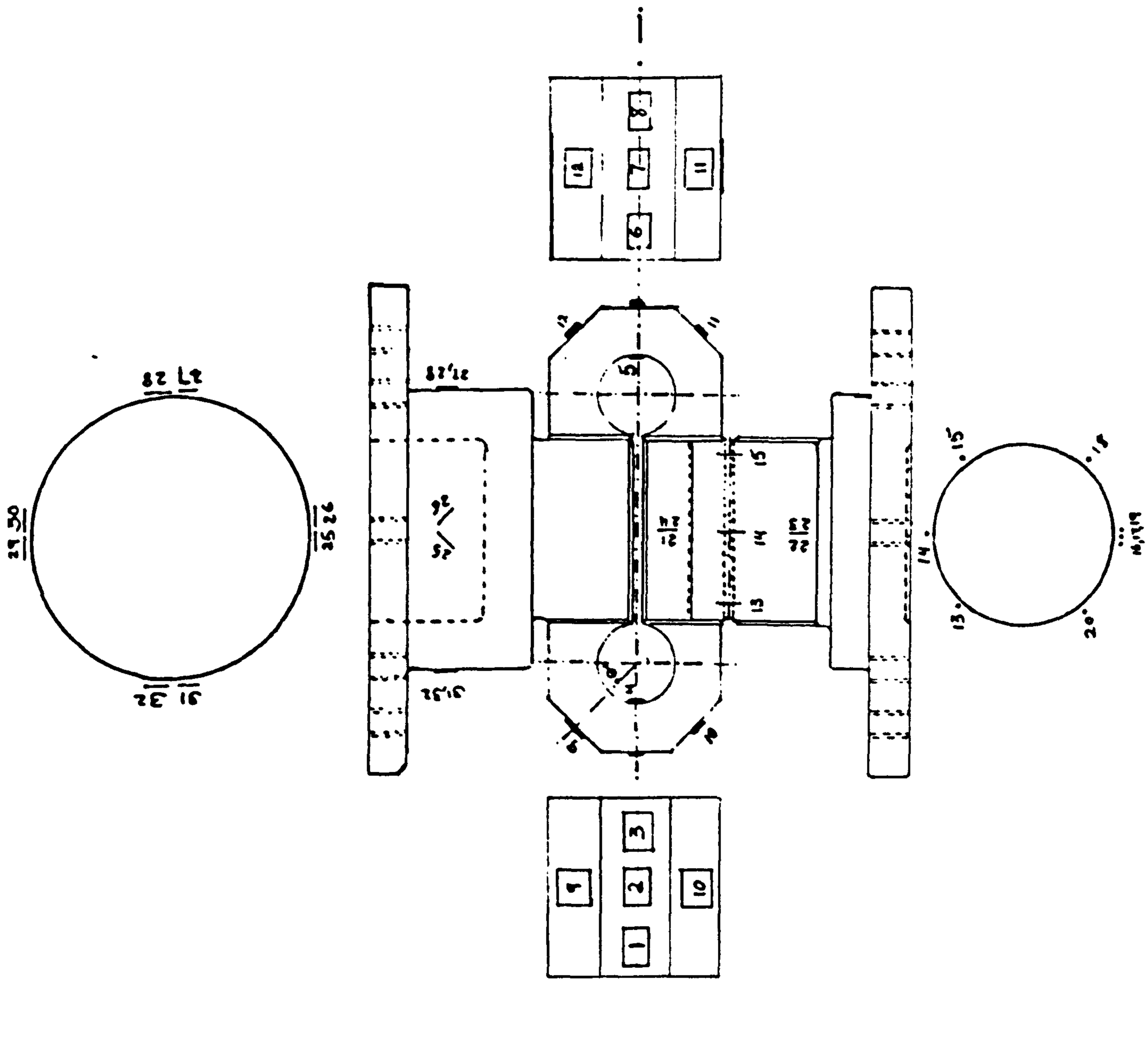

Figure 3.4. Transducer bridge circuit

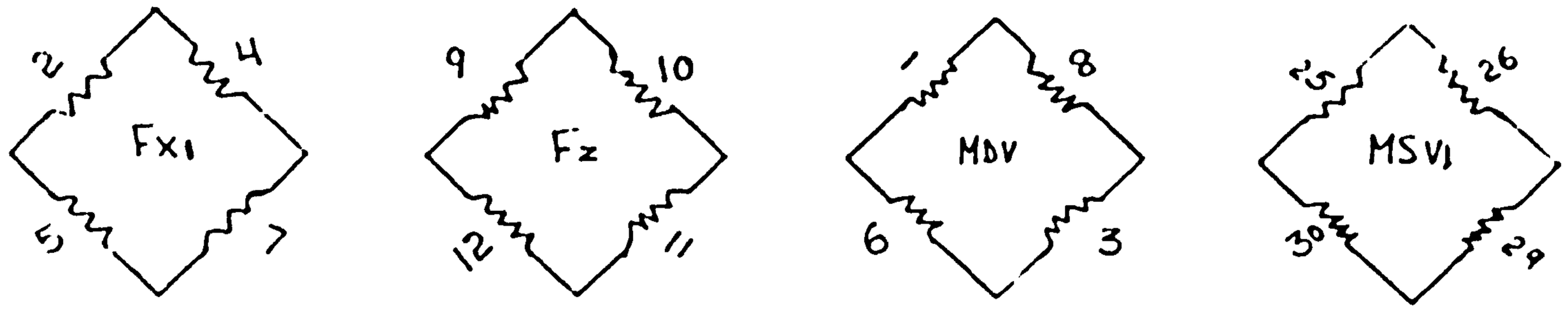

Figure 3.4. (cont'd) Transducer bridge circuit

angular limits of the ring element. This was obtained by applying a mathematical solution dependent upon the strain energy theory developed by Cook and Rabinowicz (1963) as shown in Appendix 3. The details of calculation of the position of the stress nodes were determined as follows:

i. For a simple circular ring transducer, the resulting in stress nodes at located angles of $\theta = 39.6^{\circ}$ and $\theta = 90^{\circ}$ with the limits of integration of $\theta = 0$ and π.

ii. For an octagonal ring transducer, the calculated stress nodes are located at angles of $\theta = 27.3^{\circ}$ and $\theta = 90^{\circ}$ within the limits of integration for the ring section reduced to $\theta = \pm .133\pi$ and $\theta = 1.133\pi$.

In order to verify the mathematical solution using strain energy theory for the position of the stress nodes for the extended octagonal ring transducer the strain gauges were placed at different angular locations: 34°, 27.3°, 25°, and 23° along the face AB of the ring after the recommendation of Godwin (1974) as shown in Figure 3.5a. Each gauge was wired in turn with 3 high stability 120 ohm resistances to obtain a four-arm bridge. The output from this bridge depending upon applied Fx and Fz load is shown in Figure 3.5b. The calculated angles of $\theta 27.3^{\circ}$ and $\theta = 90^{\circ}$ were actually used to locate the position of the nodes.

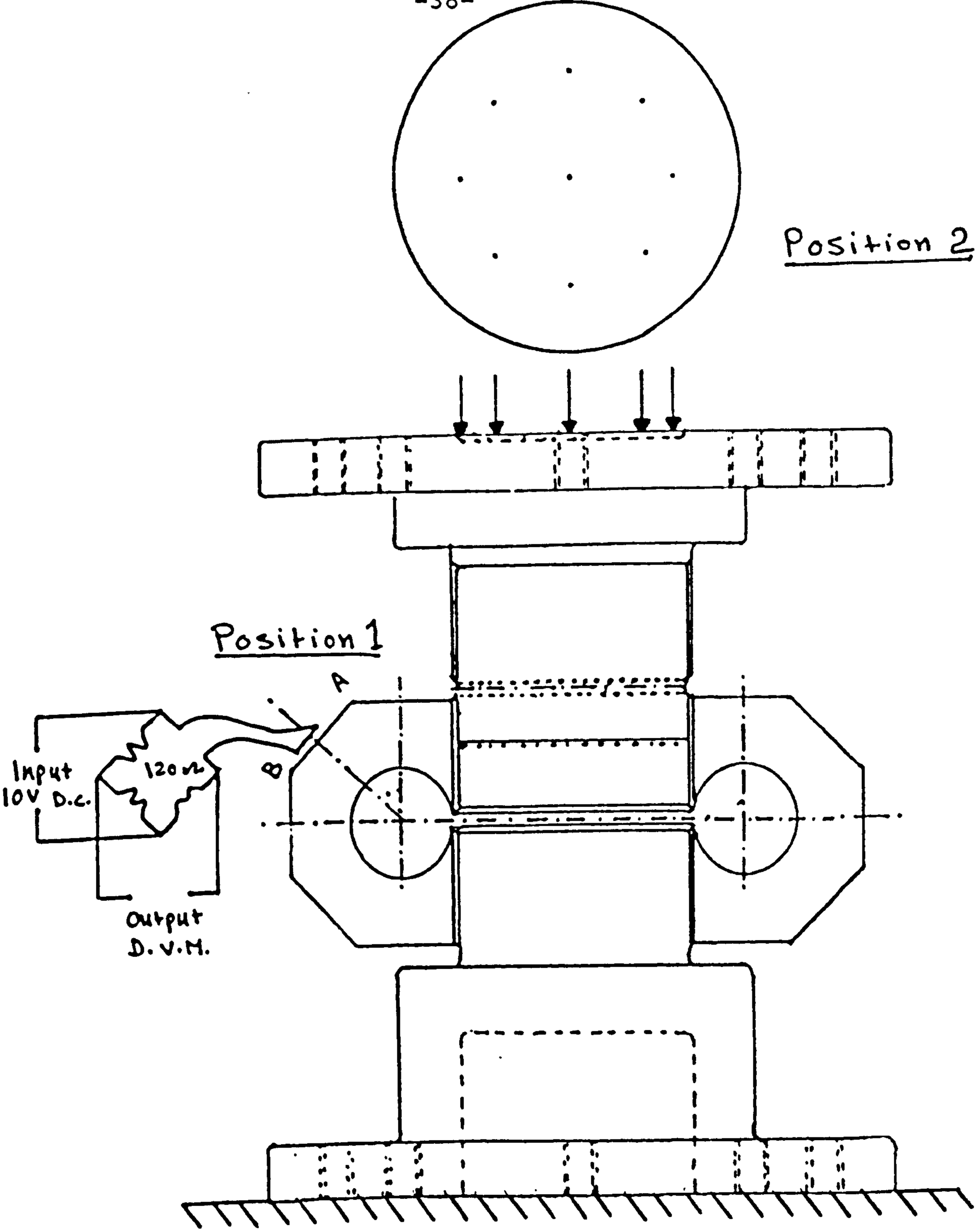

Figure 3.5.a. Diagrammatical representation of the method used to determine the strain nodes on Face AB of the transducer

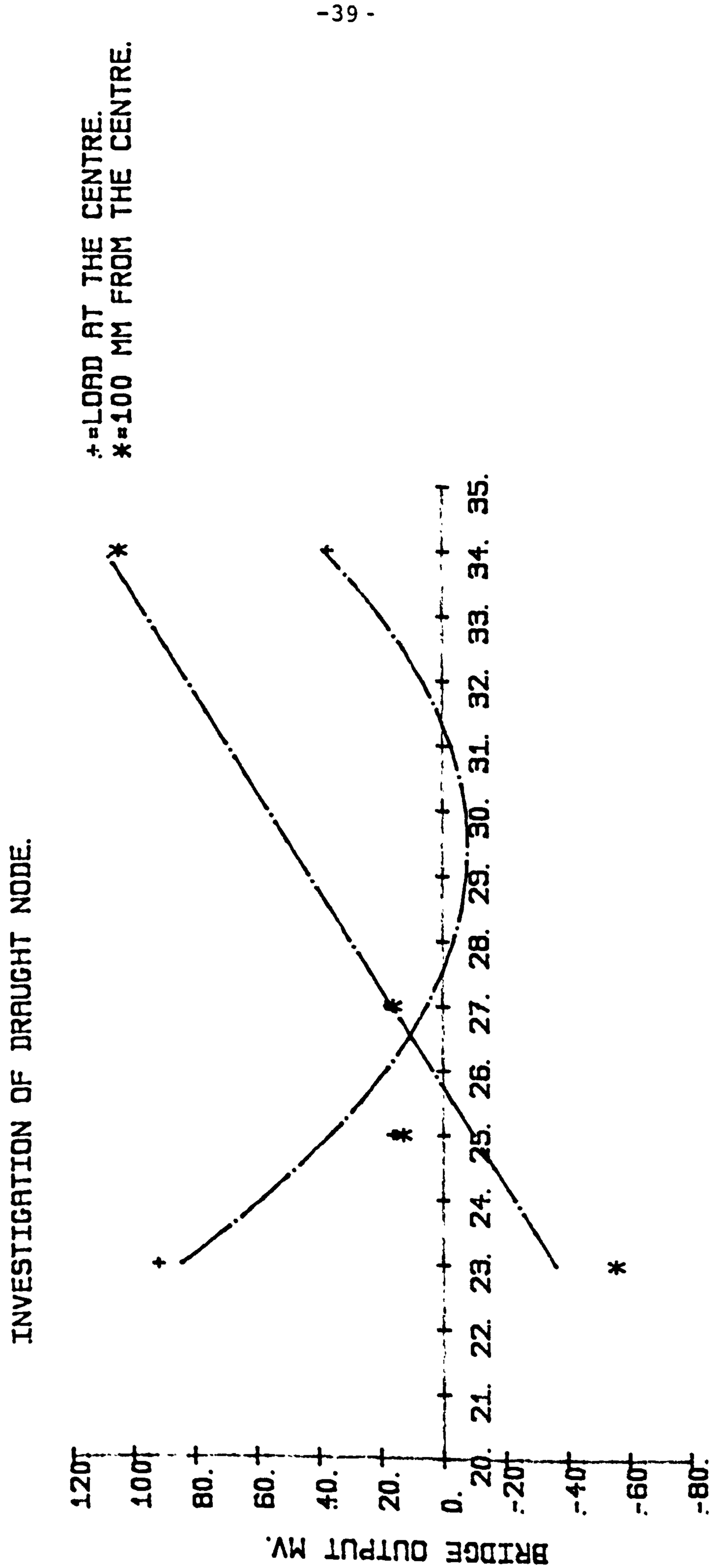

Figure 3.5.b Graph of bridge output against gauge position

The overall location of the strain gauges are shown in detail in Appendix 4. The strain gauges of the torque tube were attached at $\pm 45^{o}$ after the recommendation of Cook and Rabinowicz (1963).

3.4.1.3. Transducer calibration

A series of calibrations were used to determine the sensitivity of the channels, cross-sensitivity errors, position sensitivity, hysteresis and repeatability of the transducer outputs. The transducer was mounted on a loading floor straddled by a massive loading frame as shown in Figure 3.6. Three tension load cells were used to measure the draught, vertical and side forces. Each load cell was calibrated by a static weight test and on a universal testing machine to determine the characteristics of each. Details of the calibration of the tension load cells are shown in Appendix 1.

The tension load cells were attached to the load arm application points by chains. Three hydraulic rams were used to apply the three forces through the load cells. Strain gauge amplifiers were used to match the outputs of both the load cells and transducer circults to the recording apparatus. Before each calibration, the reference zero, gain and bridge supply were checked for each channel of the

Figure 3.6.a. The hydraulic load calibration of the transducer

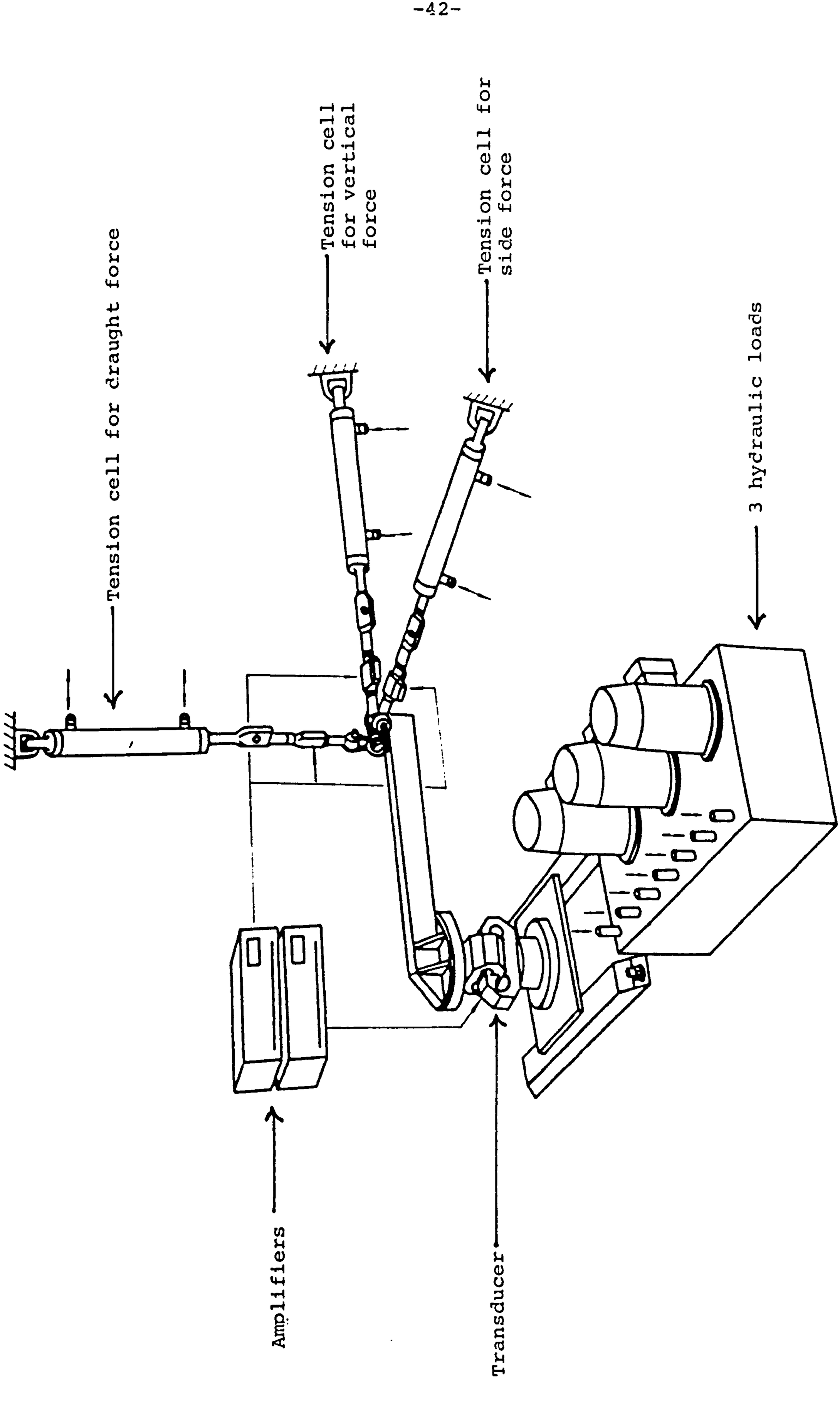

Figure 3.6.b. Diagrammatical representation of the hydraulic load calibration of transducer

amplifiers using shunt resistances to calibrate the relevant signal levels.

A range of loads (0.5 - 18 kN) were applied at 1000 mm, 900 mm and 800 mm from the centre of the transducer. By operating the hydraulic system, a different known load of tension load cells for draught force was applied to the transducer. The outputs from Fx1 and Fx2 were then reported from the second amplifier for the eight channels. The same procedure was used for calibrating vertical (Fz) and side (Fs) forces. Appendix 5 gives full details for the determination of the transducer characteristics.

3.4.1.4. Results of calibration

From the full detail in Appendix 5, the output from each of eight channels was observed as the following:

1. The transducer signal was highly linear with coefficients of determination of $r^2 = 0.9997$.

2. The error in the output of each strain gauge bridge circuit due to the position of the force was less than 2% which is acceptable within the expected working range of the transducer.

3. The cross-sensitivity error was less than 3% from

any other strain gauge circuit when a signal of known force was applied in one direction.

4. The output hysteresis effect was determined to be less than 1% and it was negative based on the hysteresis expected from the strain member. This phenomena is the net result of the combination of two hysteresis effects of opposing sense as explained by McFarland and Dimeff (1956).

5. The channel sensitivities were determined as follows:

$Fx1 = 9.8 \times 10^{-3}$ μv/N/v

$Fx2 = 1.1 \times 10^{-3}$ μv/N/v

$Fz = 4.3 \times 10^{-3}$ μv/N/v

$Fs = 4.8 \times 10^{-3}$ μv/N/v

$MVD = 4.4 \times 10^{-2}$ μv/Nm/v

$MSD = 3.7 \times 10^{-2}$ μv/Nm/v

$MSV1 = 1.4 \times 10^{-2}$ μv/Nm/v

$MSV2 = 1.6 \times 10^{-2}$ μv/Nm/v

6. The cross-sensitivities were determined as follows:

Fx1 and Fx2 effected on

i. Vertical, $Fz = 5.43 \times 10^{-4}$ μv/N/v

ii. Side, $Fs = 1.1 \times 10^{-3}$ μv/N/v

Fz effected on

i. Draught, Fx1 and Fx2 = 1.85×10^{-4} μv/N/v

ii. Side, Fs = 1.59×10^{-4} μv/N/v

Fs effected on

i. Draught, Fx1 and Fx2 = 3.94×10^{-4} μv/N/v

ii. Vertical, Fz = 1.77×10^{-4} μv/N/v

3.4.2. Signal condition and recording equipment

In this study, the signal conditioning and recording equipment is shown in Figure 3.7. The strain gauge bridge circuit outputs were amplified using DC differential amplifiers which both supplied the working potential for the strain gauge bridge circuit and amplified the voltage outputs. High impedance signals obtained from the strain gauge amplifier were connected to a digital analogue data logging unit which also incorporated shunt resistances and switches for electrical calibration of the strain gauge bridge.

By pressing the start and the stop buttons of the analyser over the predetermined test period, the data logger performs the analogue to digital conversion and the printer, which is connected to the analyser, prints the mean and the standard deviation of each circuit for the duration of the test. Three sets of readings were taken during each test

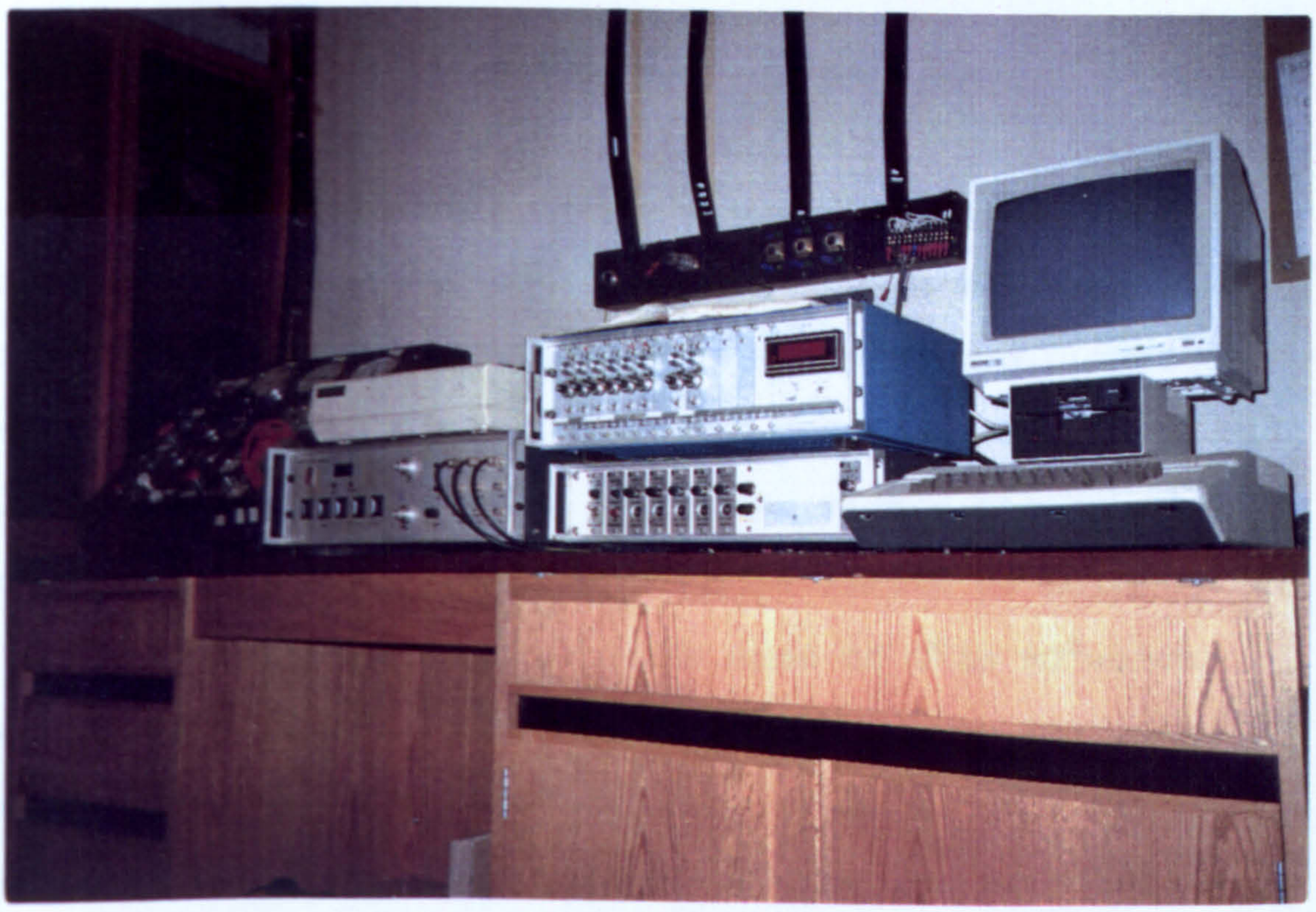

Figure 3.7. Data conditioning and recording instruments

run. Then, the output mean values were manually transformed to force units for each bridge circuit output. Before each test, the reference zero was checked for each channel of the amplifier, using the electrical calibration shunt resistances to give the relevant signal levels. Figure 3.8. shows this system diagrammatically.

3.4.3. Mounting of the transducer on the disc

The disc attachment assembly was fabricated to modify the existing disc axis to enable the disc to be varied in both the horizontal and vertical planes. The disc axis was tilted clockwise to the horizontal by drilling a series of holes in the frame within the span of 0^{o} to 75^{o}. For the disc angles, another series of holes was drilled in the plate within the span of 0^{o} to 90^{o} which mounted on the frame. The disc and tilt angles increase by steps of 2.5^{o}. The frame was fabricated so that it could be held by mounting it directly onto the extended octagonal transducer as shown in Figure 3.9.

3.5. Methodology

3.5.1. The soil

A sandy loam soil was used for the investigation. The mechanical analysis of the soil was determined using

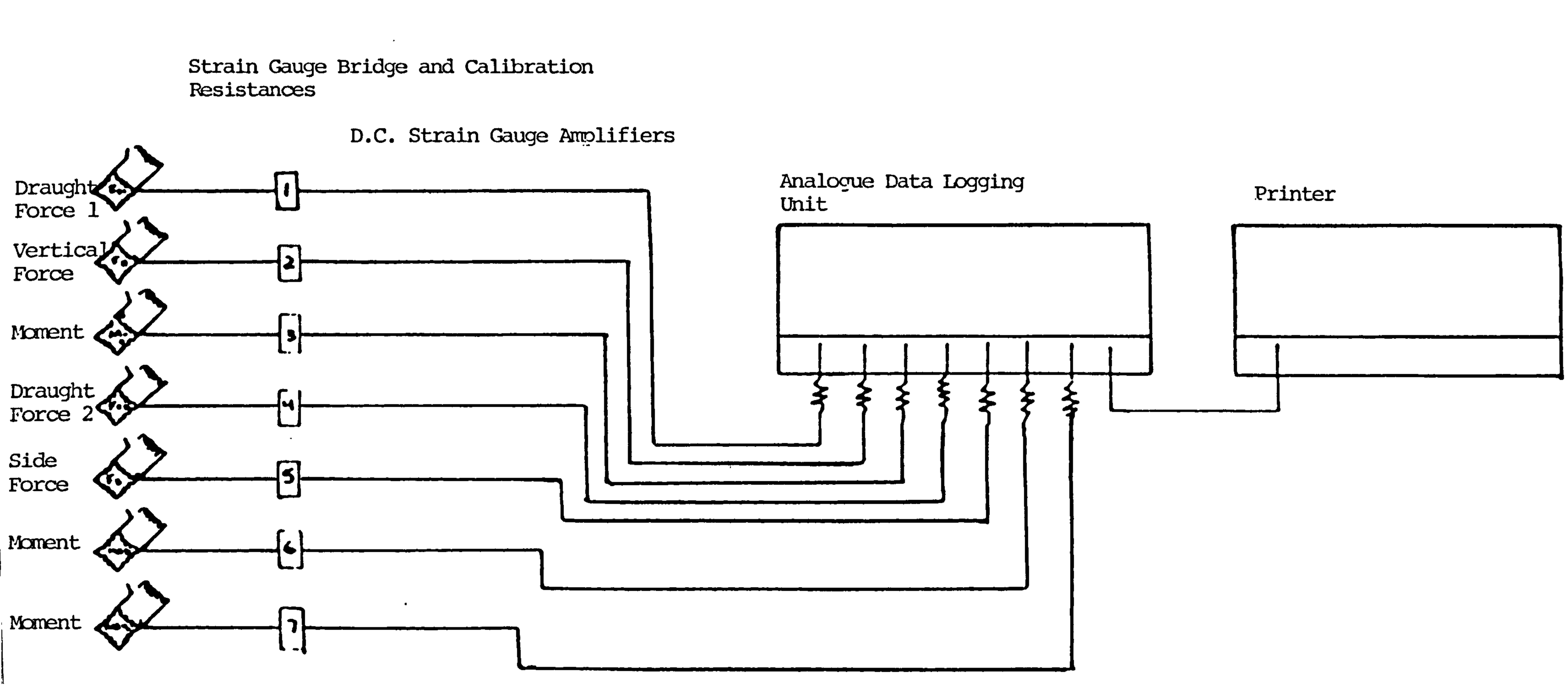

Figure 3.8. Diagrammatic representation of the signal conditioning and recording equipment used in the study

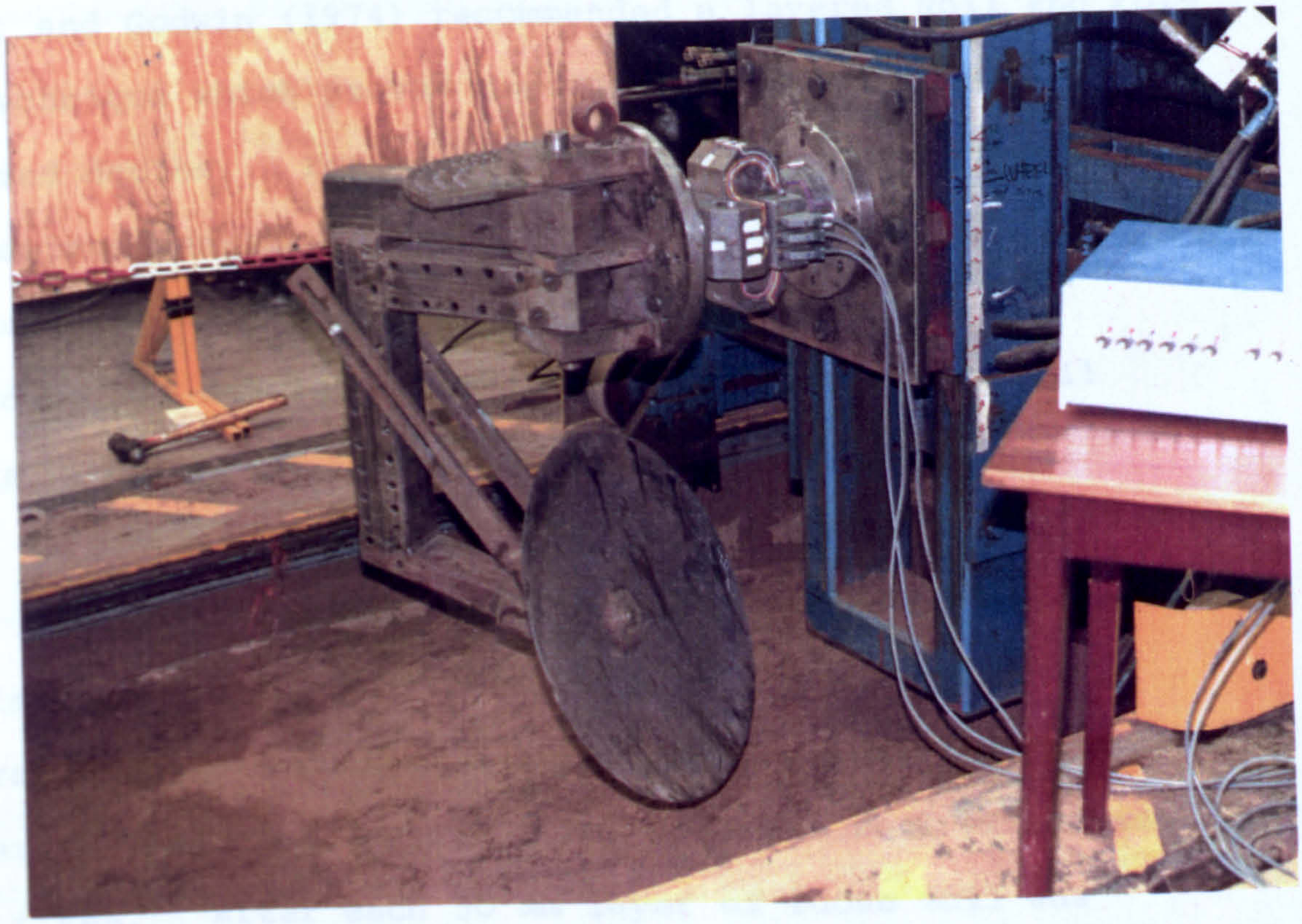

Figure 3.9. Transducer and disc mounting

Pipette method as shown in Table 3.1.

3.5.2. Soil preparation, bulk density and moisture content

The sandy loam soil in the soil bin was prepared by reducing all clods and removing foreign materials. Siemens (1963) and Godwin (1974) recommended a layered soil and roller technique which proved useful for preparing blocks of required depths. For maximum compaction and compaction to the desired density, a measured volume of soil was poured in layers of 50 mm. From their techniques, a standard procedure was developed for the preparation of the soil blocks.

The following procedure was considered to provide consistent results. The soil was compacted in 50 mm layers, using six runs of a one-tonne free rolling compaction roller. The thick layer (50 mm) of loose soil was repeated four times. After each 50 mm layer of loose soil was compacted, water was added evenly to the surface of the layer, using a fine spray hose to hold the soil moisture content within the friable range of 10.5 to 11.5% on dry basis. For each experimental run the wet bulk density was obtained by measuring the undisturbed soil at three points along the length of the bin. This gave a wet bulk density volume of 14.46 kN/m^3. After the end of the test, all the soil was scraped to the end of the bin and the compaction

procedure was repeated.

3.6. Measurement of soil properties

3.6.1. Introduction

Based upon Mohr-Coulomb soil mechanics theory, the mechanical properties of soil are:

i. Bulk density weight (wet basis).

ii. Soil shear stress parameters, angle of internal shearing resistance and apparent cohesion.

iii. Soil-metal friction and apparent adhesion.

3.6.1.1. Bulk density weight

The bulk density weight was obtained using standard density rings and inserting into the packed, undisturbed experimental soil in the soil bin. The mean bulk density was determined from the volume of the ring and weight of the soil.

3.6.1.2. Soil shear strength parameters

The shear resistance along the plane of incipient soil failure is expressed by Coulomb's equation as stated by Terzabhi (1943), given below:

$$\tau = c + \sigma \tan \phi \qquad \text{.....(3.1.)}$$

where:

τ = shearing stress at failure

c = apparent cohesion

σ = normal stress

ϕ = angle of shearing resistance

The soil strength parameters were determined by a number of standard methods. Godwin (1974) has determined a detailed analysis of different parameters of the experimental soil at three densities varying from very loose to compact, from a sandy loam soil. He concluded that various results would be expected for various density conditions and he found out that there is no single method to be used for all density conditions.

In the present investigation the parameters were determined using a standard triaxial test. Four confining pressures were used (34.5, 69, 103.5 and 138 kN/m^2)at the fastest strain rate of 2% per minute. Figure 3.10. shows the Mohr-circles which were drawn from the calculated principle stress. Using the procedure adopted by Godwin (1974), the shear strength parameters were determined on the recommendation used by Lambe and Whitman (1969). Their technique is to represent each of the Mohr-circles by a single point, with co-ordinates p, q and joining the points by straight line denoting the stress path and called as a

From linear regression model the equation of Kf line is

$q_f = a + \beta_f \tan \alpha_1$

$q_f = 8.386 + \beta_f\ 0.5446$

hence $\tan \alpha_1 = 0.5446^{0.5818}_{0.5134}$ $\quad a = 8.386 \pm 1.524$

The values of C and Ø from Lambe and Whitman (1969) and their 95% confidence limit from Steel and Torrie (1960) is given below.

$\phi = \text{Sin}^{-1}(\tan \alpha_1)$ and $C = a/\text{Cos}\ \phi$

therefore $\phi = 33^{35.57}_{30.89}$

therefore $C = 10^{12.18}_{8.0}$

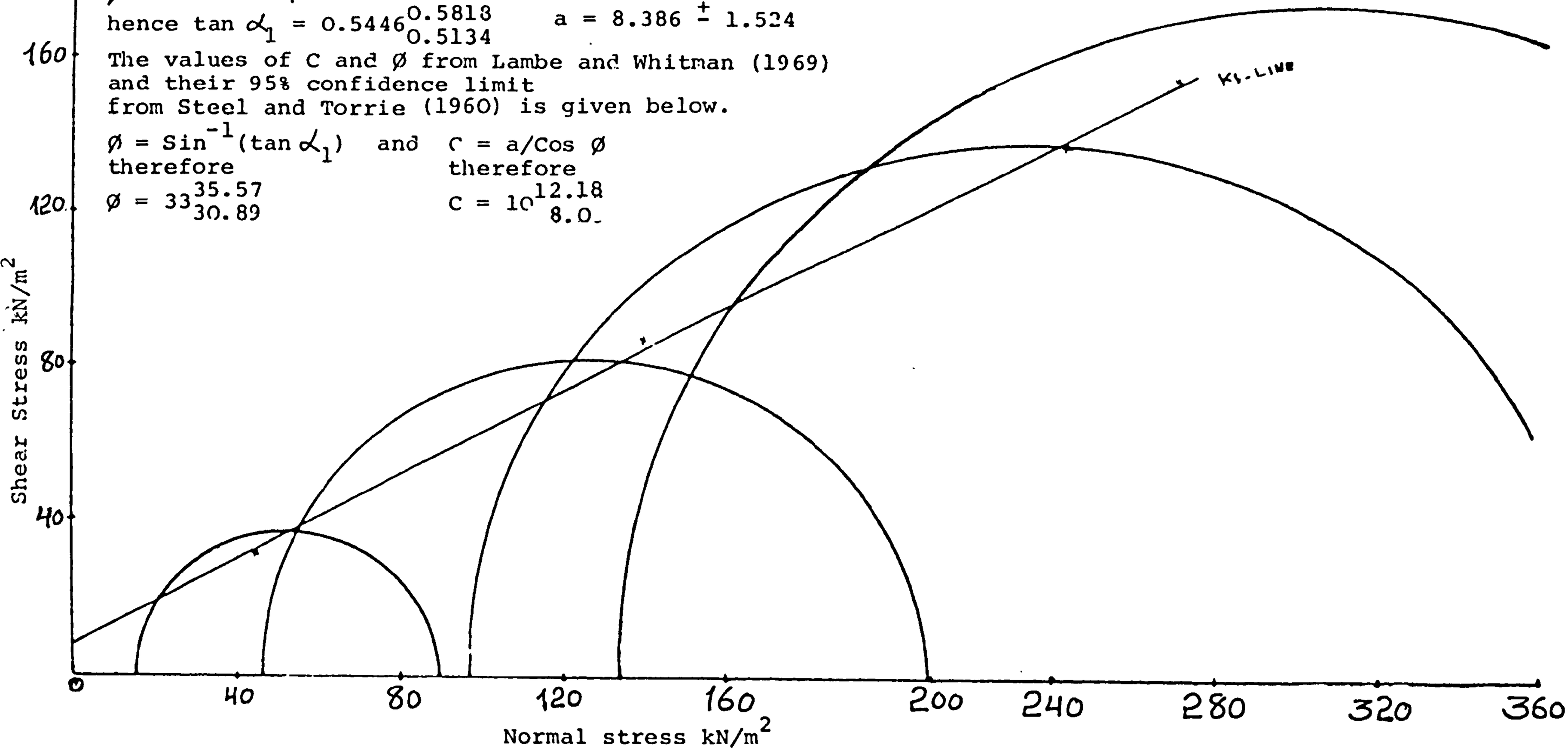

Figure 3.10. Mohr circles and the Kf line for sandy loam soil at 1.446 kg/m^3 density

Kf- line. From the trigonometric relationship that exists between the Kf- line and the Mohr-Coulomb envelope, the shear strength parameters were determined. Using the procedure outlined by Steel and Torrie (1960), the 95% confidence limits can be determined from the fitted regression model.

3.6.1.3. Soil-metal interface parameters

Payne and Fountain (1954) have suggested an equation similar to equation 3.1. which relates the normal stress and the tangential stress at a soil-metal interface as:

$$\tau = ca + \sigma \tan \delta \qquad \ldots\ldots\ldots\ldots (3.2.)$$

where the symbols are:

τ = tangential stress

ca = apparent adhesion

σ = normal stress

δ = angle of soil-metal friction

An aluminium slider size of 146 x 102 mm and weight of 42.74 grams was used. The normal weight and the force needed to pull the slider was recorded and used to determine the soil-interface parameters. The parameters were

determined from the fitted regression model as shown in Figure 3.11.

The summary of the results of the mechanical properties is given below:

Soil properties		Range
Bulk density,	kN/m^3	14.46
Cohesion, C,	kN/m^2	10 12.18 8.0
Angle of shearing resistance, Ø, deg		33 35.57 30.89
Adhesion, Ca,	kN/m^2	00
Angle of soil-metal friction, δ ,deg		20

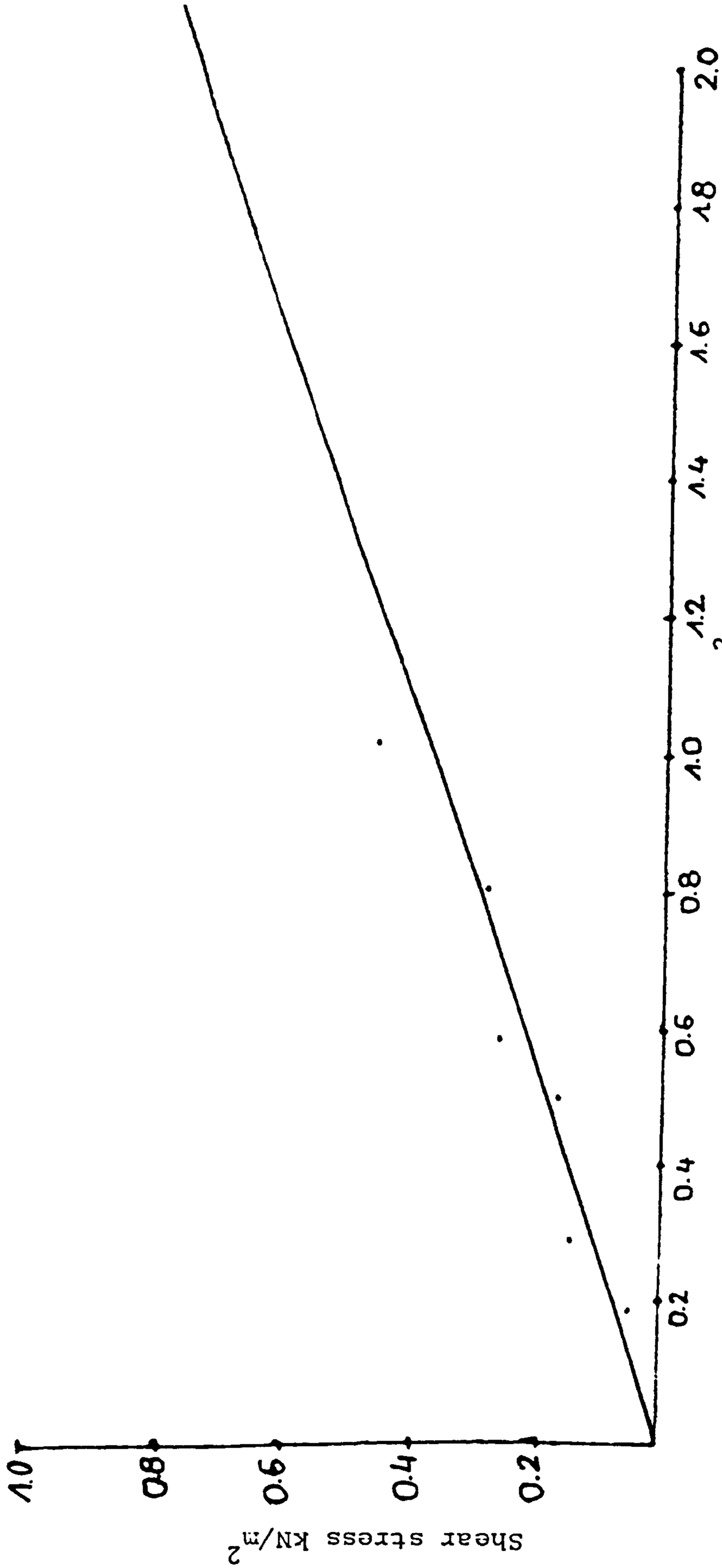

Figure 3.11. Relation between shear stress at soil/metal interface and the normal stress for sandy loam soil

CHAPTER 4

4. The geometry of the tilt disc tool

4.1. Introduction

The literature review has been concerned with the analysis of draught, vertical and side forces acting upon the vertical discs and the soil reaction upon the generalised tillage tool as it relates to the disc at a given depth and speed. The analysis divides naturally into three sections:

i. The factors of the disc geometry such as radius of curvature and disc diameter and factors of disc attitude such as disc angle and tilt angles.

ii. The type and properties of soil such as angle of shearing resistance, cohesion, moisture content, bulk density, and degree of compaction.

iii. The soil/disc interface properties such as the angle of soil/metal friction and apparent adhesion.

It is the aim of this study to investigate the geometry of the tilted axis disc and relate it to the soil reactions.

4.2. Geometry of the disc and the soil-disc interface

McCreery and Nichols (1956), Gill et al (1968) and Kepner et al (1978) defined the disc geometrically as a section of the shell of a hollow sphere. As shown in Figure 4.1., the disc consists of a segment of spherical shell with the spherical radius of curvature R and the cutting plane circle as disc edge of the radius r.

Consider the tilted disc penetrating a soil to a depth d. Then Figure 4.1. shows the elevation of the edge disc in view 1, the true shape of the disc in view 2, the elevation of the full face in view 3, the soil/disc interface as an arc of circle Rs and chord of the disc L in the plane of the disc in view 4. The plan view 4 shows its true shape and size based on the tilt angle of the disc and the depth of penetration d.

4.2.1. The mechanics of the soil failure of the disc

The summation of soil forces across the disc surface in the three dimensional reaction to the soil failure involves packing, throw, pulverization and scour caused by the disc shape, size and angle of travel. Figure 4.2. shows the dynamic situation in which the disc is ploughed at a disc angle (β) to its horizontal centerline. The magnitude of the forces is a function of this angle. View 5

View 1 = edge elevation at 0^{o} disc angle
View 2 = true disc shape
View 3 = full face elevation at 90^{o} disc angle
View 4 = plan at disc angle β

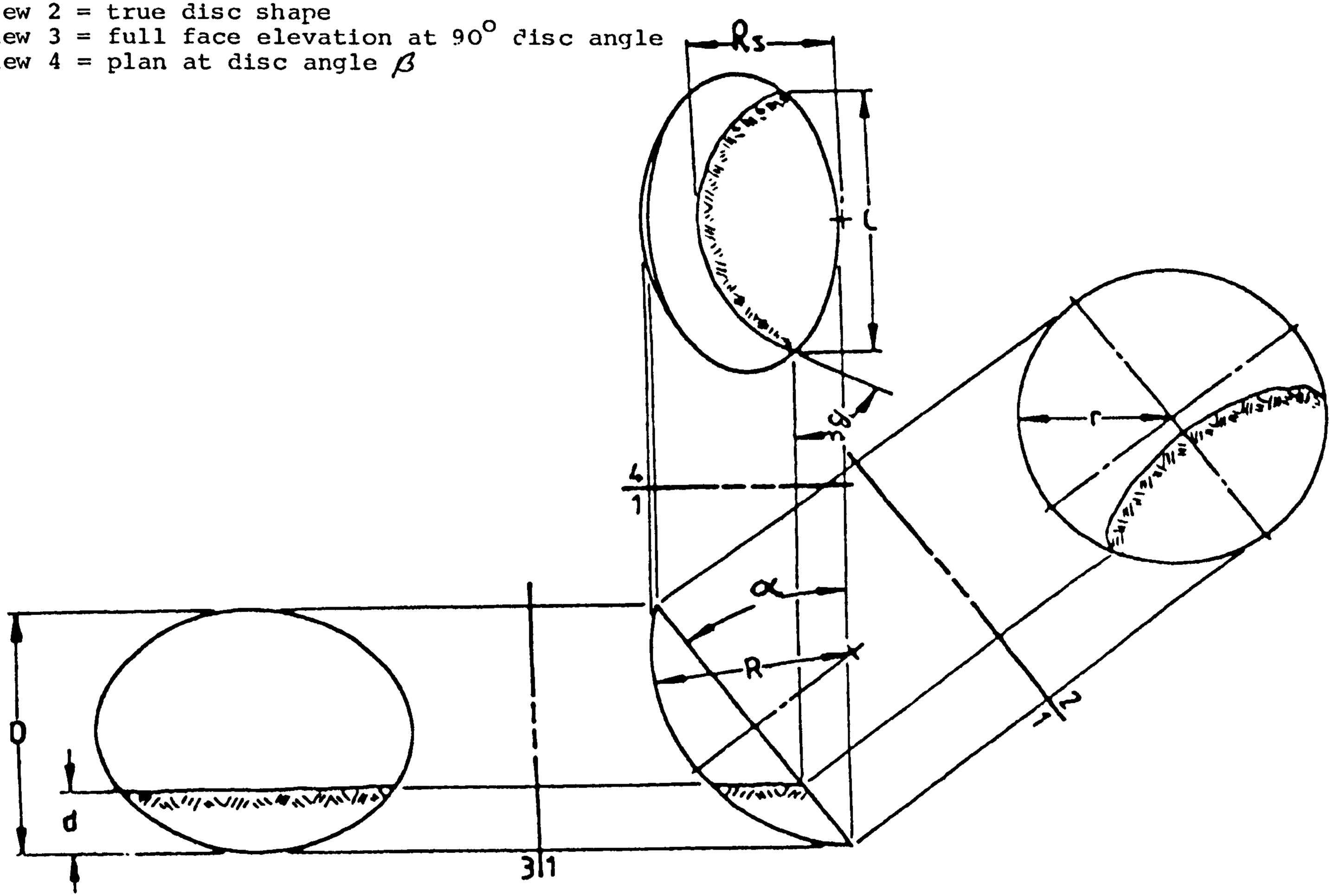

Figure 4.1. The disc as a section of a hollow sphere, ploughing the soil to a depth d.

View 1 = edge elevation at 0^{o} disc angle
View 3 = full face elevation at 90^{o} disc angle
View 4 = plan at β disc angle
View 5 = elevation at $\beta < \beta_c$

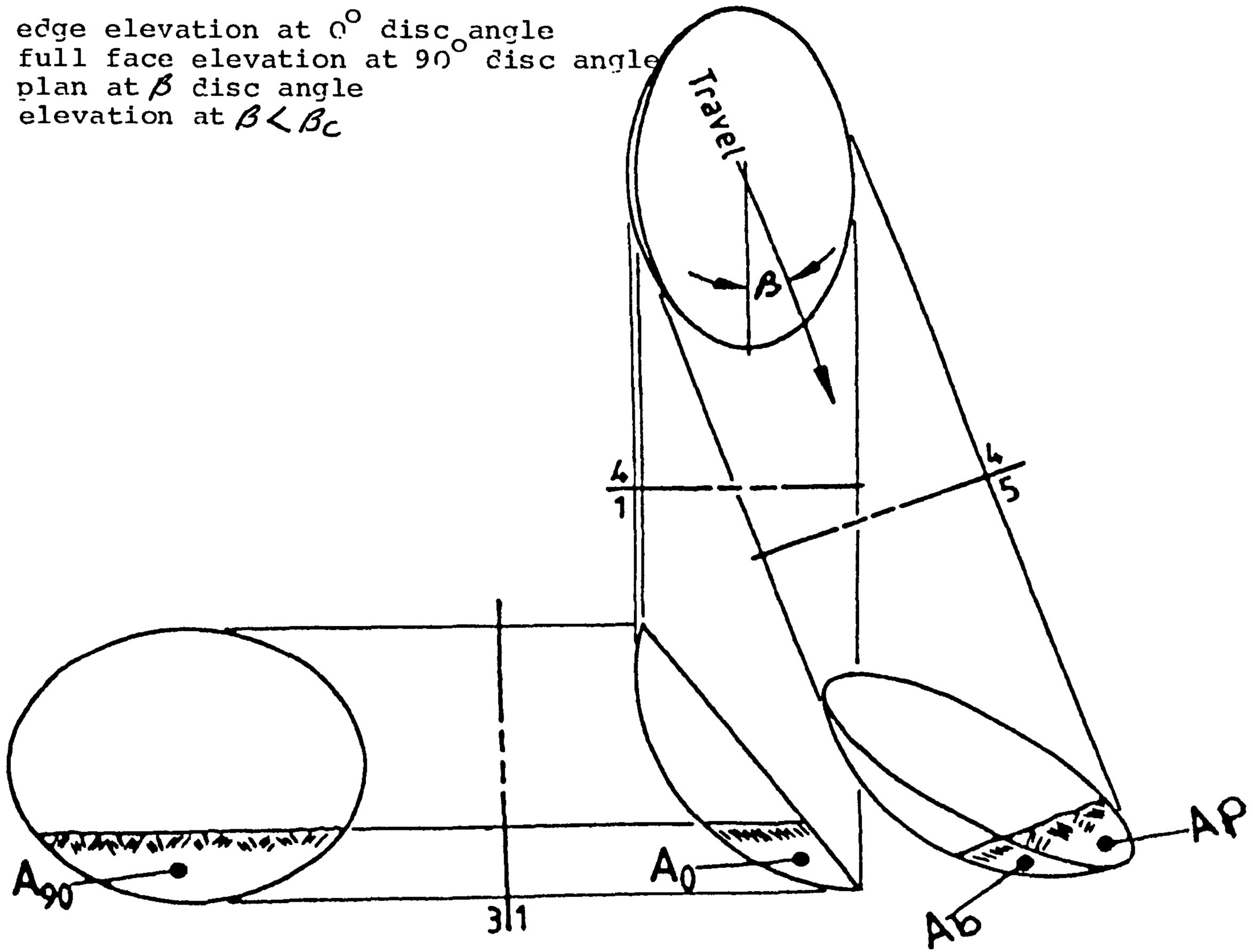

Figure 4.2. The mechanics of the soil failure caused by the disc showing various areas operating at a disc angle β and a depth d.

shows the disc as seen from directly in front and illustrates the submerged portion of the disc projected onto a plane normal to the direction of travel. In elevation, the soil circle Rs appears in edge view 1.

In the case of the limiting values seen when the disc angle is equal to zero, the whole bearing area occurs on the convex side of the disc and there is no passive reaction on the front concave side of the disc as shown in view 1 in Figure 4.2. If the disc is set so that the disc angle is 90^{o}, the maximum limiting area of the soil is reached ahead of the concave side of the disc and there is no bearing area on the edge or back of the disc as shown in view 3.

A more important limiting case occurs when the disc angle (β) is equal to the critical disc angle (β_c) and the disc is ploughed along the line of the tangent to the soil circle at the edge of the disc. This presents an optimum where the leading surface is parallel to the direction of travel, there is no bearing area in the back of the disc, as shown in plan view 4 in Figure 4.1.

When the disc angle (β) is less than the critical disc angle (β_c), pressure on the convex side of the disc occurs which exerts a pressure on the soil as shown in Figure 4.2. in view 5. Similarly, a critical tilt angle (α_c)

occurs at which the lower edge of the disc is tangent to a horizontal plane. If the tilt angle (α) is larger than the critical tilt angle (α_c), the projected area will exist below the edge of the disc.

4.2.2. Determination of the dimensions of the disc

The dimensions and the areas for the geometry of the tilted disc can be determined in terms of the known values of the radius of the edge of the disc r, the radius of curvature of the disc R and the depth of penetration d.

Figure 4.3. shows a simplified model of the element as a flat disc. The projection in plane 3 is an ellipse with the following equations:

$$\frac{X^2}{r^2} + \frac{Y^2}{(D/2)^2} = 1$$

where $X = \frac{L}{2}$

$$Y = \frac{(D - 2d)}{2}$$

For the chord of the disc L, the appropriate substitution is given by:

$$\frac{L^2}{4r^2} + \frac{(D - 2d)^2}{D^2} = 1$$

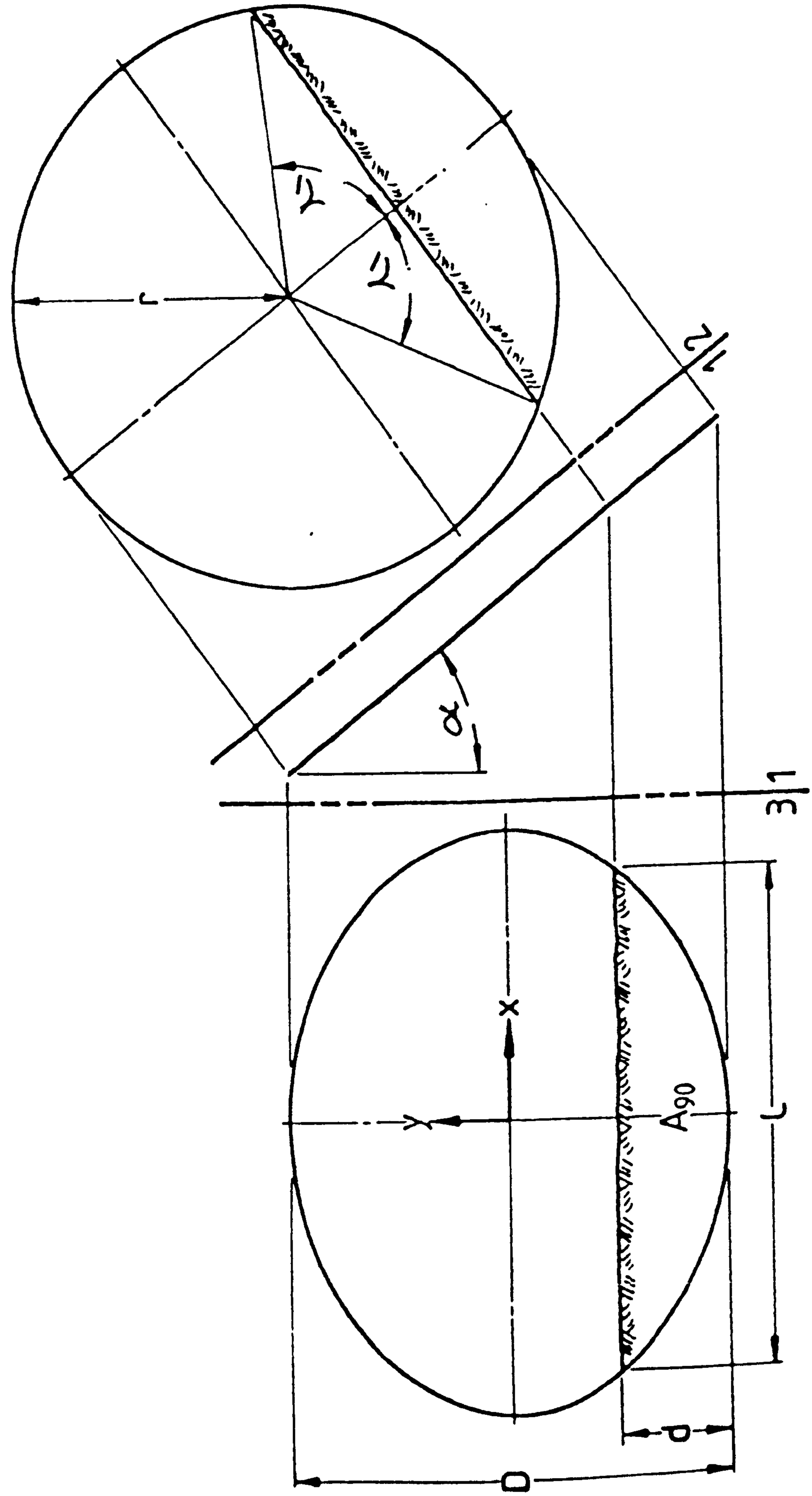

Figure 4.3. A simplified model of the element as a flat disc showing the chord of the disc L and the vertical projection of the pressure area of the disc

$$L = 2r\sqrt{\frac{(D^2 - D^2 + 4Dd - 4d^2)}{D^2}}$$

$$L = \frac{4r}{D}\sqrt{d(D - d)}$$

$$L = 2\sqrt{d(D - d)}\ \mathrm{Sec}\,\alpha$$

but $$D = 2r\ \mathrm{Cos}\,\alpha \qquad \ldots\ldots\ldots(4.1.)$$

or $$L = 2\sqrt{d(2r\mathrm{Cos}\,\alpha - d)}\ \mathrm{Sec}\alpha \ldots\ldots\ldots(4.2.)$$

From Figure 4.8. the soil/disc interface circle radius Rs is given by:

$$Rs = R\ \mathrm{Cos}\ (\alpha + \epsilon - \gamma) \qquad \ldots\ldots\ldots(4.3.)$$

where α = tilt angle

ϵ = given by equation .....(4.11.)

γ = given by equation .....(4.12.)

or .....(4.13.)

R = radius of curvature

The last two angles will be determined in turn in this chapter.

4.2.3. Determination of the angles of the disc

4.2.3.1. Introduction

The disc angle (β) is the most important parameter governing the soil circle on the soil/disc interface geometrical properties. The disc angle can be defined as the angle between the horizontal diameter of the disc and the direction of travel as shown in Figure 4.2. in view 4. Also, another important parameter is the tilt angle (α) which can be defined as the angle between the plane of the disc and a vertical plane. In other words, tilt angle (α) is the angle between the steepest line on the plane of the disc and the vertical as shown in Figure 4.1. in view 1. Some more soil/disc interface parameters are to be investigated based on their importance to the performance of the disc.

4.2.3.2. Critical disc angle β_c

The critical disc angle is an important disc parameter. This angle may be defined as the angle between the convex side of the disc at the soil surface and the line of motion for a given depth of penetration and a given tilt angle as shown in Figure 4.1. in view 4.

As shown in Figure 4.1. in view 4, for the evaluation

of the critical angle a knowledge of the soil circle radius Rs and the length of its chord L is required. This angle may be developed as follows:

$$\beta c = \text{Sin}^{-1}\frac{L}{2Rs}$$

$$= \text{Sin}^{-1}\sqrt{\frac{d(2r\ \text{Cos}\alpha - d)}{R\ \text{Cos}(\alpha + \epsilon - \gamma)}}\ \text{Sec}\alpha \qquad \ldots(4.4.)$$

where

L = given by equation ...(4.2.)

Rs = given by equation ...(4.3.)

R = radius of curvature

If the disc angle is such that $\beta > \beta_c$ there is no pressure in the convex side of the disc. While if the disc angle is such that $\beta < \beta_c$, then the convex side of the disc is engaged in the soil. McCreery and Nichols (1956) determined the critical disc angle for any depth for any disc of given diameter and radius of curvature.

It is worth mentioning here that McCreery and Nichols (1956) indicated that this critical angle can be determined, knowing radius of curvature R, disc radius r and depth of cut, but they did not indicate that the tilt angle is

another important variable in the determination of critical disc angle.

The author has found that the critical disc angle is changed when the tilt angle changes for a given radius of curvature R, disc radius r and depth of operation d, as Equation 4.4. suggests and as shown in Figure 4.5. and Table 4.2. However, McCreery and Nichols (1956) determined the critical disc angle (β_c) graphically for an 8 in disc having various radius of curvatures operating at various depths. Their results for these angles to the nearest ½ degree were tabulated.

It is useful to compare the results of their graphical determination with the analytically determined values by applying Equation 4.4. as shown in Table 4.1. and Figure 4.4. From Table 4.1. overleaf, and Figure 4.4., it may be observed that the values of the critical disc angle determined by McCreery and Nichols (1956) are very close to the values determined mathematically by Equation 4.4.

Furthermore, Table 4.2. and Figure 4.5. represent the values of critical disc angle obtained by Equation 4.4. using various tilt angles for a 610 mm disc having a radius of curvature of 700 mm. Table 4.2. and Figure 4.5. indicate that the critical disc angle increases as the tilt angle increases for all depths. The slope of the curves decreases with increasing depth. This shows that the tilt

Table 4.1. Critical disc angle. Disc diameter = 8 in

Depth of Cut (inches)	Radius of curvature of disc (inches)															
	5		7		9		11		13							
	Graphical	Analytical Eq. 4.4.	Graphical	Analytical Eq.4.4.	Graphical	Analytical Eq. 4.4.	Graphical	Analytical Eq. 4.4.	Graphical	Analytical Eq. 4.4.						
0.5	33	32.842	18.5	18.62	12.5	13.5	10.5	10.7	9	8.89						
1	41.5	41.40	25	24.729	17	18.16	14.5	14.477	12	12.07						
1.5	46	46.14	28.5	28.52	20	21.17	17	16.947	14.5	14.16						
2	49	49.1	31	31.09	22	23.25	18.5	18.67	15	15.64						
2.5	51	51.02	33	32.842	23	24.69	20	19.89	16.5	16.68						
3	52	52.41	34	33.98	24	25.65	20.5	20.7	17	17.38						
3.5	53	52.91	34.5	34.63	24.5	26.2	21	21.17	17.5	17.78						
4	53.5	53.32	35	34.859	25	26.45	21.5	21.329	18	17.96						

Disc diameter = 8 in.

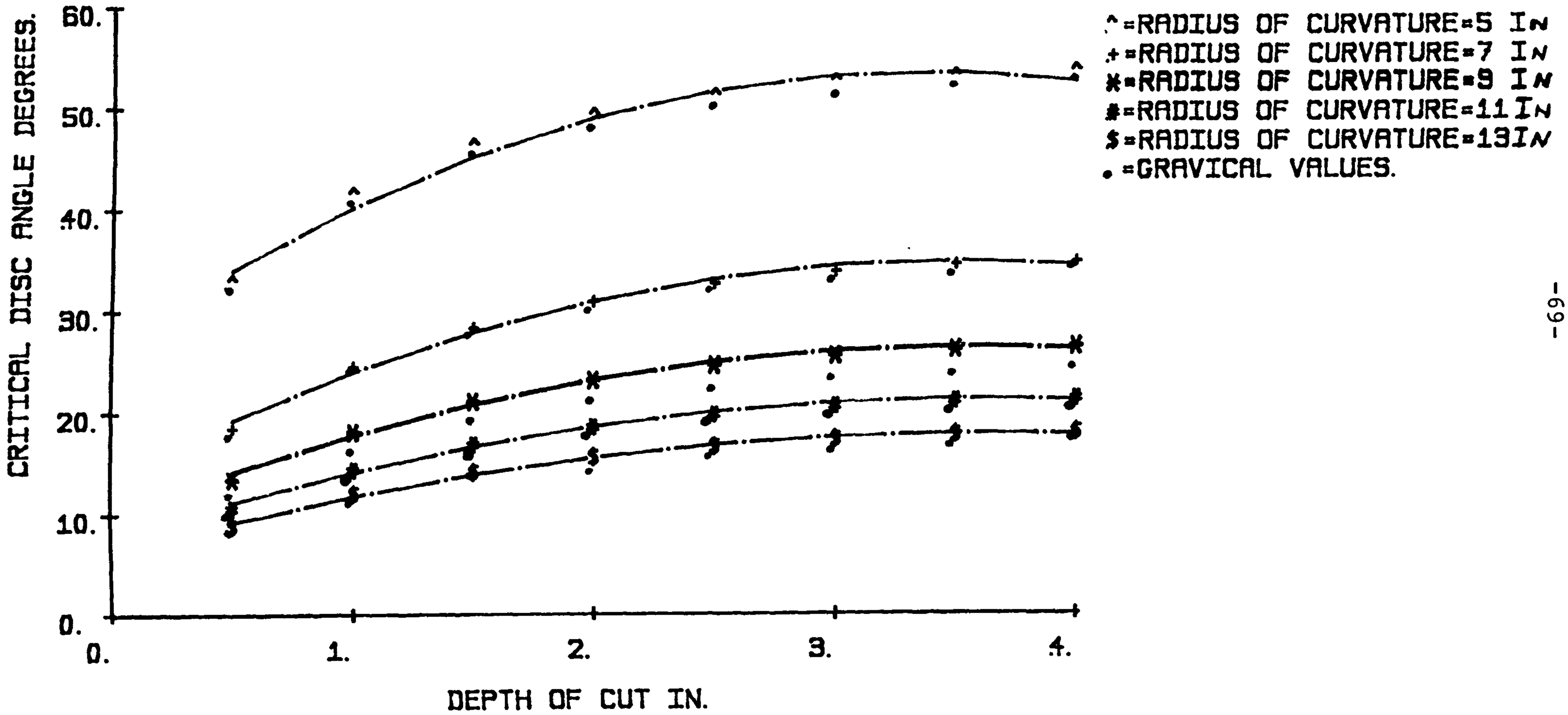

Figure 4.4. The critical disc angle determined by Equation 4.4. in comparison to the graphical values of McCreery and Nichols (1956) for an 8 in disc having different radius of curvature operating at various depths.

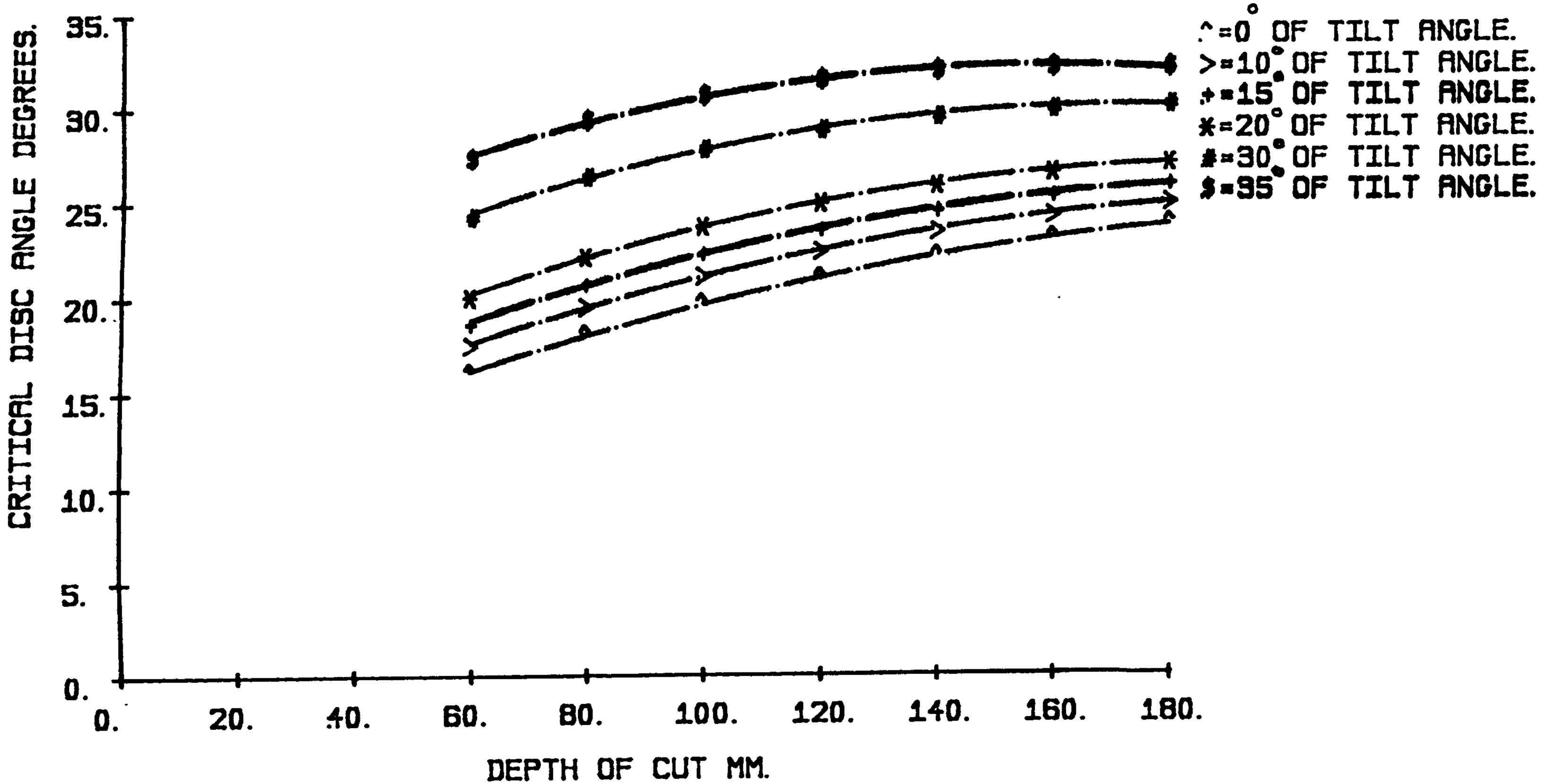

Figure 4.5. The critical disc angle obtained by Equation 4.4. for a 0.61 m disc having a radius of curvature of 0.7 m operating at various tilt angles and different depths.

angle is of importance in determination of the critical disc angles.

4.2.3.3. Critical depth dc

The critical depth dc may be defined as the depth at which the disc angle (β) is equal to the critical disc angle (β_c). Therefore, for a given disc angle there is a critical depth of operation dc at which the back side of the disc is in contact with the plane of the soil surface. The critical depth of operation (dc) may be derived as follows:

From the definition of dc above:

$$\beta = \beta_c$$

and dc = d

But, from equation 4.4.

$$\beta_c = \text{Sin}^{-1}\sqrt{\frac{d(2r\ \text{Cos}\alpha - d)\ \text{Sec}\alpha}{R\ \text{Cos}(\alpha + \epsilon - \gamma)}}$$

Substituting β in place of β_c and dc in place of d in above gives:

$$\text{Sin}\,\beta = \frac{\sqrt{dc(2r\ \text{Cos}\,\alpha - dc)}\ \text{Sec}\,\alpha}{R\ \text{Cos}(\alpha + \epsilon - \gamma)}$$

$$\text{Sin}^2\beta = \frac{dc(2r\ \text{Cos}\,\alpha - dc)\ \text{Sec}^2\alpha}{R^2\ \text{Cos}^2(\alpha + \epsilon - \gamma)}$$

From which

$$\text{Sin}^2\beta\ R^2\ \text{Cos}^2(\alpha+\epsilon-\gamma) = dc(2r\ \text{Cos}\,\alpha - dc)\text{Sec}^2\alpha$$

Therefore

$$\frac{\text{Sin}^2\beta\ R^2\text{Cos}^2(\alpha+\epsilon-\gamma)}{\text{Sec}^2\alpha} - dc(2r\ \text{Cos}\,\alpha) + dc^2 = 0$$

Therefore

$$dc = \frac{-(-2r\text{Cos}\alpha) - \sqrt{(-2r\text{Cos}\alpha)^2 - 4\left[(\text{Sin}^2\beta R^2\text{Cos}^2(\alpha+\epsilon-\gamma)/\text{Sec}^2\alpha\right]}}{2}$$

.... (4.5.)

It should be indicated here that as the disc angle (β) increases the critical depth dc increases. The critical depth equals the working depth when $\beta = \beta_c$, when $\beta > \beta_c$ critical depth is O (Figure 4.6., and Table 4.3.). As the tilt angle increases, the critical depth decreases until it vanishes at $\beta = \beta_c$. This is due to the increase of the critical disc angle as the tilt angle increases, as shown in the same Table and Figure mentioned above.

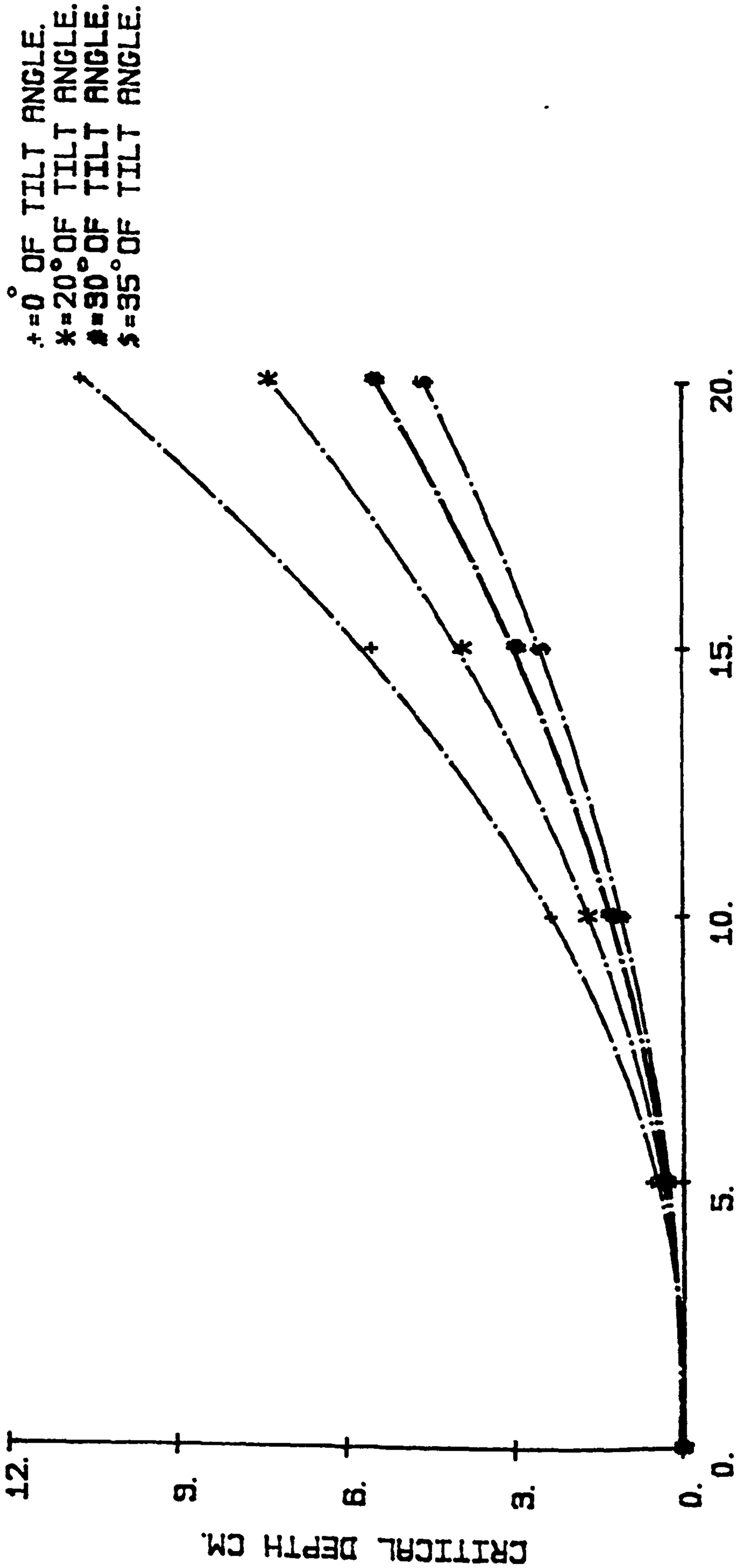

The critical depth calculated by Equation 4.5. for a O.61 m disc having a radius of curvature of 0.7 m working at various disc and tilt angles at a depth of O.14 m

Figure 4.6.

4.2.3.4. Disc angle (β)

When the disc is critically positioned, the Equation 4.4. represents the combination of disc angle and depth of cut. Equation 4.5. is the inverse function of Equation 4.4. as far as the disc angle (β) and the depth of cut d are concerned. If the depth of penetration d is considered as the independent variable, Equation 4.4. can be rewritten as given below:

$$\beta = \text{Sin}^{-1}\sqrt{\frac{d\ (2r\ \text{Cos}\alpha - d)\ \text{Sec}\alpha}{R\ \text{Cos}\ (\alpha + \epsilon - \gamma)}} \qquad \ldots\ldots\ldots (4.6.)$$

when $\beta = \beta_c$

4.2.3.5. Depth of cut d

If the disc angle (β) is the independent variable, the inverse of this function is to be determined as given below:

$$d = \frac{-(-2r\text{Cos}\alpha) - \sqrt{(-2r\text{Cos}\alpha)^2 - 4\left[(\text{Sin}^2\beta\ R^2\text{Cos}^2(\alpha+\epsilon-\gamma)/\text{Sec}^2\alpha\right]}}{2} \qquad \ldots\ldots\ldots (4.7.)$$

when d = dc

In fact, Equation 4.7. is the same as Equation 4.5. after substituting d in place of dc.

4.2.3.6. Critical tilt angle α_c

The critical tilt angle may be defined as the

angle at which the bottom of the tilted disc edge is tangent to a horizontal plane as shown in Figure 4.8. If the critical tilt angle (α_c) is exceeded such as $\alpha > \alpha_c$ a component of projected area from the bottom of the disc will appear in front face elevation of the disc.

From Figure 4.7. the following equation can be derived to determine the critical tilt angle.

$$\alpha_c = \tfrac{1}{2}\pi - \mathrm{Sin}^{-1}\frac{r}{R} \qquad \text{.....(4.8.)}$$

$$= \tfrac{1}{2}\pi - \epsilon$$

(see section 4.2.3.8.).

As shown in Table 4.2. using Equation 4.8. the critical tilt angle is not affected by disc and tilt angles for any given depth of cut d. This angle is only affected by the radius of curvature of the disc R and the radius of the edge of the disc r.

4.2.3.7. <u>Tilt angle α</u>

The inverse of Equation 4.8. can be rewritten where the disc edge is tangent to the horizontal plane in order to determine the tilt angle as follows:

$$\alpha_c = \alpha$$

$$\alpha = \tfrac{1}{2}\pi - \mathrm{Sin}^{-1}\frac{r}{R} \qquad \text{.....(4.9.)}$$

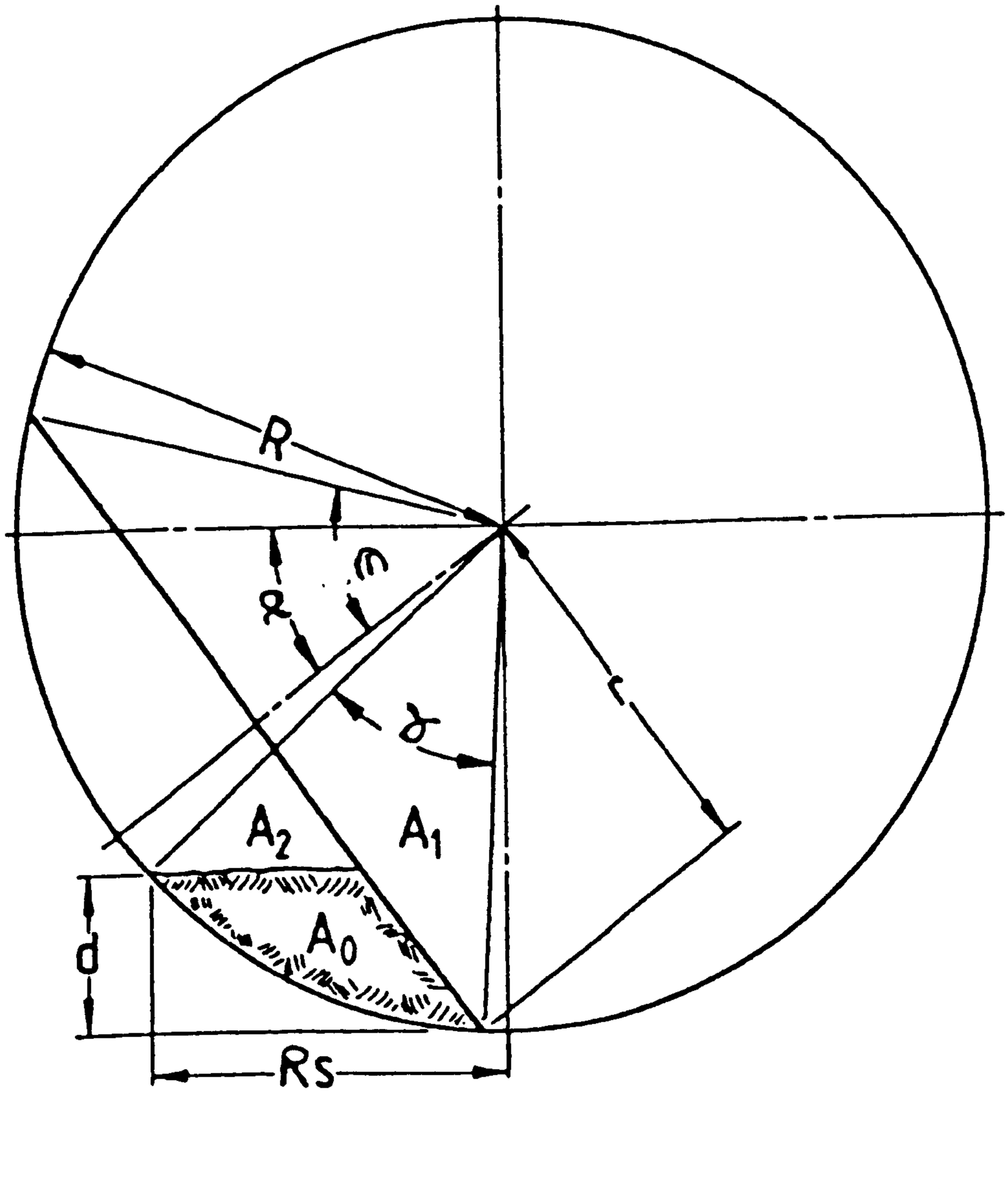

Figure 4.7. Vertical bearing area of a disc ploughing at a disc angle of 0^{o} and tilt angle of α^{o} at a depth d.

Also the tilt angle can be determined from Equation 4.1. as shown in Figure 4.3. as follows:

$$\alpha = \text{Cos}^{-1} \frac{D}{2r} \qquad \ldots(4.10)$$

where D = inside diameter of the disc.

4.2.3.8. Half cone angle ϵ

This angle may be defined as the half cone angle corresponding to the portion of spherical surface represented by the disc. As shown in Figure 4.8., this angle may be derived as given below:

$$\epsilon = \text{Sin}^{-1} \frac{r}{R} \qquad \ldots(4.11)$$

4.2.3.9. Gamma angle γ

This angle can be defined as the angle of the centreline arc of the submerged portion of the disc, as shown in Figure 4.7. It is also the difference between the rake angle at the soil surface and that at the bottom of the disc, as shown in Figure 4.9.

As shown in Figure 4.8., to determine this angle, it can be recognised that the relationship between depth of penetration d and the radius of curvature R is the difference

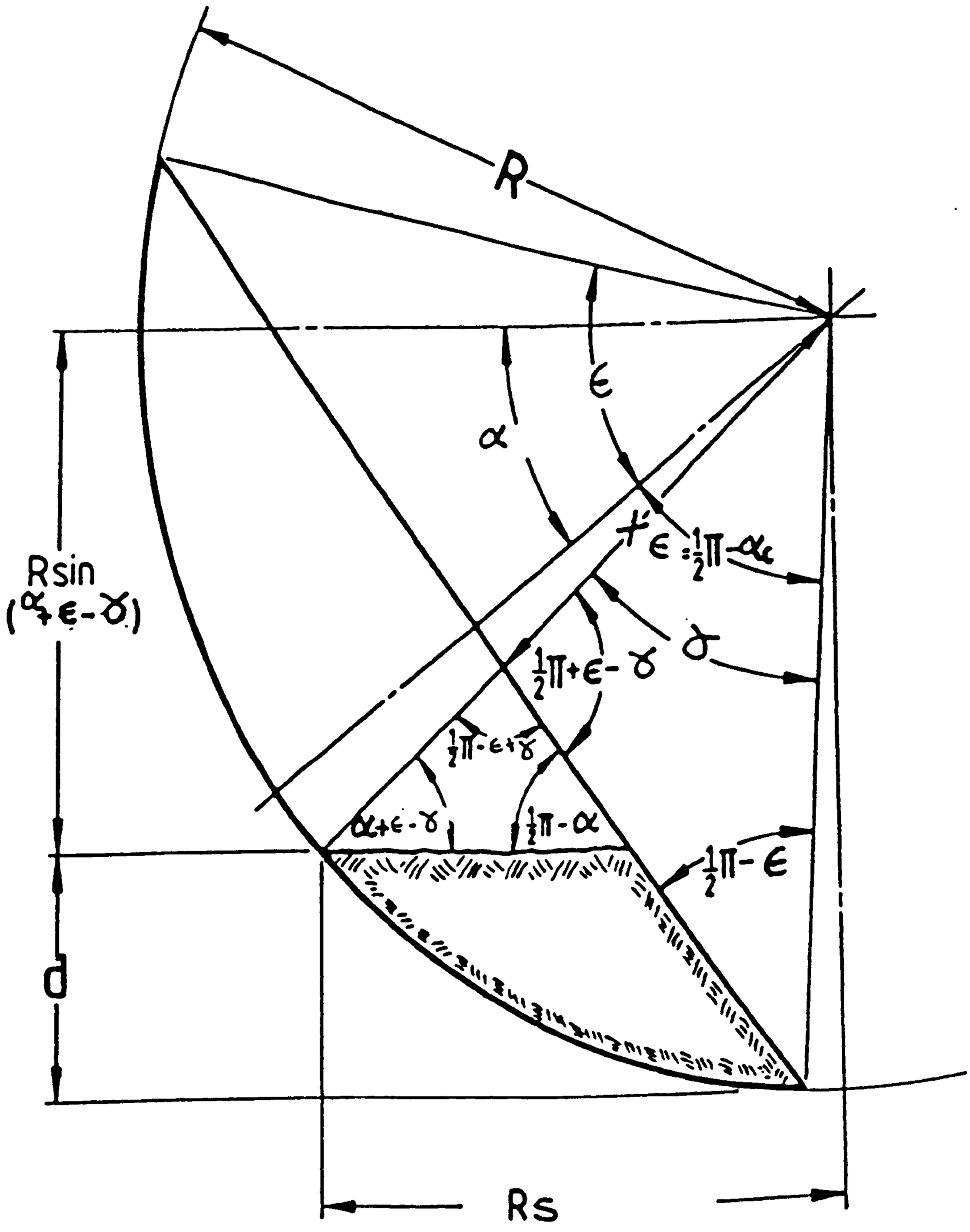

Figure 4.8. Extension of Figure 4.7. to determine the vertical bearing area of the disc working at $\beta < \beta_c$ and at tilt angle α or at a depth $d > dc$

between the size of two angles as given below:

$$\frac{d}{R} = \sin(\alpha+\epsilon) - \sin(\alpha+\epsilon-\gamma)$$

therefore

$$\frac{d}{R} = \sin(\alpha+\epsilon) - \sin(\alpha+\epsilon)\cos\gamma + \cos(\alpha+\epsilon)\sin\gamma$$

therefore

$$\left[\frac{d}{R} + \sin(\alpha+\epsilon)\cos(\gamma-1)\right]^2 = \cos^2(\alpha+\epsilon)(1-\cos^2\gamma)$$

therefore

$$\frac{d^2}{R^2}+\frac{2d}{R}\sin(\alpha+\epsilon)\cos\gamma-\frac{2d}{R}\sin(\alpha+\epsilon)+\cos^2\gamma-\cos 2(\alpha+\epsilon)-2\sin^2(\alpha+\epsilon)\cos\gamma = 0$$

therefore

$$\cos^2\gamma+\left[\frac{2d}{R}\sin(\alpha+\epsilon)-2\sin^2(\alpha+\epsilon)\right]\cos\gamma+\frac{d^2}{R^2}-\frac{2d}{R}\sin(\alpha+\epsilon)-\cos 2(\alpha+\epsilon) = 0$$

therefore

$$\cos\gamma = \sin(\alpha+\epsilon)\left[\sin(\alpha+\epsilon)-\frac{d}{R}\right] \pm \sqrt{\sin^2(\alpha+\epsilon)\left[\frac{d}{R}-\sin(\alpha+\epsilon)\right]^2-\frac{d^2}{R^2}+\frac{2d}{R}\sin(\alpha+\epsilon)+\cos 2(\alpha+\epsilon)}$$

therefore

$$\cos\gamma = \sin(\alpha+\epsilon)\left[\sin(\alpha+\epsilon) - \frac{d}{R}\right] + \sqrt{\cos 2(\alpha+\epsilon) + \sin^4(\alpha+\epsilon) + \left[2\sin(\alpha+\epsilon) - \frac{d}{R}\right]\frac{d}{R} \cdot \cos^2(\alpha+\epsilon)} \quad ..(4.12)$$

The sign in front of the square root in Equation 4.12. must be used positive for the following reasons:

i. This angle (γ) increases with tilt angle (α) if the centre of the sphere is fixed as shown in Figure 4.8.

ii. The expression inside the square root sign, however, decreases strongly with increasing tilt angle (α) whilst the expression outside the square root increases. In order for $\cos(\gamma)$ to decrease with increasing tilt angle the positive square root must be used.

Also, this angle may be developed as shown in Figure 4.8. as follows:

$$\frac{d}{R} = \sin(\alpha+\epsilon) - \sin(\alpha+\epsilon-\gamma)$$

$$\sin(\alpha+\epsilon-\gamma) = \sin(\alpha+\epsilon) - \frac{d}{R}$$

$$\alpha+\epsilon-\gamma = \sin^{-1}\left[\sin(\alpha+\epsilon) - \frac{d}{R}\right]$$

Therefore

$$\gamma = (\alpha + \epsilon) - \sin^{-1}\left[\sin(\alpha + \epsilon) - \frac{d}{R}\right] \qquad \ldots\ldots\ldots(4.13.)$$

Equation 4.12. and 4.13. give the same answer.

4.2.3.10. Rake angle $\bar{\gamma}$

The rake angle of the disc may be defined as the angle between the steepest tangent to the disc surface and the horizontal. The rake angle applies only to submerged parts of the disc. Figure 4.9. shows that (γ_1) is the rake angle at soil surface and (γ_2) is the rake angle at lower edge of disc. $\bar{\gamma}$ is defined as the mean of γ_1 and γ_2. From Figure 4.9., the rake angle may be derived as follows:

Since $\gamma = \gamma_1 - \gamma_2$

But $\gamma_2 = (\frac{1}{2}\pi - \alpha - \epsilon)$

Therefore

$$\bar{\gamma} = \frac{1}{2}(\gamma_1 + \gamma_2)$$

or

$$\bar{\gamma} = \gamma_2 + \frac{1}{2}\gamma \qquad \ldots\ldots\ldots(4.14)$$

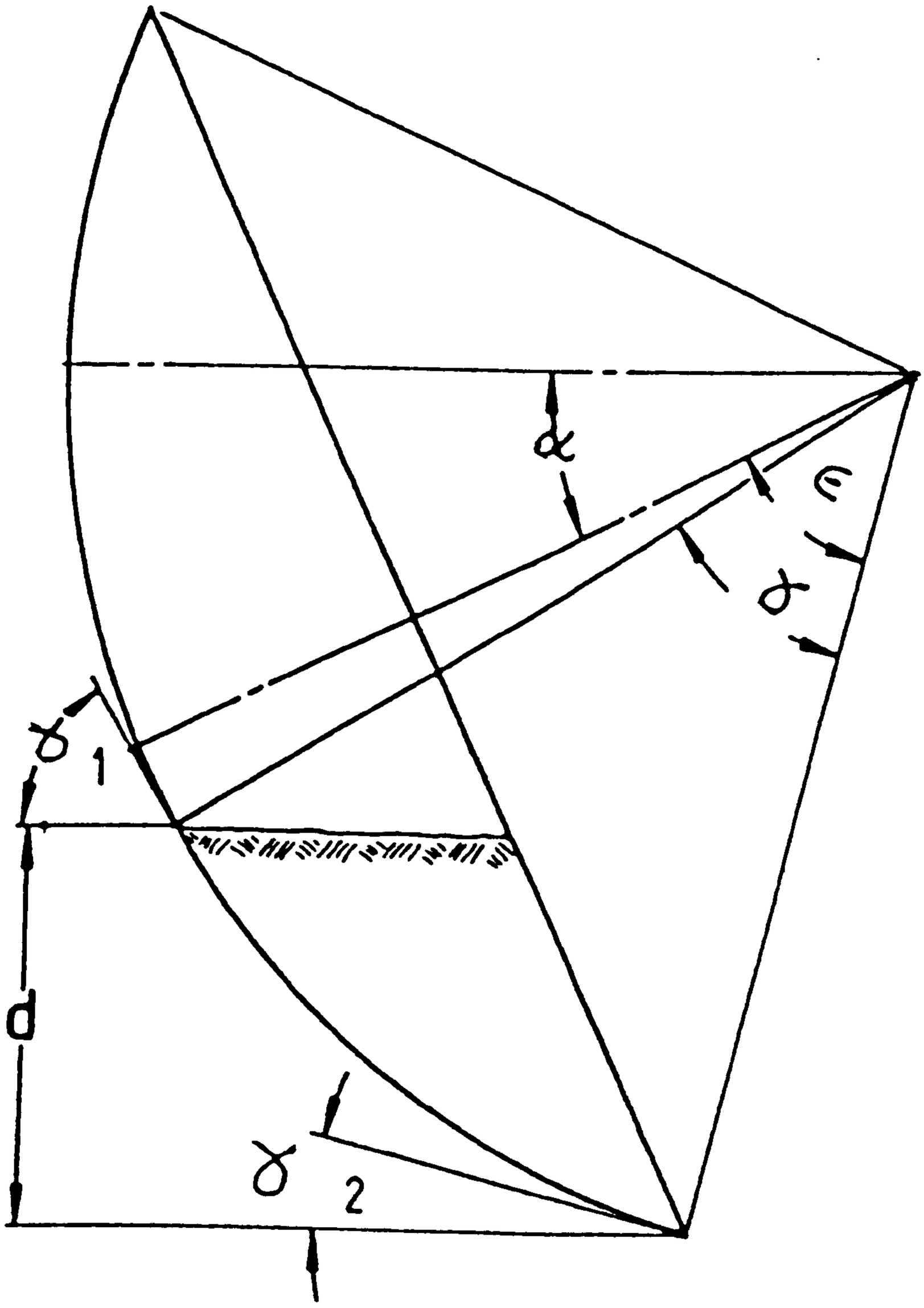

Figure 4.9. The rake angle of the disc ploughing at a depth d and at a tilt angle α

where

γ = given by Equations 4.12. or 4.13.

The rake angle can be obtained by applying Equation 4.14. as shown in Table 4.4. and Figure 4.10. The graph and table of Equation 4.14. show that the rake angle increases when the tilt angle is zero and decreases as tilt angle increases for any given depth of operation. Table 4.4. and Figure 4.10. also show that the rake angle increases as the depth increases for any given tilt angle.

4.2.4. Vertical pressure area Ap

The vertical pressure area can be defined as the projected area of the engaged concave side of the disc on the vertical plane normal to the direction of motion. As shown in Figure 4.2. and Figure 4.3., the vertical pressure area is the projected area at 90° disc angle when rotated through the horizontal angle $90^{\circ} - \beta$.

This area may be determined in terms of disc and tilt angles, the radius of the edge circle of the disc r and the depth of penetration d as shown in Figure 4.3. as follows:

$$Ap = A90 \cdot \sin \beta$$

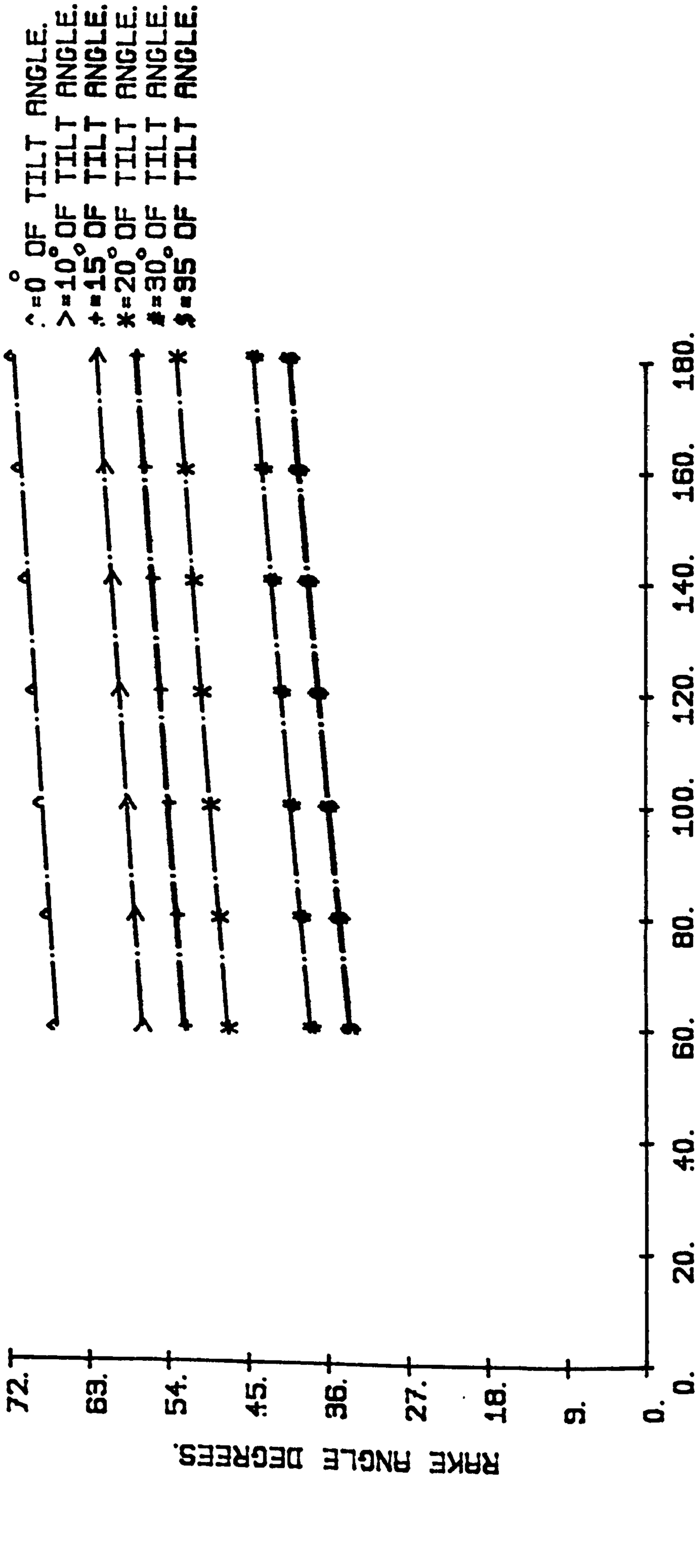

Figure 4.10. The rake angle determined by Equation 4.14. for a 0.61 m diameter disc having a radius of curvature of 0.7 m operating at different tilt angles and various depths of cut.

But

$$A90 = r^2 (\gamma_1 - \text{Sin}\,\gamma_1\,\text{Cos}\,\gamma_1)\text{Cos}\,\alpha$$

where γ_1 is given by

$$\gamma_1 = \text{Sin}^{-1}\frac{L}{2r} \qquad \text{.....(4.15)}$$

and

$$L = 2\sqrt{d(2r\,\text{Cos}\,\alpha - d)}\;\text{Sec}\alpha \text{ by Equation 4.2.}$$

Substituting Equation 4.15. and Equation 4.2., then

or

$$A90 = r^2\left[\text{Sin}^{-1}\frac{L}{2r} - \frac{L}{2r}\sqrt{1 - \frac{L^2}{4r^2}}\right]\cdot\text{Cos}\,\alpha \qquad \text{.....(4.16)}$$

Therefore

$$Ap = r^2\left[\text{Sin}^{-1}\frac{L}{2r} - \frac{L}{2r}\sqrt{1 - \frac{L^2}{4r^2}}\right]\text{Cos}\,\alpha\,\text{Sin}\,\beta$$

or

$$Ap = r^2\left[\text{Sin}^{-1}\frac{L}{2r} - \frac{L}{4r^2}\sqrt{4r^2 - L^2}\right]\text{Cos}\alpha\;\text{Sin}\beta \text{.....(4.17)}$$

McCreery and Nichols (1956) determined this pressure area for a 24 in disc operating at a depth of d = 6 in using various disc angles. McCreery and Nichols (1956) did not show how this area was calculated.

However, a comparison between the values they determined for Ap and the values obtained by applying Equation 4.17. may be useful. Table 4.5. below and Figure 4.11. show the comparison between the values of pressure area Ap in inches^2 obtained by Equation 4.17. and the values in inches^2 as reported by McCreery and Nichols (1956).

Disc angle deg.	Reported values, in^2	Values obtained by Equation 4.17., in^2
0	0	0
5	8.8	7.71
10	15.4	15.36
15	20.68	22.89
20	30.24	30.25
30	43.76	44.22

Table 4.5. Pressure area Ap (in^2)

The values of McCreery and Nichols (1956) are very close to the values obtained by Equation 4.17. as shown in Figure 4.11. and Table 4.5.

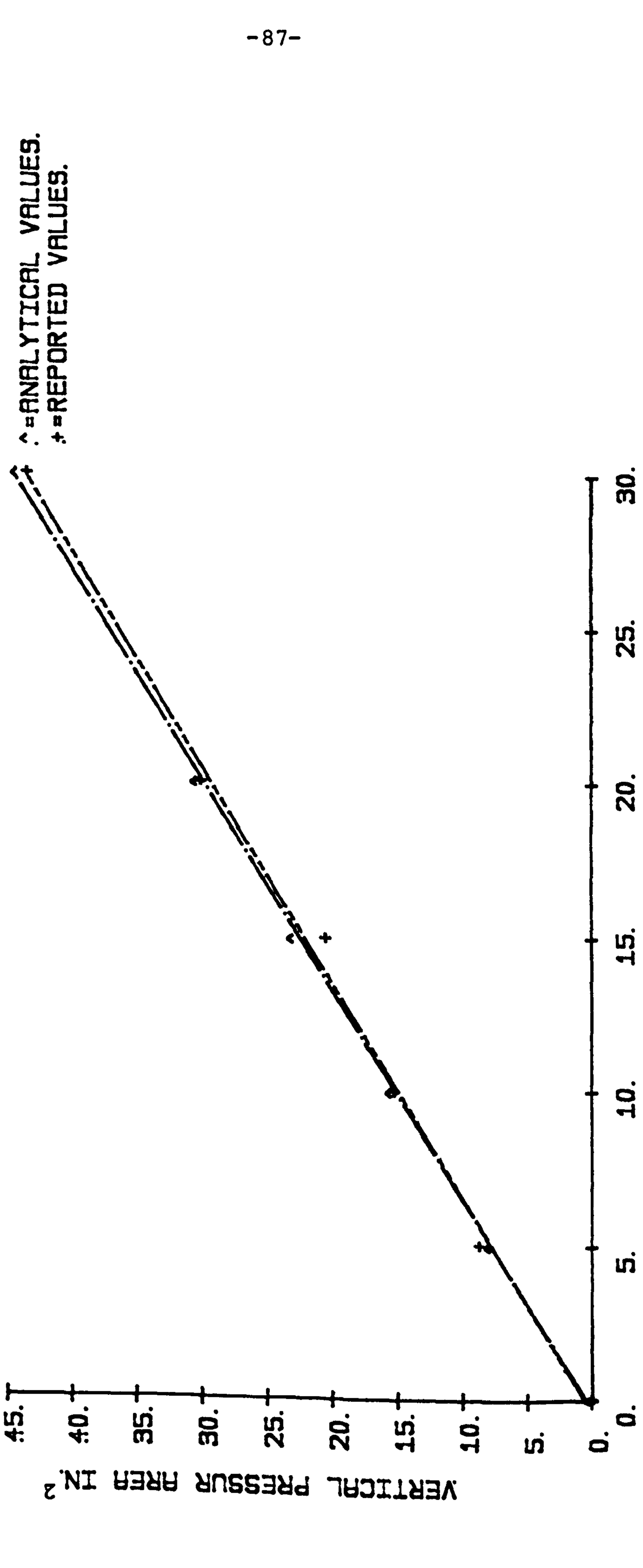

Figure 4.11. Analytically determined values of vertical pressure are in comparison to the reported values determined by McCreery and Nichols (1956) for a 24 in disc working at depth of 6 in.

The vertical pressure area is an important parameter in evaluating the draught, the side and vertical components of the soil resistance. Gupta and Pandya (1967) used this area in conjunction with the compressive stress developed in the soil to obtain the energy required for compressing the soil ahead of the disc.

Moreover, the vertical pressure area Ap is determined by using Equation 4.17. for 610 mm disc operating at various tilt angles and a depth of 140 mm as shown in Table 4.6. and Figure 4.12. From the graph and table of Equation 4.17. mentioned above, it can be seen that the pressure area Ap increases as the tilt angle increases for any given disc angle. The effect is relatively small due to the cosine effect.

4.2.5. Vertical bearing area Ab

McCreery and Nichols (1956) defined the vertical bearing area as the area between the cutting edge of the disc and the locus of the point when the direction of travel is tangent to the disc.

If the disc is in position such that $\beta = 0$, the disc will exert all pressure on the back of the disc and there is no vertical pressure area Ap in front of the disc, this area is called the shape area AO as shown in view 1 in Figure 4.1. and Figure 4.2. If the disc is angled such that

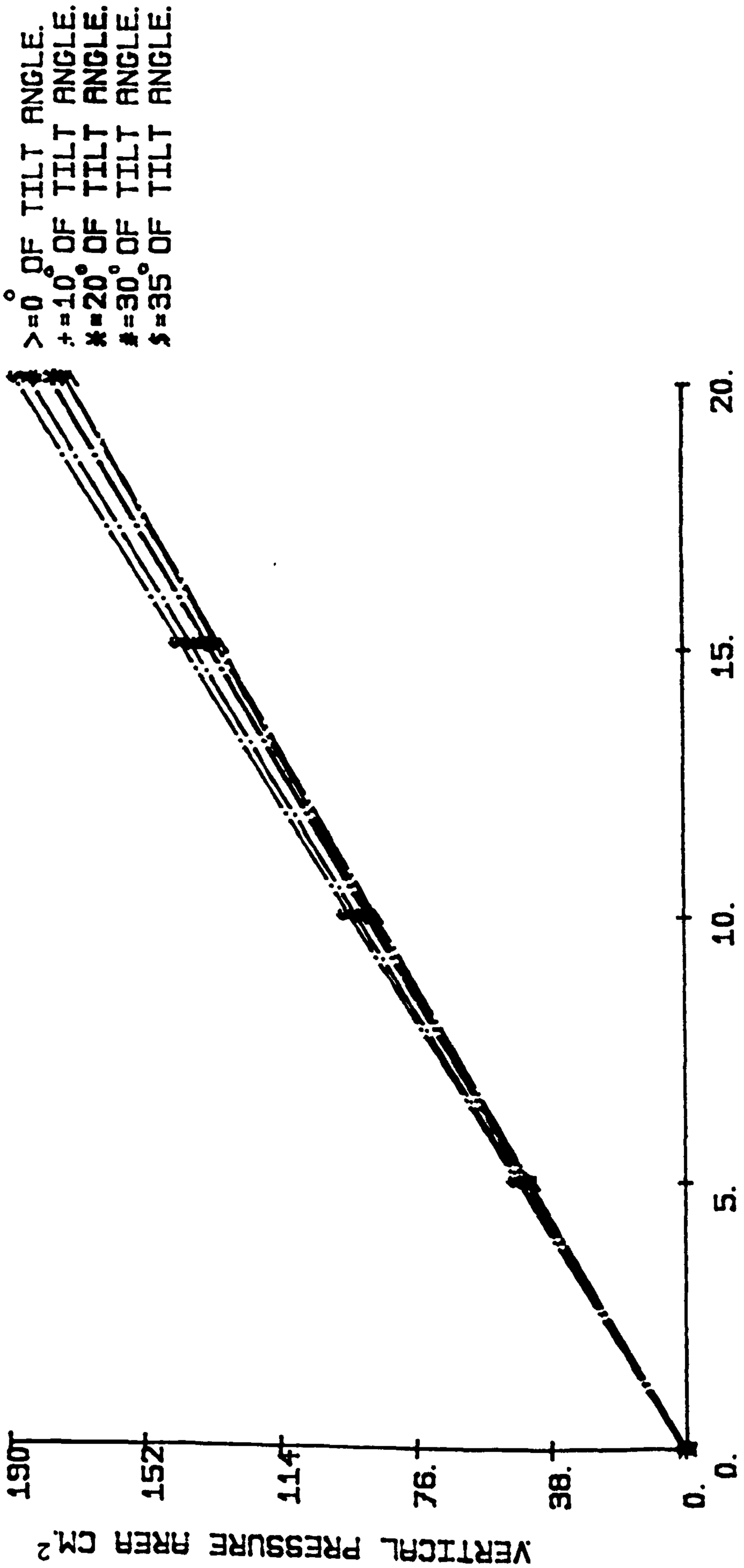

Figure 4.12. Vertical pressure area obtained by Equation 4.17. for a 0.61 m disc operating at various disc and tilt angles at a depth of 0.14 m

$\beta < \beta_c$ or d > dc, the convex side of the disc will exert pressure on the soil as shown in Figure 4.2. in view 5.

However, the vertical bearing area Ab can be analytically determined with reference to Figures 4.2., 4.7. and 4.8. as follows:

From Figure 4.7., the shape area of AO ($\beta = 0$) may be evaluated by viewing the disc on edge in view 1 in Figures 4.1. and 4.2.

Therefore

Total areas = AO + A1 + A2

$$\tfrac{1}{2} R^2 \gamma = AO + A1 + A2 \qquad \text{.....(4.18)}$$

where A1 and A2 triangles.

Figure 4.8. which expands on Figure 4.7. shows the other angles and the lengths that could aid analysis of these areas.

For the triangle A1, the following equations were developed:

$$A1 = \tfrac{1}{2} RX \cdot \sin \gamma \qquad \text{.....(4.19)}$$

since

$$\frac{X}{R} = \frac{\text{Sin}(\frac{1}{2}\pi - \epsilon)}{\text{Sin}(\frac{1}{2}\pi + \epsilon - \gamma)}$$

or

$$\frac{X}{R} = \frac{\text{Cos } \epsilon}{\text{Cos}(\epsilon - \gamma)}$$

hence

$$X = \frac{R \text{ Cos } \epsilon}{\text{Cos}(\epsilon - \gamma)} \qquad \ldots\ldots\ldots\ldots (4.20)$$

$$\frac{R - X}{R} = 1 - \frac{\text{Cos } \epsilon}{\text{Cos}(\epsilon - \gamma)}$$

or

$$R - X = \frac{\text{Cos}(\epsilon - \gamma) - \text{Cos } \epsilon}{\text{Cos } (\epsilon - \gamma)} \; R \qquad \ldots\ldots\ldots\ldots (4.21)$$

Substituting Equation 4.20. into Equation 4.19. gives:

$$2Al = R \frac{R \text{ Sin } \gamma \text{ Cos } \epsilon}{\text{Cos } (\epsilon - \gamma)}$$

or

$$2Al = R^2 \cdot \frac{\text{Sin } \gamma \text{ Cos } \epsilon}{\text{Cos } (\epsilon - \gamma)} \qquad \ldots\ldots\ldots\ldots (4.22)$$

For the triangle A2, the following equations were derived:

$$2A2 = (R - X)^2 \frac{\text{Sin } (\frac{1}{2}\pi - \epsilon + \gamma) \text{ Sin}(\alpha + \epsilon - \gamma)}{\text{Sin } (\frac{1}{2}\pi - \alpha)}$$

or

$$2A2 = (R - X)^2 \frac{\text{Cos } (\epsilon + \gamma) \text{ Sin } (\alpha + \epsilon - \gamma)}{\text{Cos } \alpha} \quad \ldots\ldots\ldots (4.23)$$

Substituting Equation 4.21. into Equation 4.23.gives:

$$A2 = \frac{1}{2} \frac{[\text{Cos } (\epsilon - \gamma) - \text{Cos}\epsilon]^2}{\text{Cos}^2 (\epsilon - \gamma)} \cdot \frac{\text{Sin } (\alpha + \epsilon - \gamma) \text{ Cos } (\epsilon + \gamma)}{\text{Cos } \alpha} R^2$$

Therefore

$$2A2 = \frac{[\text{Cos}(\epsilon - \gamma) - \text{Cos}\epsilon]^2}{\text{Cos } (\epsilon - \gamma)} \cdot \frac{\text{Sin } (\alpha + \epsilon - \gamma)}{\text{Cos } \alpha} R^2 \quad \ldots\ldots\ldots (4.24)$$

For the shape of AO, the following equations were developed:

$AO = \frac{1}{2} R^2 \gamma - A1 - A2$ given by Equation 4.18.

Therefore

$$\frac{2AO}{R^2} = \gamma - \frac{2A1}{R^2} - \frac{2A2}{R^2} \quad \ldots\ldots\ldots (4.25)$$

Substituting Equations 4.22. and 4.24. into Equation 4.25. gives:

$$\frac{2AO}{R^2} = \gamma - \frac{\sin\gamma\cos\epsilon}{\cos(\epsilon-\gamma)} - \frac{\left[\cos(\epsilon-\gamma) - \cos\epsilon\right]^2}{\cos(\epsilon-\gamma)} \cdot \frac{\sin(\alpha+\epsilon-\gamma)}{\cos\alpha}$$

Therefore

$$\frac{2AO}{R^2} = \gamma\frac{\cos(\epsilon-\gamma)\cos\alpha - \sin\gamma\cos\epsilon\cos\alpha - \left[\cos(\epsilon-\gamma) - \cos\epsilon\right]^2 . \sin(\alpha+\epsilon-\gamma)}{\cos(\epsilon-\gamma)\cos\alpha}$$

or

$$AO = \frac{\left[\gamma(\cos\alpha)\cos(\epsilon-\gamma) - \left[\sin(\gamma).\cos(\epsilon).\cos(\alpha)\right] - \left[\cos(\epsilon-\gamma) - \cos\epsilon\right]^2 . \sin(\alpha+\epsilon-\gamma)\right] R^2}{2\left[\cos(\alpha).\cos(\epsilon-\gamma)\right]}$$

.....(4.26)

To find Ab it can be recognised that

$Ab = 0^\circ$ at $\beta = \beta_c$

and

$Ab = AO$ at $\beta = 0^\circ$

It is not obvious how Ab might be integrated directly or indeed whether it is possible. In the absence of a better alternative, a linear interpolation between $\beta = 0^\circ$ and $\beta = \beta_c$ is proposed.

Therefore

$$Ab = AO \frac{(\beta_c - \beta)^K}{\beta_c}$$

Substituting Equation 4.26. gives:

$$Ab = \left[\frac{\gamma(\cos\alpha)\cos(\epsilon-\gamma) - [\sin(\gamma).\cos(\epsilon).\cos(\alpha)] - [\cos(\epsilon-\gamma) - \cos\epsilon]^2.\sin(\alpha+\epsilon-\gamma)}{2[\cos(\alpha).\cos(\epsilon-\gamma)]}\right]_R^2 . \frac{(\beta_c - \beta)^K}{\beta_c} \quad \ldots\ldots\ldots (4.27)$$

where

γ = given by Equation 4.12. or 4.13.

ϵ = given by Equation 4.11.

K = $1 < K < 2.5$

α = tilt angle

β_c = given by Equation 4.4.

β = disc angle

R = Radius of curvature

McCreery and Nichols (1956) determined and tabulated values of Ab for four 24 in discs having different radius of curvature when operated at various disc angles and 6 inches depth. McCreery and Nichols (1956) did not show how these values for the vertical bearing area were obtained.

However, it may be useful to compare the values of these areas calculated by Equation 4.27. at the same depth of 6 in with the values reported by McCreery and Nichols (1956) as shown in Table 4.7. below and Figure 4.13.

Table 4.7. Vertical bearing area Ab (in^2)

Radius of curvature of disc, R (inches)	Disc angle deg.								
			0	5	10	15	20	30	Critical disc angle deg. by Eq. 4.4.
37	21.07	Analytical by Eq. 4.27.	9.81	6.32	3.7	1.87	0.732	0.001	30.96
		Reported	10	6.44	3.6	2.16	0.8	---	
	25.5	Analytical by Eq. 4.27.	7.72	4.39	2.12	0.76	0.126	---	24.79
		Reported	7.8	4.32	1.64	0.8	0.12	---	
	28.74	Analytical by Eq. 4.27.	6.71	3.49	1.43	0.35	0.01	---	21.69
		Reported	6.76	3.52	1.12	0.48	---	---	
28.74		Analytical by Eq. 4.27.	5.06	2.06	0.44	0.013	---	---	16.54
		Reported	5.12	1.96	0.2	0.16	---	---	

Diameter of disc = 24 in
or r = 12 in
depth = 6 in

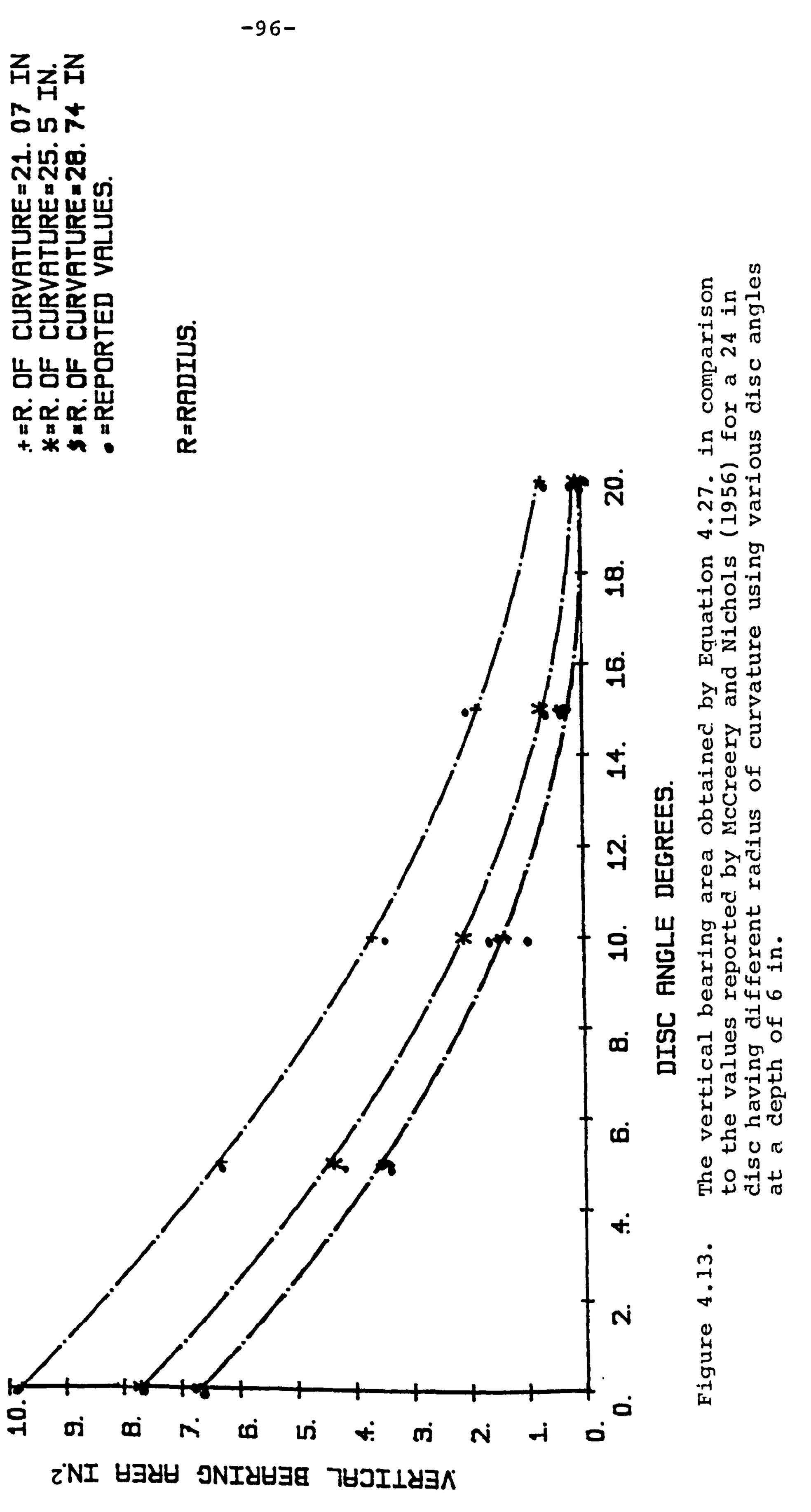

Figure 4.13. The vertical bearing area obtained by Equation 4.27. in comparison to the values reported by McCreery and Nichols (1956) for a disc having different radius of curvature using various disc angles at a depth of 6 in.

It can be seen from Table 4.7. and Figure 4.13. that the reported values are very close to the calculated values obtained by Equation 4.27.

Furthermore, Equation 4.27. is used to determine the values of this area Ab for a 61 cm disc having radius of curvature 70 cm, operated at various disc and tilt angles at 14 cm depth, as shown in Table 4.8. and Figure 4.14. Table 4.8. and Figure 4.14. indicate that the value of the vertical bearing area increases as the tilt angle increases for any given disc angle. This is caused by the increase of critical disc angle as the tilt angle increases as Equation 4.4. suggests.

4.2.6. Horizontal bearing area Abh

The horizontal bearing area may be defined as the area of soil in contact with the back of the disc projected onto the horizontal plane normal to the direction of travel. As shown in Figure 4.15, this area may be developed as follows:

$$2Abh = Rs^2\left[\textcircled{H} - \sin\textcircled{H}\cos\textcircled{H}\right]$$

where $\textcircled{H}$ is given by

$$\textcircled{H} = \left(\sin^{-1}\frac{L}{2RS}\right) - \beta \qquad \text{.....(4.28)}$$

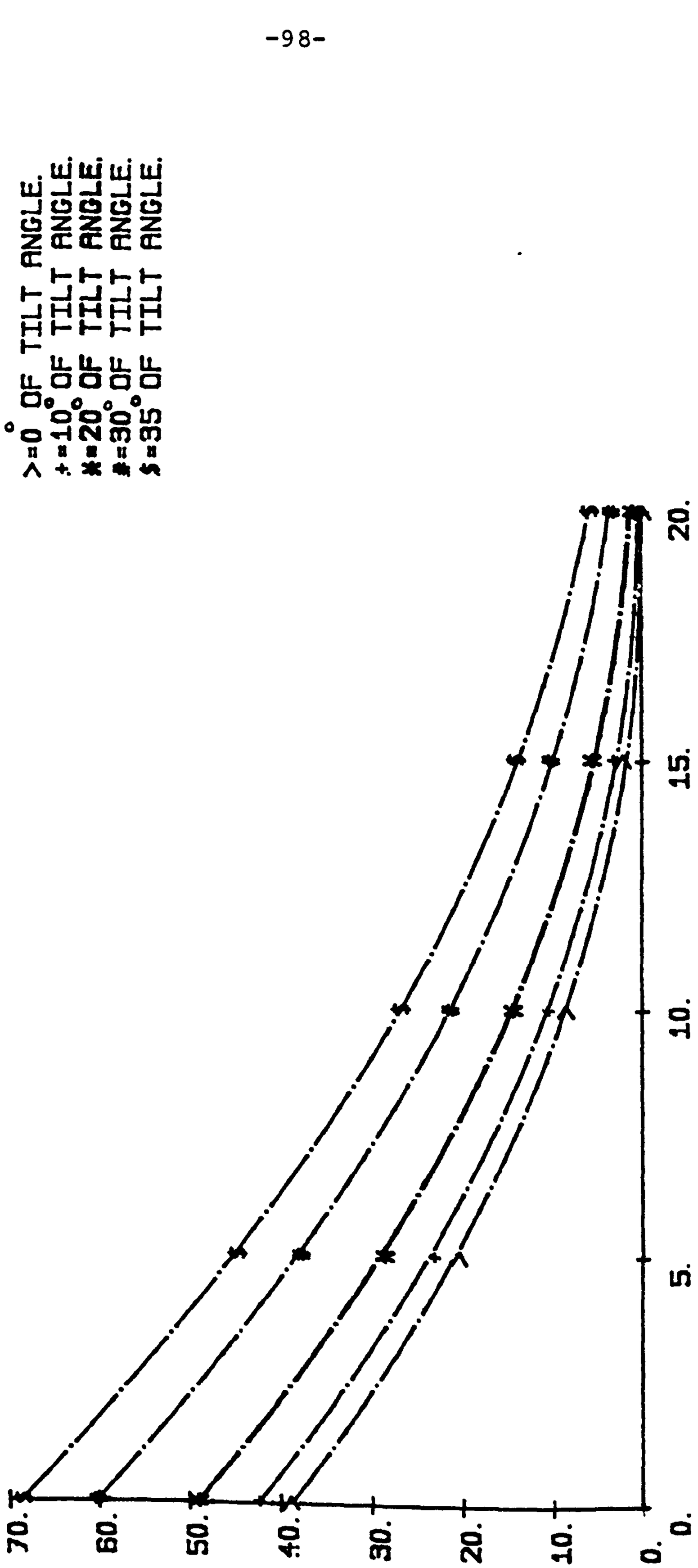

Figure 4.14. Vertical bearing area calculated by Equation 4.27. for a 0.61 m disc having a radius of curvature of 0.7 m operating at various disc and tilt angles at a depth of 0.14 m

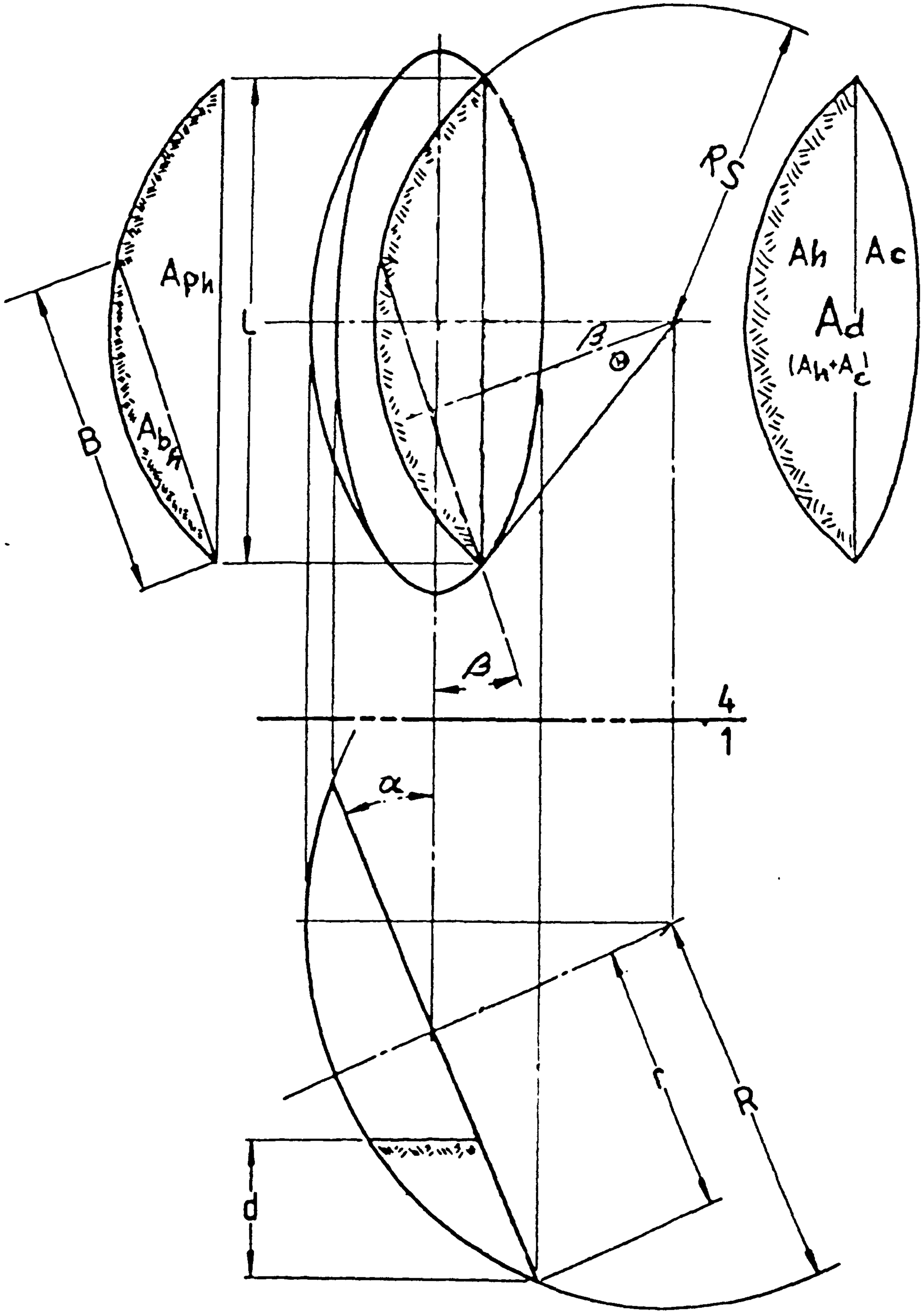

Figure 4.15. The submerged areas of disc projected into the horizontal plane at a soil surface

and L = given by Equation 4.2.

Substituting Equation 4.28. gives:

therefore

$$2Abh=Rs^{2}\left[\left(Sin^{-1}\frac{L}{2RS}\right)-\beta\right)-Sin\left(Sin^{-1}\frac{L}{2RS}\right)-\beta\right)\cdot Cos\left(Sin^{-1}\frac{L}{2RS}\right)-\beta\right)\Bigg] \quad \ldots\ldots\ldots (4.29)$$

where Rs = given by Equation 4.3.

Equation 4.29. is used to calculate a value of twice the horizontal bearing area. As shown in Figure 4.15, only the front half of this area is pressing the soil. Abo El Eas and Wills (1986) determined this area for a 0.457 m disc having a radius of curvature of 0.61 m and operating at various depth and different disc angles.

It may be useful to compare the values of this area obtained by Abo El Eas and Wills (1986) and the values determined by Equation 4.29. According to Figure 4.16, the reported values determined by Abo El Eas and Wills (1986) and the values determined by Equation 4.29. are very close.

Equation 4.29. is also used to determine the horizontal bearing area for a 610 mm disc having radius of curvature R, 700 mm at 140 mm depth and at various tilt and disc angles

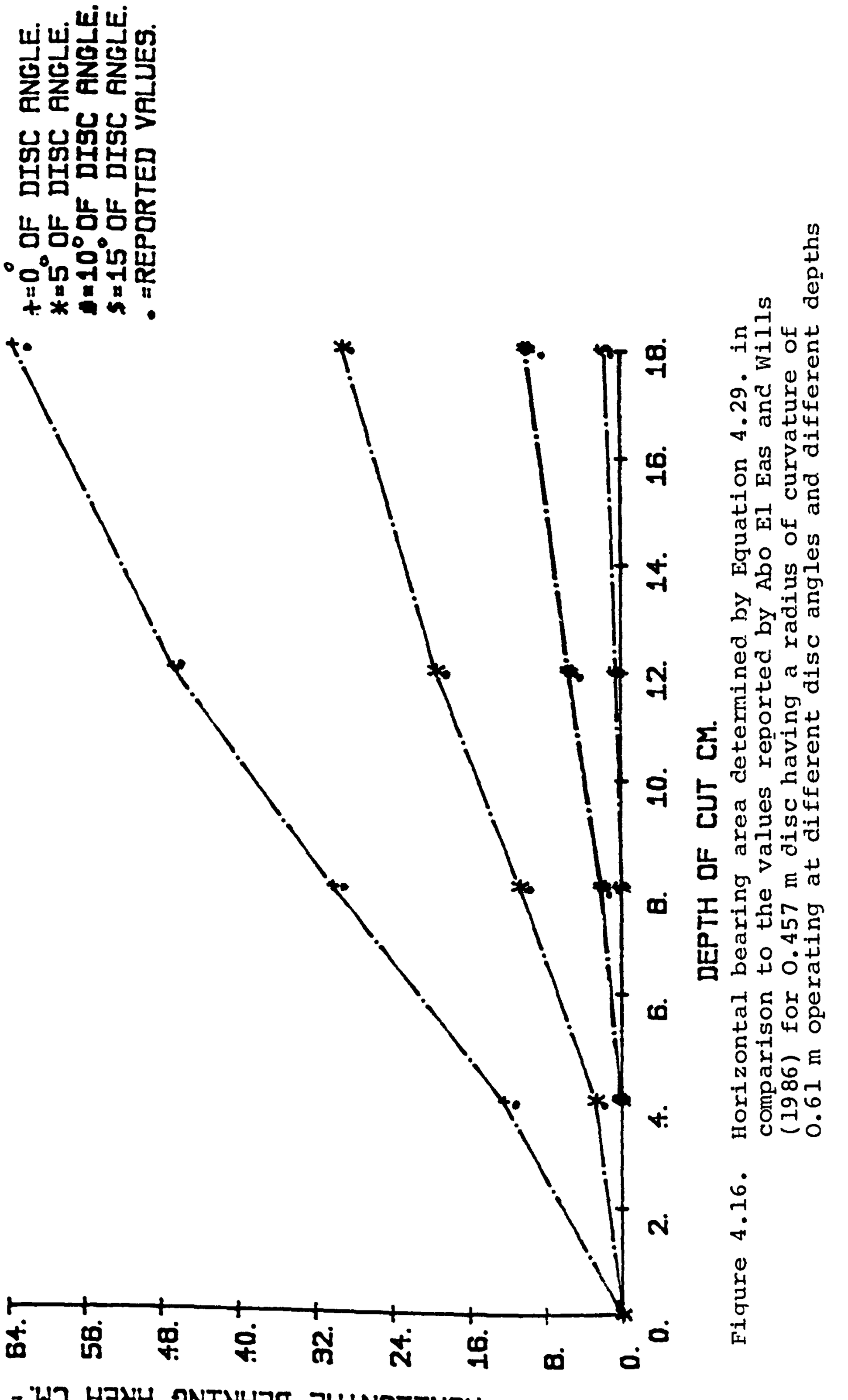

Figure 4.16. Horizontal bearing area determined by Equation 4.29. in comparison to the values reported by Abo El Eas and Wil (1986) for 0.457 m disc having a r 0.61 m operating at different disc depths

as shown in Table 4.9. and Figure 4.17. The values for this area increase as the tilt angle increases for any given disc angle as indicated in Table 4.9. and Figure 4.17.

It should be mentioned here that this area disappears when the disc angle is equal to critical disc angle $\beta = \beta_c$ and the depth of penetration is equal to critical depth d = dc at which point it has the same behaviour as the vertical bearing area (Ab).

4.2.7. Horizontal pressure area Aph

Horizontal pressure area is the projection of submerged area onto the horizontal plane of the concave side of the disc with respect to the travel direction. As shown in Figure 4.15, this area may be derived as follows:

$$Aph = Rs^2 \left[\left(\sin^{-1} \frac{L}{2RS}\right) - \textcircled{H} + \sin \textcircled{H} \,.\, \cos \textcircled{H} - \left(\frac{L}{4RS}\sqrt{4 - \frac{L^2}{RS^2}}\right) \right] \qquad \ldots\ldots\ldots(4.30)$$

where

L = given by Equation 4.2.

RS = given by Equation 4.3.

$\textcircled{H}$ = given by Equation 4.28.

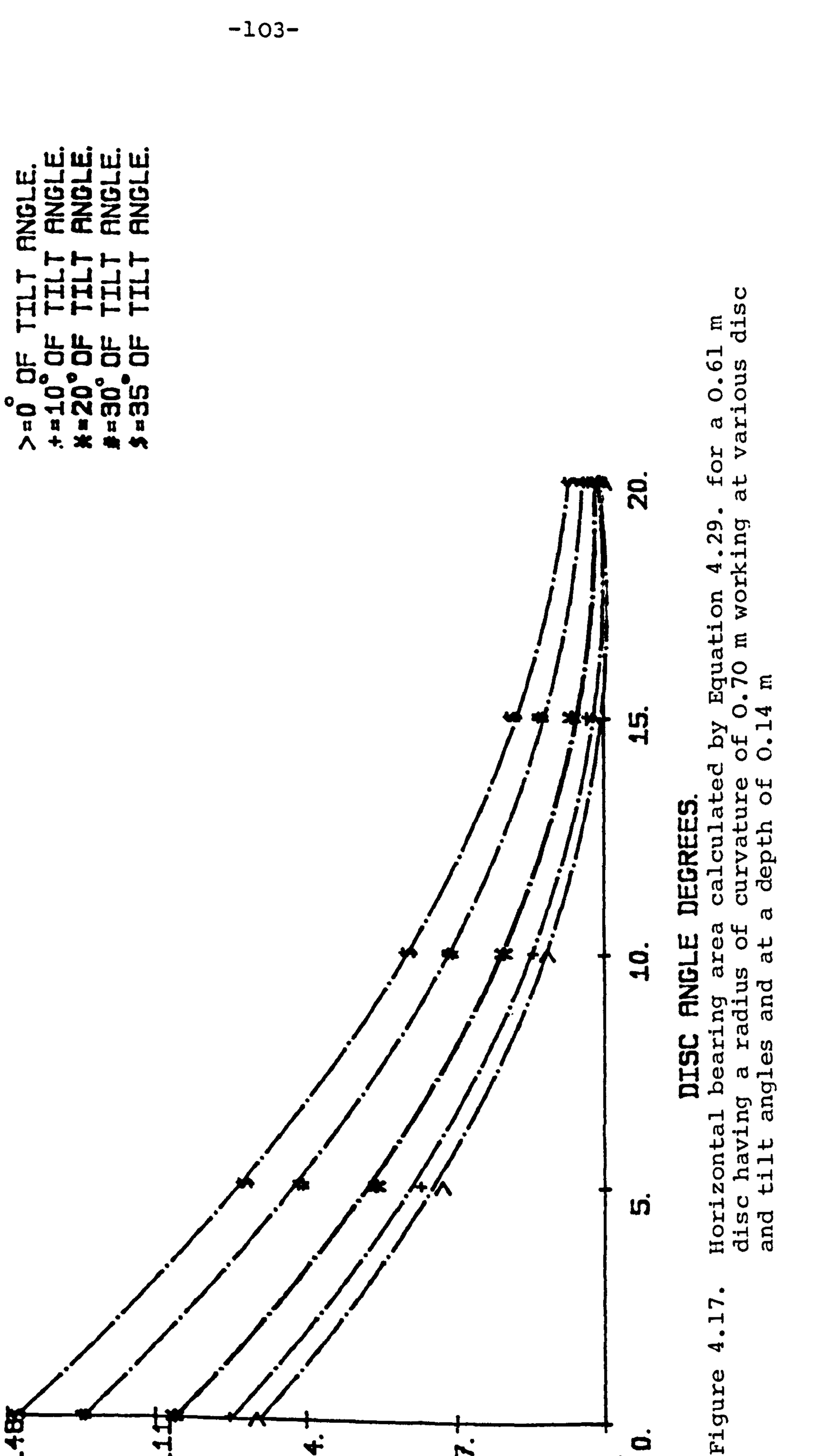

Figure 4.17. Horizontal bearing area calculated by Equation 4.29. for a 0.61 m disc having a radius of curvature of 0.70 m working at various disc and tilt angles and at a depth of 0.14 m

Abo El Eas and Wills (1986) determined this area mathematically but they did not give values for it. However, Figure 4.18. shows this area by applying Equation 4.30. for the same disc used by Abo El Eas and Wills (1986) to determine the horizontal bearing area.

It should be mentioned here that the horizontal pressure area and the horizontal bearing area are equal to the horizontal component area Ah as shown in Figure 4.15. The horizontal component Ah will be explained in turn. This indicates that the values of horizontal pressure area Aph obtained by Equation 4.30. should be the same or very close to the values of Abo El Eas and Wills if their values were given.

Furthermore, Equation 4.30. is applied to determine the values of this area for 610 mm disc having radius of curvature of 700 mm operating at various disc and tilt angles at 140 mm depth as shown in Table 4.10. and Figure 4.19. The values of the horizontal pressure area Aph are independent of the disc angle as $\beta \geq \beta_c$ and d = dc. If the disc angle decreases from the critical disc angle to zero, the horizontal pressure area continues to decrease until it becomes zero for any depth as shown in Figure 4.18. This area and the horizontal bearing area are important parameters to determine the soil volume on the front and back

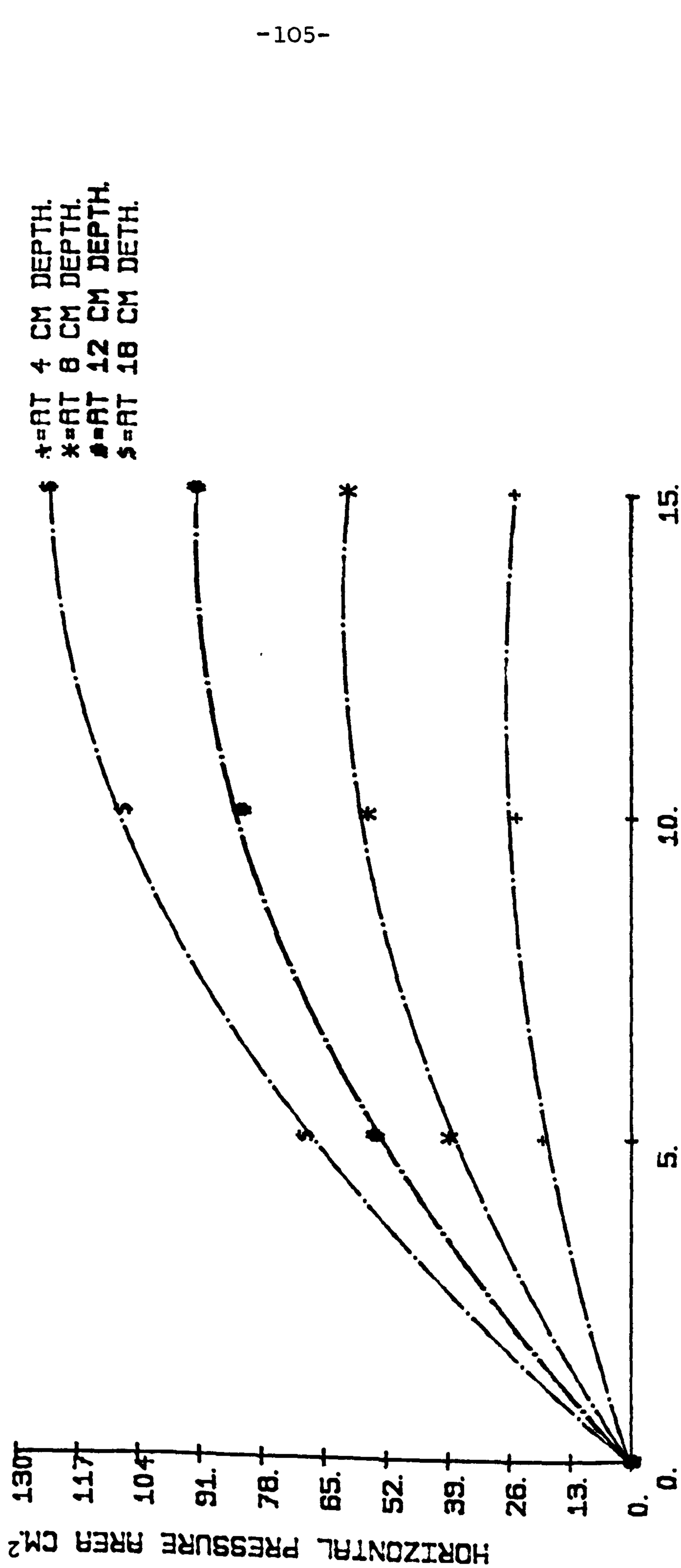

Figure 4.18. Horizontal pressure area determined by Equation 4.30. for a disc having a radius of curvature of 0.61 m operating at different disc angles and different depths.

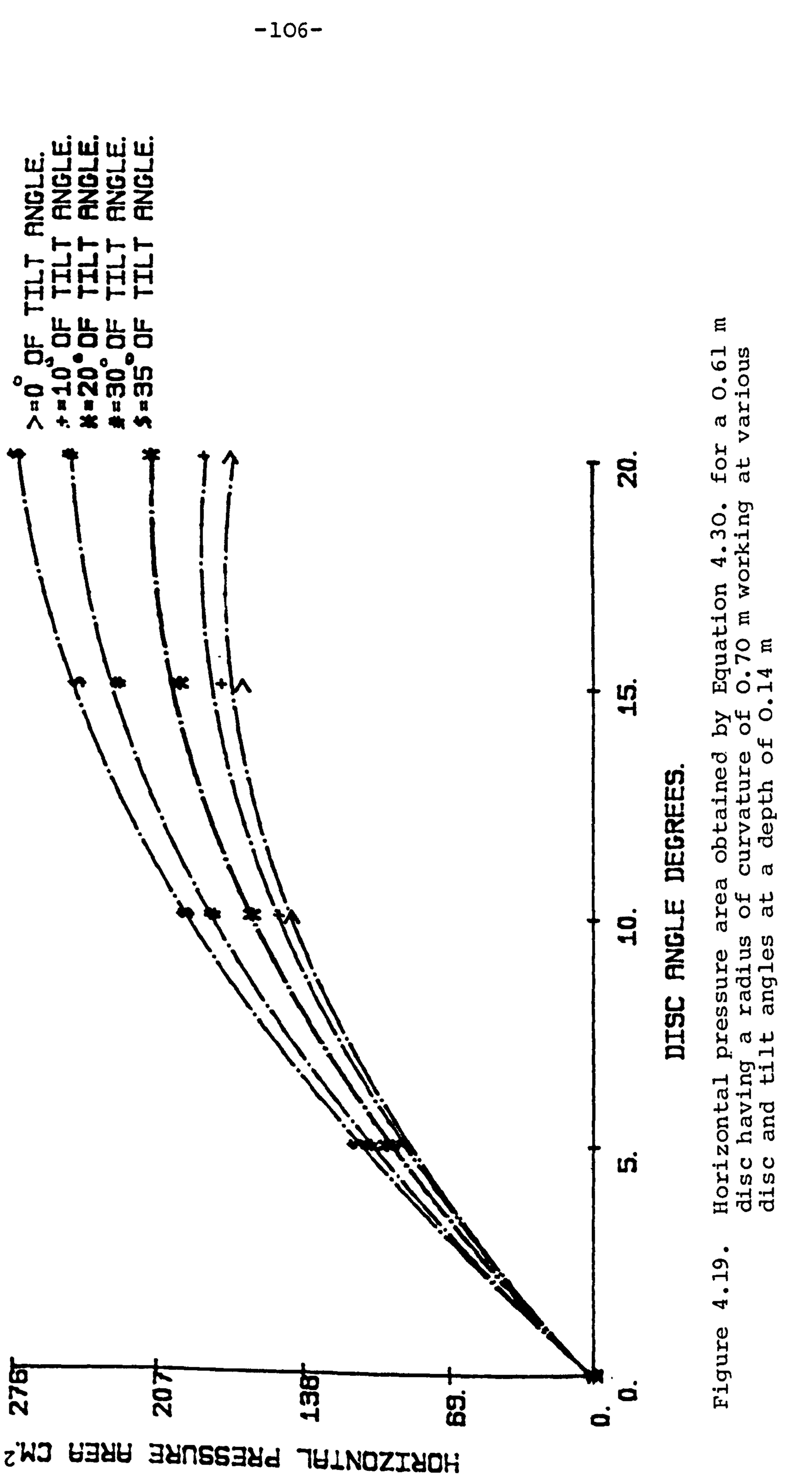

Figure 4.19. Horizontal pressure area obtained by Equation 4.30. for a disc having a radius of curvature of 0.70 m working at various disc and tilt angles at a depth of 0.14 m

of the disc respectively.

4.2.8. Horizontal area Ah

The horizontal area is the total horizontal component of the horizontal bearing area Abh and the horizontal pressure area Aph with respect to the direction of travel in the horizontal plane. As shown in Figure 4.15, the horizontal component area may be broken into two further parts, corresponding to the horizontal pressure area, Aph and horizontal bearing area Abh. These two areas are separated by the chord of length (B).

According to the Figure 4.15, B and Ah are developed as follows:

$$B = 2RS \sin \textcircled{H} \qquad \text{.....(4.31)}$$

$$Ah = RS^2 \left(\sin^{-1} \frac{L}{2RS}\right) - \left(\frac{L}{2}\sqrt{RS^2 - \frac{L^2}{4}}\right) \qquad \text{.....(4.32)}$$

where

Rs = given by Equation 4.3.

L = given by Equation 4.2.

$\textcircled{H}$ = given by Equation 4.28.

The values of this area are determined by applying Equation 4.32. for 610 mm disc having radius of curvature R = 700 mm operating at various tilt angles and different depth as shown in Table 4.11. and Figure 4.20. According to Table 4.11. and Figure 4.20, it may be observed that the horizontal area Ah is equal to zero at zero depth for any given values of disc angle. In other words, the values of this area are not affected by disc angle but this area is affected by changing the tilt angle and depth of penetration.

4.2.9. Inclination area Ac

Inclination area is the projected area through the tilt angle in the horizontal plane of the part of the concave side of the disc.

From Figure 4.15, the inclination area can be derived as follows:

$$Ac = \left[r^2 \left(\mathrm{Sin}^{-1} \frac{L}{2r}\right) - \left(\frac{L}{2}\sqrt{r^2 - \frac{L^2}{4}}\right)\right] \mathrm{Sin}\,\alpha \qquad .....(4.33)$$

where

r = disc radius

α = tilt angle

L = given by Equation 4.2.

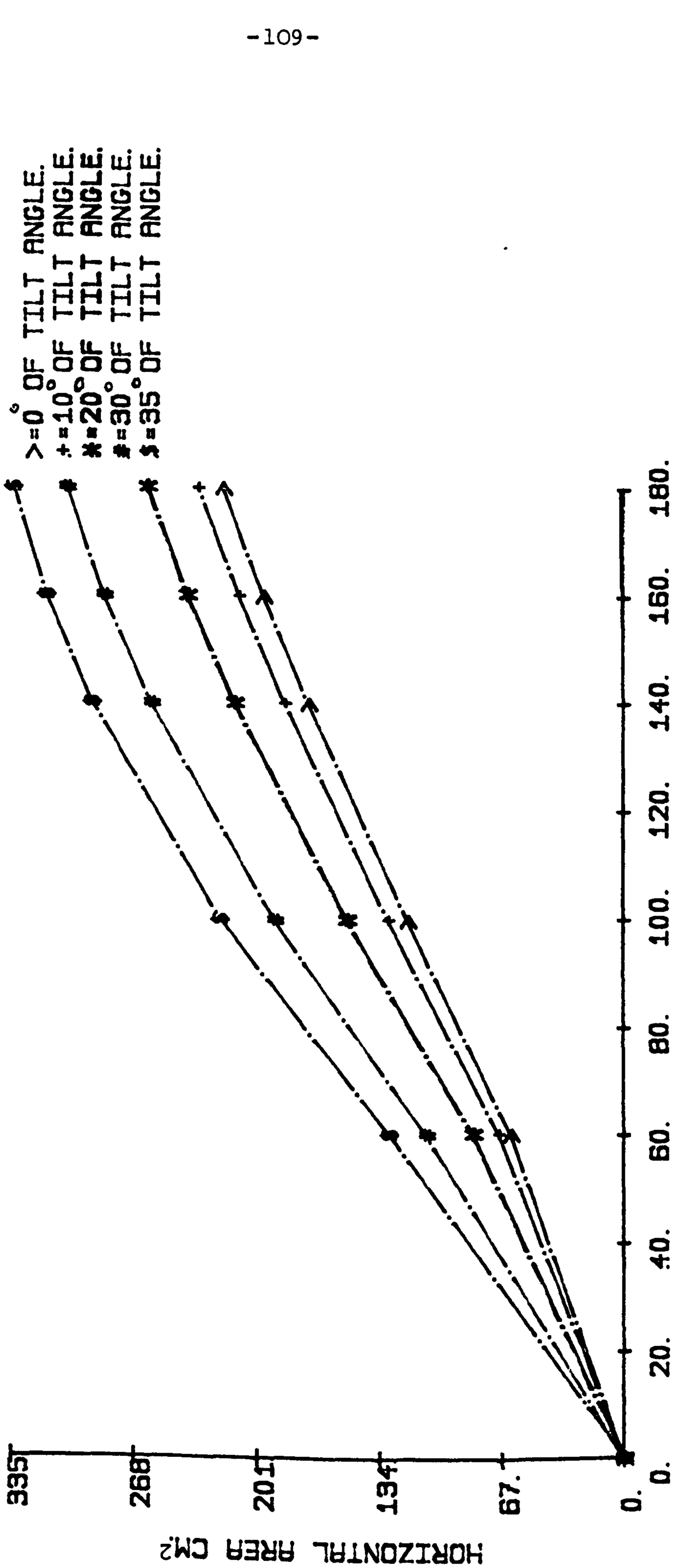

Figure 4.20. Horizontal area determined by Equation 4.32. for a 0.61 m disc having a radius of curvature of 0.7 m working at various angles of tilt and different depths

The values of this area are calculated using Equation 4.33. for 610 mm disc having radius of curvature of 700 mm operating at different tilt angles and various depths as shown in Table 4.12. and Figure 4.21. The values of this area are not affected by disc angle but are affected by changing the tilt angle and depth. This area is always equal to zero when the disc is in vertical position. As shown in Figure 4.21, the inclination area increases as the tilt angle increases for any given depth.

4.2.10. Loading area Ad

The loading area is conveniently broken down into the projected areas of the horizontal area, Ah and inclination bounding area in the horizontal plane, Ac. The loading area seen from below represents the convex area in the horizontal plane and from above represents the horizontal area, Ah plus an inclination area Ac. As shown in Figure 4.15, this area may be developed as follows:

$$Ad = Ah + Ac \qquad \text{.....(4.34)}$$

where

Ah = given by Equation 4.32.

Ac = given by Equation 4.33.

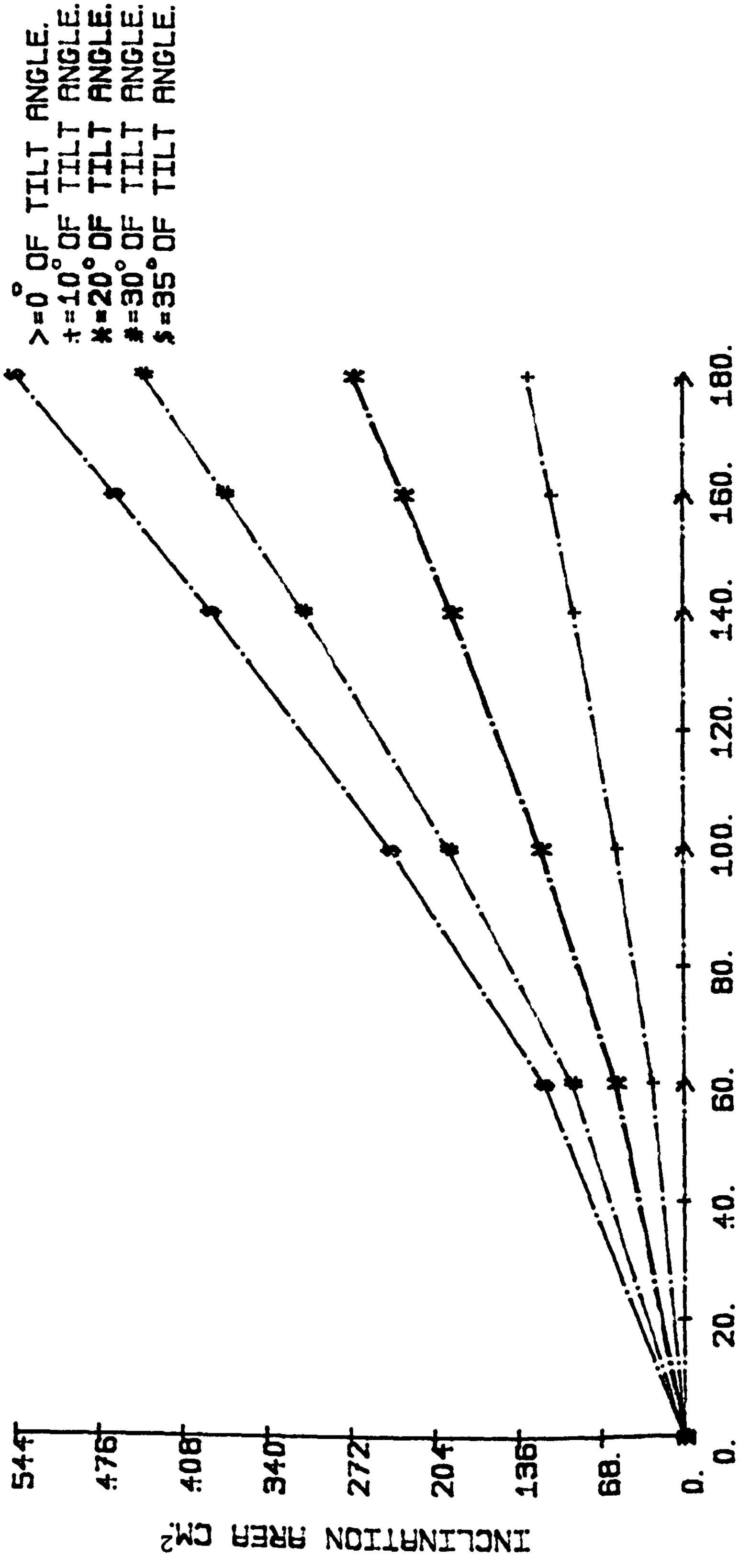

Figure 4.21. Inclination area obtained by Equation 4.33. for a 0.61 m disc operating at different tilt angles and various depths

The values of this area are obtained by using Equation 4.34. for 610 mm disc having radius of curvature of 700 mm operating at various tilt angles and different depths as shown in Table 4.13. and Figure 4.22. The behaviour of this area is the same as the horizontal and inclination areas which are not changed for any given disc angle and is affected for any given tilt angle and depth as shown in the Table and the Figure mentioned above.

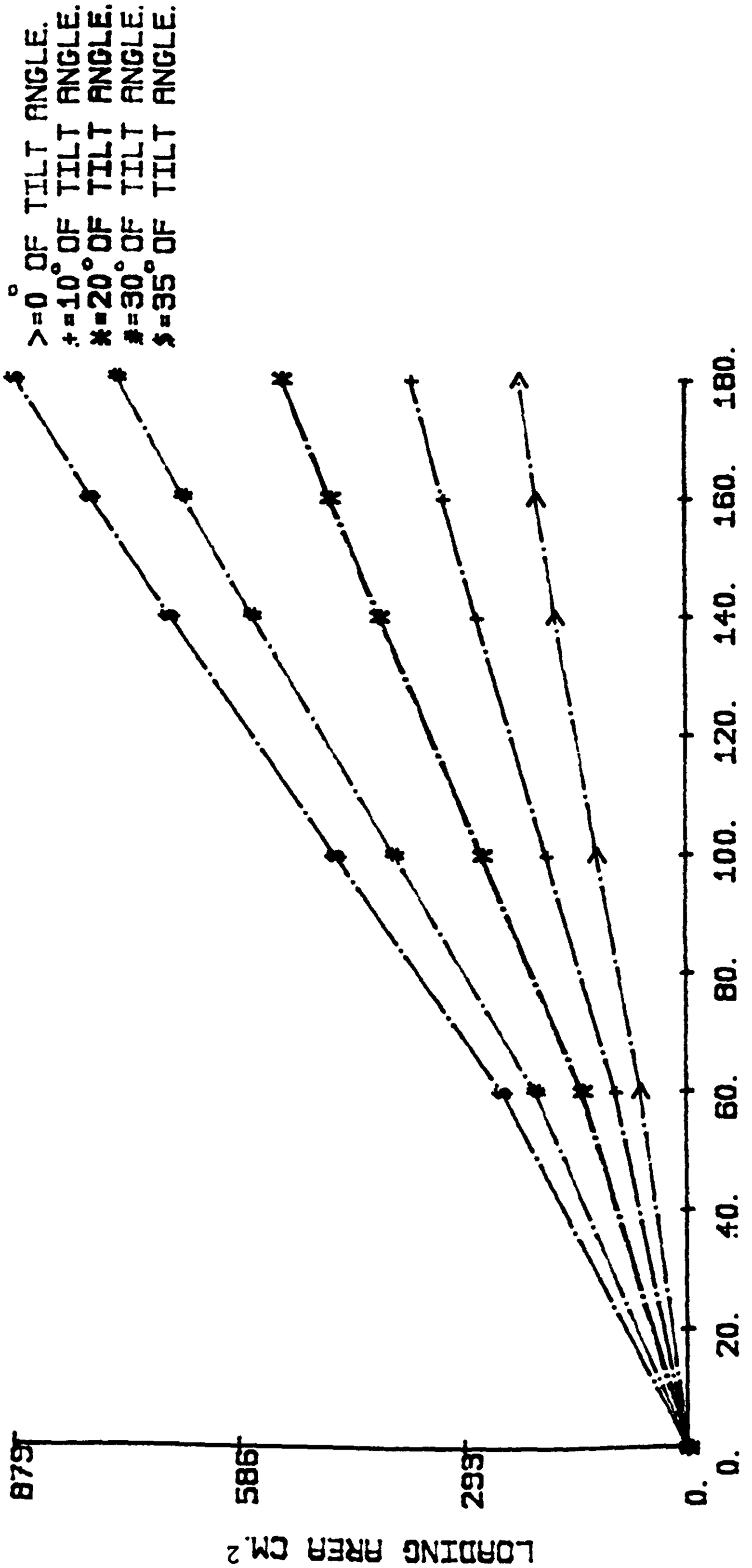

Figure 4.22. Loading area determined by Equation 4.34. for a 0.61 m disc having a radius of curvature of 0.7 m using various tilt angles and different depths

CHAPTER 5

5. Determination of disturbance area caused by rotating discs

5.1. Introduction

A knowledge of the soil-disc geometry will provide the means for improving the design and the use of discs. The disturbance area of the soil is an important factor in the determination of the specific resistance. Methods are developed for determination of overlap area, the vertical pressure area and the gang area as formed by rotating discs. The information is important in the design and use of the discs. It is the purpose of this line of study to determine the gang area as an important variable in the disturbance of the soil caused by rotating soil-cutting discs. This actual disturbance area can then be used to determine the specific resistance as will be shown.

5.2. Overlap area (Aov)

Overlap area may be defined as the area cut by a following disc, below the soil surface which has been cleared of soil by the previous disc measured in the vertical of the disc normal to the direction of travel, as shown in Figures 5.1. and 5.2. The overlap area can be evaluated by setting the tilt angle to zero and the disc angle to

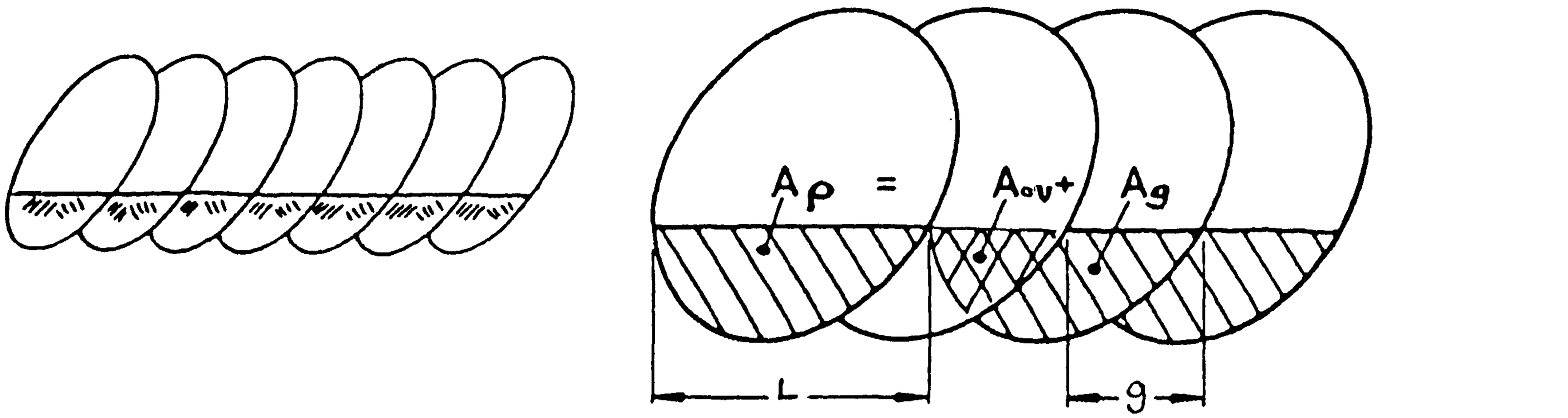

Figure 5.1. Various areas cut by rotating disc at different disc angles and at zero tilt angles

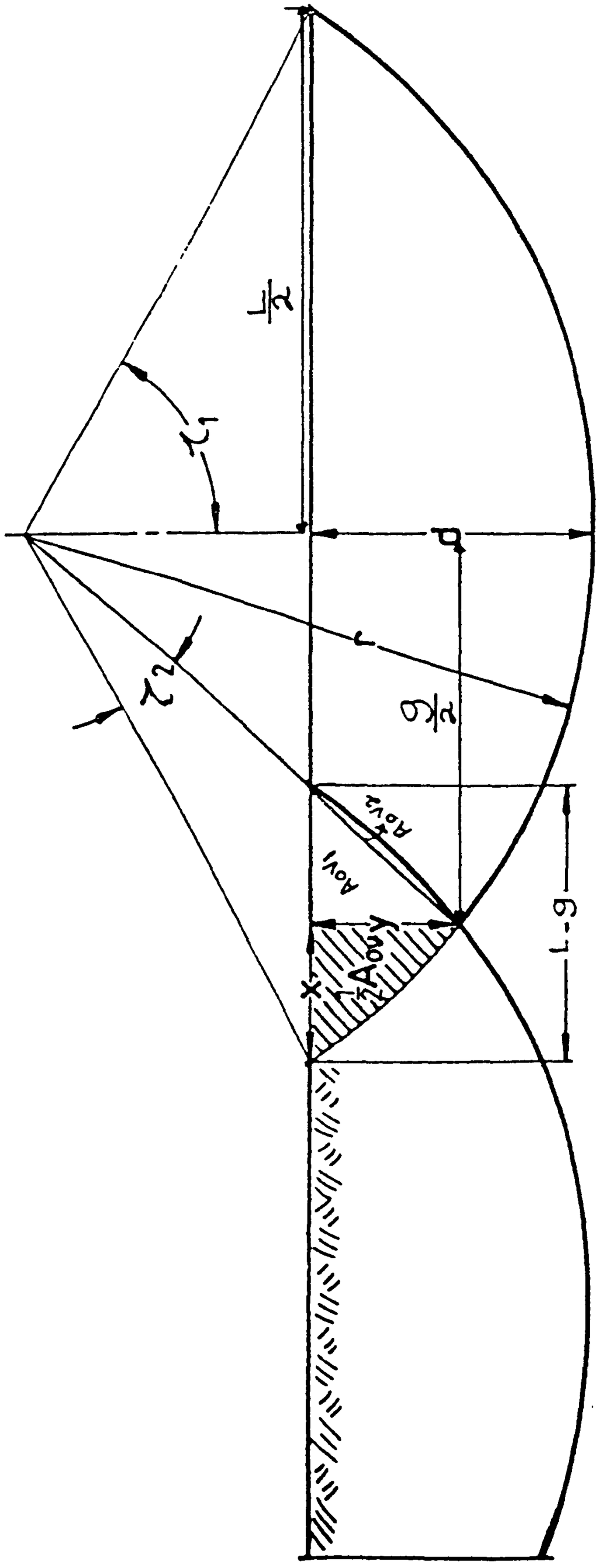

Figure 5.2. Determination of overlap area, vertical pressure area and gang area at different disc angles

90^{o}, as shown in Figure 5.2. For this situation the projected width L is given as follows:

$$\frac{L}{2} = r \, Sin \, \gamma_1$$

or

$$\frac{L^2}{4} = r^2 \, Sin^2 \, \gamma_1 \qquad .....(5.1)$$

$$r - d = r Cos \, \gamma_1$$

or

$$(r - d)^2 = r^2 \, Cos^2 \, \gamma_1 \qquad .....(5.2)$$

Adding Equations 5.1. and 5.2. gives:

$$\frac{L^2}{4} + (r - d)^2 = r^2 \, (Sin^2 \, \gamma_1 + Cos^2 \, \gamma_2)$$

$$L^2 = 4 \, (2rd - d^2)$$

$$L = 2 \sqrt{d \, (2r - d)} \qquad .....(5.3)$$

where

r = disc radius

d = depth of cut

This overlapping area may be calculated as shown in Figure 5.2.

as follows:

$$\tfrac{1}{2}\ Aov = Aov_1 + Aov_2 \qquad \ldots\ldots\ldots(5.4)$$

But

$$Aov_1 = \tfrac{1}{2} \cdot XY \qquad \ldots\ldots\ldots(5.5)$$

and

$$Aov_2 = \tfrac{1}{2}\ r^2\ \gamma_2 - \tfrac{1}{2}\ r^2\ \text{Sin}\ \gamma_2$$

$$= \tfrac{1}{2}\ r^2\ (\gamma_2 - \text{Sin}\ \gamma_2) \qquad \ldots\ldots\ldots(5.6)$$

Substituting Equations 5.5. and 5.6. into Equation 5.4. gives:

$$\tfrac{1}{2}\ Aov = \tfrac{1}{2}\ .XY + \tfrac{1}{2}\ r^2\ (\gamma_1 - \text{Sin}\ \gamma_2)$$

$$Aov = XY + r^2\ (\gamma_1 - \text{Sin}\ \gamma_2) \qquad \ldots\ldots\ldots(5.7)$$

Where

$$X = r\left[\text{Sin}\ \gamma_1 - \text{Sin}\ (\gamma_1 - \gamma_2)\right]$$

$$= r\left[2\ \text{Sin}\ \frac{\gamma_2}{2}\ \text{Cos}\ (\gamma_1 - \frac{\gamma_2}{2})\right] \qquad \ldots\ldots\ldots(5.8)$$

$$Y = r\left[\text{Cos}(\gamma_1 - \gamma_2) - \text{Cos}\ \gamma_1\right]$$

$$= r\left[2\ \text{Sin}\ \frac{\gamma_2}{2}\ \text{Sin}\ (\gamma_1 - \frac{\gamma_2}{2})\right] \qquad \ldots\ldots\ldots(5.9)$$

Substituting Equations 5.8. and 5.9. into Equation 5.7. gives:

$$\text{Aov} = r^2\left[(1 - \text{Cos}\ \gamma_2)\ (\text{Sin}\ (2\gamma_1 - \gamma_2) + \gamma_2 - \text{Sin}\ \gamma_2\right]$$

$\ldots\ldots\ldots(5.10)$

Where

γ_1 = given by Equation 4.15

γ_2 = given by Equation 5.14

5.3. Vertical pressure area Ap

The vertical pressure area can be determined by setting the tilt angle α to zero and the disc angle β to 90° as shown in Figure 5.2. For this situation the vertical pressure area is derived as follows:

$$\text{Ap} = r^2\ (\gamma_1 - \text{Sin}\ \gamma_1\ \text{Cos}\ \gamma_1) \qquad \ldots\ldots\ldots(5.11)$$

The vertical pressure area projected through the

disc angle in the direction of travel is developed as below:

$$Ap = r^2 \left(\gamma_1 - \text{Sin}\, \gamma_1 \text{ Cos } \gamma_1 \right) \text{Sin}\beta \qquad \ldots\ldots\ldots(5.12)$$

Where

$\gamma_1 = \text{Sin}^{-1} \frac{L}{2r}$ given by Equation 4.15

L = given by Equation 4.2

As shown in Figure 5.2., the gang spacing g is given by

$$\frac{g}{2} = r \text{ Sin } (\gamma_1 - \gamma_2)$$

or

$$\gamma_1 - \gamma_2 = \text{Sin}^{-1} \frac{g}{2r} \qquad \ldots\ldots\ldots(5.13)$$

Subtracting Equation 5.13. from Equation 4.14. gives:

$$\gamma_2 = \text{Sin}^{-1} \frac{L}{2r} - \text{Sin}^{-1} \frac{g}{2r} \qquad \ldots\ldots\ldots(5.14)$$

5.4. Gang area Ag

The gang area may be defined as the area projected by a single disc working between other discs at the same depth and angle setting in the vertical plane of the concave side of the disc normal to the direction of motion. This area can be evaluated as shown in Figure 5.1. by the relation below:

$$Ag = Ap - Aov \qquad \ldots\ldots\ldots (5.15)$$

Equation 5.15. can be valid as long as vertical pressure area Ap, the overlap area Aov and the gang area Ag are constants as shown in Figure 5.1. If the shapes are distorted by tilt and disc angles, Equation 5.15. cannot be used in this case. It may be taken from ideal case ($\alpha = 0$, $\beta = 90^{o}$) to general case by transporting invariant area on the ratio (Aov/Ap). As indicated in Figure 5.2. the ratios Aov/Ap can be developed based on Equation 5.10. and Equation 5.11. as follows:

$$\frac{Aov}{Ap} = \frac{r^2 \left[(1 - \cos \gamma_1)\ (\sin\ (2\gamma_1 - \gamma_2) + \gamma_2 - \sin \gamma_2\right]}{r^2 \left[\gamma_1 - \sin \gamma_1 \cos \gamma_1\right]}$$

$$= \frac{\left[(1 - \cos \gamma_1)\ (\sin\ (2\gamma_1 - \gamma_2) + \gamma_2 - \sin \gamma_2\right]}{\left[\gamma_1 - \sin \gamma_1 \cos \gamma_1\right]} \qquad \ldots\ldots\ldots (5.16)$$

When the tilt angle $\alpha > 0$ and disc angle $\beta < 90^{\circ}$, the gang area is developed by the relation below:

$$Ag = Ap - Aov$$

$$= Ap\ (1 - Aov/Ap) \qquad \text{.....(5.17)}$$

where

Ap = given by Equation 5.12

Aov/Ap = given by Equation 5.16.

Equation 5.17. is applied to determine gang area for a 0.61 m disc at 0.14 m depth operating at different disc and tilt angles. As shown in Table 5.1. and Figure 5.3., the gang area increases for any given disc angle and increases as tilt angle increases.

The increases in the gang area may be caused by increasing critical disc angle which reduces the soil disturbance as the tilt angle increases.

Moreover, Equation 5.17. is evaluated to determine the gang areas at 0.1 m and 0.08m depths for a 0.61 m disc setting at various disc and tilt angles as shown in Table 5.2. and Figures 5.4. and 5.5. This table and these figures

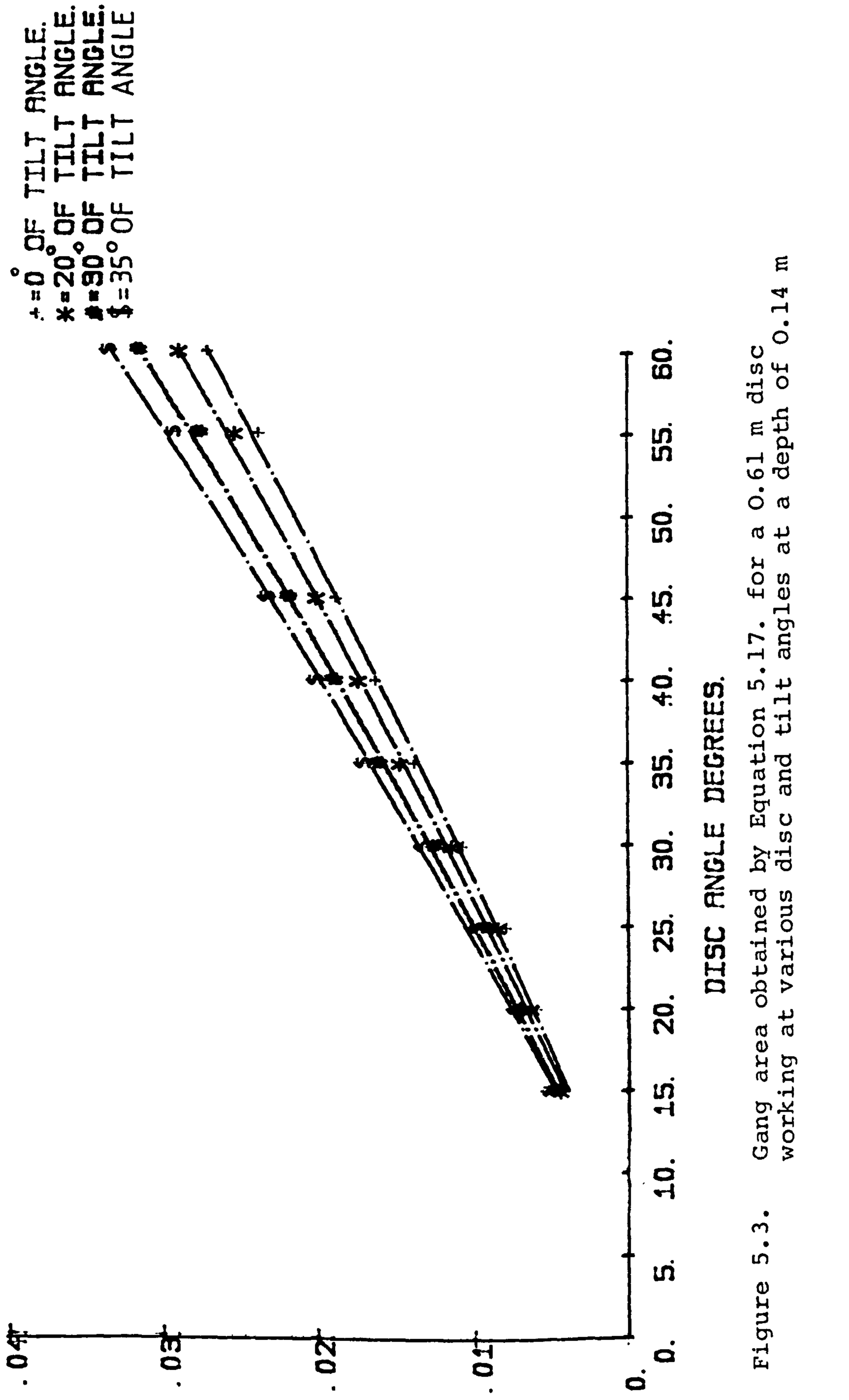

Figure 5.3. Gang area obtained by Equation 5.17. for a 0.61 m disc working at various disc and tilt angles at a depth of 0.14 m

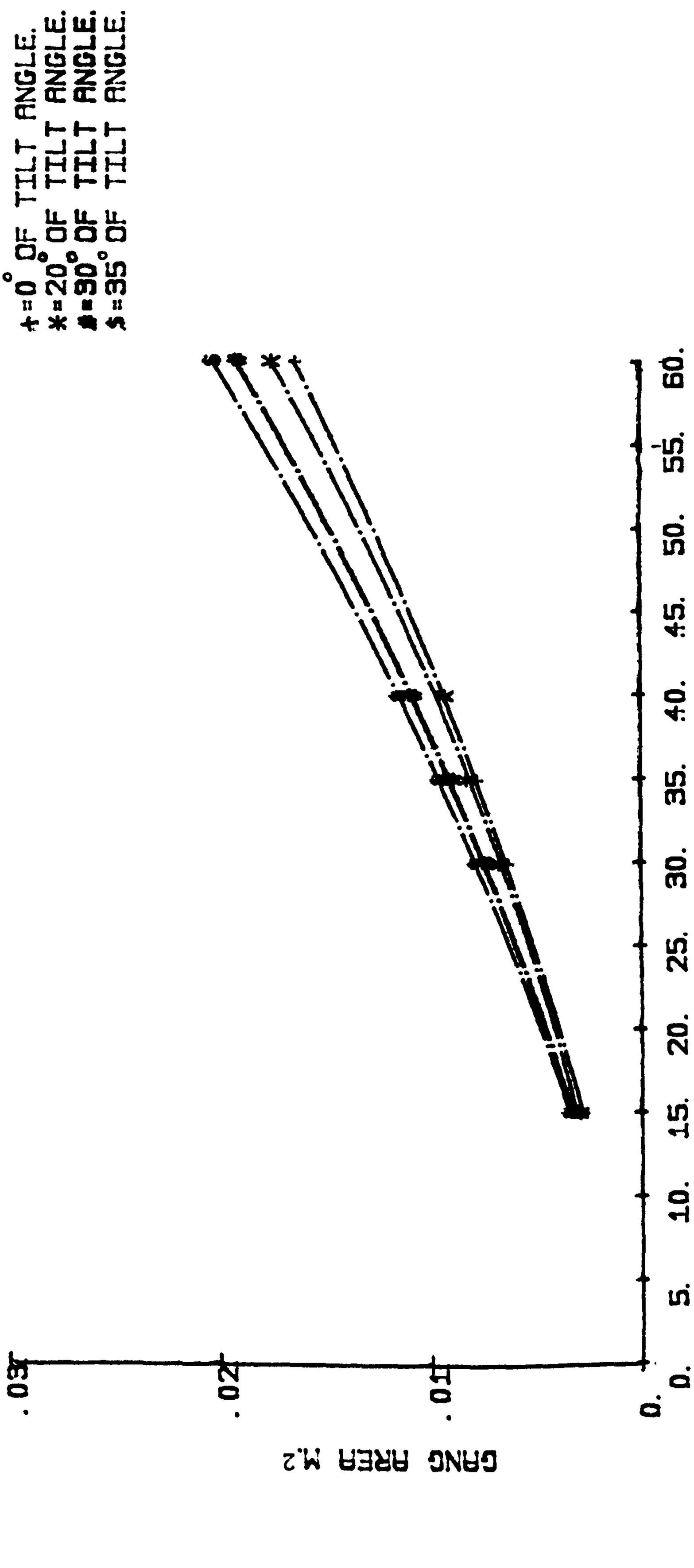

Figure 5.4. Gang area calculated by Equation 5.17. for a 0.61 m disc using various disc and tilt angles at a depth of 0.1 m

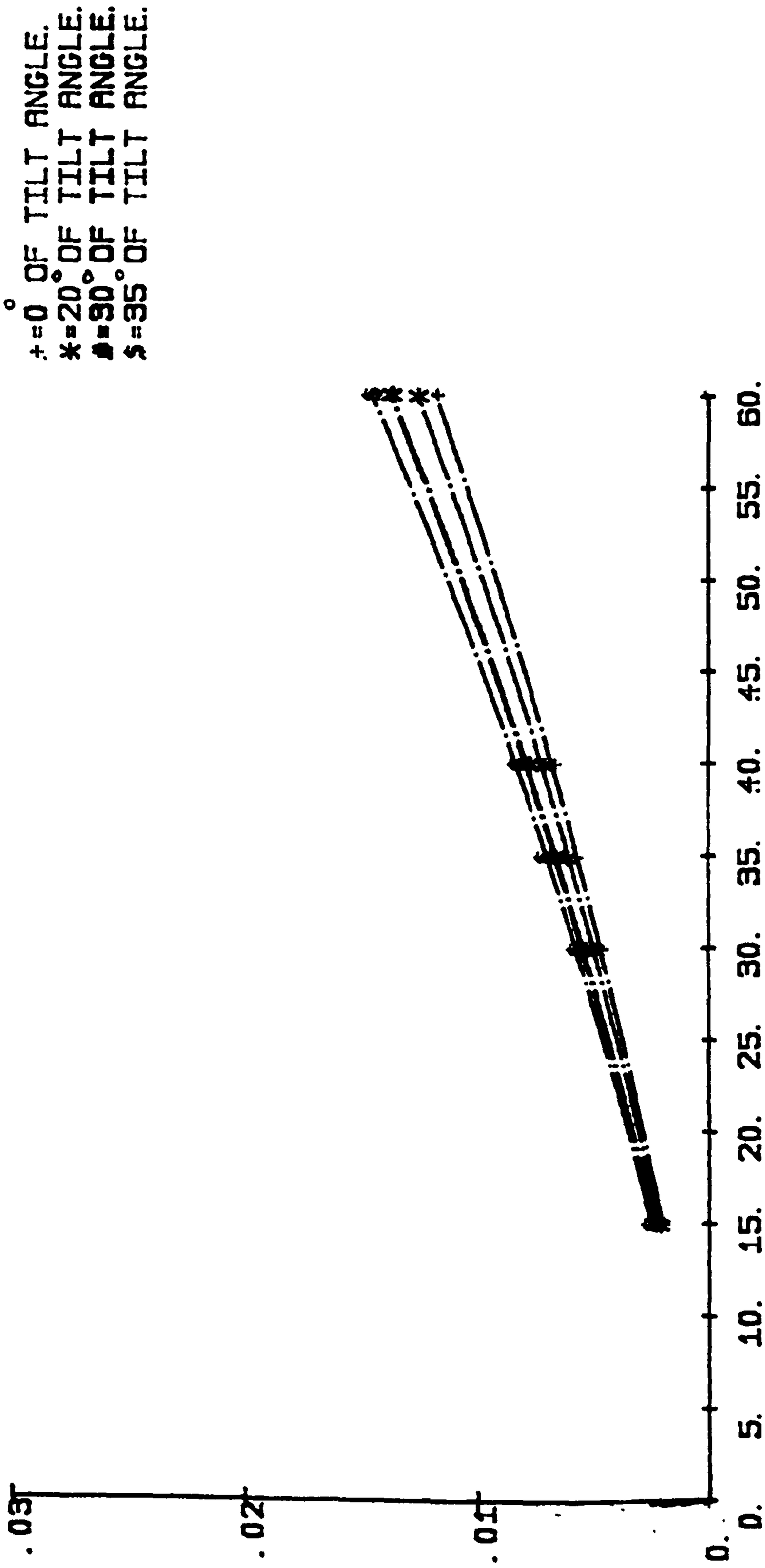

Figure 5.5. Gang area determined by Equation 5.17. for a 0.61 m disc operating at different disc and tilt angles at a depth of 0.08 m

mentioned over, show that the gang area decreases as the depth of operation decreases for any given disc and tilt angles.

Also, Equation 5.17. is used to calculate the gang areas at different gang spacings for a 0.61 m disc operating at various disc and tilt angles and different depths as shown in Table 5.2. and Figures 5.6., 5.7. and 5.8. The results from this table and these figures show that as the gang spacing increases the gang area increases for any given disc and tilt angles and any given depth as long as overlap area occurs in the soil.

5.4.1. Conclusions

As Equation 5.17. suggests, the influences of disc angle, disc radius, depth of operation and gang spacing are important variables in the disturbance of the soil by rotating discs.

5.5. Specific resistance

5.5.1. Introduction

The specific resistance of ploughs are widely varied under different conditions such as the soil type and conditions, friction characteristics of soil engaging surfaces,

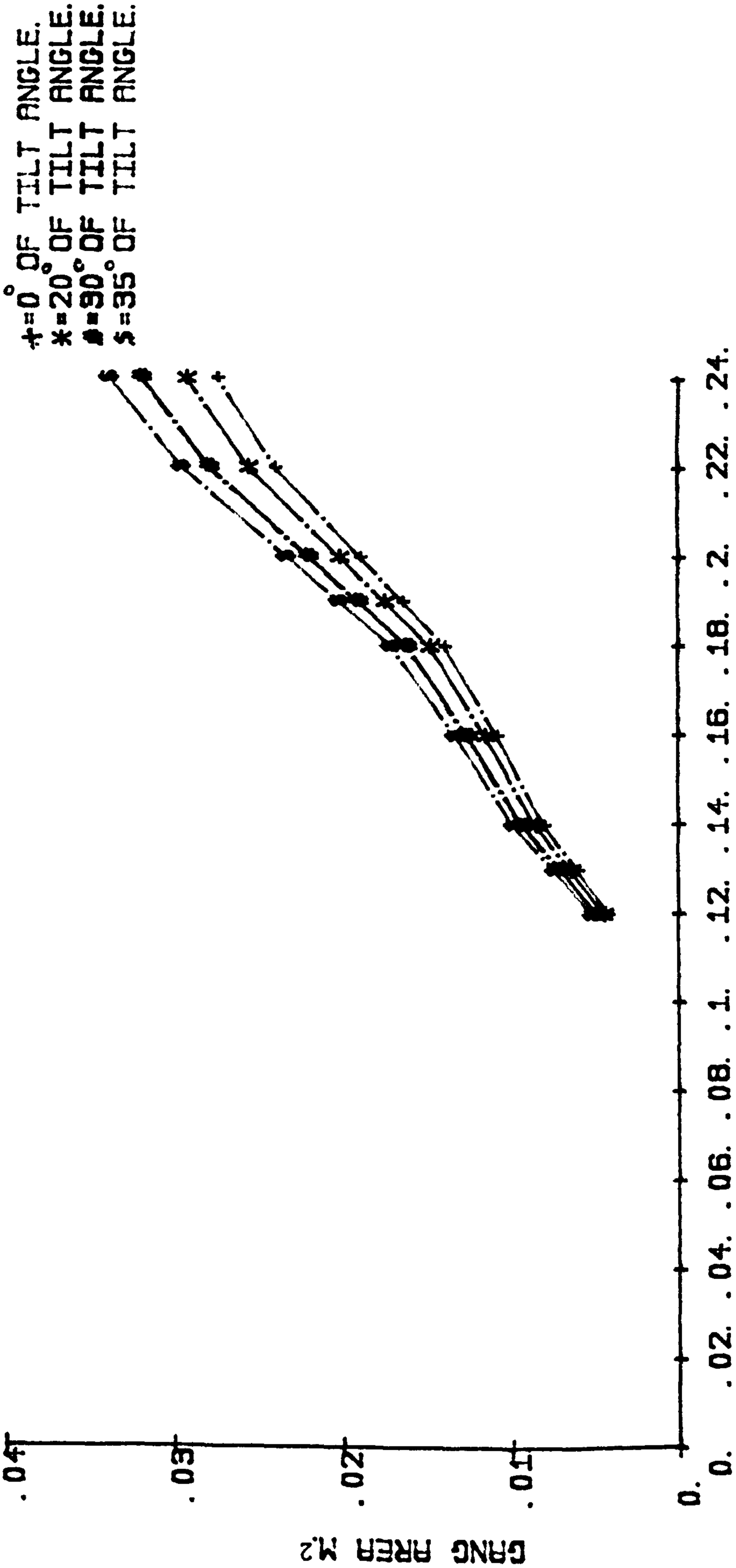

Figure 5.6. Gang area determined using Equation 5.17. for a 0.61 m disc ploughing at various disc and tilt angles and different gang spacings at a depth of 0.14 m

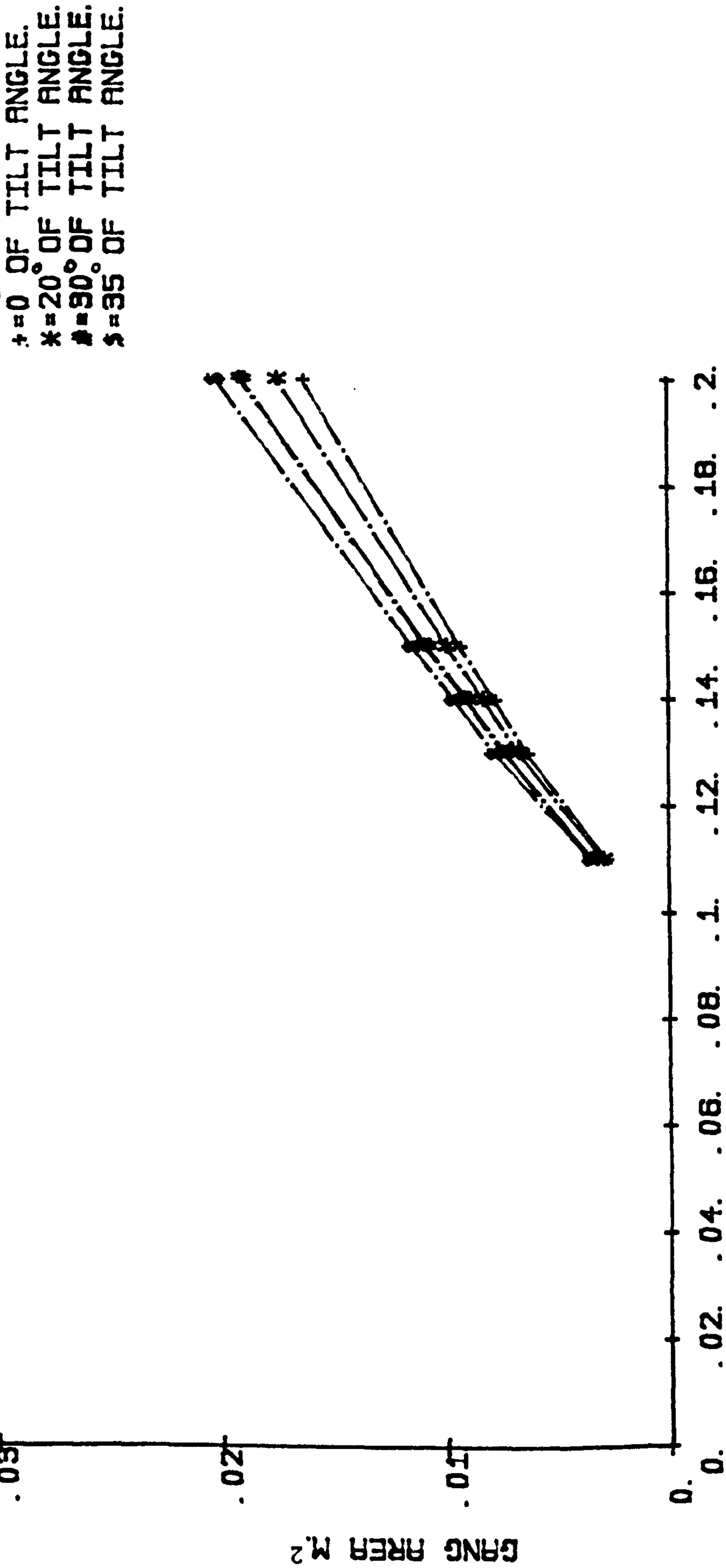

Figure 5.7. Gang area obtained by Equation 5.17. for a 0.61 m disc operating at different disc and tilt angles and various gang spacings at a depth of 0.1 m

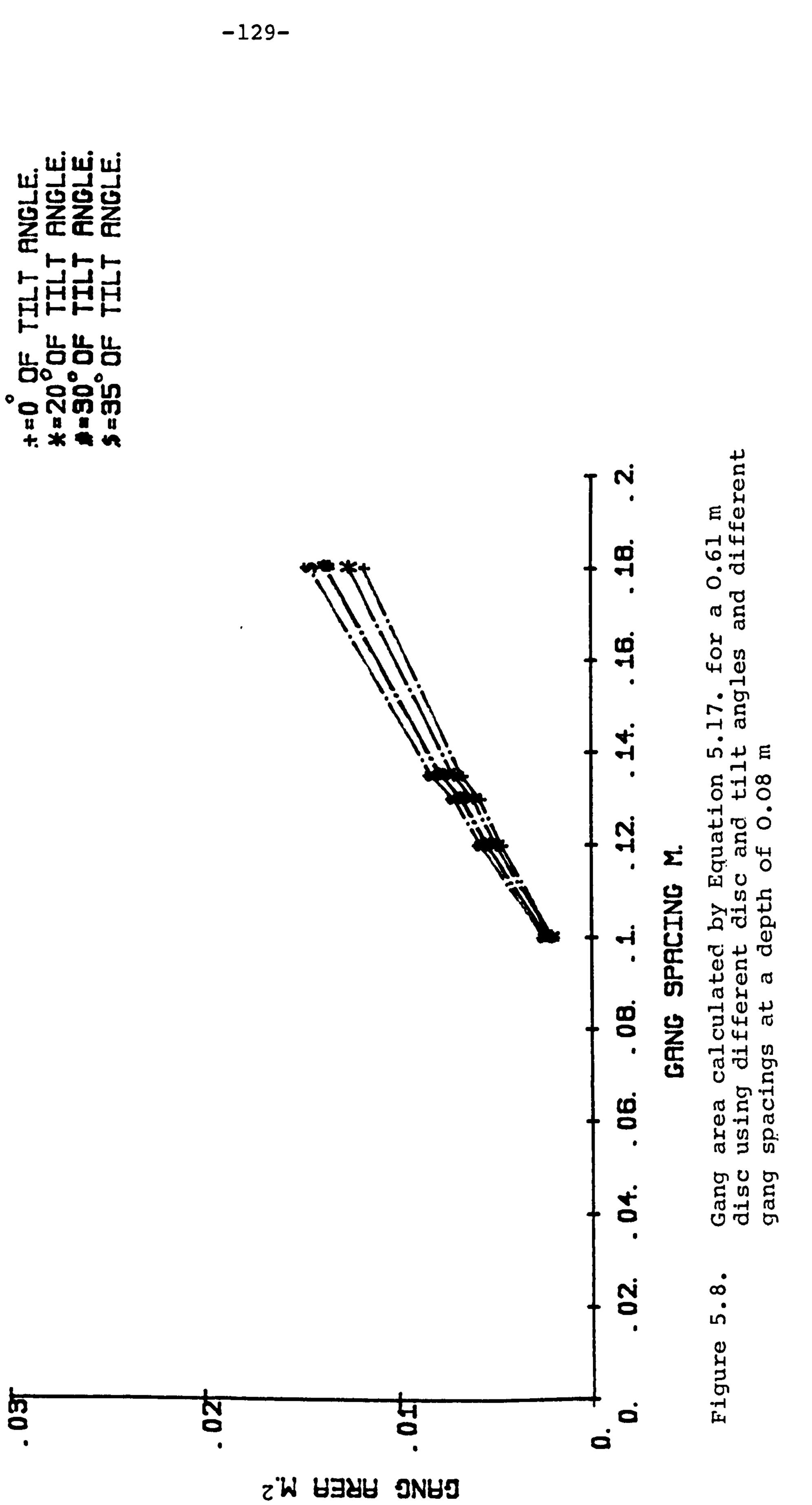

Figure 5.8. Gang area calculated by Equation 5.17. for a 0.61 m disc using different disc and tilt angles and different gang spacings at a depth of 0.08 m

soil-disc interface, disc sharpness and shape, speed, depth of operation and width of cut. Many workers have done a lot of work to evaluate different factors and investigate possible means for reducing draught. O'Callaghan and McCoy (1965) have derived a mathematical method for predicting the draught of a mouldboard bottom depending upon experimentally determined equations for soil paths. In disc ploughs, most researchers have studied the specific resistance but they did not show how the area of soil disturbance was obtained to determine the specific resistance. In other words, the specific resistance is the draught force per unit area which means that the area may be developed in terms of various areas such as the full vertical pressure area (Equation 4.17 and Equation 5.12) or gang area (Equation 5.17).

5.5.2. Objectives

The purpose of this study is to determine the specific resistance based on gang area developed by Equation 5.17 for predicting the draught forces on the concave side of the disc.

5.5.3. Methods

The draught forces measured from the first experiments for disc concavities at various disc and tilt angles and operating at 0.14 m depth were used to calculate the specific

draught dependent upon gang area determined by Equation 5.17.

5.5.4. Results

Figure 5.9. and Figure 5.10. show that the specific resistance decreases as the disc angle increases for any given tilt angle. The specific draught increases as the tilt angle increases with small disc angles as shown in Figures 5.9. and 5.10. In shallow inside sharpened disc the specific resistance is smaller than in the shallow outside sharpened disc for any given disc and tilt angle except for 15^{o} and 20^{o} of disc angle at a tilt angle of 35^{o} as shown in the figures mentioned above. Generally, the lowest specific resistance in a gang disc occurs in the region of 40^{o} disc angle. The effect of sharpening method is highly significant at the angle of lowest specific resistance as shown in Figures 5.9. and 5.10., where increasing tilt angle causes little increase in specific resistance.

5.5.5. Conclusions

As Equation 5.17. suggests, the following are observed:

1. The most important factors affecting the specific resistance are:

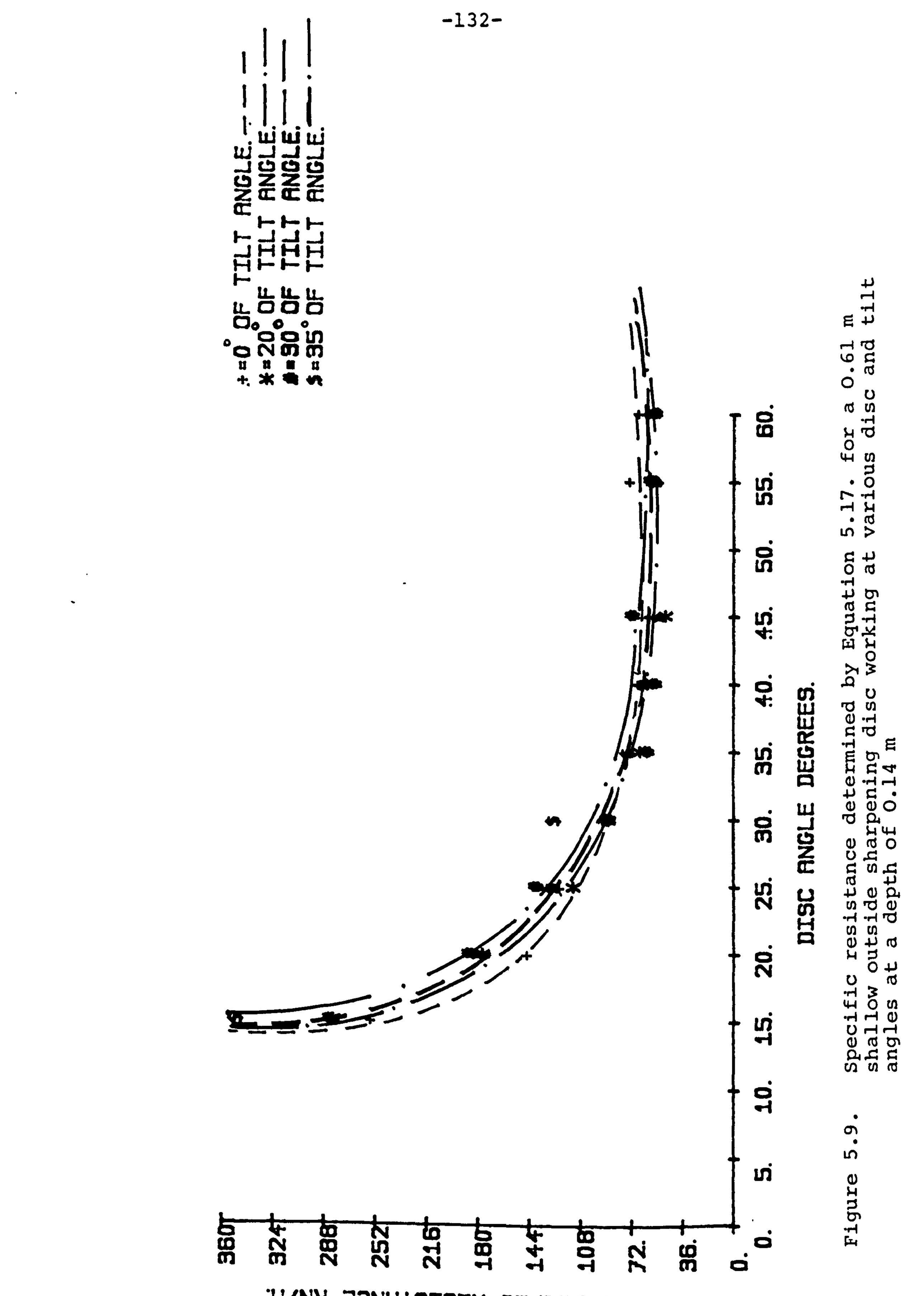

Figure 5.9. Specific resistance determined by Equation 5.17. for a shallow outside sharpening disc working at various disc angles at a depth of 0.14 m and tilt

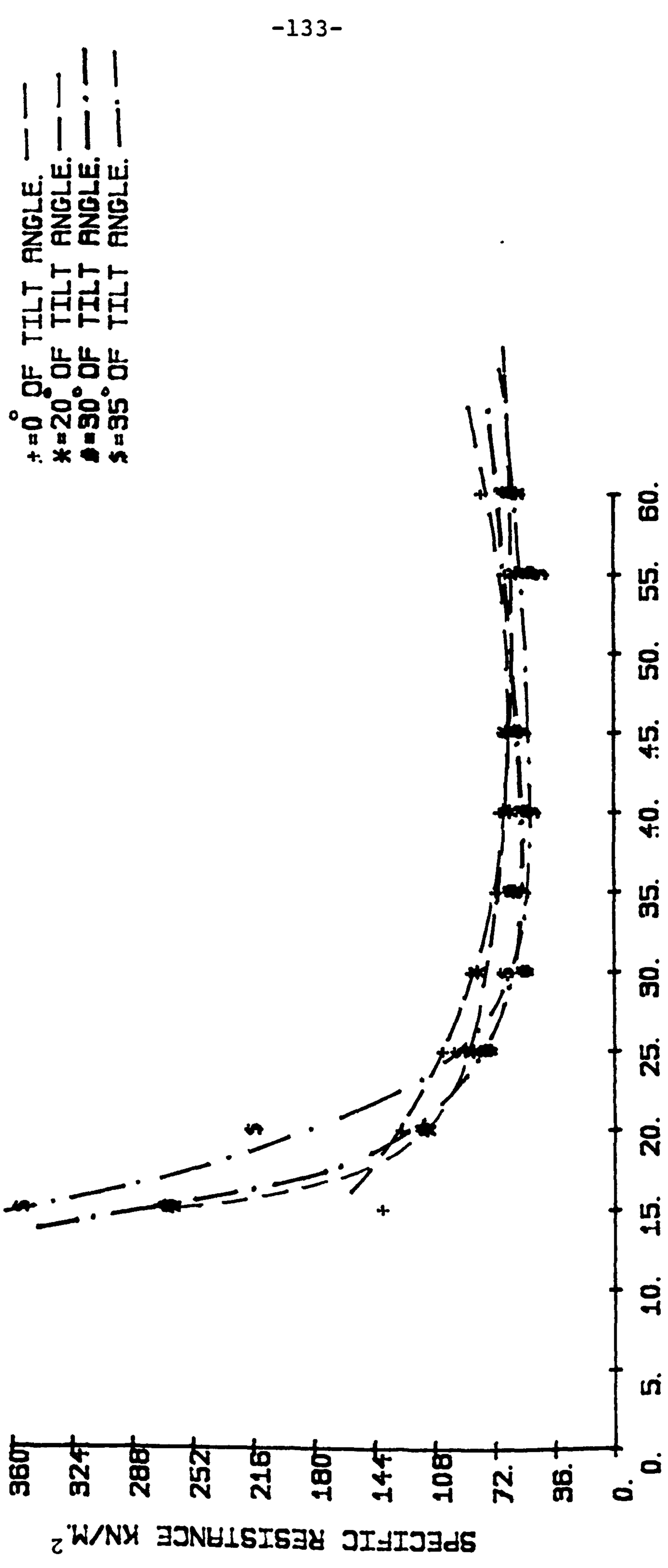

Specific resistance calculated by Equation 5.17. for a 0.61 m shallow inside sharpening disc operating at various disc and tilt angles at a depth of 0.14 m

Figure 5.10.

i. disc angle

ii. disc diameter

iii. depth of cut

iv. gang spacing

As these factors increase, the area of soil disturbance increases and the specific resistance decreases.

2. The specific resistance may be calculated by applying Equation 4.16. for full area of soil disturbances. The full vertical pressure area obtained by Equations 4.17. is larger than the gang area calculated by Equation 5.17.

5.5.6. Soil movement observed through transparent discs

5.5.6.1. Introduction

It has been generally recognised that there is a movement of soil during tillage operations. There is a lack of experimental data concerning such movement of soil. It is the purpose of this study to investigate the nature of the flow, disturbance and finish using video film and photography. The filming then was taken from front and rear of

a transparent disc with a soil bed prepared with colour tracers.

5.5.6.2. Methodology

The soil box was 2400 mm long, 1200 mm wide and 210 mm deep and five different colour chalks (Yellow, red, green, white and blue) were used as tracers in the soil. Video film and photography were taken from front and rear of the outside sharpened transparent disc, as shown in Figure 5.11. The box was filled with the soil to a depth of 130 mm and levelled.

The first colour rows were traced at 80 mm horizontal distances by using the stencil size 220 mm long, 20 mm wide and 3 mm deep. The tracers were covered and levelled with 20 mm of soil using a sieve. The second, the third and the fourth horizontal colour rows were traced in the same way. The topmost tracers were not covered with the soil.

The box was laid in the soil bin. The removable ends of the box had been removed so that the transparent disc could enter the box. The disc, 415 mm in diameter and 540 mm in radius of curvature, was attached to the carrier frame. It was mounted at 20^{o}, 30^{o}, 40^{o} and 50^{o} disc angle with respect to the direction of travel and tilt

angles with respect to the vertical of 0^{o}, 15^{o}, 25^{o} and 35^{o} for each run. The depth of 80 mm and speed of 0.5 m/sec were held constant. The depth was checked by putting the disc at the surface of the soil on the box before every run was started.

For every run, two rows were ploughed and the tracers were analysed for positional displacement and angular change at several points along the rows. Before every run was started the disc was moved to the next two rows dependent upon the required gang spacing for each disc and tilt angle.

5.5.6.3. Results

Analysis of the results showed that the geometry of the disc has an effect on the rotation and displacement of the soil slice. With increase in the disc angles from 20^{o} to 50^{o} and tilt angle 0^{o} more inversion of the soil occurs as shown in Figure 5.12. As the tilt angle increases from 0^{o} to 35^{o} with constant disc angle of 20^{o}, there is initially a slight inversion of the soil which reduces with greater tilt angles. When the disc angle is 40^{o} and tilt angle increases from 0^{o} to 35^{o}, there is a good inversion of soil which reduces to no soil inversion at larger tilt angles. With a disc angle of 30^{o} and tilt angle varying from 0^{o} to 35^{o} the soil is shifted sideways and there is no inversion.

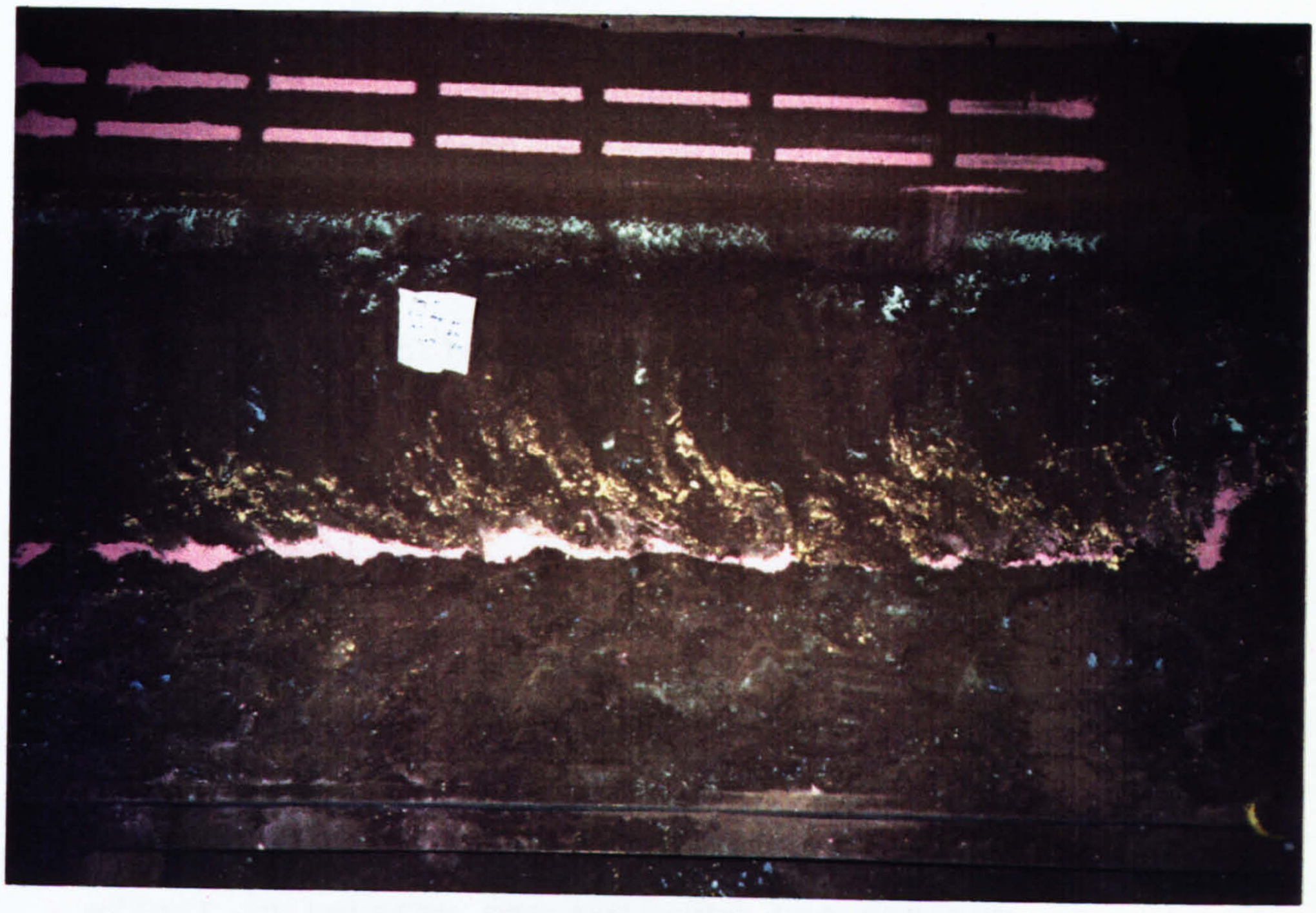

Figure 5.12. Inversion of the soil at various disc angles and zero tilt angle at a depth of 0.08 m

When the disc angle is 50^{o} and tilt angles are 0^{o} and 15^{o} there is good inversion of the soil while less effective and non-effective in inversion with tilt angles 25^{o} and 35^{o}.

5.5.6.4. Conclusions

1. With a disc angle of 20^{o} to 40^{o} and tilt angle of 35^{o}, there is good cutting with sideways movement of the soil, while the inversion of the soil is little, as shown in Figure 5.13.

2. Good inversion and mixing of the soil can be achieved with disc angle of 40^{o} to 50^{o} and tilt angle of 0^{o}, as shown in Figure 5.14.

3. The disc angle is the most important parameter effect in turning the soil and the maximum effect of the tilt angle occurs at a small disc angle.

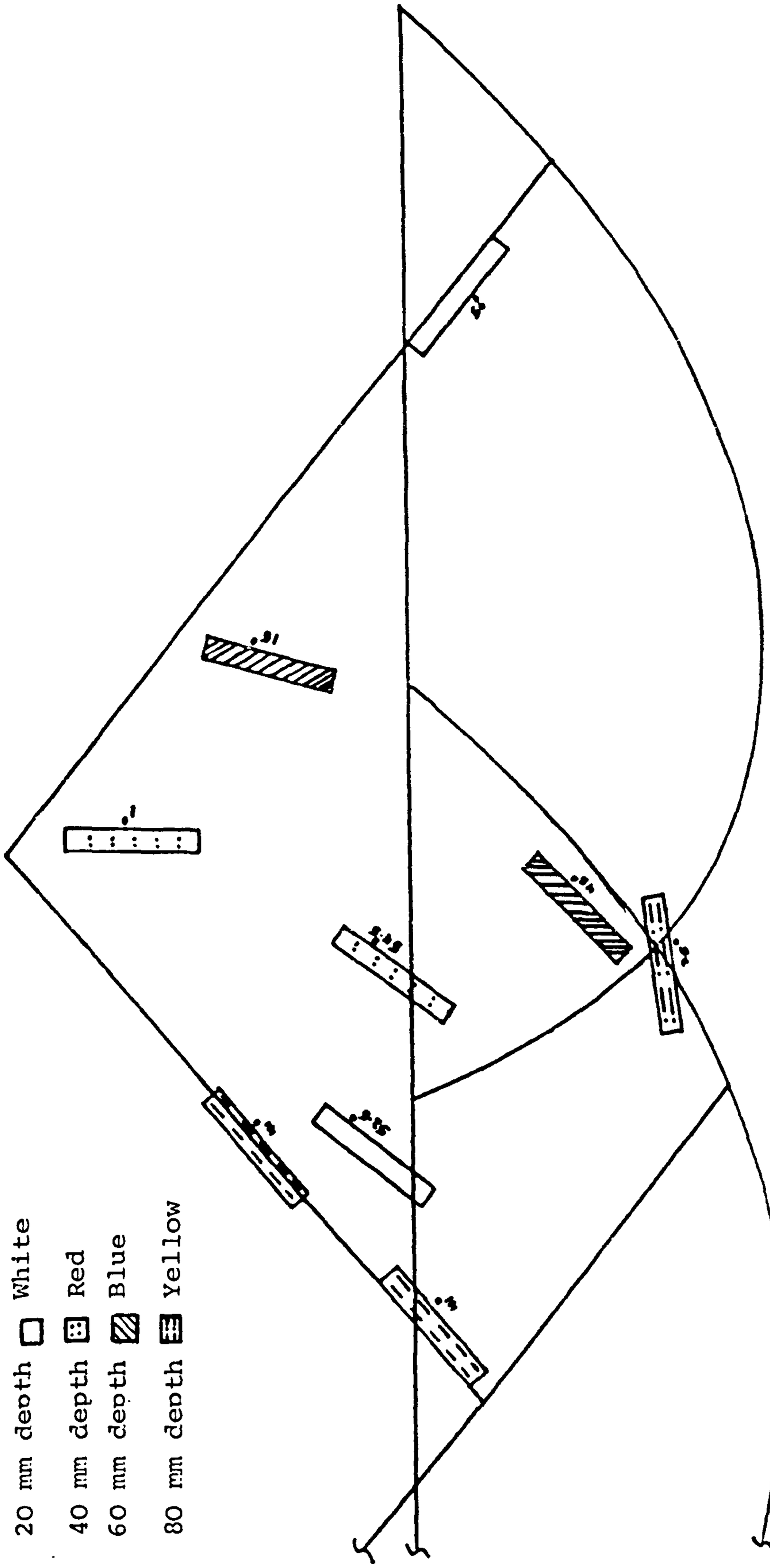

Figure 5.13. Sideways movement of the soil for a $O_{\circ}415$ m transparent disc working at various disc angles and 35° tilt angle at a depth of 0.08 m

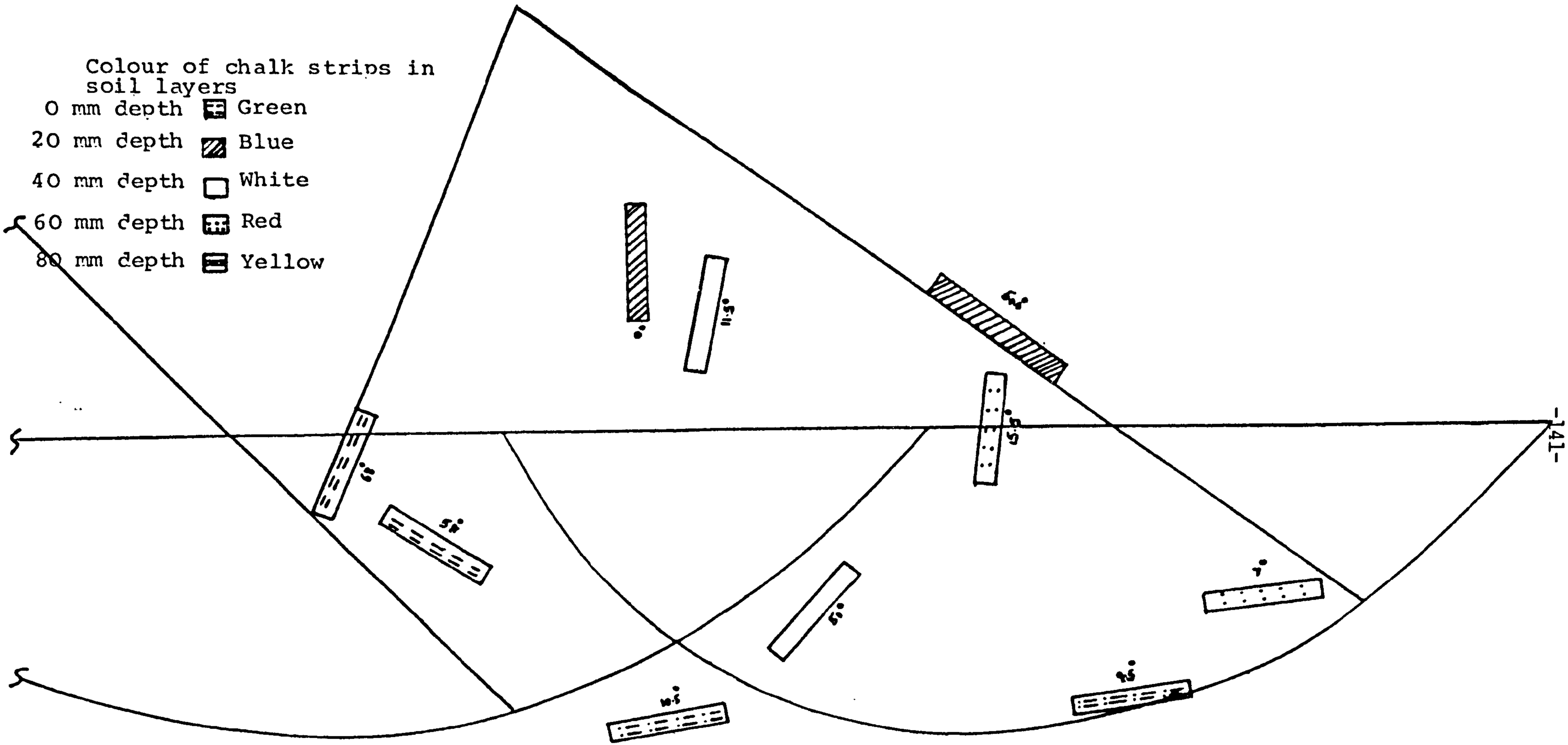

Figure 5.14. Inversion and mixing of the soil for a 0.415 m transparent disc using different disc angles and tilt angle of 0^{o} at a depth of 0.08 m

CHAPTER 6

6. Development of the force prediction model

6.1. Introduction

The literature review reported in Chapter 2 indicates that there are no proven soil mechanics models developed to explain the behaviour of the tilted disc and relate the forces on the disc to the properties of the soil. Some prediction models have been developed for other tillage implements that depend on Mohr-Coulomb soil mechanics theory by Payne (1956), O'Callaghan and Farrely (1964), Hettiaratchi et al (1966), Hettiaratchi and Reece (1967) and Godwin and Spoor (1977). These models are useful to the tillage engineering designer in understanding the soil failure and predicting the forces involved. Godwin et al (1987) developed a model based on Mohr-Coulomb theory to predict the force acting on the vertical disc. A force prediction model based on the theories of Mohr-Coulomb soil mechanics is developed here to predict the force reacting on the tilt discs.

6.2. Assumptions

i. The soil is homogeneous and isotropic.

ii. The geometry of the disc is sssumed to have the radius of curvature R, the radius of the edge circle of the disc r and depth of operation as shown in Figure 4.1.

iii. The critical disc angle β_c is taken as the angle between the direction of travel and the tangent to the convex side of the disc in the horizontal plane at soil surface as shown in Figure 4.1. in plan view 4. This angle to be calculated as developed by Equation 4.4.

iv. The rake angle $\bar{\gamma}$ of the disc is the mean of the rake angle γ_1 at the soil surface and the rake angle γ_2 at the lower edge of the disc as shown in Figure 4.9. This angle should be calculated as derived by Equation 4.14.

v. The vertical pressure area Ap on the concave side of the disc acts normal to the chord of the disc at the soil surface. This area has maximum value when the disc angle $\beta = 90^{\circ}$ as shown in Figure 4.3. and given by Equation 4.16 and reduced to zero when the disc angle rotated through the horizontal angle $90^{\circ} - \beta$ as developed by Equation 4.17.

vi. The value of the vertical bearing area on the convex side of the disc is a maximum when the disc angle $\beta = 0^{o}$ as shown in Figure 4.7. and calculated by derived Equation 4.26.

This area reduces to zero as the disc angle becomes equal to the critical disc angle βc or with the working depth d equal to the critical depth dc, and should be calculated as developed by Equation 4.27.

vii. The vertical bearing area vanishes when disc angle $\beta \geq \beta_c$ or d>dc as shown in Figure 4.2.

viii. The surcharge reaction is a maximum when disc angle $\beta = 90^{o}$ and reduces to zero when the disc angle $\beta = 0^{o}$. This is based on the assumption that the surcharge mechanism applies independently of tilt angle α as shown in Figure 6.1.

6.3. The concept of the prediction model

As shown in Figure 4.2. the mechanics of soil failure were observed as follows:

i. The cutting reaction on the face of the disc has a maximum value when the disc angle $\beta = 90^{o}$ as shown in Figure 4.2. in view 3. and reduces to zero at disc angle $\beta = 0^{o}$ as shown in view 1.

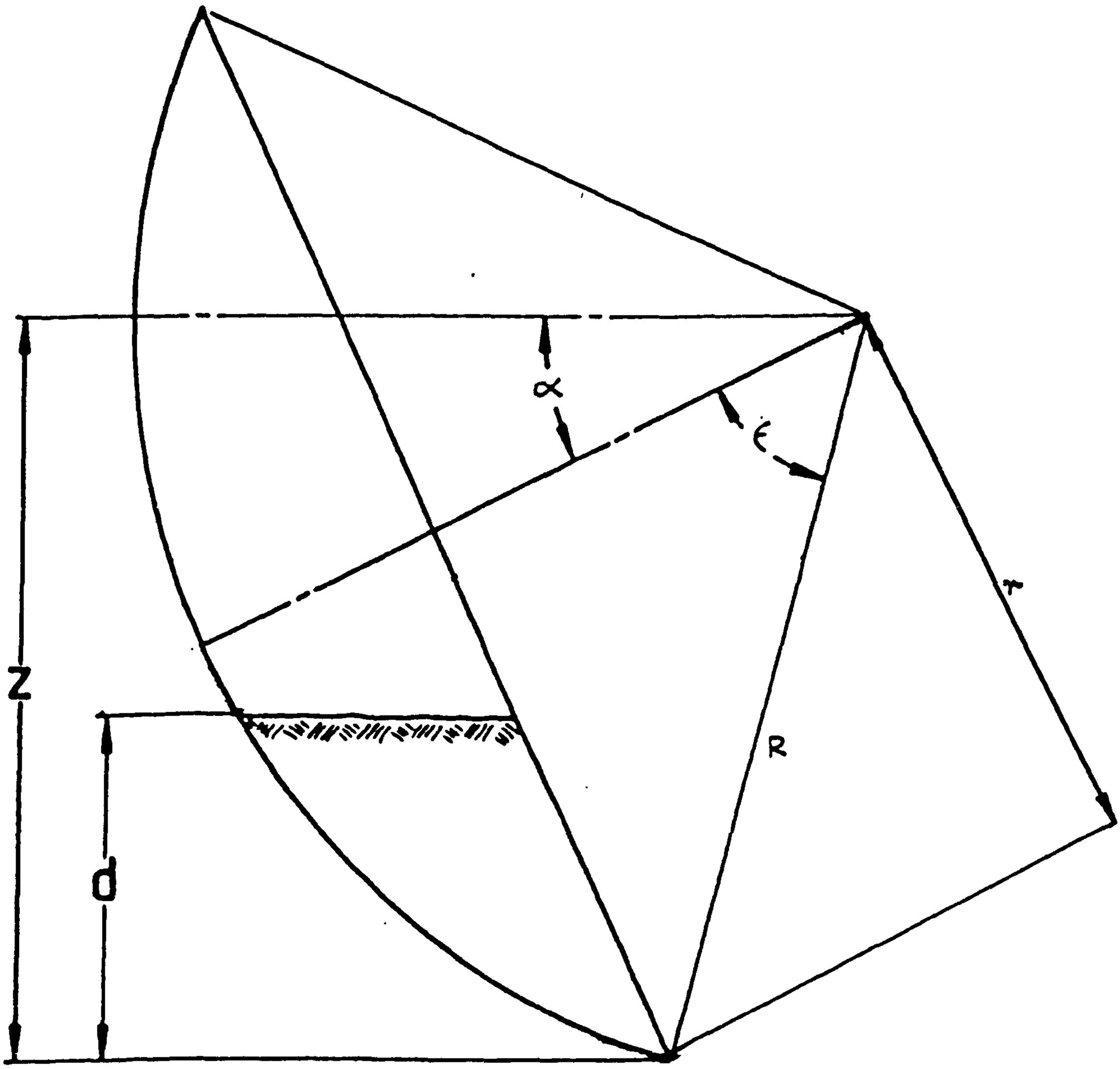

Figure 6.1. Surcharge reaction at disc angle β, tilt angle α and depth d

ii. The bearing reaction on the convex side of the disc is maximum when the disc angle $\beta = 0^{\circ}$ as shown in view 1 and reduces as the disc angle $\beta \geq \beta c$ and there is no further bearing area on the back of the disc as shown in view 5.

6.4. The theory of the prediction model

6.4.1. Concave side of the disc

Prediction of the forces acting upon the vertical pressure area on the concave or face of the disc is dependent on the passive soil cutting solution developed by Hettiaratchi et al (1966) for simple blades given below:

$$P = (\gamma i d^2 N_{\gamma} + C d N_{ca} + q d N_q) m \qquad \ldots\ldots\ldots (6.1)$$

where

P = Passive cutting force kN

d = depth of blade (constant over complete width of disc) m

γ = soil bulk unit weight (i : initial, f : final) $\frac{kN}{m^3}$

C = cohesion $\frac{kN}{m^2}$

q = surcharge stress $\frac{kN}{m^2}$

$N\gamma$, N_{ca}, N_q Dimensionless factors by Hettiaratchi et al (1966) and Hettiaratchi and Reece (1974) given in Figure 6.2.

m = the projected width is found from tilt angle (α), disc angle (β), disc radius r and depth of operation d as follows:

$$m = 2\sqrt{d(2r\,\mathrm{Cos}\,\alpha - d)}\;\mathrm{Sec}\,\alpha\,\mathrm{Sin}\,\beta \qquad \ldots\ldots\ldots(6.2)$$

The rake angle of the disc is calculated as shown in Figure 4.9. and given by Equation 4.14. as follows:

$$\bar{\gamma} = \gamma_2 + \frac{1}{2}\gamma \qquad \ldots\ldots\ldots(4.14)$$

where

γ = given by Equation 4.12 or 4.13

$\gamma_2 = \frac{1}{2}\pi - \alpha - \epsilon$

α = tilt angle

$\epsilon = \mathrm{Sin}^{-1}\frac{r}{R}$ given by Equation 4.11.

where

R = radius of curvature

r = radius of disc

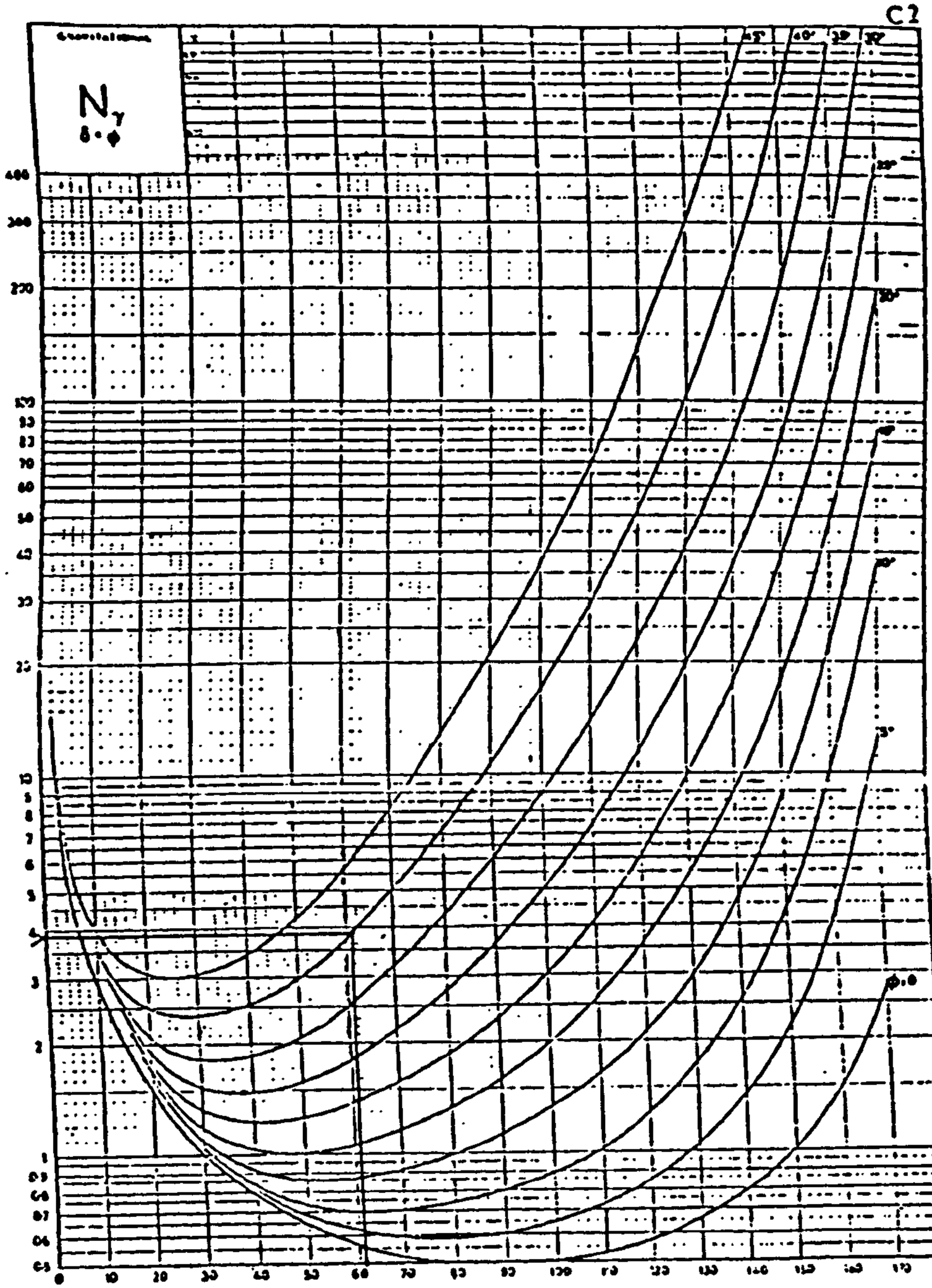

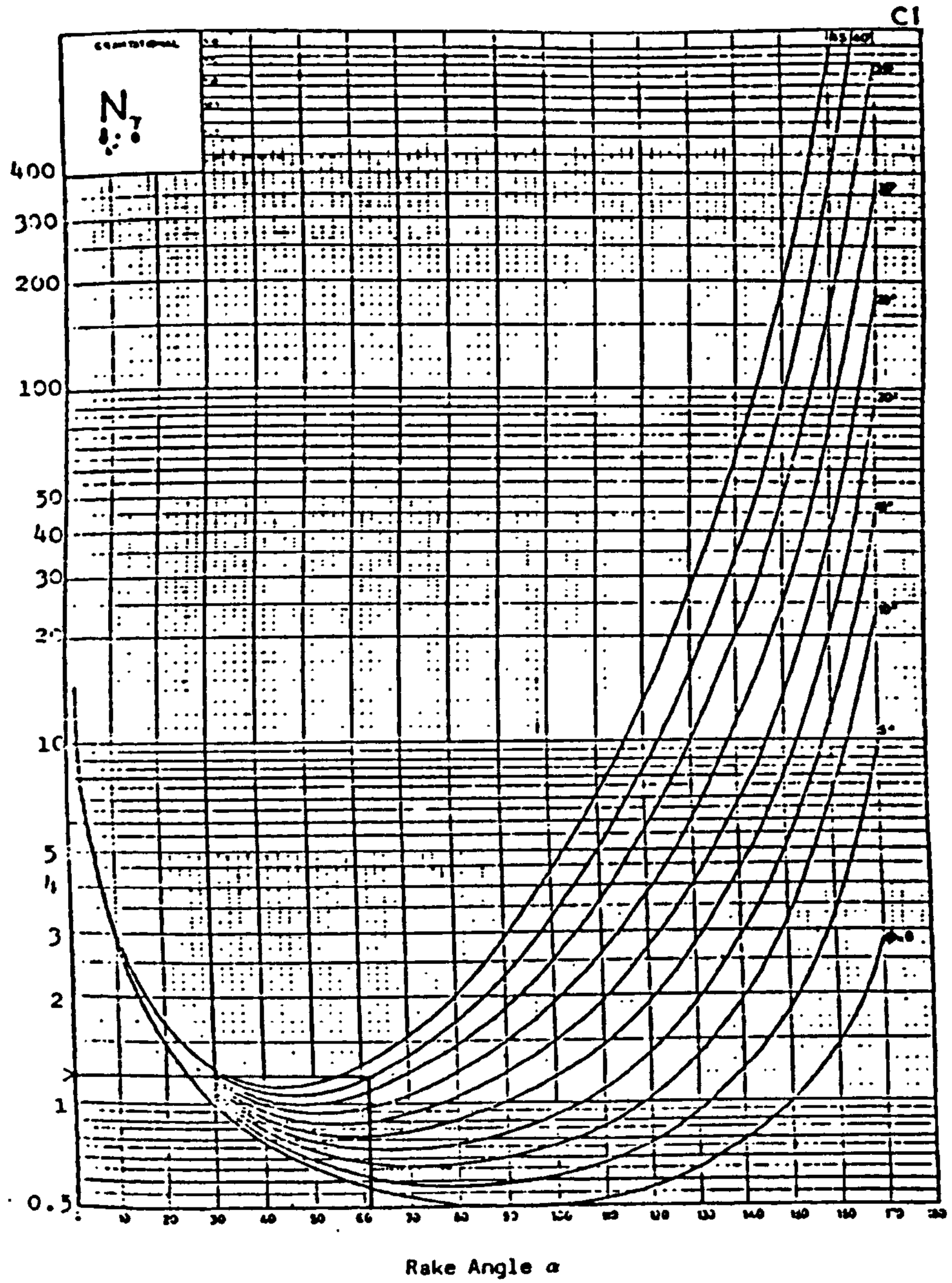

Figure 6.2. N factors for calculation of passive reaction (after Hettiaratchi et al (1966) and Hettiaratchi & Reece (1974))

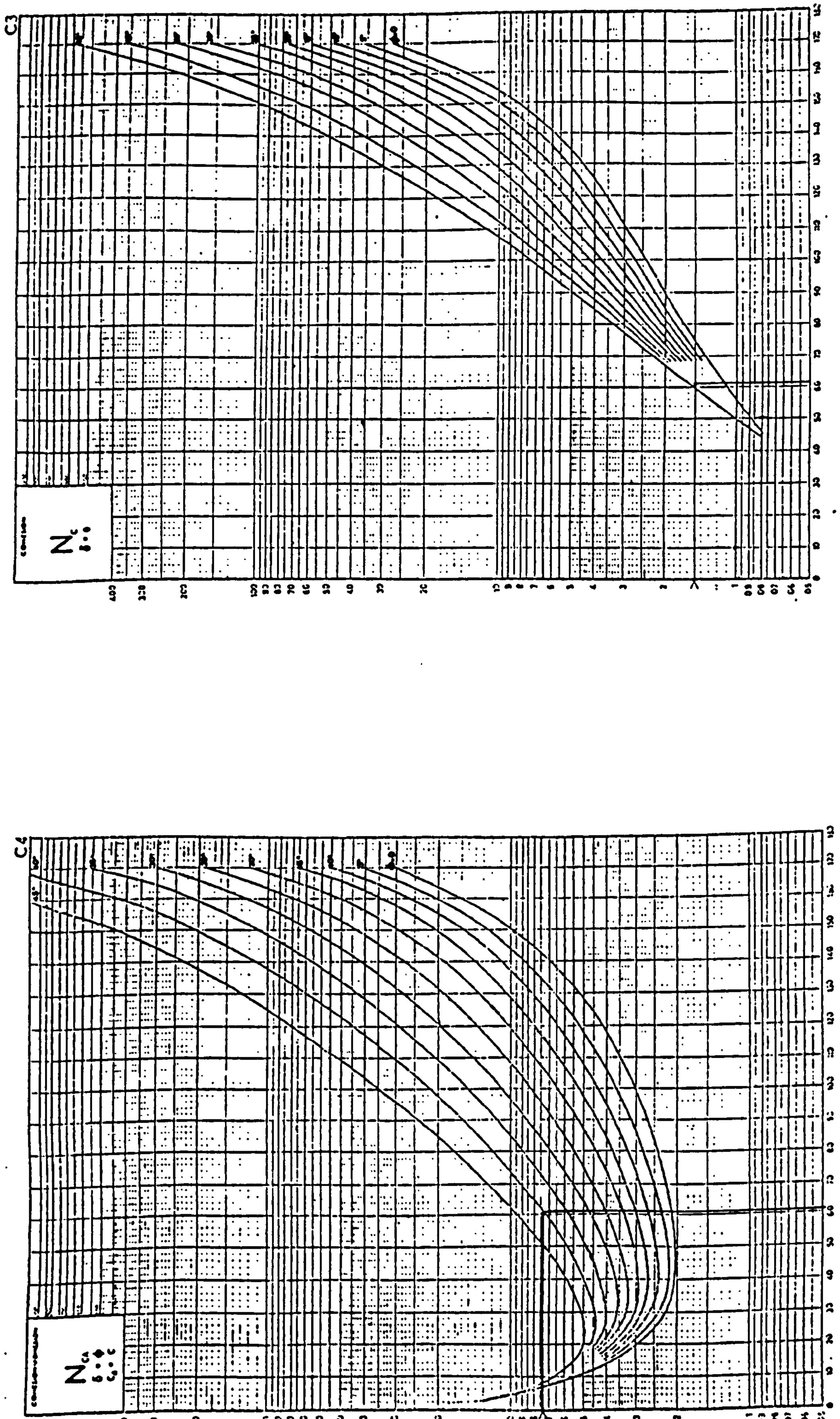

Figure 6.2. (cont'd) N factors for calculation of passive reaction (after Hettiaratchi et al (1966) and Hettiaratchi & Reece (1974))

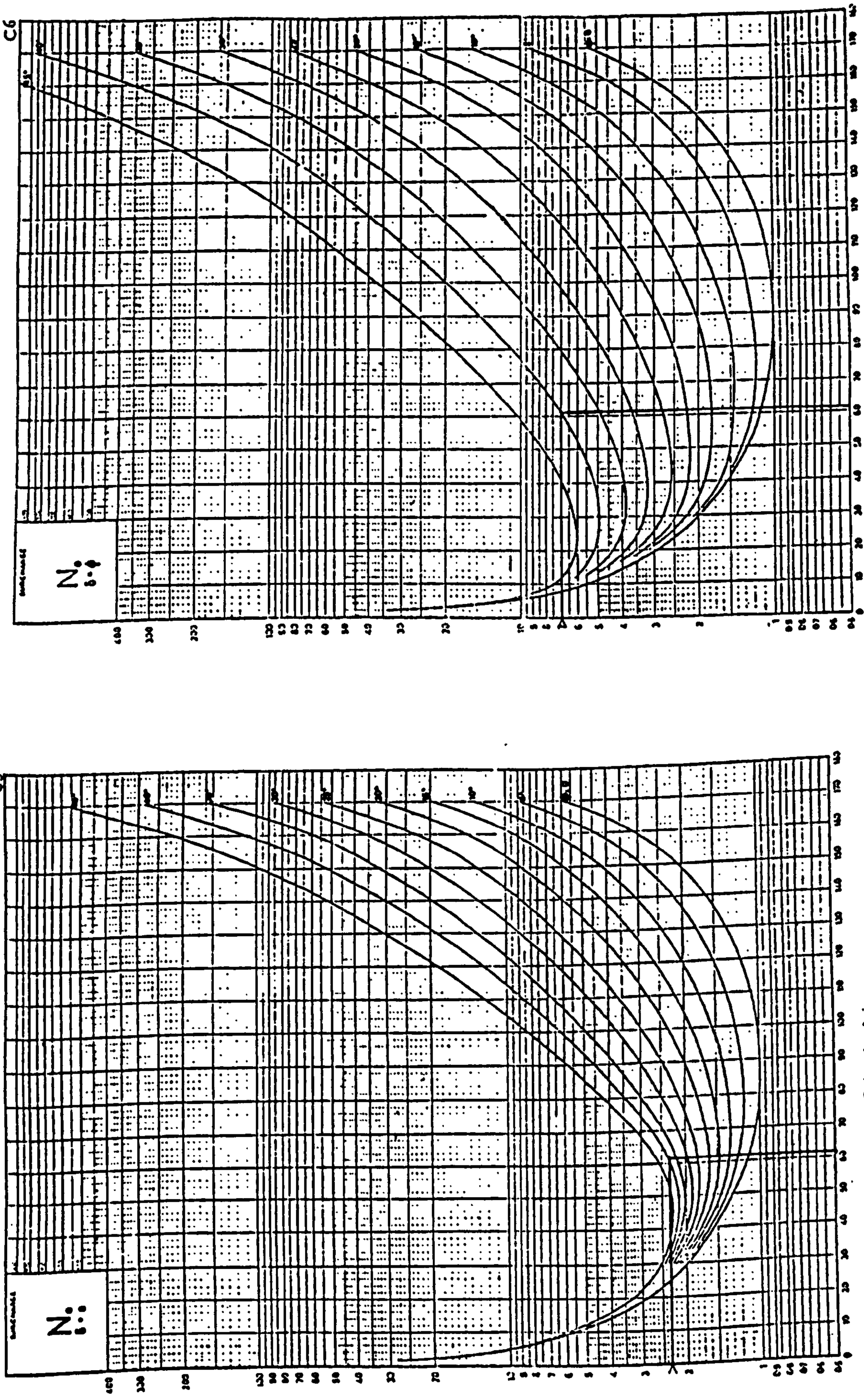

Figure 6.2. (cont'd) N factors for calculation of passive reaction (1966) and Hettiaratchi & Reece (1974))

The surcharge reaction q is a function of disc angle β and tilt angle α. As shown in Figure 6.1. the surcharge may be determined as follows:

$$Z = R \sin(\alpha + \epsilon)$$

$$= R(\sin\alpha\cos\epsilon + \cos\alpha\sin\epsilon) \qquad \ldots\ldots\ldots(6.3)$$

But

$$r = R \sin\epsilon \qquad \ldots\ldots\ldots(6.4)$$

and

$$R\cos\epsilon = \sqrt{R^2 - r^2} \qquad \ldots\ldots\ldots(6.5)$$

Substituting Equation 6.4. and 6.5. into Equation 6.3. gives:

$$Z = (\sqrt{R^2 - r^2}.\ \sin\alpha + r\cos\alpha) \qquad \ldots\ldots\ldots(6.6)$$

hence

$$q = (Z - d)\,\gamma_f.\ \sin\beta \qquad \ldots\ldots\ldots(6.7)$$

Substituting Equation 6.6. into Equation 6.7. gives:

$$\therefore q = \left[(\sqrt{R^2 - r^2}.\ \sin\alpha + r\cos\alpha) - d\right]\gamma_f.\sin\beta \qquad \ldots\ldots(6.8)$$

hence, substituting Equation 6.2. and 6.8. into Equation 6.1. gives:

$$P = \left[\gamma i d^2 N\gamma + CdNca + \left[\left(\sqrt{P^2 - r^2}.\sin\alpha + r\cos\alpha\right) - d\right]. \gamma_f \sin\beta\, dNg\right]. 2\sqrt{d(2r\cos\alpha - d)}\ \sec\alpha \sin\beta \quad .....(6.9)$$

The partitioning P into three force components given by Godwin et al (1987) is:

$$Hp = P\sin(\bar{\gamma} + \delta) \quad .....(6.10)$$

$$Vp = -p\cos(\bar{\gamma} + \delta) \quad .....(6.11)$$

(+ve Forces upward)

$$Dp = Hp\sin\beta = p\sin(\bar{\gamma} + \delta)\sin\beta \quad .....(6.12)$$

$$Sp = Hp\cos\beta = p\sin(\bar{\gamma} + \delta)\cos\beta \quad .....(6.13)$$

6.4.2. The forces acting on convex side of the disc

Prediction of the forces acting on this section of the disc is determined based on the bearing capacity reaction developed by Meyerhof (1961) for computing the maximum vertical stress under shallow footings:

$$\bar{q} = CN\bar{c} + poN\bar{q} + \frac{\gamma B}{2} N\bar{\gamma} \quad .....(6.14)$$

where

$\bar{q}$ = maximum vertical stress

c = cohesion

po = surcharge stress

γ = soil bulk unit weight

B = footing width

$N\bar{c}$, $N\bar{q}$, $N\bar{\gamma}$ dimensionless factors, $N\bar{c}$ given in Figure 6.3.

Godwin et al (1987) observed that there is no soil surcharge at the back of the disc, the effect of soil bulk density is neglected and the depth of cut is relatively shallow.

Hence, Equation 6.14. simplifies to:

$$\bar{q} = CN\bar{c} \qquad \text{.....(6.15)}$$

therefore, the maximum vertical force (Vm) after Godwin et al (1987) is:

$$Vm = \bar{q}\ Ab$$

or

$$Vm = Ab\ CN\bar{c} \qquad \text{.....(6.16)}$$

where

Ab is the vertical bearing area as shown in Figures 4.7. and 4.8. and given by Equation 4.27.

Solid line : Surface perfectly smooth $\delta = 0$

Broken line : Surface perfectly rough $\delta = \phi$

The N factor for an intermediate value (δ) is determined by linear interpolation.

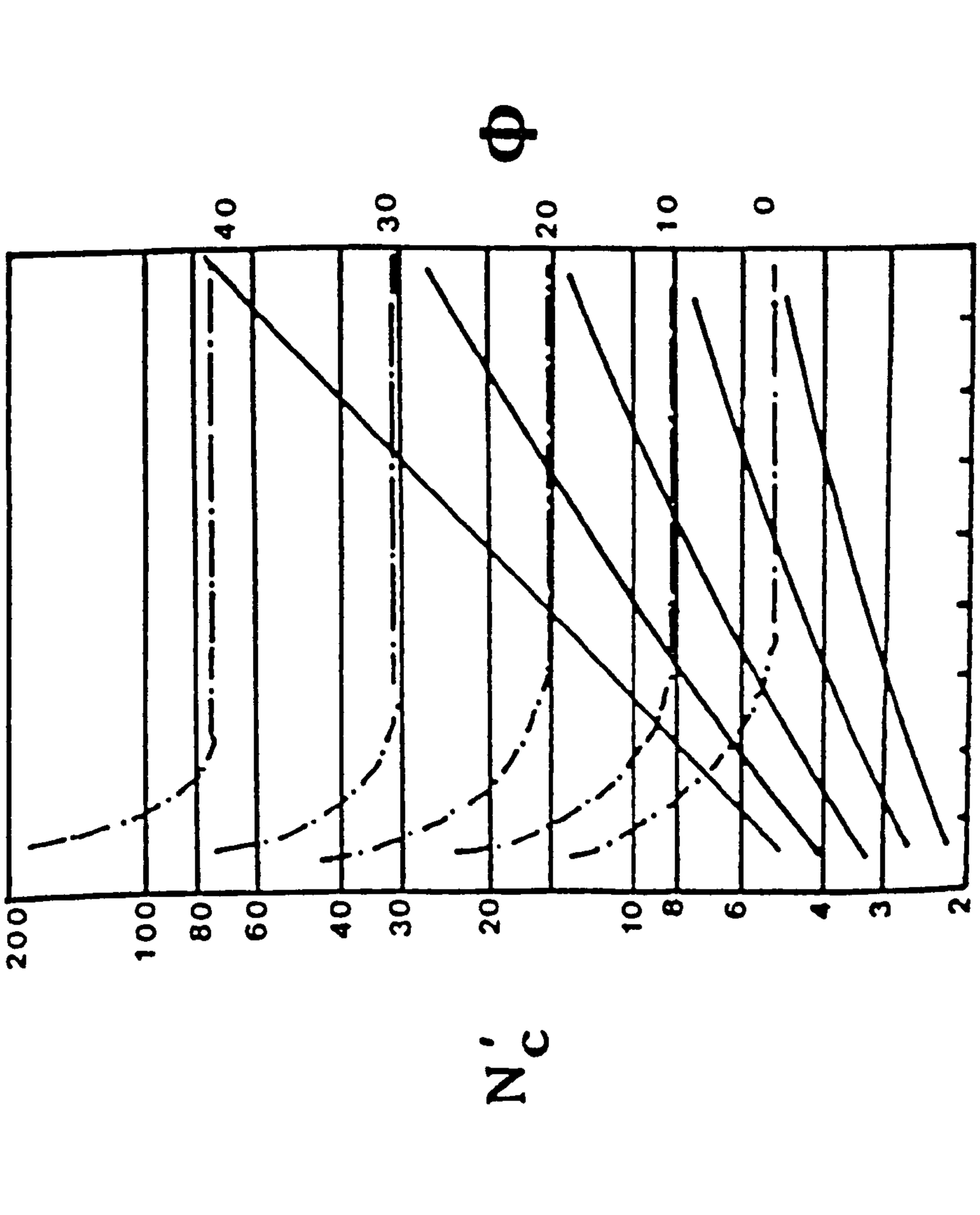

Figure 6.3. Bearing capacity factors for wedge footing (after Meyerhof (1961))

The partitioning of bearing reaction into three forces given by Godwin et al (1987) is:

$$Hm = Vm \tan (\bar{\gamma} - \delta) \qquad \text{.....(6.17)}$$

$$Dm = Hm \sin (\beta_c - \beta) = Vm \tan (\bar{\gamma} - \delta) \sin (\beta_c - \beta)$$

The last Equation (Dm) was amended to include a proportional factor to account for convex side friction, as shown below:

$$Dm = \left[Hm \sin (\beta_c - \beta) \right]^F = \left[Vm \tan (\bar{\gamma} - \delta) \sin (\beta_c - \beta) \right]^F \qquad \text{.....(6.18)}$$

where

$$F = 0.01 < F < 0.1$$

$$Sm = Hm \cos (\beta_c - \beta) = Vm \tan (\bar{\gamma} - \delta) \cos (\beta_c - \beta) \qquad \text{...(6.19)}$$

The total draught D, vertical V and side forces after Godwin et al (1987) are:

$$D = Dp + Dm \text{ (+ve force opposing the direction of motion)} \qquad \text{.....(6.20)}$$

$$V = Vp + Vm \text{ (+ve force opposing penetration of the disc)} \qquad \text{.....(6.21)}$$

S = Sp - Sm (+ve forces act from the concave to the convex face of the disc) .....(6.22)

6.5. Sample calculations

Disc geometry:

Radius of curvature R	= 0.7 m
Disc diameter 2r	= 0.61 m
Disc angle β	= 15^{o}
Tilt angle α	= 20^{o}
Depth of cut	= 0.14 m

Soil properties:

γ_i	= 14.46 $\frac{kN}{m^3}$
γ_f	= 10.45 $\frac{kN}{m^3}$
c	= 10 $\frac{kN}{m^2}$
ø	= 33^{o}
δ	= 20^{o}
Ca	= 0.0 $\frac{kN}{m^2}$

Determination of parameters of the disc

1. Chord of the disc L

From Equation 4.2. pp. 64

$$L = 2\sqrt{0.14m(2 \times 0.305m \cos 20^{\circ} - 0.14m)} \sec 20^{\circ}$$

$$= 0.522 \text{ m}$$

2. Half cone angle (ϵ)

From Equation 4.11. pp. 77

$$\epsilon = \sin^{-1} \frac{0.305m}{0.7 \text{ m}} = 25.83^{\circ}$$

3. Gamma angle (γ)

From Equation 4.12. or 4.13. pp. 80, 81

$$\cos \gamma = \sin(20^{\circ}+25.83^{\circ})\left(\sin(20^{\circ}+25.83^{\circ}) - \frac{0.14m}{0.7 \text{ m}}\right) + \sqrt{\cos 2(20^{\circ}+25.83^{\circ}) + \sin^4(20^{\circ}+25.83^{\circ}) + \left[2\sin(20^{\circ}+25.83^{\circ}) - \frac{0.14m}{0.7 \text{ m}}\right] \times \frac{0.14m}{0.7 \text{ m}} \cos^2(20^{\circ}+25.33^{\circ})}$$

$\gamma = 14.68^{\circ}$ (Equation 4.12)

or $\gamma = (20^{\circ}+25.83^{\circ}) - \sin^{-1}\left[\sin(20^{\circ}+25.83^{\circ}) - \frac{0.14m}{0.7 \text{ m}}\right]$

$= 14.69^{\circ}$ (Equation 4.13)

4. Critical disc angle β_c

From Equation 4.4. pp.66

$$\beta_c = \text{Sin}^{-1}\sqrt{\frac{0.14m\ (2 \times 0.305m\ \text{Cos}20^\circ - 0.14m)\ \text{Sec}20^\circ}{0.7m\ \text{Cos}(20^\circ + 25.83^\circ - 14.68^\circ)}}$$

$$= 25.94^\circ$$

5. Rake angle

From Equation 4.14. pp.31

$$\bar{\gamma} = (\tfrac{1}{2}\pi - 20^\circ - 25.83^\circ) + \tfrac{1}{2}\ 14.68^\circ$$

$$= 51.51^\circ$$

6. Critical depth

From Equation 4.5. pp. 72

$$dc = \frac{2 \times 0.305m\ \text{Cos}\ 20^\circ - \sqrt{(-2 \times 0.305m\ \text{Cos}20^\circ)^2 - 4\ \left[(\text{Sin}^2 15^\circ (0.7m)^2 \times \text{Cos}^2(20^\circ + 25.83^\circ - 14.68^\circ)/\text{Sec}^2 20^\circ\right]}}{2}$$

$$= 5.59\ \text{cm}$$

7. Vertical pressure area

From Equation 4.17. pp.85

$$Ap = (0.305m)^2 \left[\text{Sin}^{-1}\frac{0.522m}{2 \times 0.305m} - \frac{0.522m}{4 \times (0.305m)}2\sqrt{4(0.305m)^2 - (0.522m)^2}\right] \times \text{Cos}\ 20^\circ\ \text{Sin}\ 15^\circ$$

$= 0.013445\ m^2$

8. Vertical bearing area

From Equation 4.27. pp. 94

$$Ab = \left[\frac{\left[14.68^\circ \cdot \cos 20^\circ (\cos(25.83^\circ - 14.68^\circ)) - (\sin 14.68^\circ \cos 25.83^\circ \cos 20^\circ) - \left(\sin(20^\circ + 25.83^\circ - 14.68^\circ) \left[\cos(25.83^\circ - 14.68^\circ) - \cos 25.83^\circ \right]^2 \right] \right] \times (0.7m)^2}{2 \left[\cos 20^\circ (\cos (25.83^\circ - 14.68^\circ) \right]} \right]$$

$$\times \left(\frac{25.94^\circ - 15^\circ}{25.94^\circ} \right)^{2.5}$$

$= 5.674 \times 10^{-4}\ m^2$

Determination of N Factors

$N\gamma = 0.83$

$\delta = 0$

$N\gamma = 2.63$

$\delta = \phi$

$Nc = 1.04$

$\delta = 0$

$Nc = 5.08$

$\delta - \phi$

Hence $N\gamma = 0.83 \left(\frac{2.63}{0.83}\right) \frac{20}{33}$

$\delta = 20^\circ$

$= 1.6$

Hence $Nc = 1.04 \left(\frac{5.08}{1.04}\right) \frac{20}{33}$

$\delta = 20^\circ$

$= 3.1$

N_g = 1.6

δ = 0

N_g = 4.9

δ = ϕ

Hence N_g = $1.6(\frac{4.9}{1.6})\ \frac{20}{33}$

δ = 20°

= 2.98

Determination of forces acting on concave side of the disc

From Equation 6.9. pp.152

$$p = \left[(14.46 \frac{kN}{m^3} \times 0.14^2 m^2 \times 1.6) + (10 \frac{kN}{m^2} \times 0.14\ m \times 3.1) + \left[(\sqrt{0.7^2 m^2 - 0.305^2 m^2} \times \text{Sin } 20^\circ) + 0.305m \times \text{Cos } 20^\circ - 0.14m \right] \times (10.45 \frac{kN}{m^3} \times \text{Sin } 15^\circ \times 0.14m \times 2.98) \right] \times$$

$$2 \sqrt{0.14m\ (2 \times 0.305m \text{ Cos } 20^\circ - 0.14m)\ \text{Sec } 20^\circ \text{ Sin } 15^\circ}$$

= 0.71 kN

Determination of forces acting on convex side of the disc

N Factors from Fig. 6.3.

N_c^- for B = 38.49° = 15.3

δ = 0

N_c^- for B = 38.49° = 93

δ = ϕ

Hence N_c^- = $((93 - 15.3)\frac{20}{33}) + 15.3$ = 62.4

δ = 20

From Equation 6.16 pp. 153.

$Vm = 5.6741 \times 10^{-4} \times 10 \times 62.4$

$= 0.354$ kN

Determination of draught, vertical and side forces acting on concave side of the disc

From Equation 6.10. and 6.11. pp. 152

$Hp = 0.71$ kN Sin $(51.51^{\circ} + 20^{\circ})$

$= 0.67$ kN

$Vp = -0.71$ kN Cos $(51.51^{\circ} + 20^{\circ})$

$= -0.22$ kN

From Equation 6.12. and 6.13. pp. 152

$Dp = 0.67$ Sin 15°

$= 0.17$ kN

$Sp = 0.67$ Cos 15°

$= 0.64$ kN

Determination of the draught, vertical and side forces acting on convex side of the disc

From Equation 6.18. and 6.19. pp.155

$$Dm = \left[0.354\ kN\ Tan(51.51^{\circ} - 20^{\circ})\ Sin\ (25.94^{\circ} - 15^{\circ})\right]^{0.1}$$
$$= \left[0.041\ kN\right]^{0.1}$$
$$= 0.73\ kN$$

$$Sm = 0.354\ kN\ Tan\ (51.51^{\circ} - 20^{\circ})\ Cos\ (25.94^{\circ} - 15^{\circ})$$
$$= 0.212\ kN$$

Total forces

From Equation 6.20., 6.21., and 6.22. pp. 155, 156

$D = 0.17 + 0.73 = 0.90\ kN$

$V = -0.22 + 0.354 = 0.134\ kN$

$S = 0.64 - 0.212 = 0.428\ kN$

Determination of the magnitude of the resultant forces

$$\bar{R} = \sqrt{D^2 + V^2 + S^2}$$
$$= \sqrt{(0.9)^2 + (0.134)^2 + (0.43)^2}$$
$$= 1.01\ kN$$

Determination of the direction of the resultant forces

$$\cos^{-1}\frac{D}{\bar{R}} = \frac{0.9}{1.01} = 26.98^{\circ}$$

$$\cos^{-1}\frac{V}{\bar{R}} = \frac{0.134}{1.01} = 82.37^{\circ}$$

$$\cos^{-1}\frac{S}{\bar{R}} = \frac{0.428}{1.01} = 64.92^{\circ}$$

Determination of the areas on the horizontal plane

1. The soil/disc interface circle radius (RS)

From Equation 4.3. pp. 64

$$RS = 0.7m \cos (20^{\circ} + 25.83^{\circ} - 14.68^{\circ})$$

$$= 0.599 \text{ m}$$

2. From Equation 4.28. pp. 97

$$\hat{H} = (\sin^{-1} \frac{0.522m}{2 \times 0.599m}) - 15^{\circ}$$

$$= 10.94^{\circ}$$

$$= 0.191 \text{ rad.}$$

3. Horizontal bearing area (Abh)

From Equation 4.29. pp.100

$$2Abh = (0.599m)^2 \left[0.191 - \sin 10.94^{\circ} \times \cos 10.94^{\circ}\right]$$

$$= 1.65 \times 10^{-3} \text{ m}^2$$

Therefore

$$Abh = 8.25 \times 10^{-4} \text{m}^2$$

4. Horizontal pressure area (Aph)

From Equation 4.30. pp.102

$$Aph = (0.599\ m)^2 \left[\left(\sin^{-1} \frac{0.522\ m}{2 \times 0.599\ m} \right) - 0.191 + \right.$$
$$\left. \sin 10.94^\circ \times \cos 10.94^\circ - \left(\frac{0.522\ m}{4 \times 0.599 m} \sqrt{4 - \frac{(0.522m)^2}{(0.599m)^2}} \right) \right]$$
$$= 0.01966\ m^2$$

5. Horizontal area (Ah)

From Equation 4.32. pp. 107

$$Ah = (0.599m)^2 \cdot \left(\sin^{-1} \frac{0.522\ m}{2 \times 0.599m} \right) - \left(\frac{0.522m}{2} \sqrt{(0.599m)^2 - \frac{(0.522m)^2}{4}} \right)$$
$$= 0.02132\ m^2$$

6. Inclination area (Ac)

From Equation 4.33. pp. 108

$$Ac = \left[(0.305m)^2 \left(\sin^{-1} \frac{0.522m}{2 \times 0.305m} - \left(\frac{0.522m}{2} \right) \sqrt{(0.305m)^2 \left(\frac{0.522m}{4} \right)^2} \right] \times \sin 20^\circ \right.$$
$$= 0.01891\ m^2$$

7. Loading area (Ad)

From Equation 4.34. pp. 110

$$Ad = 0.02132 m^2 + 0.01891 m^2$$
$$= 0.04023 m^2$$

CHAPTER 7

7. DISCUSSION OF EXPERIMENTAL AND PREDICTED RESULTS

7.1. Introduction

This chapter describes the results obtained using the prediction model developed in Chapter 6. in association with the experimental results. The sample calculations for the prediction of the forces on the discs are reported in Chapter 6. This chapter, therefore, is concentrated on the discussion of the experimental results in some detail and on the correlation between the observed and predicted results.

7.2. The reaction of disc forces

The analysis of the draught, vertical and side forces are discussed below:

7.2.1. Draught force

With shallow outside sharpened discs, at low disc angles, the draught force is large. This is due to the excessive scrubbing reaction on the convex side of the disc. In the tested region this force has reduced for the 15^{o} disc angle to give draught of 1.8 kN for a large tilt angle (35^{o})

and 1.2 kN for a vertical disc, as shown in Table 7.1. and Figure 7.1. As the disc angle is increased the draught force reduces to a minimum value of 1.4 kN for a large tilt angle of 35^{o} and 1.0 kN for a vertical disc, as shown in Table 7.1. and Figure 7.1. Figure 7.1. shows that the minimum draught force occurs between 25^{o} and 35^{o} of disc angle, depending upon the tilt angle. The maximum draught force (2 kN) occurs at a large disc angle (60^{o}) together with a large tilt angle (35^{o}), as indicated in Table 7.1. and Figure 7.1. Draught forces between 1.3 kN and 1.6 kN are produced with tilt angle of 20^{o}, as shown in Figure 7.1. and Table 7.1.

As with shallow outside sharpened discs, at low disc angles, the draught force is large for shallow inside sharpened disc. This has reduced to 1.6 kN for a large tilt angle (35^{o}) and 0.7 kN for a vertical disc and 20^{o} disc angle, as shown in Table 7.2. and Figure 7.2. The effect of a shallow inside sharpened disc appears to be a reduction of the minimum draught disc angle. For the vertical disc minimum, this has reduced to a smallest draught 0.7 kN, at a 15^{o} disc angle, as shown in Table 7.2. and Figure 7.2. With 20^{o} and 30^{o} tilt angles the minimum draught occurs at 20^{o} and 30^{o} disc angles, respectively. With a 35^{o} tilt angle the draught angle has no obvious minimum. As indicated in Table 7.2. and Figure 7.2., the minimum value of draught is not significantly reduced,

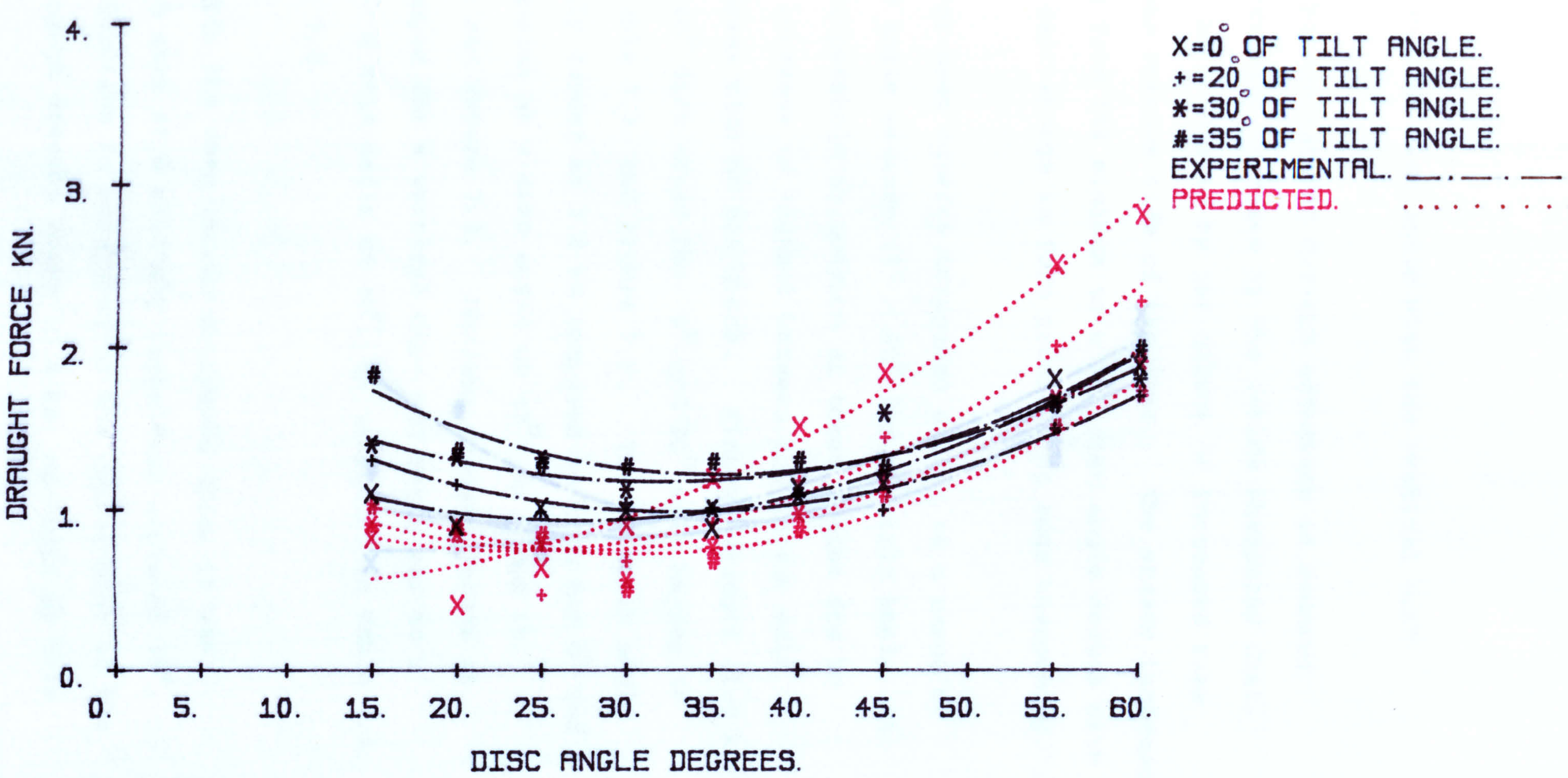

Figure 7.1. Draught force for a 0.61 m shallow outside sharpening disc having a radius of curvature of 0.7 m operating at various disc and tilt angles at a depth of 0.14 m in comparison to the predicted values

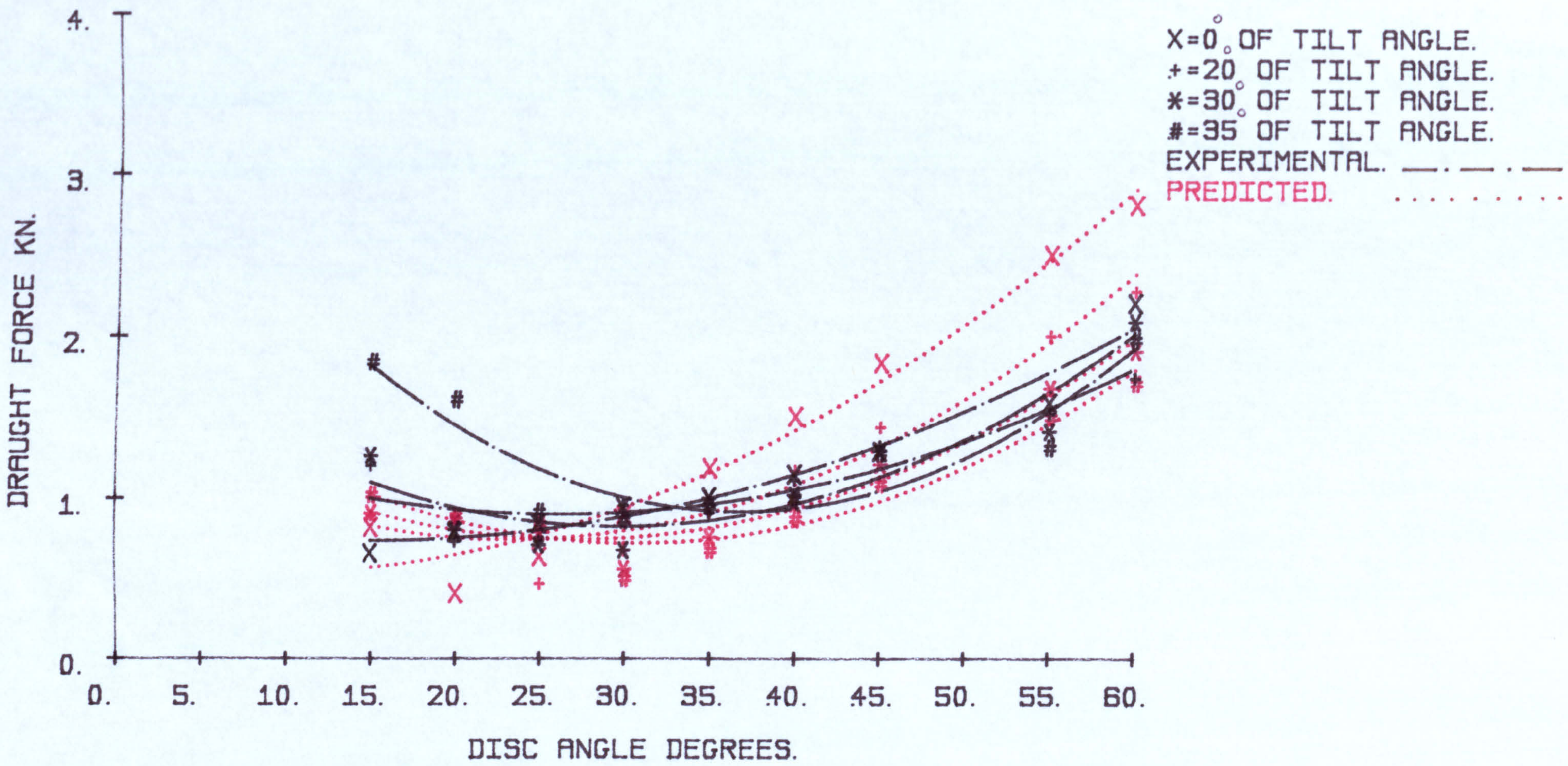

Figure 7.2. Draught force for a 0.61 m shallow inside sharpening disc having a radius of curvature of 0.7 m working at different disc and tilt angles at a depth of 0.14 m in comparison to the predicted values

except at the 15° disc angle with the vertical disc.

The theoretical draught advantage of reduced chamfer scrubbing, created by the inside sharpened disc, appears to be countered by the effect of increased rake angle on the concave side of the disc. The steady increase of draught from its minimum to a 60° disc angle occurs with no significant change in form produced by edge sharpening.

For deep outside sharpened discs, at a range of small disc angle between 15° - 30° for any tilt angle, it was found impossible to operate at these angles due to the large increase in contact between the furrow wall and the convex side of the discs. Minimum draught (1.0 kN) occurs at 40° disc angle for 0° and 20° tilt angles as shown in Table 7.3. and Figure 7.3. The 30° tilt angle was slightly larger at 1.2 kN compared to 1 kN for 0° and 20° tilt angles at a disc angle of 40°, as shown in Table 7.3. and Figure 7.3. Maximum draught occurs at 60° disc angle for a vertical disc and decreases to a minimum for a tilt angle of 30°, as indicated in Table 7.3. and Figure 7.3.

With the deep inside sharpened disc, it was possible to work at a slightly lower disc angle of 35°, due to a reduction in scrubbing on the convex side of the disc. Minimum draught force (0.8 kN) occurred at this

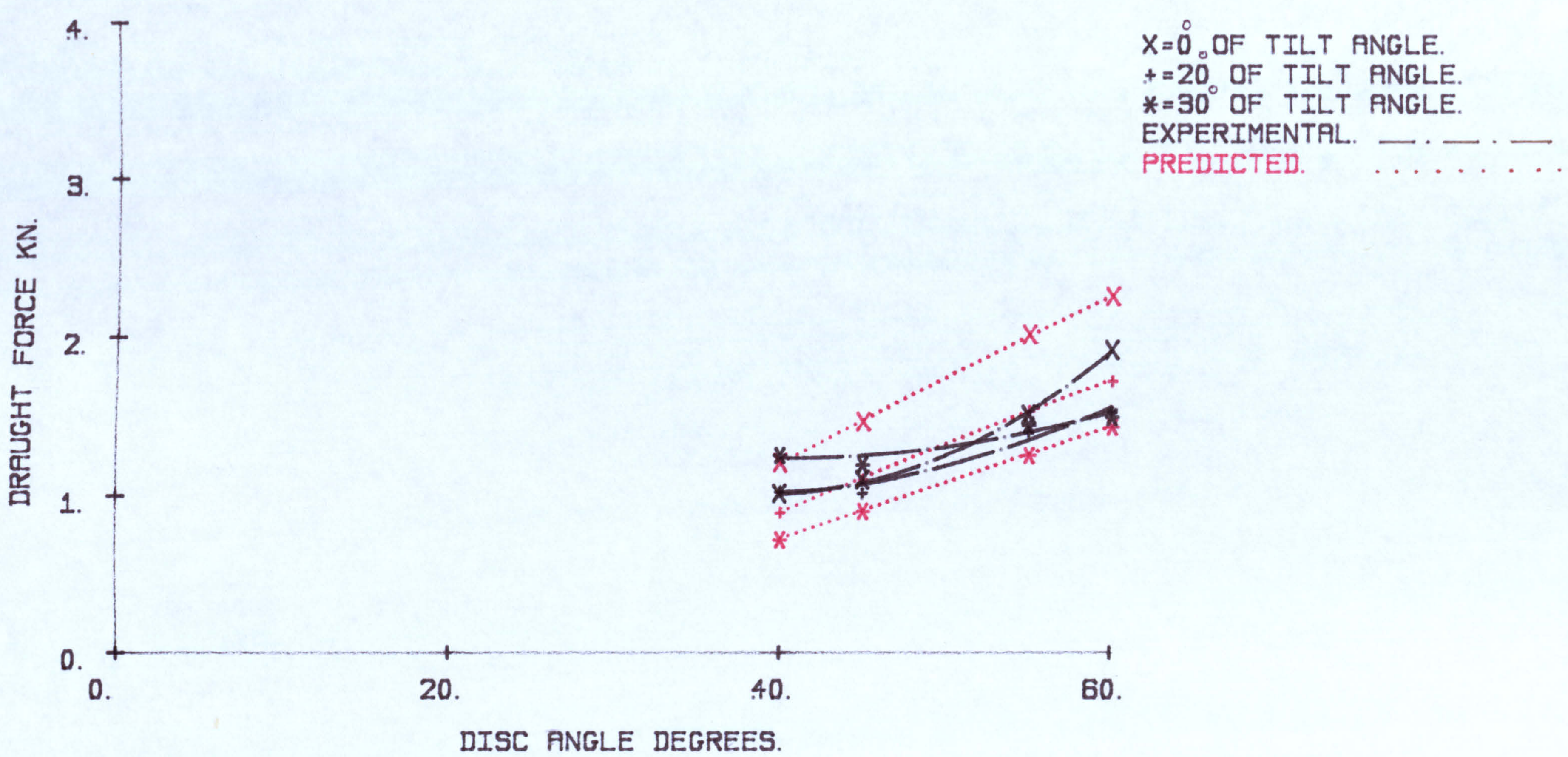

Figure 7.3. Draught force for a 0.61 m deep outside sharpening disc having a radius of curvature of 0.54 m operating at different disc and tilt angles at a depth of 0.14 m in comparison to the predicted values

value for 0° and 20° tilt angles, as shown in Figure 7.4. and Table 7.4. The minimum draught force (0.75 kN) for a 20° tilt occurred at the 40° disc angle and the minimum (1.0 kN) for the 30° tilt angle at 45° disc angle, as shown in Figure 7.4. and Table 7.4.

The draught for the 60° disc angle was similar to that of the outside sharpened disc at 1.8 kN for 0° tilt angle and 1.4 kN for 20° and 30° tilt angles, as shown in Figure 7.4. and Table 7.4.

7.2.2. Vertical forces

Vertical forces are stated with the convention that a negative force is a force resisting penetration.

With the shallow outside sharpened disc, at small disc angles of less than 15° the vertical forces developed on the convex side of the disc were large. In the rigid structure of the experimental rig it was found impossible to work at these low angles.

Within the operating range, negative vertical forces were large at 15° disc angle for each tilt angle, equal to -1.8 kN for the vertical disc and -4.1 kN for the 35° tilt disc, as shown in Table 7.1. and Figure 7.5. Increasing the tilt angle giving high scrubbing on the

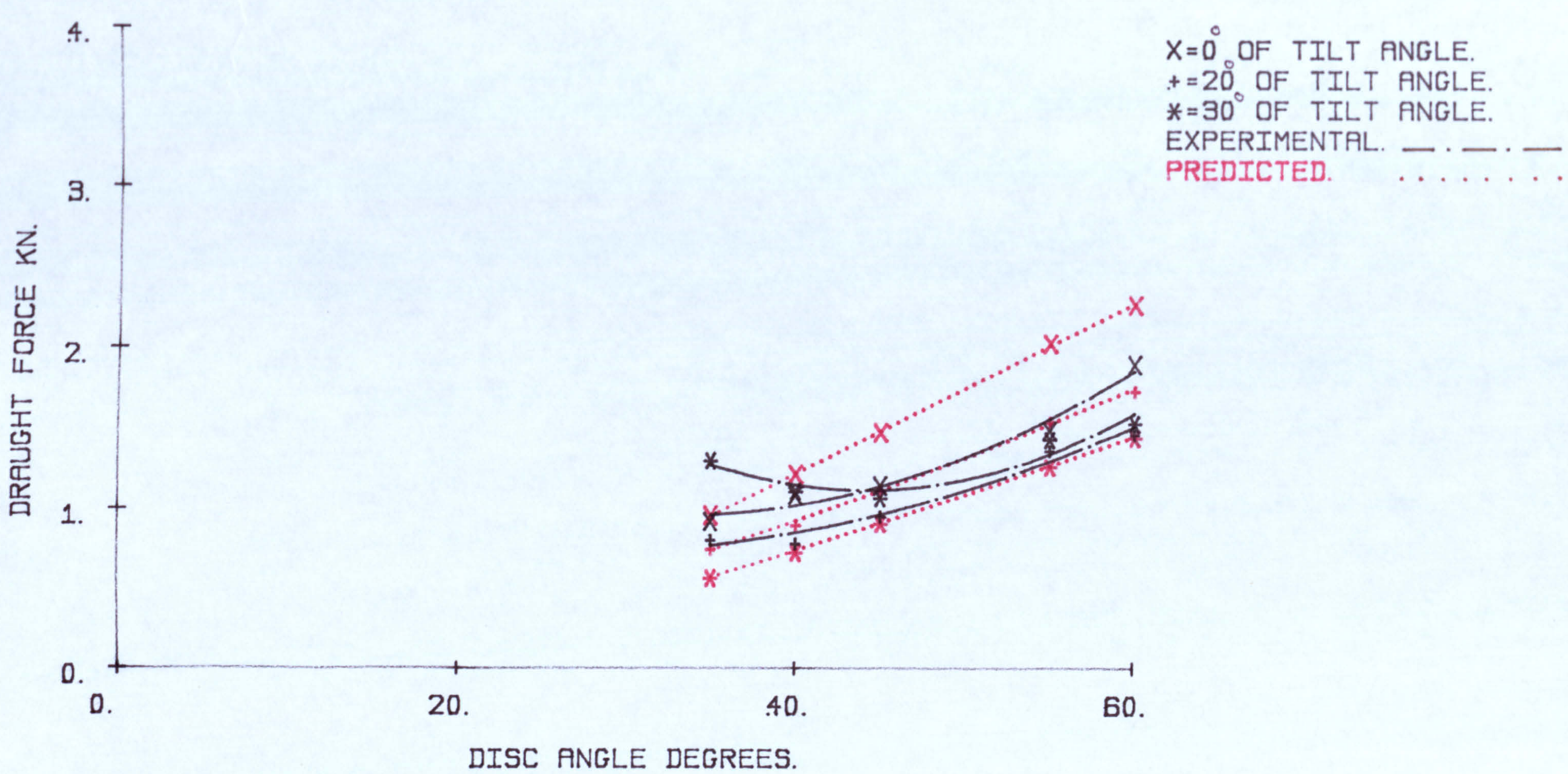

Figure 7.4. Draught force for a 0.61 m deep inside sharpening disc having a radius of curvature of 0.54 m operating at various disc and tilt angles at a depth of 0.14 m in comparison to the predicted values

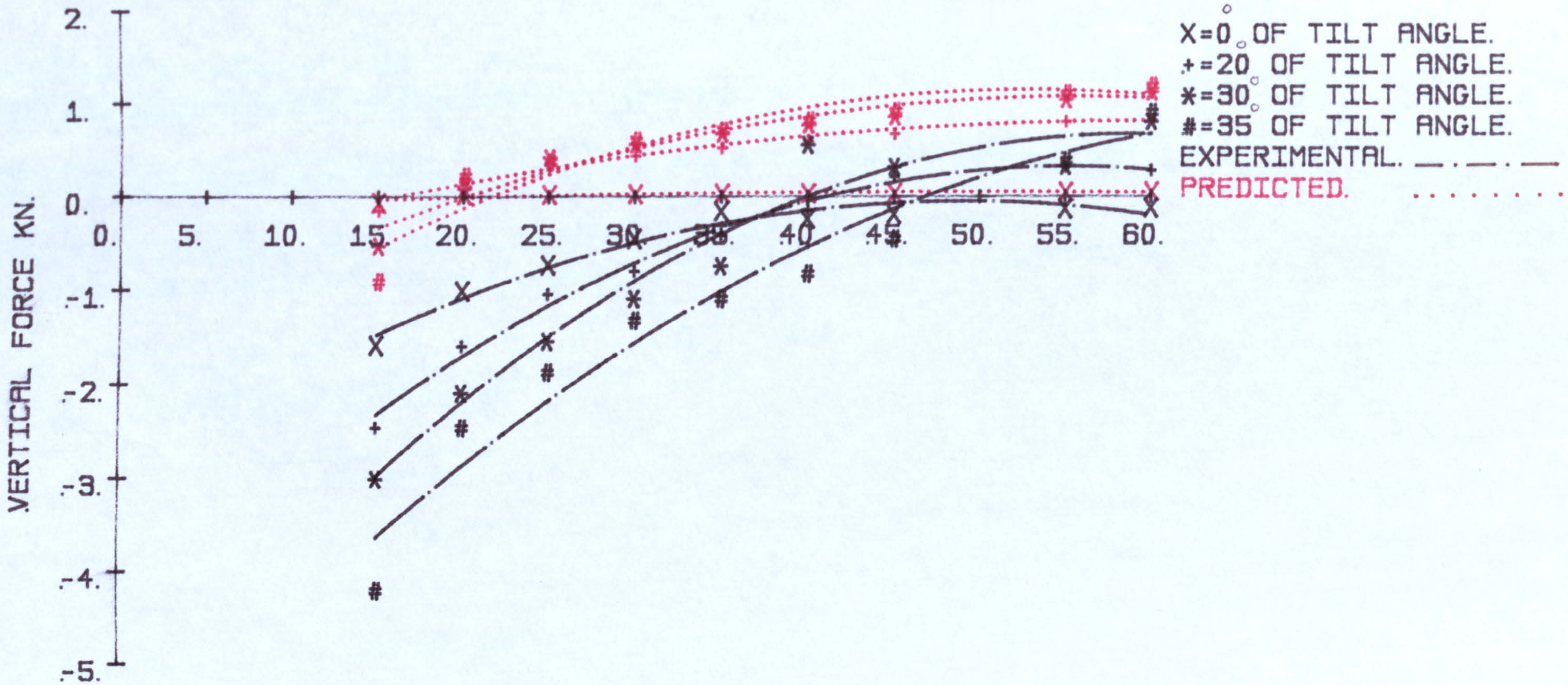

Figure 7.5. Vertical force for a 0.61 m shallow outside sharpening disc having a radius of curvature of 0.7 m operating at various disc and tilt angles at a depth of 0.14 m in comparison to the predicted values

convex side of the disc. As shown in Table 7.1. and Figure 7.5., this negative force steadily decreases in quantity to zero for the vertical disc, a maximum occurring at 50^{o} disc angle and then increasing to -0.2 kN at a 60^{o} disc angle. At no time does the vertical disc achieve a penetrating force. In the tilted discs, the same pattern follows an increase in disc angle, but the forces become positive, given penetration as shown in Table 7.1. and Figure 7.5. The change occurred at 40^{o} disc angle, for 20^{o} and 30^{o} of tilt angle, and at 45^{o} disc angle for the 35^{o} tilted disc, as indicated in Table 7.1. and Figure 7.5.

With the shallow inside sharpened disc, between 15^{o} and 45^{o} disc angles for the tilted discs shows a decrease of negative force with increasing disc angle, as shown in Table 7.2. and Figure 7.6. Force approaches zero at 25^{o} disc angle with a 30^{o} tilt angle and at a 30^{o} disc angle for 20^{o} and 35^{o} tilt angles, as shown in Table 7.2. and Figure 7.6. The resulting positive penetration force is in the useful range of 30^{o} to 60^{o} of disc angle. The change in vertical force is then small between 45^{o} and 60^{o} of disc angle, resulting with a flattened curve.

With the deep outside sharpened disc, within the range of the experiment, increasing disc angle decreases the negative vertical force at all tilt angles, as shown in

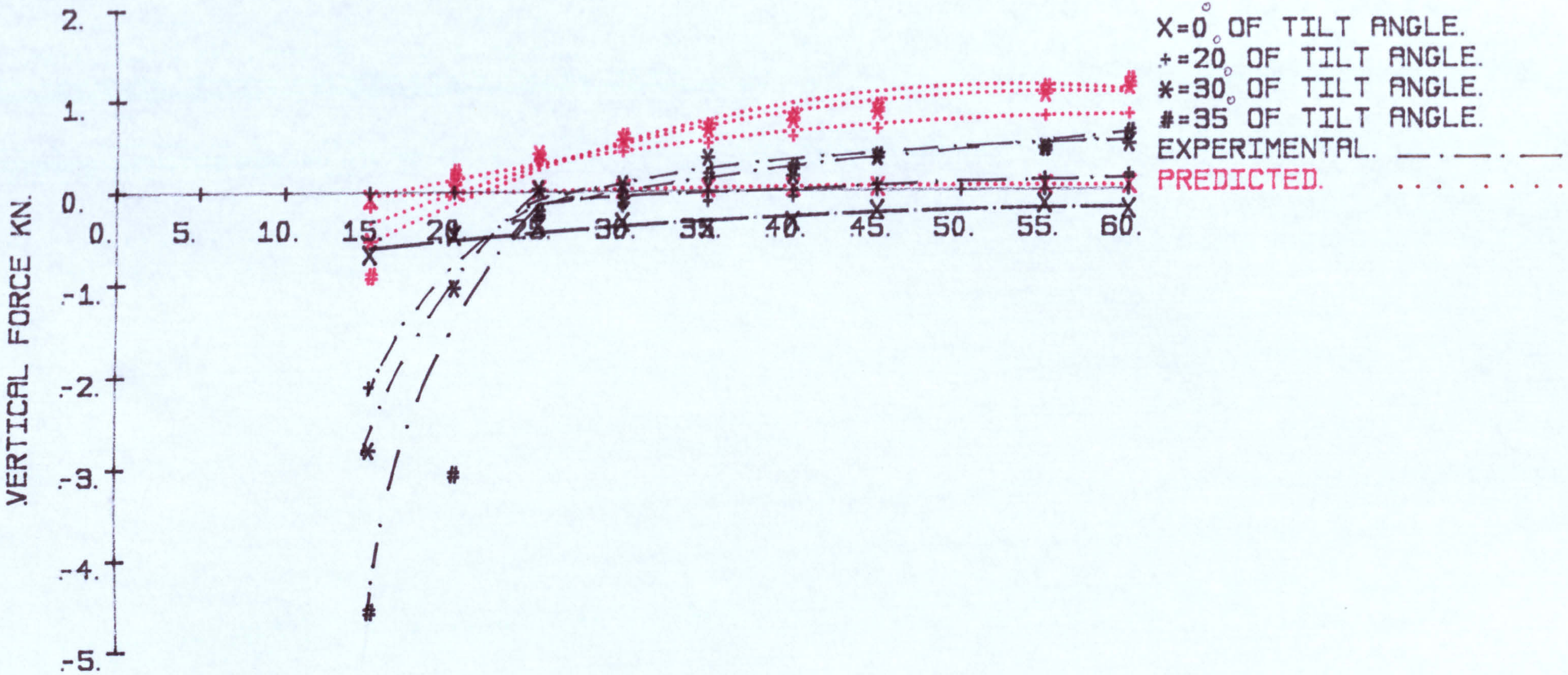

Figure 7.6. Vertical force for a 0.61 m shallow inside sharpening disc having a radius of curvature of 0.7 m ploughing at various disc and tilt angles at a depth of 0.14 m in comparison to the predicted values

Table 7.3. and Figure 7.7. The total range -1.1 kN to 0.4 kN is small, but increasing tilt angle does resist penetration. A 30^{o} tilt angle does not achieve penetration until a 60^{o} disc angle is reached, as shown in Table 7.3. and Figure 7.7. The deep inside sharpened disc is detrimental to penetration for a 0^{o} tilt angle and 20^{o} tilt angle and has only a small effect for the 30^{o} tilt, resulting in a slight reduction in negative force between 40^{o} and 50^{o} disc angle, as shown in Table 7.4. and Figure 7.8.

7.2.3. Side force

With shallow outside sharpened disc as shown in Table 7.1. and Figure 7.9., the side force is negative at small disc angles for all disc types and tilt angles. Within the operating range a shallow outside sharpened disc at 15^{o} disc angle and 0^{o} tilt angle generates -0.6 kN, and 35^{o} tilt angle -0.4 kN, as shown in Table 7.1. and Figure 7.9. The force on the convex side of the disc then reduces as critical angle is approached and a passive cutting area increases, generating positive forces. Zero value is reached when the forces are balanced in the region of 20^{o} disc angle for all tilt angles, when a passive component is generated.

The 0^{o} tilt angle and the 20^{o} tilt angle produce

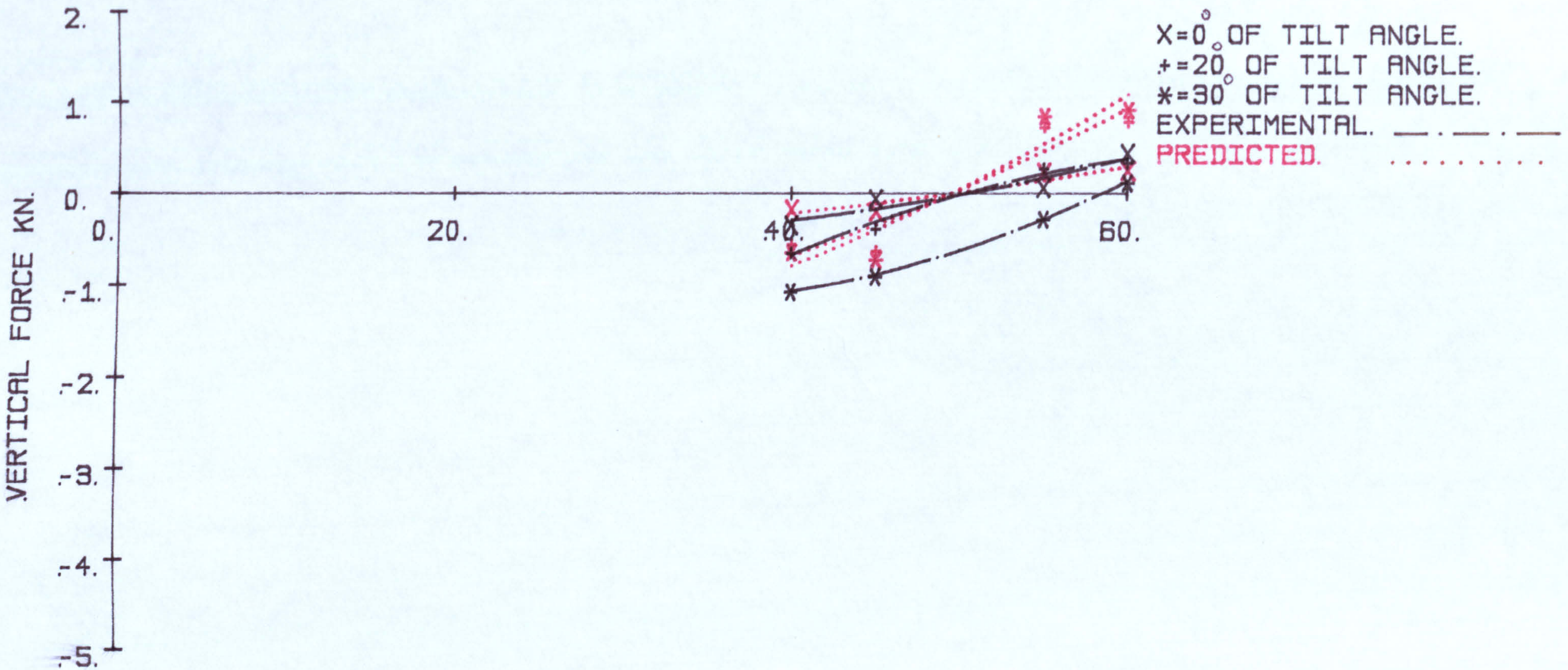

Figure 7.7. Vertical force for a 0.61 m deep outside sharpening disc having a radius of curvature of 0.54 m working at various disc and tilt angles at a depth of 0.14 m in comparison to the predicted values

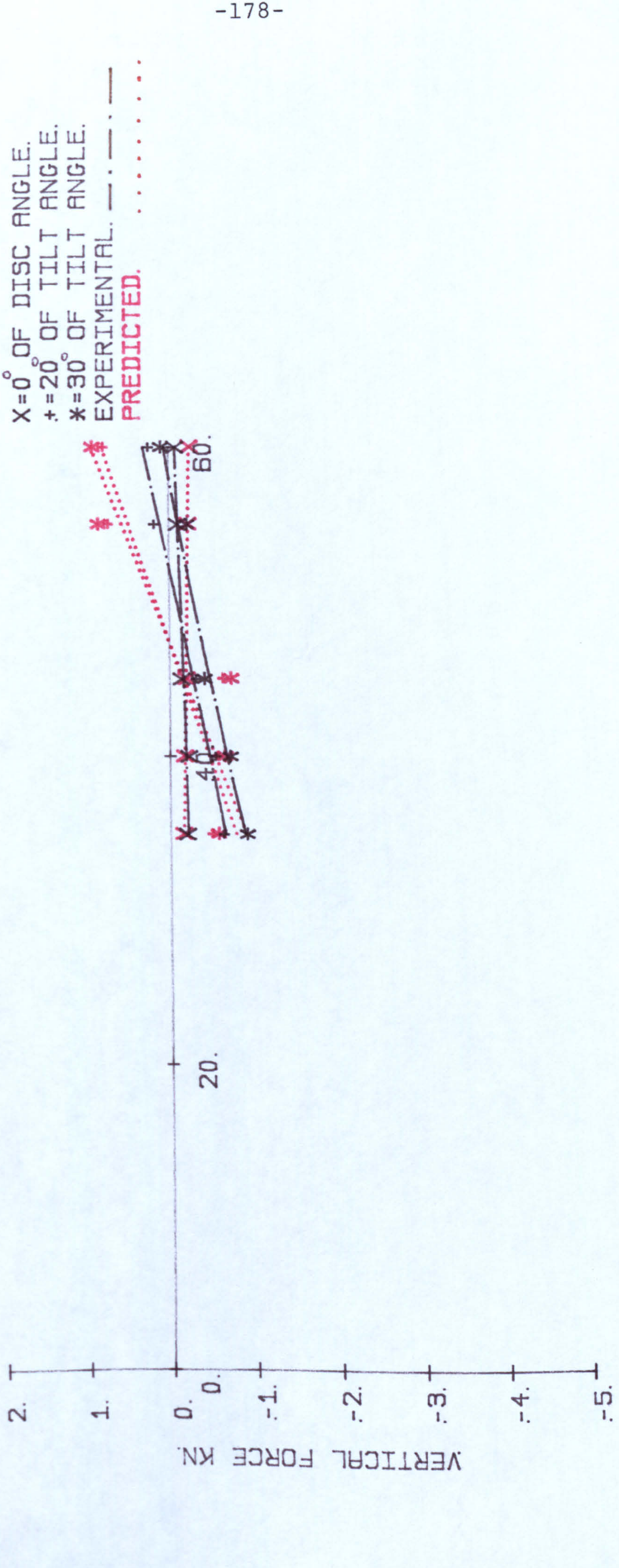

Figure 7.8. Vertical force for a 0.61 m deep inside sharpening disc having a radius of curvature of 0.54 m working at different disc angles of tilt at a depth of 0.14 m in comparison to the predicted values

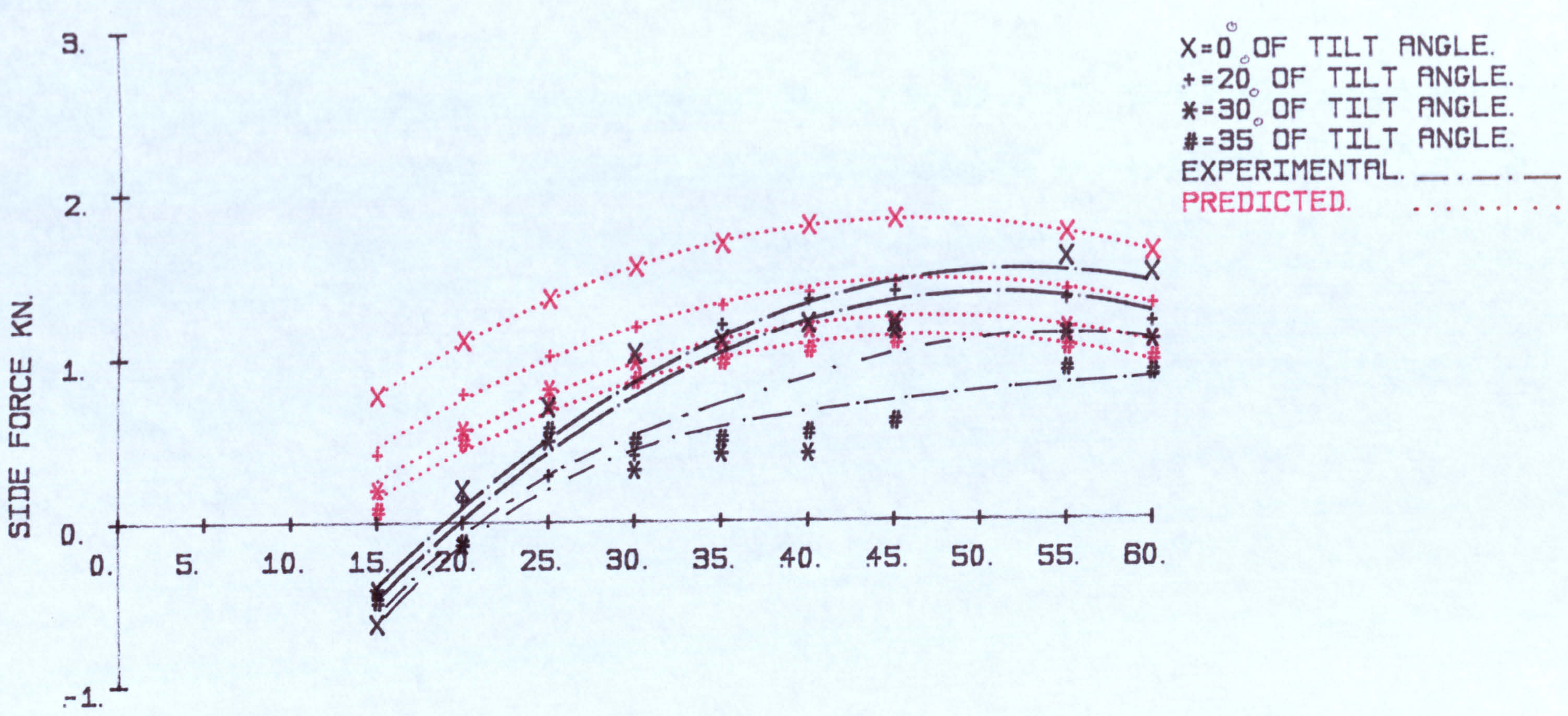

Figure 7.9. Side force for a 0.61 m shallow outside sharpening disc having a radius of curvature of 0.7 m operating at various disc and tilt angles at a depth of 0.14 m in comparison to the predicted values

larger side forces then larger tilt angles, as indicated in Table 7.1. and Figure 7.9. At a 40° disc angle, 0° and 20° tilt angles give side forces of 1.1 kN and 1.3 kN. The 30° and 35° tilt angles give 0.4 kN and 0.5 kN, respectively, as represented in Table 7.1. and Figure 7.9. Figure 7.9. shows that maxima of the curves occur at 55° disc angle for all discs, as the side component of the cutting resultant decreases.

The effect of inside sharpening on shallow concavity discs is to create a fall in convex side forces as the critical angle is approached. By a 25° disc angle, the curve has flattened and a slow rise in side force results up to a 60° disc angle, as shown in Figure 7.10.

For deep concavity discs, the side force is positive within the experimental range, except for the -0.1 kN side force produced by 35° disc angle at a 30° tilt angle in the inside sharpened deep disc, because this configuration is not above its critical angle and the convex side force is still present, as shown in Figures 7.11. and 7.12. and Tables 7.3. and 7.4.

The force rises from 0.7 kN at 40° disc angle and 0° tilt angle, with a maximum of 1.1 kN at 55° disc angle, falling slightly to 1.0 kN at 60° disc angle, as shown in Figures 7.11. and 7.12.

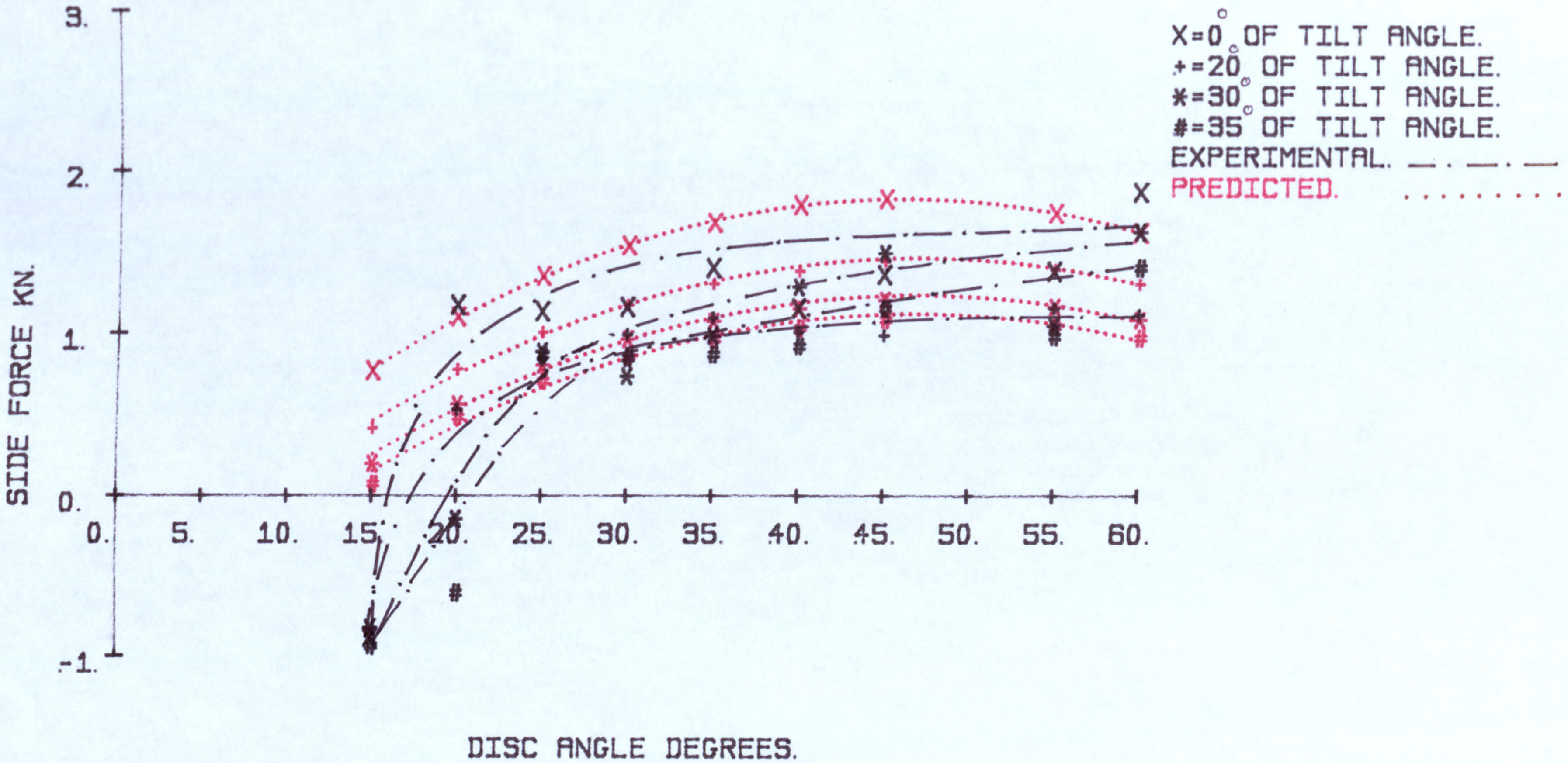

Figure 7.10. Side force for a 0.61 m shallow inside sharpening disc having a radius of curvature of 0.7 m operating at various disc and tilt angles at a depth of 0.14 m in comparison to the predicted values

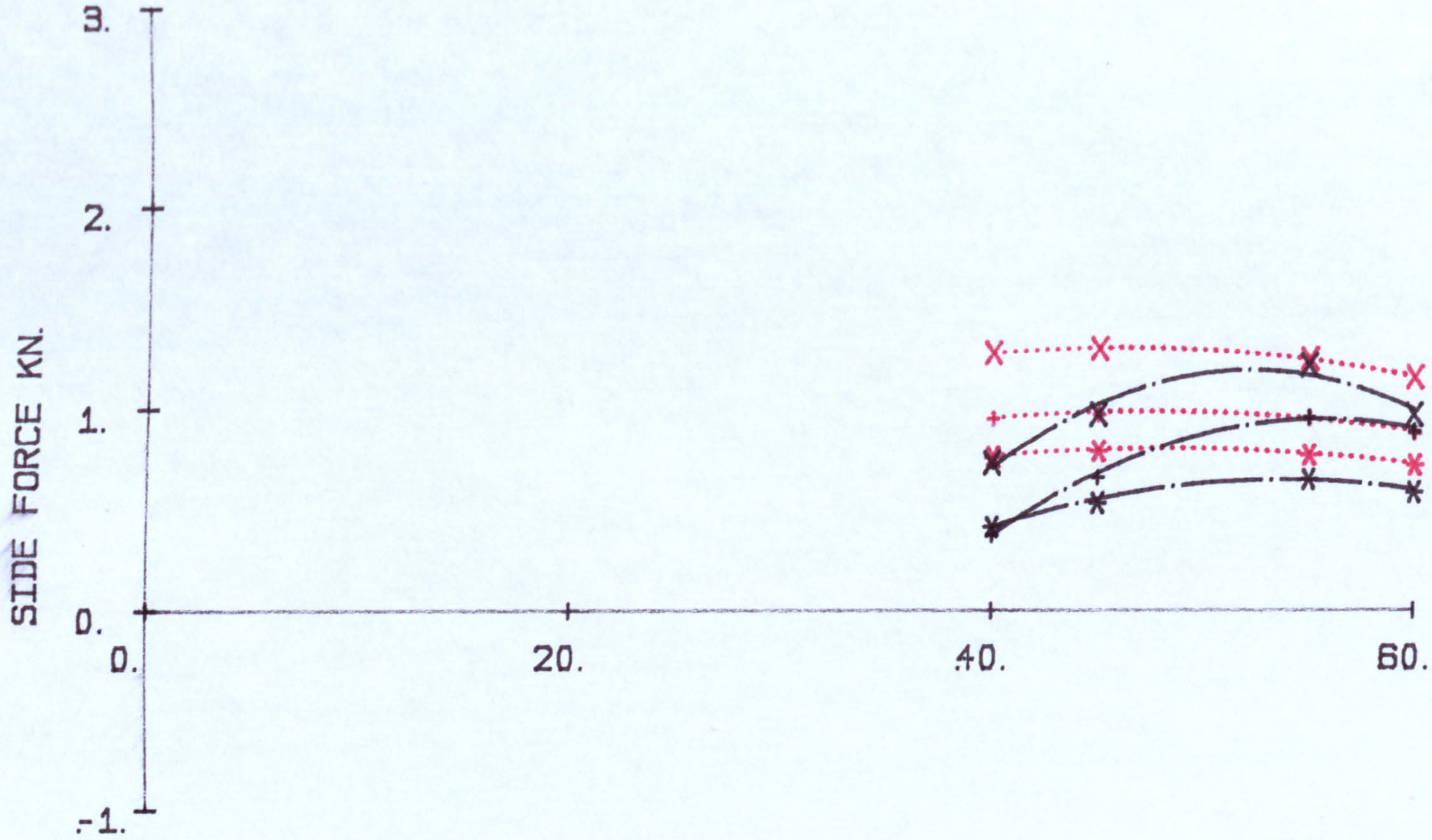

Figure 7.11. Side force for a 0.61 m deep outside sharpening disc having a radius of curvature of 0.54 m ploughing at different disc and tilt angles at a depth of 0.14 m in comparison to the predicted values

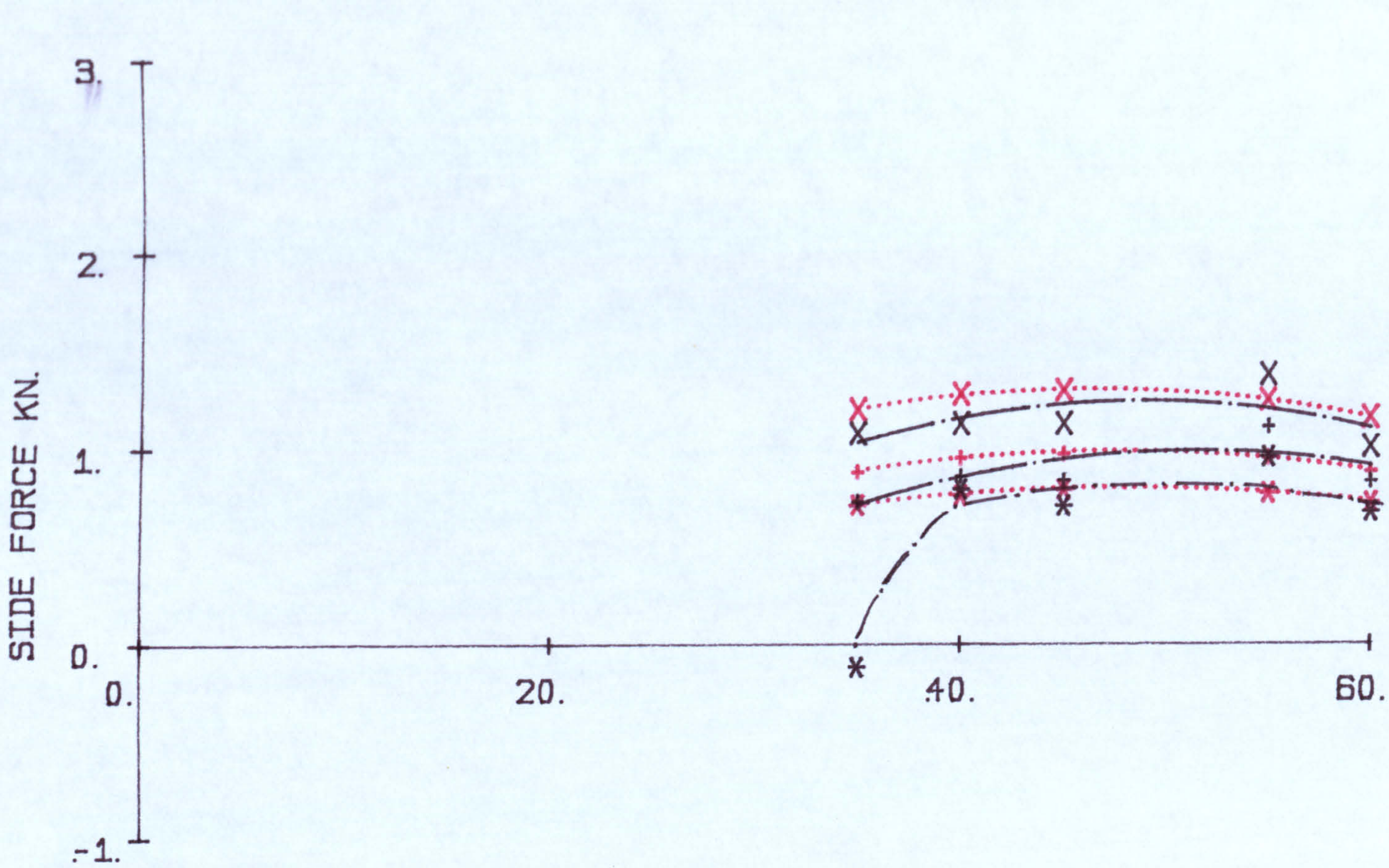

Figure 7.12. Side force for a 0.61 m deep inside sharpening disc having a radius of curvature of 0.54 m ploughing at various disc and tilt angles at a depth of 0.14 m in comparison to the predicted values

Increasing the tilt angle reduces the passive component of side force for the 45° and 55° disc angles. This results in values at a 55° disc angle of 1.1 kN at 30° tilt angle, 0.9 kN at 20° tilt angle and 0.7 kN at a 30° tilt angle, as shown in Figure 7.11. Inside sharpening of the deep discs increases the passive side force in the experimental range, due to the large side rake angles produced at these disc angles.

7.3. Depth experiments

In order to limit the size of the experiments a representation pattern of disc configuration was operated for both shallow and deep discs, at three depths, 80 mm, 100 mm and 140 mm. While the pattern was not intended for strict graphical interpretation some trends are indicated.

Overall averages show all forces increasing with increasing depth, a 25% depth increase producing close to 23% force increase and a 75% depth increase producing 92% extra force.

7.3.1. Draught force

The rate of increase of draught force with depth

is not as great with discs as with most rigid tine implements. The mean slope of curves shows a rate of rise of 0.0118 kN/mm for shallow outside sharpened disc, as shown in Table 7.5. For shallow inside sharpened disc, the rate of rise was 0.0106 kN/mm, as shown in Table 7.5. The mean slope of curves for the deep outside and inside sharpened discs is 0.0128 kN/mm and 0.0112 kN/mm respectively, as indicated in Table 7.6.

The limited disc configuration shows that the small disc angle combination gave a slightly lower rate of rise of 0.01 kN/mm at 15° disc angle and 0° tilt angle than at higher disc angle of 60° and 0° tilt angle (0.014 kN/mm) for shallow outside sharpened disc, as shown in Figure 7.13.

The variable gang spacing makes interpretation difficult as it has a large influence on the length of the effective shear plane and, therefore, upon the draught. As the depth increases the shortest shear plane available a brittle failure tends to surface on the precut face not on the true ground surface. The draught component in a heavy scrubbing situation is not however subject to this limitation. As large convex side exposures result from a small disc angle and large tilt angle configuration with an increase in depth, a correspondingly sharp rise in draught occurs, eg. 0.021 kN/mm at a 15° disc angle and

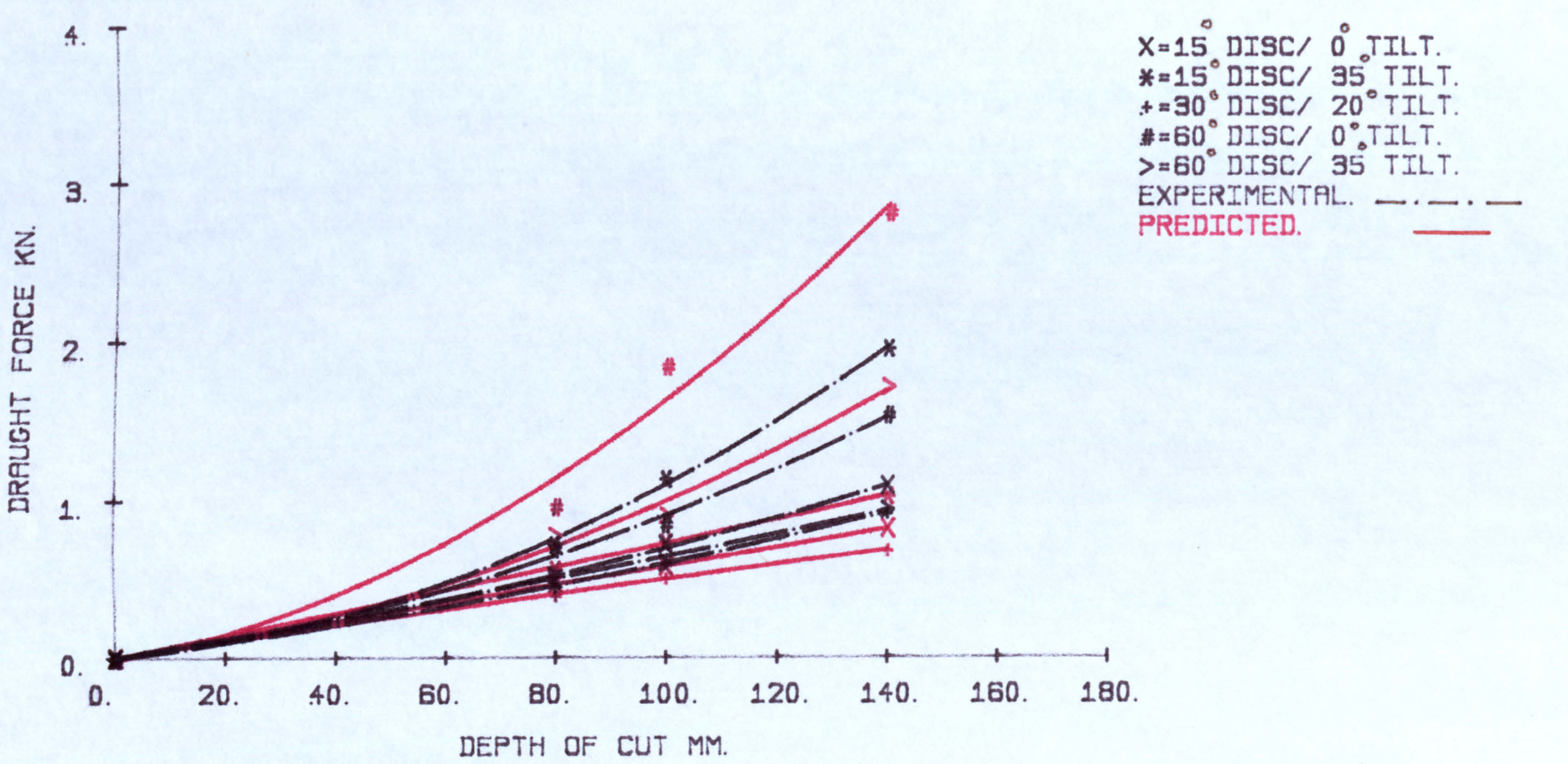

Figure 7.13. Draught force for a 0.61 m shallow outside sharpening disc having a radius of curvature of 0.7 m operating at combinations of disc and tilt angles at different depths in comparison to the predicted values

35^{o} tilt angle, as shown in Figure 7.13. These combinations are not useable in the field as the implement will not penetrate to a deep condition.

7.3.2. Vertical force

The mean slope of the curves for shallow outside sharpened disc shows that the rate of rise is 0.00101 kN/mm as shown in Table 7.5. The mean slope of the curves for the shallow inside sharpened disc is 0.00182 kN/mm, as indicated in Table 7.5. For the deep outside and inside sharpened discs, the mean slope of curves are 0.00588 kN/mm and 0.00165 kN/mm respectively, as indicated in Table 7.6.

Except for the 15^{o} disc angle and 35^{o} tilt angle configuration, vertical force changes are small and the change in the balance of opposing forces is not greatly altered by increasing depth, as shown in Figure 7.14. The rate of change for shallow inside sharpened disc is 3.4×10^{-3} kN/mm at 60^{o} disc angle and 0^{o} tilt angle, as shown in Figure 7.14. At 30^{o} disc angle and 20^{o} tilt angle, the rate of change is 8×10^{-4} kN/mm, as indicated in Figure 7.14. This rate of change is small as the force balance is maintained. In the case of the 15^{o} disc angle and 35^{o} tilt angle, heavy scrubbing occurs and the rise in vertical force opposing penetration is large

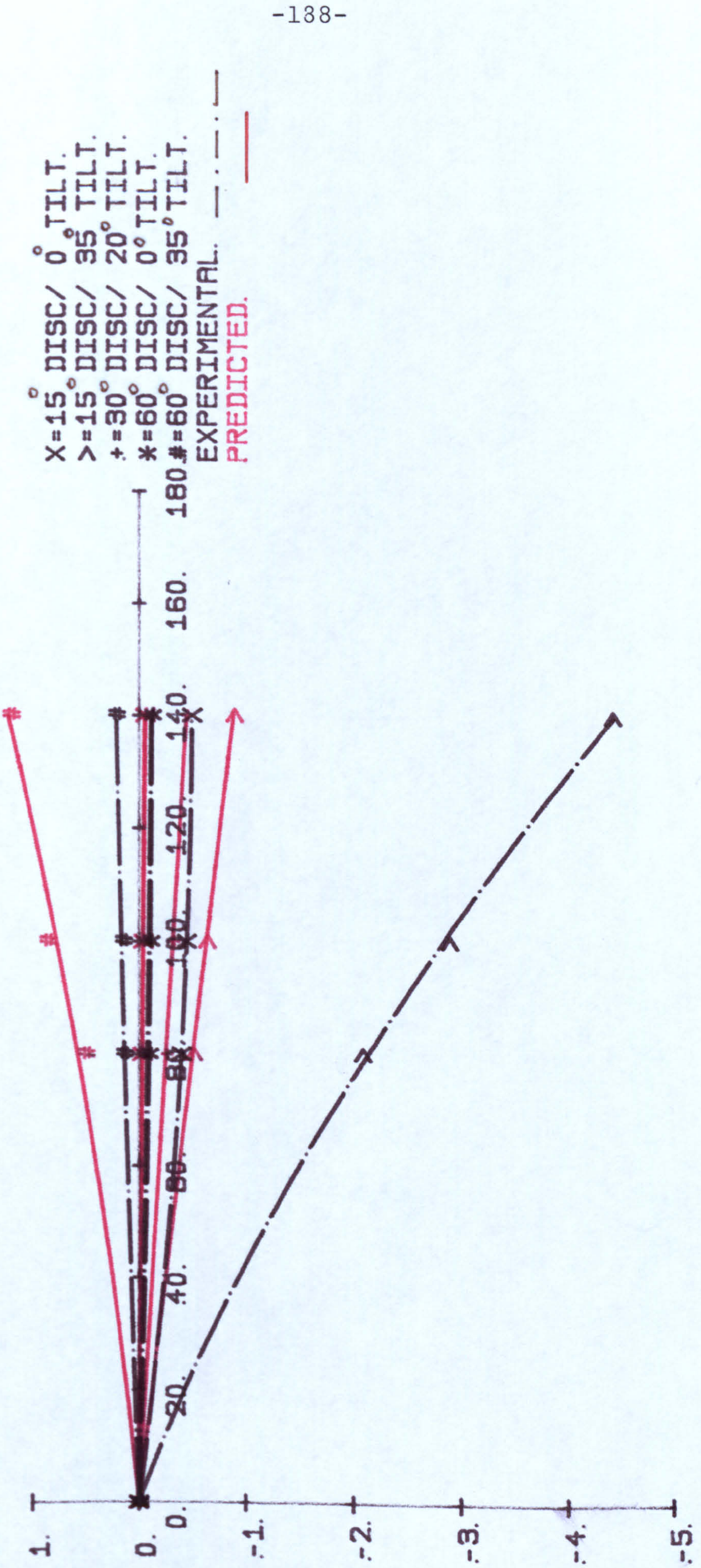

Figure 7.14. Vertical force for a 0.61 m shallow inside sharpening disc having a radius of curvature of 0.7 m operating at combinations of disc and tilt angles at various depths in comparison to the predicted values

(0.0405 kN/mm), as shown in Figure 7.14. This combination reaches a critical depth at less than 75 mm depth. This type of configuration is unworkable in the field situation.

7.3.3. Side force

The mean slope of the curves for shallow outside sharpened disc show that the rate of rise is 0.00694 kN/mm, as shown in Table 7.5. For the shallow inside sharpened disc, the mean slope of the curves shows that the rate of rise is 0.00716 kN/mm, as shown in Table 7.5. For the deep outside and inside sharpened discs, the mean slopes of the curves are 0.00475 kN/mm and 0.00494 kN/mm, respectively, as shown in Table 7.6.

Side forces are larger, in general, than vertical forces. All side forces increase in magnitude in their own direction. At a 15^{o} disc angle and 35^{o} tilt angle, the rate of change is -0.0116 kN/mm, as shown in Figure 7.15. For the 30^{o} disc angle and 20^{o} tilt angle, the rate of change is 6.98×10^{-3} kN/mm, as indicated in Figure 7.15. Where side forces are well balanced and, therefore, low they remain lower as depth increases, eg. 1.475×10^{-3} kN/mm at a 15^{o} disc angle and 0^{o} tilt angle, as shown in Figure 7.15. Where side forces are higher, a more rapid rise occurs, eg. 0.011 kN/mm at 60^{o} disc angle and 0^{o} tilt angle, as shown in Figure 7.15. The pattern

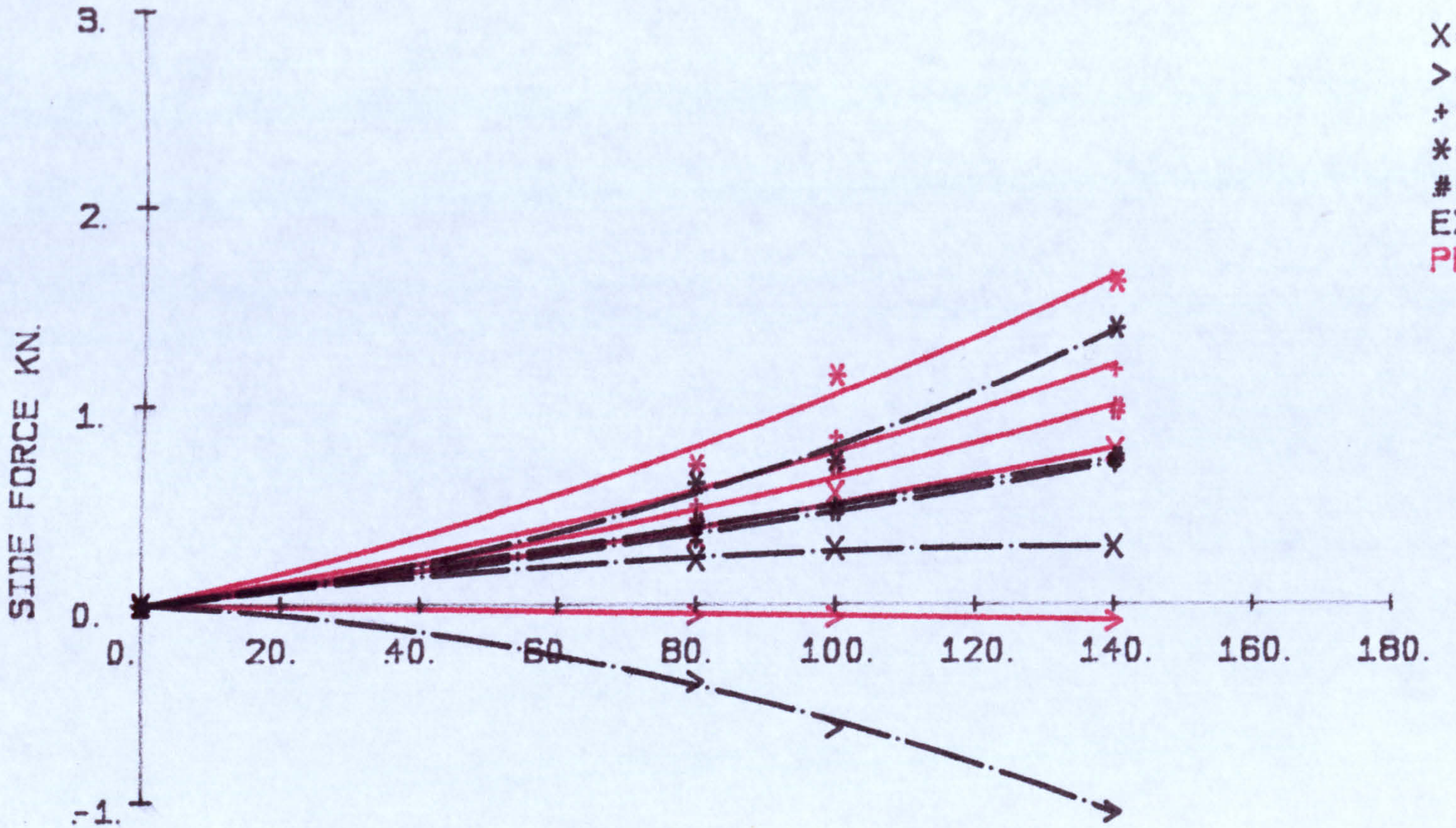

Figure 7.15. Side force for a 0.61 m shallow inside sharpening disc having a radius of curvature of 0.7 m operating at combinations of disc and tilt angles at different depths in comparison to the predicted values

of disc combinations is too limited to allow interpretation of a critical depth point and if the change to scrubbing forces changes the curve. In the field situation, higher convex side forces tend to be self correcting as the implement swings, increasing the disc angle and reducing the convex side forces.

There is little evidence of an interaction of depth with inside and outside sharpened discs within the narrow range of the depth experiments with deep concavity. The same trends appear for rates of force change with depth which are of the same order as for the shallow concavity.

7.4. Speed experiments

In order to limit the size of the experiment, a representative range of disc angles and tilt angles was used. Five combinations were chosen for the shallow outside and inside sharpened disc and four for deep outside and inside sharpened discs.

No distinct trends could be determined due to variations of disc angle, tilt angle, concavity or sharpening type on the measured forces with variations in cutting speed.

Overall averages show all forces increasing with

increasing speed. A 33% increase in speed (from 0.75 m/s to 1 m/s) produced nearly a 10% force increase and a 100% speed increase (from 0.75 m/s to 1.5 m/s) produced a 27% increase in force.

7.4.1. Draught force

The average rate of change of draught force for all disc angles and tilts from 0.75 m/s to 1.5 m/s was 0.513 $kNm^{-1}s$ for shallow outside sharpened disc, as shown in Table 7.7. For the shallow inside sharpened disc, the mean slope of curves for all disc angles and tilts from 0.75 m/s to 1.5 m/s was 0.601 $kNm^{-1}s$, as indicated in Table 7.7. The mean slope of the curves for the deep outside and inside sharpened discs for all disc angles and tilts for 0.75 m/s to 1.5 m/s was 0.623 $kNm^{-1}s$ and 0.405 $kNm^{-1}s$ respectively as shown in Table 7.8. At 15^{o} disc angle and 35^{o} tilt angle, the rate of rise for 0.75 m/s to 1.5 m/s is 0.379 $kNm^{-1}s$ for the shallow outside sharpened disc, as indicated in Table 7.7. This rate of rise is reduced to 0.29 $kNm^{-1}s$ for the shallow inside sharpened disc, as represented in Table 7.7.

7.4.2. Vertical force

In the non-scrubbing situation, vertical forces are generally small. The mean slope of the curves for the

shallow outside sharpened disc show that the rate of rise for 0.75 m/s to 1.5 m/s was 0.123 $kNm^{-1}s$, as shown in Table 7.7. For the shallow inside sharpened disc, the mean slope of the curves for 0.75 m/s to 1.5 m/s was 0.209 $kNm^{-1}s$, as indicated in Table 7.7. The mean slope of the curves for the deep outside sharpened disc and the deep inside sharpened disc for 0.75 m/s to 1.5 m/s was 0.282 $kNm^{-1}s$ and 0.272 $kNm^{-1}s$, as shown in Table 7.8. The range of vertical force within the pattern of configuration was large. In the case of the 15^{o} disc angle and 35^{o} tilt angle, heavy scrubbing occurs and the rate of rise in the vertical force opposing penetration was large (0.239 $kNm^{-1}s$) for the shallow outside sharpened disc, as shown in Table 7.7., probably due to disc distortion increasing the tilt angle. This rate of change in vertical forces is reduced to 0.122 $kNm^{-1}s$ for the shallow inside sharpened disc, as shown in Table 7.7.

7.4.3. Side force

The mean slope of the curves for the shallow outside sharpened disc show that the rate of increase for 0.75 m/s to 1.5 m/s was high at 0.459 $kNm^{-1}s$, as shown in Table 7.7. For the shallow inside sharpened disc, the mean slope of the curves for 0.75 m/s to 1.5 m/s was 0.396 $kNm^{-1}s$ as shown in Table 7.7. The deep outside sharpened disc and the deep inside sharpened disc gave

mean slopes of curves plotted against speed of 0.157 $kNm^{-1}s$ and 0.358 $kNm^{-1}s$, respectively, as shown in Table 7.8.

The range of side force within the pattern of configuration was small. In the case of 15^{o} disc angle and 0^{o} tilt angle, the mean slope of the curves for 0.75 m/s to 1.5 m/s was 0.348 $kNm^{-1}s$ for the shallow outside sharpened disc, reducing to 0.064 $kNm^{-1}s$ for the shallow inside sharpened disc, as shown in Table 7.7. In the scrubbing situation, the side forces were large. At a 15^{o} disc angle and 35^{o} tilt angle, the mean slope of the curves for 0.75 m/s to 1.5 m/s was 0.9 $kNm^{-1}s$ for the shallow outside sharpened disc, as shown in Table 7.7. This rate of rise was reduced to 0.38 $kNm^{-1}s$ for the shallow inside sharpened disc, as indicated in Table 7.7. The effect of speed for the side force was greater than for the vertical force.

7.5. A comparison of experimental and predicted results

7.5.1. Introduction

The results for the sample calculations are tabulated in Tables 7.9., 7.10. and 7.11. for the soil parameters obtained as a result of soil treatments. The predicted results are discussed below:

7.5.2. Draught force

The predicted and measured draught forces were similar in form, as shown in Figures 7.1., 7.2., 7.3. and 7.4. In most cases, the predicted forces showed a good measure of agreement with experimental draught forces, except for the 0^{o} tilt angle at large disc angles when the predicted magnitude was higher than the observed values. At low disc angles, the predicted results were lower than those observed. The model predicts that increasing tilt angle increases draught forces for large disc angles. This is based on the assumption that the same surcharge mechanism applies independently of tilt angle. The experimental results suggest that draught is independent of tilt angle at large disc angle, hence there must be some change in the surcharge process as tilt angle is varied. The model was expected to establish a reasonably good prediction of forces over a range of disc angles from 0^{o} to 60^{o} and it was hoped to be able to predict forces at low disc angles. However, in the limit of small disc angle, this would lead to the prediction of small draught force. The assumption may be made that soil/metal friction plays no part in partitioning the normal force into draught and side components. Therefore, some convex side friction was included in the calculation at small disc angles, which increased the draught force, for example, from 0.04 kN to 0.73 kN for a 15^{o} disc angle

at a 20^{o} tilt angle, as shown in Equation 6.18. For the shallow concavity, inside sharpened disc, the agreement between the predicted and the experimental results are better than for the outside sharpened disc with the exception of the 0^{o} tilt angle, at large disc angles (Figure 7.2.). The experimental forces were larger than predicted forces for 35^{o} tilt angle low disc angles (15^{o} and 20^{o}) because of greater scrubbing on the convex side of the disc. With outside sharpening of the shallow concavity the chamfer scrubbing force results in an increase in draught force above the predicted values at low disc angles, when the chamfer has reached its own critical angle, as shown in Figure 7.1.

With deep outside and inside sharpened discs, the draught force prediction is adequate within the working range, as shown in Figures 7.3. and 7.4. The greatest discrepancy again arises for the greatest tilt angle used (30^{o}) at the largest disc angles employed.

7.5.3. Vertical force

In a prediction of the vertical forces the model shows better agreement with the experimental results for the inside sharpened disc than for the outside sharpened disc, as shown in Figure 7.6. The form of the curves with change of disc angle showed good agreement, above the

critical angle of the disc configuration, as shown in Figure 7.6. The rapid increase of convex side forces at disc angles below about 25^{o}, particularly at higher tilt angles, was not predicted by the model in its present form, because of high scrubbing focus.

The effect of outside sharpening of the disc shows as the upward scrubbing forces resulting in negative forces up to a disc angle well above the geometrical critical disc angle, as shown in Figure 7.5. The true radius of the chamfer give a critical angle above 40^{o}.

For the deep concavity, for both outside and inside sharpened discs, the vertical forces are generally well predicted in the working region but the model gives rather higher values for the force at large disc angle, as shown in Figure 7.7. and 7.8. This is probably due to the effect of increased effective cutting area.

7.5.4. Side force

A comparison of the predicted and experimental forces shows underestimate of convex side force at the lowest disc angles. The measured rise in these forces at low disc angle was extremely rapid for the inside sharpened disc, but above the critical disc angle the model gives good prediction up to a 60^{o} disc angle, as shown in Figure 7.10.

The predicted decrease in side force between 50^{o} and 60^{o}, although small, is not followed by the experimental results for the inside sharpened discs, probably due to the increased bulldozing at these angles observed in the experiments (Figure 7.10.)

The outside sharpened disc again shows the effect of scrubbing in low disc angles, but good prediction is shown in the variation of force with tilt angle change, as shown in Figure 7.9. The high disc angle predictions are good, as shown in Figure 7.9. No excessive bulldozing was observed with this disc configuration. With deep concavity inside sharpening disc, the side prediction is generally good, as shown in Figure 7.12., predicting the variation with both disc angle and tilt angle. For the 35^{o} disc angle at a 30^{o} tilt angle (a lower scrubbing situation) the model did not successfully predict the scrubbing force (Figure 7.12.).

With the deep concavity, outside sharpened disc, the relationship between the predicted and the experiment shows that the effect for the outside chamfer and high critical disc angle affects the measured forces so that the model gives an under-prediction of the convex side force to a 45^{o} disc angle (Figure 7.11.). The effect of tilt angle is well predicted, as shown in Figure 7.11.

7.5.5. Depth experiments

7.5.5.1. Draught force

The form of the predicted draught curves showed good agreement with those of the experimental results (Figure 7.13.). In these experiments, the increase of draught force with increasing depth was less rapid than for a rigid tined implement. The measured forces for the 60^{o} disc angle and 0^{o} tilt angle configuration were lower than those predicted, as shown in Figure 7.13., as the model is unable to predict the presence of a failure plane to the previous cut surface instead of the true soil surface.

7.5.5.2. Vertical force

The relationship between the vertical force prediction curves and the vertical force measurement generally compared well, as shown in Figure 7.14. The model did not predict the rapid decrease of vertical force with depth for the 15^{o} disc angle and 35^{o} tilt angle, as shown in Figure 7.14. The model over-predicts the increase in vertical force at 60^{o} disc angle and 35^{o} tilt angle (Figure 7.14.). This configuration is most likely to produce failure to the pre-cut surface of the gang spacing rather than to the true soil surface. It also clears soil, so limiting the effects of surcharge on the failure plane.

7.5.5.3. Side force

The side force predictions were generally of the correct form and magnitude, as shown in Figure 7.15. The model does not predict the rapid rate of increase of convex side force that occurs for the 15^{o} disc angle and 35^{o} tilt angle combination, as shown in Figure 7.15. This combination was unstable and distortion of the disc was observed. The distortion tends to increase the tilt angle, so producing greater scrubbing and, therefore, increased side force.

7.5.6. Speed experiments

The model was not intended to investigate the effect of speed on the disc forces and, therefore, no comparisons could be made on this basis with the experimental results.

7.5.7. Conclusions

The mechanism of force production in agricultural discs is extremely complex, being essentially a three-dimensional problem. When a full comparison between the predicted and experimental forces was made, within the useful range of disc and tilt angles, the model showed a good ability to predict the passive cutting forces of a geometric disc. Variations occur due to the effect of sharpening technique

and soil clearance after cutting. The effect of variations in tilt angle is seen clearly for large concavity discs, where the predicted force is significantly different between the angles.

The mechanism of convex side scrubbing failure with a rotating disc at small disc angles is not fully understood, and further work needs to be initiated in order to establish surcharge mechanisms and factors from this type of sliding compressive failure.

The model is totally dependent upon disc concavity, as this is an integral part of the geometry, while sharpening method is also important. The model assumes an idealised geometrically perfect disc. The outside surface of an inside sharpened disc is close to this form, but the internal rake angles are changed in passive cutting. An outside sharpened disc gives valid results for passive cutting forces, but the outside chamfer has its own radius of curvature, which is smaller than that of the true disc. These practical differences account for some of the differences between the forces predicted by the model and those measured experimentally.

CHAPTER 8

8. CONCLUSIONS

The following conclusions relate to studies conducted with two disc concavities with two sharpening techniques operating over a range of (i) disc angles between 15^{o} and 60^{o}, (ii) tilt angles between 0^{o} and 35^{o}, (iii) depths of cut between 80 mm and 140 mm, and (iv) speeds between 0.75 m/s and 1.5 m/s.

The experiments were conducted under laboratory conditions in a sandy loam soil with a density of 1.446 kg/m^{3}.

A dynamometer was designed, constructed and calibrated to measure independently the draught, vertical and side forces acting on a disc. This was based on the use of two extended octagonal ring transducers, together with a torque tube employing strain gauge measuring elements. The calibrations showed linear characteristics, with no appreciable hysteresis and acceptable levels of interaction between the force measuring bridges. The mounting distance of the disc from the axis of symmetry of the dynamometer had no significant effect on the dynamometer sensitivity.

1. Investigations showed that there were two forms of soil failure affecting the magnitude and direction of the force acting on the disc. These are:

(a) A passive reaction on the concave side of the disc produced by the vertical pressure area. The limiting vertical pressure area reached a maximum when the disc angle was equal to 90^{o} and reduced to zero at a disc angle of 0^{o}.

(b) The force carried by the vertical bearing area on the convex side of the disc. The limiting area of the soil reached a maximum when the disc angle was equal to zero and reduced to zero when the disc angle was equal to the critical angle and the working depth was equal to the critical depth.

2. A rigorous theoretical analysis of the disc geometry was carried out. This analysis made it possible to determine the most important disc parameters, such as critical disc angle and the critical depth of cut. These parameters are important as far as the soil reaction on the disc is concerned. This analysis enabled the factors required for the prediction of the draught, vertical and side components of the soil reaction on the disc to be determined.

3. The theoretical analysis of the disc geometry was carried out for both vertical and tilted disc.

4. It was possible to predict the draught, vertical and side components of the soil reaction on a vertical and tilted disc, in respect of diameter, radius of curvature, disc angle, tilt angle and depth of work, using Mohr-Coulomb soil mechanics principles.

5. Studies of the disturbance of the soil revealed that:

   (a) The disturbance area of the soil caused by the rotating soil-cutting disc is an important variable in determining the specific resistance.

   (b) The specific resistance was determined using the developed gang area and was shown to be affected by disc angle, disc diameter, depth of cut and gang spacing. As these factors increased, the gang area of soil disturbance increased and the specific resistance decreased.

   (c) The lowest specific resistance in a gang disc occurred for a disc angle of about 40^{o}.

6. The major factors controlling inversion of the soil were:

   (a) Increasing the disc angle increased inversion.

   (b) Increasing the tilt angle decreased inversion.

7. The draught component decreased as the disc angle increased up to a particular value, or range of values, of disc angle slightly above the critical disc angle, dependent upon the concavity, radius and depth of the disc, at which point the draught force became a minimum. Further increases in disc angle resulted in an increase in the passive pressure area. The rate of increase in draught was reduced by the disappearance of the vertical bearing area and its scrubbing force.

8. The passive vertical component is developed on the concave side of the disc and was generally small and downwards. At small disc angles it was negated by large upward forces developed on the convex side bearing area. As the critical angle is approached this area falls to zero and the downwards passive forces create disc penetration into the soil.

9. The side forces due to the convex side decreased as the disc angle increased and increased at low disc angles with increasing tilt angle as the bearing area was increased. The side force passive component rose slowly above the critical disc angle as the disc angle increased.

10. The critical disc angle was controlled primarily by

the radius of the soil circle, the chord of the disc and the depth of work. However, a given disc at a fixed depth increased its critical disc angle as the tilt angle increased.

11. Speed changes had a smaller effect upon the measured forces than other variables. The average change being near a 27% force increase for a 100% speed increase. The relative force values were generally unchanged.

12. The depth of cut was a significant factor in the force generation of the agricultural disc. The relative force values, however, remained generally constant as the forces rise with increasing depth. A 75% increase in depth resulted in an overall increase in force of 92%.

CHAPTER 9

9. FURTHER STUDIES

1. Further investigation is required of the effect of sliding wedge compaction, as found under the convex side of the scrubbing disc so as to establish the dynamic characteristics of this type of bearing failure.

2. Further mathematical study of the areas and effective angles of the chamfered edge region of both inside and outside sharpened discs, at various stages of wear.

3. A study of the moments producing torque and hence rotation of the disc.

4. Further mathematical study of the soil volume disturbance on both the concave and convex sides of the disc in the horizontal plane.

REFERENCES

Abo El Eas, N.A.E.H. & Wills, B.M.D. (1986). An analysis of the geometric and soil working parameters of a curved vertical disc. Journal of Agricultural Engineering Research 35, pp. 277-286

Barnes, K.K., Bockhop, C.W. & McLead, H.E. (196). Similitude in studies of tillage implement forces. Agricultural Engineering 41(1), pp. 32-37, 42

Baver, L.D. (1932). The physical properties of soil of interest to agricultural engineering. Agricultural Engineering 13, pp. 324-327

Box, G.E.P. & Wilson, K.B. (1951). The experimental attainment of optimum conditions. Journal of the Royal Statistical Society. XIII No.1.

Boyd, R.J. & Nalezny, C.L. (1967). A model of vibratory soil cutting. Society of Automotive Engineers. Paper no. 670750, presented at the Farm Construction and Industrial Machinery Meeting, Milwaukee.

Chisholm, T.S. (1970). Three-dimensional interference between two tillage tools. Unpublished Ph.D. thesis Oklahoma State University, Stillwater, Oklahoma.

Cook, N.H. & Rabinowicz, E. (1963). Physical measurement and analysis. Addison-Wesley Publishing Co., New York.

Clyde, A.W. (1936). Measurement of forces on soil tillage tools. Agricultural Engineering 17(1), pp. 5-9

Clyde, A.W. (1937). Load studies on tillage tools. Agricultural Engineering 18(3), pp. 117-121

Clyde, A.W. (1939). Improvement of disc tools. Agricultural Engineering 20(6), pp. 215-221

Clyde, A.W. (1944). Technical features of tillage tools. Pennsylvania Agricultural Experiment Station Bulletin 465, Part 2.

Clyde, A.W. (1954). Pitfalls in applying the science of mechanics to tractor and implements. Agricultural Engineering 35(19), pp. 79-83

Clyde, A.W. & Tanquary, E.W. (1957). New principles in tractor hitch design. Agricultural Engineering 38, pp. 88-93

Gill, W.R. & Vanden Berg, G.E. (1968). Soil dynamics in tillage and traction. Agriculture handbook no. 316. Agricultural Research Service. United States Department of Agriculture.

Gill, W.R. & Hedrick, J.G. (1976). The irregularity of soil disturbance depth by circular and rotating tillage tools. American Society of Agricultural Engineers Transactions 19(2). pp. 230-232

Gill, W.R., Reaves, C.R. & Bailey, A.C. (1980a). The effect of geometric parameters on disc forces. American Society of Agricultural Engineers Transactions 23(2). pp. 266-269

Gill, W.R., Reaves, C.A. & Bailey, A.C. (1980b). The influence of velocity and disc angle on the kinematic parameter of discs. American Society of Agricultural Engineers Transactions 23(6). pp. 1344-1348

Gill, W.R., Reaves, C.A. & Bailey, A.C. (1981a). The influence of width and depth of cut on disc forces. American Society of Agricultural Engineers Transactions. 24(3). pp. 572-578

Gill, W.R., Reaves, C.A. & Bailey, A.C. (1981b). The influence of harrow disc curvature on forces. American Society of Agricultural Engineers Transactions. 24(3) pp. 579-583

Gill, W.R., Bailey, A.C. & Reaves, C.A. (1982). The influence of harrow disc curvature on soil penetration. American Society of Agricultural Engineers Transactions 25, pp. 1173-1179

Godwin, R.J. (1974). An investigation into the mechanics of narrow tines in frictional soil. Ph.D. thesis. University of Reading.

Godwin, R.J. (1975). An extended octagonal ring transducer for use in tillage studies. Journal of Agricultural Engineering Research 20(4), pp. 347-352

Godwin, R.J. & Spoor, G. (1977). Soil failure with narrow tines. Journal of Agricultural Engineering Research 22, pp. 213-228

Godwin, R.J., Spoor, G. & Kilgour, J. (1980). The design and operation of a simple low cost soil bin. Journal of Agricultural Engineering Research 25, pp. 99-104

Godwin, R.J., Seig, D.A. & Allott, M. (1987). Soil failure and force prediction for soil engaging discs. Soil Use and Management 3(3), pp. 106-114

Gorden, E.D. (1941). Physical reaction of soil on plow disks. Agricultural Engineering 22(6), pp. 205-208

Gupta, C.P. & Pandya, A.C. (1967). Behaviour of soil under dynamic loading: its application to tillage implements. American Society of Agricultural Engineers Transactions 10, pp. 352-358, 363

Harrison and Thivavarnvongs (1976). Soil reaction forces from laboratory measurements with discs. Canadian Journal of Agricultural Engineering 18(1),pp. 49-53

Hendrick, J.G. & Buchele, W.F. (1963). Tillage energy of a vibrating tillage tool. American Society of Agricultural Engineers Transactions 6(3), pp. 213-216

Hettiaratchi, D.R.P., Witney, D.B. & Reece, A.R. (1966). The calculation of passive pressure in two dimensional soil failure. Journal of Agricultural Engineering Research 11, pp. 89-107

Hettiaratchi, D.R.P. & Reece, A.R. (1967). Symmetrical three dimensional soil failure. Journal of Terramechanics 4, pp. 45-67

Hettiaratchi, D.R.P. & Reece, A.R. (1974). The calculation of passive soil resistance. Geotechnique 24, pp. 289-310

Ingersoll, R.C. (1926). The development of the disc plow. Agricultural Engineering 7(5), pp. 172-175

Johnston, R.C.R. & Birtwistle, R. (1963). Wheatland disc plough investigations. II. Disc forces. Journal of Agricultural Engineering Research 8(4), pp. 312-326

Kepner, R.A., Bainer, R. & Barger, K.L. (1978). Principles of farm machinery. 5th ed. Avi Publishing Co. Inc., Westport, Connecticut.

Lamb, T.W. & Whitman, R.V. (1969). Soil mechanics. John Wiley & Sons, New York.

McCreery, W.F. & Nichols, M.L. (1956). The geometry of discs and soil relationships. Agricultural Engineering 37, pp. 808-812, 820

McFarland, I.H. & Dimff, J. (1956). Problems involved in precision measurements with resistance strain gages. Agard Report 12, 8th Meeting of the Wind Tunnel and Model Testing Panel, 20th - 25th February. Rome

Meyerhof, G.G. (1961). The ultimate bearing capacity of wedge shaped foundations. Proc. 5th International Conference on Soil Mechanics and Foundation Engineering Vol. 11. Division 313, Dunod, Paris.

Morling, R.V. (1963). Soil force analysis as applied to tillage equipment. American Society of Agricultural Engineers Annual Meeting. Paper 63-149

Murphy, G. (1950). Similitude in engineering. Ronald Press Company.

Nichols, M.L. (1930). Dynamic properties of soil affecting implement design. Agricultural Engineering 11(6), pp. 201-204

Nichols, M.L. (1931). The dynamic properties of soils. II. Soil and metal friction. Agricultural Engineering 12, pp. 321-324

Nichols, M.L. (1931). The dynamics of soil I. An explanation of the dynamic properties of soils by means of colloidal films. Agricultural Engineering 12,pp. 259-264

O'Callaghan, J.R. & Farelly, K.M. (1964). Cleavage of soil by tined implements. Journal of Agricultural Engineering Research 9, pp. 259-270

O'Callaghan, J.R. & McCoy, J.G. (1965). The handling of soil by mouldboard ploughs. Journal of Agricultural Engineering Research 10, pp. 23-25

Payne, P.C.J. & Fountain, E.R. (1954). The mechanism of scouring for cultivation implements. Technical Memorandum no. 116. National Institute of Agricultural Engineering, Silsoe, Bedford

Payne, P.C.J. (1956). The relationship between the mechanical properties of soil and the performance of simple cultivation implements. Journal of Agricultural Engineering Research 1(1), pp. 23-50

Rogers, D.J.J. (1955). Soil loads on plough bodies. Technical Memorandum no. 105. National Institute of Agricultural Engineering, Silsoe, Bedford

Seig, D.A.T. (1982). An investigation into the forces acting on plough share points. M.Sc. Thesis, National College of Agricultural Engineering, Silsoe, Bedford

Siemens, J.C. (1963). Principles of soil mechanics. Addison-WEsley Pub. Co. Inc., Reading, Massachusetts

Siemens, J.C., Weber, J.A. & Thornborn, T.H. (1965). Mechanics of soil as influenced by model tillage tools. American Society of Agricultural Engineers Transactions 8(1), pp. 1-7

Spoor, G. (1969a). Design of soil engaging implements. Farm Machine Design Engineering 3. Sept., pp. 22-25

Spoor, G. (1969b). Design of soil engaging implements. Farm Machine Design Engineering 3 Dec, p. 14

Steel, R.G.P. & Torrie, J.H. (1960). Principles and procedures of statistics. McGraw-Hill Book Co. Inc., New York.

Tanner, D.W. (1960). Further work on the relationship between rake angle and the performance of simple cultivation implements. Journal of Agricultural Engineering Research 3, pp. 307-313

Taylor, P.A. (1967). Field measurements of forces and moments on wheatland plough discs. American Society of Agricultural Engineers Transactions 10(6), pp. 762-768, 770

Terzaghi, K. (1943). Theoretical soil mechanics. John Wiley & Sons, New York.

T A B L E S

Table 3.1. Soil mechanical analysis (Pipette method)

Fraction	Rep.1	Rep.2	Rep.3	Mean
Coarse sand	7.0145	10.5108	8.5391	8.68
Sand	33.1818	39.82	40.0558	37.68
Fine sand	25.7839	18.2649	20.7773	21.61
Silt	21.7908	22.3123	19.9767	21.36
Clay	12.229	9.0916	10.651	10.67
Mean %	100	99.99	99.99	100

Sand 67.98%

Silt 21.36%

Clay 10.66%

Hence, the soil bin soil is a sandy loam by the International Society of Soil Science Classification

Table 4.2. Critical disc and critical tilt angles at different tilt angles by Equation 4.4. and 4.8. respectively

Depth mm	Tilt angle deg.	Critical tilt angles obtained by Eq. 4.8. deg.	Critical disc angles obtained by Eq. 4.4. deg.
60	0	25.83	16.08
80	0	25.83	18.1
100	0	25.83	19.72
120	0	25.83	21.05
140	0	25.83	22.15
160	0	25.83	23.07
180	0	25.83	23.82
60	10	25.83	17.56
80	10	25.83	19.61
100	10	25.83	21.22
120	10	25.83	22.50
140	10	25.83	23.53
160	10	25.83	24.35
180	10	25.83	24.99
60	15	25.83	18.68
80	15	25.83	20.76
100	15	25.83	22.37
120	15	25.83	23.62
140	15	25.83	24.59
160	15	25.83	25.35
180	15	25.83	25.93

Radius of curvature, R = 700 mm

Disc diameter = 610 mm

Table 4.2. (cont'd)

Depth mm	Tilt angle deg.	Critical tilt angle obtained by Eq. 4.8. deg.	Critical disc angle obtained by Eq. 4.4. deg.
60	20	25.83	20.12
80	20	25.83	22.24
100	20	25.83	23.83
120	20	25.83	25.03
140	20	25.83	25.94
160	20	25.83	26.62
180	20	25.83	27.1
60	30	25.83	24.34
80	30	25.83	26.46
100	30	25.83	27.92
120	30	25.83	28.93
140	30	25.83	29.59
160	30	25.83	29.99
180	30	25.83	30.18
60	35	25.83	27.36
80	35	25.83	29.39
100	35	25.83	30.69
120	35	25.83	31.5
140	35	25.83	31.95
160	35	25.83	32.13
180	35	25.83	32.08

Radius of curvature, R = 700 mm

Disc diameter = 610 mm

Table 4.3. Critical depth at different tilt angles determined by Equation 4.5. in cm.

Disc angle deg.	Tilt angle deg.	Critical depth obtained by Eq. 4.5. cm.
0	0	0
5	0	0.58
10	0	2.38
15	0	5.59
20	0	10.77
0	20	0
5	20	0.4
10	20	1.72
15	20	3.97
20	20	7.43
0	30	0
5	30	0.32
10	30	1.3
15	30	2.99
20	30	5.51
0	35	0
5	35	0.27
10	35	1.11
15	35	2.54
20	35	4.64

Disc diameter = 61 cm

Radius of curvature = 70 cm

Depth of cut = 14 cm

Table 4.4. Rake angle values at different tilt angles obtained by Equation 4.14

Depth mm	Tilt angle deg.	Rake angle obtained by Eq. 4.14. deg.
60	0	66.84
80	0	67.71
100	0	68.57
120	0	69.42
140	0	70.27
160	0	71.12
180	0	71.94
60	20	47.50
80	20	48.54
100	20	49.55
120	20	50.54
140	20	51.50
160	20	52.46
180	20	53.39
60	30	38.15
80	30	26.46
100	30	40.48
120	30	41.59
140	30	42.66
160	30	43.69
180	30	44.7

Radius of curvature, R = 700 mm

Disc diameter = 610 mm

Table 4.4. (cont'd)

Depth mm	Tilt angle deg.	Rake angle obtained by Eq. 4.14. deg.
60	35	33.61
80	35	34.9
100	35	36.13
120	35	37.3
140	35	38.43
160	35	39.52
180	35	40.57

Radius of curvature, R = 700 mm

Disc diameter = 610 mm

Table 4.6. Vertical pressure area, Ap in $cm.^2$ at different tilt angles obtained by Equation 4.17.

Disc angle deg.	Tilt angle deg.	Values obtained by Eq. 4.17. cm^2
0	0	0
5	0	44.12
10	0	87.91
15	0	131.03
20	0	173.15
0	10	0
5	10	44.4
10	10	88.47
15	10	131.86
20	10	174.25
0	20	0
5	20	45.27
10	20	90.21
15	20	134.45
20	20	177.68
0	30	0
5	30	46.81
10	30	93.26
15	30	139.01
20	30	183.7

Disc diameter = 61 cm

Depth of cut = 14 cm

Radius of curvature = 70 cm

Table 4.6. (cont'd)

Disc angle deg.	Tilt angle deg.	Values obtained by Eq. 4.17. cm^2
0	35	0
5	35	47.86
10	35	95.36
15	35	142.14
20	35	187.85

Disc diameter = 61 cm

Depth of cut = 14 cm

Radius of curvature = 70 cm

Table 4.8. Vertical bearing area at different tilt angles in cm^2 obtained by Equation 4.27.

Disc angle deg.	Tilt angle deg.	Values determined by Eq. 4.27. cm^2
0	0	39.08
5	0	20.62
10	0	8.71
15	0	2.31
20	0	0.115
0	10	42.54
5	10	23.41
10	10	10.66
15	10	3.36
20	10	0.37
0	20	49.1
5	20	28.75
10	20	14.53
15	20	5.67
20	20	1.23
0	30	60.35
5	30	38.0
10	30	21.53
15	30	10.30
20	30	3.61

Radius of curvature, R = 70 cm

Depth of cut, d = 14 cm

Disc diameter = 61 cm

Table 4.8. (cont'd)

Disc angle deg.	Tilt angle deg.	Values determined by Eq. 4.27. $cm.^2$
0	35	68.61
5	35	44.83
10	35	26.84
15	35	14.06
20	35	5.87

Radius of curvature, R = 70 cm

Depth of cut, d = 14 cm

Disc diameter = 61 cm

Table 4.9. Horizontal bearing area at different tilt angles obtained by Equation 4.29. in cm^2

Disc angle deg.	Tilt angle deg.	Values obtained by Eq. 4.29. cm^2
0	0	86.53
5	0	40.65
10	0	14.65
15	0	2.99
20	0	0.082
0	10	93.14
5	10	46.08
10	10	18.11
15	10	4.57
20	10	3.25
0	20	106.58
5	20	56.87
10	20	25.37
15	20	8.27
20	20	1.33
0	30	129.41
5	30	75.51
10	30	38.71
15	30	16.16
20	30	4.62

Radius of curvature, R = 70 cm

Depth of cut, d = 14 cm

Disc diameter = 61 cm

Table 4.9. (cont'd)

Disc angle deg.	Tilt angle deg.	Values obtained by Eq. 4.29. cm^2
0	35	145.55
5	35	88.94
10	35	48.78
15	35	22.73
20	35	8.03

Radius of curvature, R = 70 cm

Depth of cut, d = 14 cm

Disc diameter = 61 cm

Table 4.10. Horizontal pressure area at different tilt angles determined by Equation 4.30. in $cm.^2$

Disc angle deg.	Tilt angle deg.	Values determined by Eq. 4.30. $cm.^2$
0	0	0
5	0	91.75
10	0	143.88
15	0	167.07
20	0	172.89
0	10	0
5	10	94.13
10	10	150.06
15	10	177.15
20	10	185.64
0	20	0
5	20	99.4
10	20	162.41
15	20	196.62
20	20	210.50
0	30	0
5	30	107.78
10	30	181.40
15	30	226.49
20	30	249.56

Radius of curvature, R = 70 cm

Depth of cut, d = 14 cm

Disc diameter = 61 cm

Table 4.10. (cont'd)

Disc angle deg.	Tilt angle deg.	Values determined by Eq. 4.30. cm^2
0	35	0
5	35	113.21
10	35	193.54
15	35	245.64
20	35	275.03

Radius of curvature, R = 70 cm

Depth of cut, d = 14 cm

Disc diameter = 61 cm

Table 4.11. Horizontal area at different tilt angles determined by Equation 4.32. in cm^2.

Depth cm	Tilt angle deg.	Values calculated by Eq. 4.32. cm^2
0	0	0
6	0	62.41
10	0	118.89
14	0	173.05
16	0	197.53
18	0	219.63
0	10	0
6	10	69.20
10	10	129.86
14	10	186.29
16	10	211.12
18	10	233.06
0	20	0
6	20	83.02
10	20	152.1
14	20	213.16
16	20	238.78
18	20	260.53
0	30	0
6	30	108.73
10	30	191.6

Radius of curvature, R = 70 cm

Disc diameter = 61 cm

Table 4.11. (cont'd)

Depth cm	Tilt angle deg.	Values calculated by Eq. 4.32. $cm.^2$
14	30	258.82
16	30	284.65
18	30	304.86
0	35	0
6	35	129.08
10	35	221.18
14	35	291.11
16	35	316.06
18	35	334.08

Radius of curvature, R = 70 cm

Disc diameter = 61 cm

Table 4.12. Inclination area at different tilt angles determined by Equation 4.33. in cm^2

Depth cm	Tilt angle deg.	Inclination area obtained by Eq. 4.33. cm^2
0	0	0
6	0	0
10	0	0
14	0	0
16	0	0
18	0	0
0	10	0
6	10	26.36
10	10	55.49
14	10	89.83
16	10	108.45
18	10	127.82
0	20	0
6	20	55.62
10	20	116.95
14	20	189.08
16	20	228.10
18	20	268.65
0	30	0
6	30	91.64
10	30	192.27

Disc diameter = 61 cm

Radius of curvature = 70 cm

Table 4.12. (cont'd)

Depth cm	Tilt angle deg.	Inclination area obtained by Eq. 4.33. cm^2
14	30	310.09
16	30	373.59
18	30	439.38
0	35	0
6	35	114.04
10	35	238.87
14	35	384.55
16	35	462.83
18	35	543.74

Disc diameter = 61 cm

Radius of curvature = 70 cm

Table 4.13. Loading area at different tilt angles obtained by Equation 4.34. in cm^2

Depth cm	Tilt angle deg.	Loading area determined by Eq. 4.34. cm^2
0	0	0
6	0	62.41
10	0	118.89
14	0	173.05
16	0	197.53
18	0	219.63
0	10	0
6	10	95.56
10	10	185.36
14	10	276.13
16	10	319.57
18	10	360.89
0	20	0
6	20	138.65
10	20	269.05
14	20	402.25
16	20	466.88
18	20	529.18
0	30	0
6	30	200.36
10	30	383.88

Radius of curvature, R = 70 cm

Disc diameter = 61 cm

Table 4.13. (cont'd)

Depth cm	Tilt angle deg.	Loading area determined by Eq. 4.34. cm^2
14	30	568.92
16	30	658.25
18	30	744.25
0	35	0
6	35	243.13
10	35	460.06
14	35	675.66
16	35	778.89
18	35	877.83

Radius of curvature, R = 70 cm

Disc diameter = 61 cm

Table 5.1. Determination of values of gang area at different disc and tilt angles, by Equation 5.17, in m^2

Disc angle deg.	Gang Spacing (m)	Gang area (m^2)at a depth = 0.14 m			
		Tilt angle, deg.			
		0	20	30	35
15	0.12	0.004287	0.004566	0.004959	0.005246
20	0.13	0.006121	0.006521	0.007084	0.007495
25	0.14	0.008124	0.008655	0.009405	0.00995
30	0.16	0.010917	0.011636	0.012649	0.01338
35	0.18	0.013991	0.0149186	0.016227	0.0171824
40	0.19	0.016486	0.017584	0.019138	0.02026
45	0.2	0.019013	0.020283	0.02207	0.02338
55	0.22	0.024013	0.025633	0.027916	0.029584
60	0.24	0.027422	0.02929	0.03192	0.033846

disc diameter = 0.61 m

depth of operation = 0.14 m

radius of curvature = 0.7 m

Table 5.2. Determination of gang area at different disc and tilt angles and different depths obtained by Equation 5.17, in m^2

Disc Angle Deg.	Gang area (m^2) at a depth = 0.1 m					Gang area (m^2) at a depth = 0.08 m				
	Gang Spacing (m)	Tilt angle, deg.				Gang Spacing (m)	Tilt angle, deg.			
		0	20	30	35		0	20	30	35
15	0.11	0.002799	0.002982	0.003240	0.003428	0.1	0.002035	0.002168	0.002355	0.002492
30	0.13	0.006348	0.006766	0.007354	0.007784	0.12	0.004681	0.004989	0.005424	0.005741
35	0.14	0.007813	0.008328	0.009055	0.009586	0.13	0.005792	0.006175	0.006715	0.00711
40	0.15	0.009343	0.009961	0.010834	0.011471	0.135	0.006724	0.007169	0.007789	0.008257
60	0.20	0.0163	0.017469	0.019037	0.020182	0.18	0.011771	0.012572	0.01370	0.014525

disc diameter = 0.61 m

radius of curvature = 0.7 m

Table 7.1. Results of tests for shallow outside sharpening disc at different disc and tilt angles at a depth of 140 mm

Disc angle, ^{o}	Tilt angle 0^{o}				Tilt angle 20^{o}				Tilt angle 30^{o}				Tilt angle 35^{o}			
	Force kN				Force kN				Force kN				Force kN			
	D	V	S	$\bar{R}$	D	V	S	$\bar{R}$	D	V	S	$\bar{R}$	D	V	S	$\bar{R}$
15	1.1	-1.58	-0.62	2.02	1.31	-2.45	-0.42	2.81	1.41	-3.0	-0.4	3.33	1.84	-4.2	-0.47	4.61
20	0.9	-1.01	0.2	1.36	1.16	-1.58	+0.14	1.96	1.33	-2.08	-0.13	2.47	1.37	-2.45	-0.12	2.81
25	1.01	-0.73	0.7	1.43	0.99	-1.03	0.29	1.45	1.32	-1.53	0.5	2.08	1.28	-1.86	0.57	2.33
30	0.989	-0.45	1.02	1.49	1.042	-0.784	0.41	1.65	1.13	-1.08	0.32	1.59	1.27	-1.31	0.49	1.89
35	0.88	-0.16	1.1	1.42	1.01	-0.40	0.61	1.62	1.01	-0.73	0.42	1.31	1.3	-1.08	0.51	1.77
40	1.13	-0.24	1.2	1.66	1.1	-0.13	1.35	1.75	1.09	0.57	0.42	1.3	1.31	-0.81	0.55	1.64
45	1.16	-0.19	1.2	1.68	1.00	0.23	1.4	1.73	1.6	0.33	1.16	2.00	1.26	-0.44	0.61	1.47
55	1.8	-0.13	1.6	2.41	1.5	0.33	1.35	2.04	1.66	0.34	1.14	2.04	1.65	0.4	0.93	1.93
60	1.88	-0.12	1.5	2.41	1.7	0.29	1.21	2.11	1.81	0.82	1.1	2.27	2.0	0.92	0.9	2.38

D = Draught

V = Vertical

S = Side

$\bar{R}$ = Resultant

Table 7.2. Results of tests for shallow inside sharpening disc at different disc and tilt angles at a depth of 140 mm

Disc angle ^{O}	Tiltangle 0^{O}				Tiltangle 20^{O}				Tiltangle 30^{O}				Tilt angle 35^{O}			
	Force kN				Force kN				Force kN				Force kN			
	D	V	S	$\bar{R}$	D	V	S	$\bar{R}$	D	V	S	$\bar{R}$	D	V	S	$\bar{R}$
15	0.66	-0.675	-0.88	1.29	1.21	-2.1	-0.846	2.57	1.27	-2.79	-0.81	3.17	1.86	-4.55	-0.923	5.00
20	0.79	-0.467	1.18	1.49	0.74	-0.389	0.544	0.99	0.813	-1.03	-0.135	1.32	1.62	-3.05	-0.592	3.5
25	0.845	-0.378	1.14	1.47	0.74	-0.248	0.85	1.15	0.72	0.046	0.91	1.66	0.926	-0.213	0.879	1.29
30	0.949	-0.336	1.17	1.54	0.966	-0.15	1.006	1.4	0.687	0.092	0.75	1.37	0.873	-0.088	0.86	1.23
35	1.01	-0.409	1.14	1.78	0.919	-0.097	1.11	1.44	1.01	0.379	1.00	1.47	0.959	-0.18	0.88	1.31
40	1.15	-0.336	1.16	1.66	1.12	-0.055	1.02	1.51	1.03	0.176	1.3	1.66	1.002	0.276	0.936	1.39
45	1.29	-0.216	1.37	1.89	1.33	0.086	1.001	1.66	1.3	0.372	1.5	2.09	1.29	0.39	1.17	1.78
55	1.59	-0.151	1.39	2.12	1.53	0.137	1.17	1.93	1.42	0.47	1.06	1.83	1.32	0.46	0.997	1.71
60	2.21	-0.212	1.88	2.9	1.75	0.177	1.13	2.09	2.1	0.51	1.64	2.71	1.99	0.64	1.42	2.53

D = Draught

V = Vertical

S = Side

$\bar{R}$ = Resultant

Table 7.3. Results of tests for deep outside sharpening disc at different disc and tilt angles at a depth of 140 mm

Disc angle, ^{o}	Tilt angle 0^{o}				Tilt angle 20^{o}				Tilt angle 30^{o}			
	Force KN				Force KN				Force KN			
	D	V	S	$\bar{R}$	D	V	S	$\bar{R}$	D	V	S	$\bar{R}$
40	1.014	-0.35	0.736	1.3	1.03	-0.644	0.382	1.27	1.26	-1.07	0.424	1.7
45	1.11	-0.06	0.975	1.47	1.02	-0.379	0.669	1.28	1.2	-0.901	0.544	1.59
55	1.51	0.062	1.22	1.94	1.4	0.284	0.968	1.72	1.45	-0.273	0.666	1.57
60	1.92	0.444	0.974	2.19	1.53	0.348	0.899	1.81	1.5	0.131	0.595	1.62

D = Draught

V = Vertical

S = Side

$\bar{R}$ = Resultant

Table 7.4. Results of tests for deep inside sharpening disc at different disc and tilt angles at a depth of 140 mm

Disc angle, ^{o}	Tilt angle 0^{o}				Tilt angle 20^{o}				Tilt angle 30^{o}			
	Force KN				Force KN				Force KN			
	D	V	S	$\bar{R}$	D	V	S	$\bar{R}$	D	V	S	$\bar{R}$
35	0.916	-0.199	1.08	1.43	0.805	-0.62	0.739	1.26	1.3	-0.9	-0.108	1.91
40	1.08	-0.223	1.13	1.57	0.784	-0.52	0.869	1.28	1.11	-0.7	0.801	1.53
45	1.14	-0.138	1.13	1.61	0.955	-0.3	0.847	1.31	1.07	-0.4	0.718	1.34
55	1.48	-0.099	1.38	1.99	1.36	0.193	1.12	1.77	1.43	-0.2	0.966	1.73
60	1.89	-0.075	1.01	2.14	1.46	0.26	0.839	1.7	1.53	0.11	0.683	1.78

D = Draught

V = Vertical

S = Side

$\bar{R}$ = Resultant

Table 7.5. *Results of tests for shallow outside and inside* sharpening discs at combinations of disc and tilt angles at various depths

تاريخ mm	Disc angle 15°, Tilt angle 0°				Disc angle 15°, Tilt angle 35°				Disc angle 30°, Tilt angle 20°				Disc angle 60°, Tilt angle 0°				Disc angle 60°, Tilt angle 35°			
	Force kN				Force kN				Force kN				Force kN				Force kN			
	D	V	S	R̄	D	V	S	R̄	D	V	S	R̄	D	V	S	R̄	D	V	S	R̄
Shallow outside																				
80	0.502	-0.77	0.23	0.95	0.726	-1.9	-0.073	2.03	0.453	-0.511	0.15	0.699	0.685	-0.087	0.512	0.86	0.535	0.091	0.229	0.58
100	0.722	-0.81	0.31	1.13	1.14	-2.62	-0.262	2.87	0.606	-0.71	0.151	0.945	0.85	-0.093	0.648	1.07	0.608	0.109	0.334	0.70
140	1.09	-1.41	0.487	1.85	1.96	-4.23	-0.76	4.72	0.921	-0.824	0.312	1.27	1.54	-0.121	1.19	1.95	0.944	0.238	0.526	1.11
Shallow inside																				
80	0.301	-0.4	0.23	0.57	0.74	-2.03	-0.38	2.24	0.352	-0.069	0.33	0.63	0.84	-0.091	0.623	1.05	0.594	0.147	0.416	0.74
100	0.361	-0.447	0.284	0.64	1.11	-2.89	-0.612	3.15	0.442	-0.084	0.512	0.68	1.02	-0.104	0.733	1.26	0.784	0.157	0.483	0.93
140	0.56	-0.498	0.234	0.8	1.87	-4.41	-1.04	4.9	0.653	-0.108	0.707	0.97	1.82	-0.116	1.4	2.29	1.1	0.221	0.747	1.34

D = Draught

V = Vertical

S = Side

R̄ = Resultant

Table 7.6. Results of tests for deep outside and inside sharpening discs at combinations of disc and tilt angles at different depths

Depth mm	Disc angle 35°, Tilt angle 30°				Disc angle 40°, Tilt angle 20°				Disc angle 60°, Tilt angle 0°				Disc angle 60°, Tilt angle 30°			
	Force kN				Force kN				Force kN				Force kN			
	D	V	S	R̃	D	V	S	R̃	D	V	S	R̃	D	V	S	R̃
Deep outside																
80	0.578	-0.798	0.153	0.997	0.534	-0.62	0.11	0.825	0.516	-0.033	0.495	0.72	0.551	-0.15	0.24	0.62
100	0.737	-0.947	0.174	1.24	0.782	-0.86	0.134	1.17	0.689	-0.104	0.533	0.88	0.791	-0.18	0.262	0.85
140	1.54	-1.56	0.303	2.21	1.21	-0.984	0.31	1.59	1.38	-0.119	1.1	1.7	1.12	-0.4	0.424	1.26
Deep inside																
80	0.481	-0.967	0.24	1.1	0.412	-0.051	0.328	0.523	0.659	-0.031	0.47	0.81	0.583	-0.143	0.439	0.74
100	0.578	-1.04	0.269	1.22	0.516	-0.065	0.428	0.67	0.734	-0.04	0.504	0.89	0.775	-0.176	0.5	0.94
140	1.3	-1.13	0.377	1.76	0.861	-0.077	0.712	1.12	1.46	-0.05	1.06	1.3	1.19	-0.331	0.714	1.4

D = Draught

V = Vertical

S = Side

R̃ = Resultant

Table 7.7. Results of tests for shallow outside and inside sharpening discs at combinations of disc and tilt angles at different speeds at a depth of 140 mm

Speed m/sec	Disc angle 15°, Tilt angle 0°				Disc angle 15°, Tilt angle 35°				Disc angle 30°, Tilt angle 20°				Disc angle 60°, Tilt angle 0°				Disc angle 60°, Tilt angle 35°			
	Force kN				Force kN				Force kN				Force kN				Force kN			
	D	V	S	$\bar{R}$	D	V	S	$\bar{R}$	D	V	S	$\bar{R}$	D	V	S	$\bar{R}$	D	V	S	$\bar{R}$
Shallow outside																				
.75	1.12	-1.7	-0.146	2.04	2.67	-4.22	-1.12	5.11	1.05	-0.832	+0.408	1.4	1.88	0.103	1.58	2.46	1.12	0.499	0.80	1.46
1.0	1.19	-1.06	-0.233	1.61	2.99	-4.59	-1.39	5.65	1.06	-0.765	+0.497	1.39	2.09	0.131	1.67	2.67	1.164	0.461	0.921	1.55
1.5	1.28	-1.56	-0.407	2.05	3.23	-4.63	-1.66	5.88	1.095	-0.736	+0.548	1.43	2.76	0.218	+2.16	3.51	1.4	0.697	1.0	1.85
Shallow inside																				
.75	0.6	-0.627	0.103	0.87	2.0	-3.54	-1.31	4.27	0.531	+0.01	0.896	1.04	2.0	0.03	1.42	2.45	1.07	0.476	0.782	1.41
1.0	0.62	-0.635	0.119	0.89	2.21	-3.67	-1.42	4.51	0.685	+0.015	0.962	1.18	2.04	0.042	1.67	2.57	1.17	0.546	0.87	1.56
1.5	0.66	-0.646	0.165	0.94	2.25	-3.8	-1.55	4.68	0.983	+0.25	1.22	1.58	2.97	0.088	1.92	3.54	1.59	0.686	1.14	2.07

D = Draught

V = Vertical

S = Side

$\bar{R}$ = Resultant

Table 7.8. Results of tests for deep outside and inside sharpening discs at combinations of disc and tilt angles at different speeds at a depth of 140 mm

Speed m/sec	Disc angle 35°, Tilt angle 30°				Disc angle 40° Tilt angle 20°				Disc angle 60°, Tilt angle 0°				Disc angle 60°, Tilt angle 30°			
	Force kN				Force kN				Force kN				Force kN			
	D	V	S	R	D	V	S	R	D	V	S	R	D	V	S	R
Deep outside																
.75	1.62	-1.41	0.577	2.22	1.32	-0.801	0.481	1.62	1.48	0.233	1.3	1.98	1.27	0.2	0.712	1.47
1.0	1.64	-1.48	0.634	2.29	1.39	-0.87	0.543	1.72	1.7	0.317	1.33	2.18	1.39	0.24	0.822	1.63
1.5	2.04	-1.9	0.734	2.88	1.42	-0.876	0.581	1.77	2.61	0.368	1.38	2.46	1.49	0.345	0.845	1.75
Deep inside																
.75	1.29	-0.751	0.171	1.5	0.926	0.067	0.932	1.31	1.67	0.093	1.33	2.14	1.07	0.476	0.782	1.41
1.0	1.37	-0.858	0.233	1.63	0.962	0.147	0.941	1.35	1.71	0.137	1.39	2.2	1.17	0.546	0.87	1.56
1.5	1.51	-0.937	0.319	1.83	1.12	0.272	1.16	1.63	1.95	0.257	1.67	2.58	1.59	0.686	1.14	2.13

D = Draught

V = Vertical

S = Side

$\bar{R}$ = Resultant

Table 7.9. Predicted values for shallow outside and inside sharpening discs at different disc and tilt angles at a depth of 140 mm

Disc angle ^{o}	Tilt angle 0^{o}				Tilt angle 20^{o}				Tilt angle 30^{o}				Tilt angle 35^{o}			
	Force kN				Force kN				Force kN				Force kN			
	D	V	S	$\bar{R}$	D	V	S	$\bar{R}$	D	V	S	$\bar{R}$	D	V	S	$\bar{R}$
15	0.82	-0.062	0.778	1.13	0.9	-0.134	0.43	1.01	0.917	-0.51	0.21	1.07	1.03	-0.89	0.08	1.36
20	0.42	0.024	1.11	1.19	0.896	0.223	0.794	1.22	0.86	0.104	0.579	1.04	0.9	0.237	0.50	1.05
25	0.64	0.025	1.36	1.5	0.477	0.379	1.02	1.19	0.8	0.430	0.82	1.22	0.85	0.389	0.72	1.17
30	0.9	0.03	1.55	1.79	0.685	0.45	1.19	1.44	0.57	0.58	0.98	1.27	0.511	0.62	0.87	1.18
35	1.19	0.035	1.69	2.07	0.92	0.54	1.32	1.69	0.77	0.69	1.09	1.5	0.688	0.73	0.98	1.4
40	1.51	0.039	1.8	2.35	1.18	0.61	1.4	1.93	0.98	0.79	1.17	1.72	0.88	0.84	1.05	1.6
45	1.84	0.04	1.84	2.6	1.45	0.69	1.46	2.17	1.22	0.88	1.22	1.94	1.1	0.94	1.1	1.82
55	2.51	0.052	1.75	2.8	2.01	0.824	1.41	2.59	1.69	1.06	1.18	2.32	1.51	1.13	1.06	2.16
60	2.82	0.055	1.63	3.25	2.29	0.88	1.32	2.78	1.92	1.14	1.1	2.49	1.72	1.21	0.99	2.32
Critical disc angle				22.15^{o}				25.95^{o}				29.6^{o}				31.9^{o}
Rake angle				70.3^{o}				51.51^{o}				42.7^{o}				38.4^{o}

D = Draught

V = Vertical

S = Side

$\bar{R}$ = Resultant

Table 7.10. Predicted values for deep outside and inside sharpening discs at various disc and tilt angles at a depth of 140 mm

Disc angle ^{o}	Tilt angle 0^{o}				Tilt angle 20^{o}				Tilt angle 30^{o}			
	Force				Force				Force			
	D	V	S	$\bar{R}$	D	V	S	$\bar{R}$	D	V	S	$\bar{R}$
35	0.954	-0.16	1.2	1.54	0.7	-0.49	0.89	1.23	0.57	0.56	0.72	1.07
40	1.21	-0.176	1.28	1.21	0.9	0.55	0.96	1.43	0.73	0.64	0.77	1.24
45	1.47	-0.199	1.3	1.97	1.11	0.62	0.98	1.60	0.91	0.72	0.8	1.41
55	2.02	-0.23	1.25	2.38	1.54	0.74	0.96	1.96	1.26	0.86	0.78	1.71
60	2.26	-0.25	1.16	2.55	1.73	0.8	0.89	2.1	1.44	0.93	0.73	1.86
Critical disc angle				29.92^{o}				35.6^{o}				40.59^{o}
Rake angle				63.9^{o}				45.99^{o}				37.81^{o}

D = Draught

V = Vertical

S = Side

$\bar{R}$ = Resultant

7.11. Predicted values for shallow outside and inside sharpening discs at combinations of disc and tilt angles at various depths

Depth mm	Disc angle 15°, Tilt angle 0°				Disc angle 15°, Tilt angle 35°				Disc angle 30°, Tilt angle 20°				Disc angle 60°, Tilt angle 0°				Disc angle 60°, Tilt angle 35°			
	Force kN				Force kN				Force kN				Force kN				Force kN			
	D	V	S	$\bar{R}$	D	V	S	$\bar{R}$	D	V	S	$\bar{R}$	D	V	S	$\bar{R}$	D	V	S	$\bar{R}$
80	0.47	-0.035	0.34	0.58	0.57	-0.51	-0.0457	0.76	0.4	-0.257	0.51	0.69	0.966	-0.031	0.71	1.19	0.784	0.5	0.42	1.02
100	0.58	-0.044	0.563	0.81	0.74	-0.635	-0.057	0.97	0.51	-0.32	0.85	1.04	1.85	-0.039	1.16	2.18	0.91	0.864	0.71	1.44
140	0.82	-0.062	0.778	1.13	1.03	-0.89	-0.08	1.36	0.685	-0.45	1.19	1.44	2.82	-0.055	1.63	3.25	1.72	1.21	0.99	2.32

D = Draught

V = Vertical

S = Side

$\bar{R}$ = Resultant

A P P E N D I C E S

APPENDIX 1

CALIBRATION OF TENSION LOAD CELLS

A1.1. Introduction

Due to the difficulty in calibrating the octagonal ring transducer for applying static weights in three principal directions at the load levels required, the three principal forces were applied simultaneously using hydraulic rams with load cells to record each applied load. Three tension load cells were used for the draught, vertical, and side forces to calibrate the transducer. The tension load cells were calibrated before they were used to calibrate the octagonal ring transducer.

The calibration of these cells have been used on static weight and on an Avery Universal testing machine. An amplifier with three channels was used to increase the signal level for the tension load cells. The low range of 1000 with a gain of 1000 was used for all the cells. The output from each of the three channels was recorded in Tables A1.1. and A1.2. when loaded both with static weights and the Universal testing machine respectively.

A1.2. Result of calibration

From Table A1.1., Table A1.2. and Figure A1.1. the

following results were observed:

i. Tension load cell for draught force = 0.0532 v/kN

ii. Tension load cell for vertical force = 1.32 v/kN

iii. Tension load cell for side force = 0.151 v/kN

Load kN	Tension load draught		Tension load vertical		Tension load side	
	Load	Unload	Load	Unload	Load	Unload
0	0	0	0.03	0.02	0.01	0.01
0.196	0.012	0.012	0.255	0.258	0.03	0.031
0.392	0.023	0.023	0.511	0.513	0.059	0.06
0.588	0.034	0.035	0.767	0.769	0.088	0.089
0.785	0.045	0.045	1.024	1.025	0.118	0.118
0.981	0.056	0.056	1.279	1.281	0.147	0.147
1.177	0.068		1.4		0.176	

Table A1.1. Bridge output static weight, v.

Load kN	Tension load draught		Tension load vertical		Tension load side	
	Load	Unload	Load	Unload	Load	Unload
0	0.002	0.001	0.03	0.03	0.02	0.02
1	0.054	0.056	1.35	1.39	0.17	0.18
2	0.105	0.011	2.61	2.69	0.32	0.33
3	0.162	0.166	3.96	4.06	0.47	0.48
4	0.213	0.218	5.33	5.3	0.64	0.63
5	0.268	0.27	6.62	6.63	0.78	0.78
6	0.322	0.325	7.9	8.03	0.91	0.94
7	0.37	0.371	9.13	9.13	1.06	1.07
8	0.427	0.429	10.55	10.59	1.21	1.24
9	0.479	0.483	11.75	11.95	1.36	1.39
10	0.532	0.537	13.22		1.5	1.54
11	0.587	0.587			1.67	1.69
12	0.638	0.641			1.81	1.84
13	0.691	0.697			1.95	1.99
14	0.746	0.751			2.11	2.15
15	0.797	0.805			2.26	2.3
16	0.853	0.862			2.41	2.43
17	0.906	0.912			2.56	2.6
18	0.962	0.967			2.12	2.75
19	1.017	1.017			2.88	2.89
20	1.066				3.02	

Table A1.2. Bridge output Universal testing machine, V.

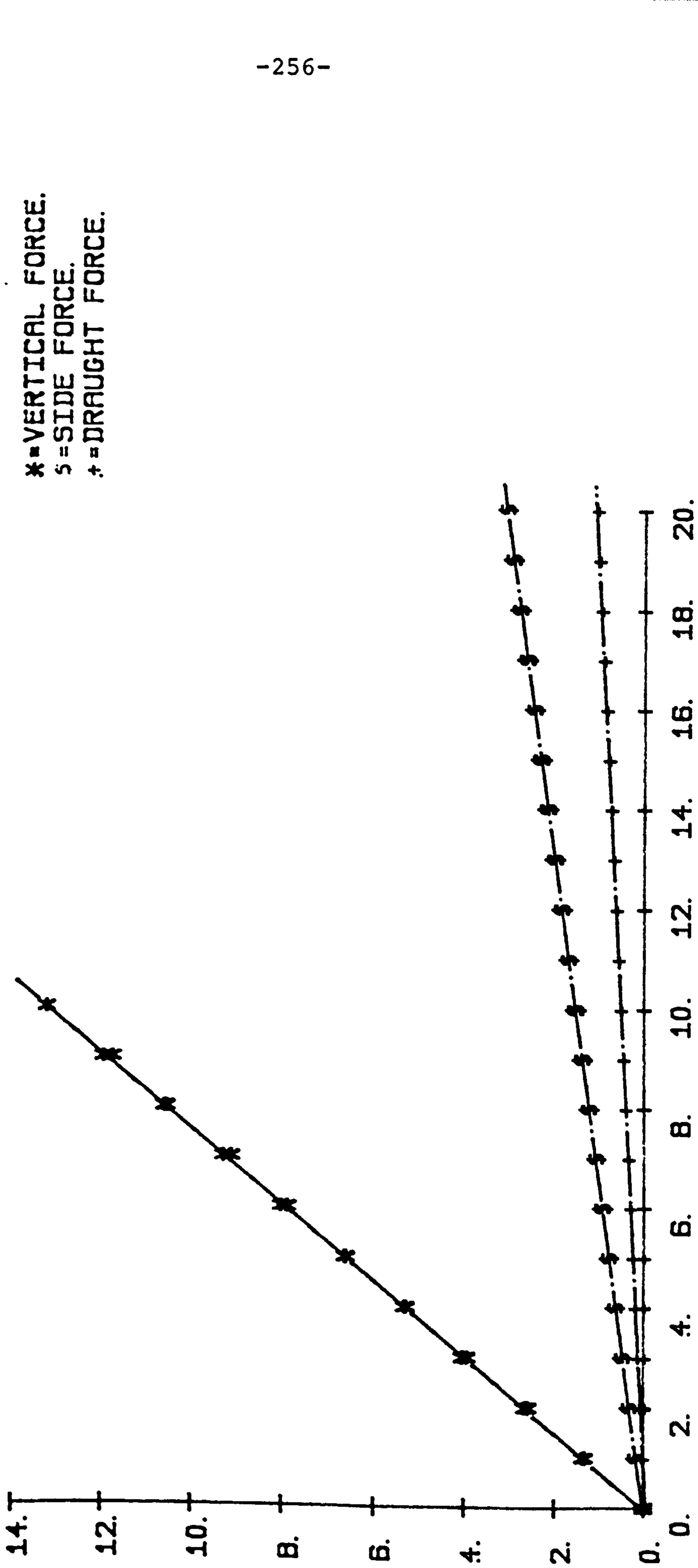

Figure A1.1. Tension load cells bridge output characteristics

APPENDIX 2

EXTENDED OCTAGONAL RING TRANSDUCER DESIGN

For the design of the octagonal transducer ring, it was decided to use as material an alloy steel, EN 24A, subsequently heat treated to an Ultimate Tensile Stress of 1132 MN/m^2 (73.3 ton/in^2) and Yield stress of 1052 MN/m^2 (68.1 ton/in^2) which gave high strength and produced a compact design. The modulus of elasticity was 206.8 GN/m^2 (30 x 10^6 lbf/in^2).

Detail of the design

Working stress = 558.63 MN/m^2

The largest size of an alloy steel of EN 24A stock readily available and requiring the least machining resulted in a K value of 3.3.

From Cook and Rabinowicz (1963), for K = 3.3, the following was determined.

The strain dimensionless group $\frac{\epsilon Ebt^2}{M}$ = 0.28 ....(A2.1)

The deflection dimensionless group $\frac{\emptyset Ebt^3}{Mr}$ = 0.12 ....(A2.2)

where:

$$K = \frac{L}{r}$$

2L = distance between the ring centres (165 mm)

r = ring radius (25 mm)

E = modulus of elasticity (206.7 GN/m^2)

b = transducer width (110 mm)

M = applied moment (91.19 kN.m)

σ = working stress

ϵ = strain

t = thickness of the ring

ϕ = angular deflection in radians

For a perfectly elastic material $E = \frac{\sigma}{\epsilon}$ hence, Equation A2.1. becomes:

$$\frac{\sigma bt^2}{M} = 0.28 \qquad \text{.....(A2.3.)}$$

which solving for t using the design working stress gives a thickness of ring of 30 mm.

The transducer deflection from Equation A2.2. is 4.46×10^{-4} radians (0.026^{o}).

For determining the rotation of the tube at 45^{o} after the recommendation of Cook and Rabinowicz (1963), the following formula was used:

$$\phi = \frac{2ML}{\pi G(ro^4 - ri^4)} \qquad \text{.....(A2.4)}$$

where:

ϕ = the rotation in radians

M = applied moment (91.19 kN.m)

L = length of the tube (50 mm)

ro = outer radius (85 mm)

ri = inner radius (55 mm)

G = shear modulus (8.268×10^{10} N/m^2)

based on the above the rotation of the tube is 8.13287×10^{-3} radians (0.04^{o}).

The working drawing is shown in Figure A2.1.

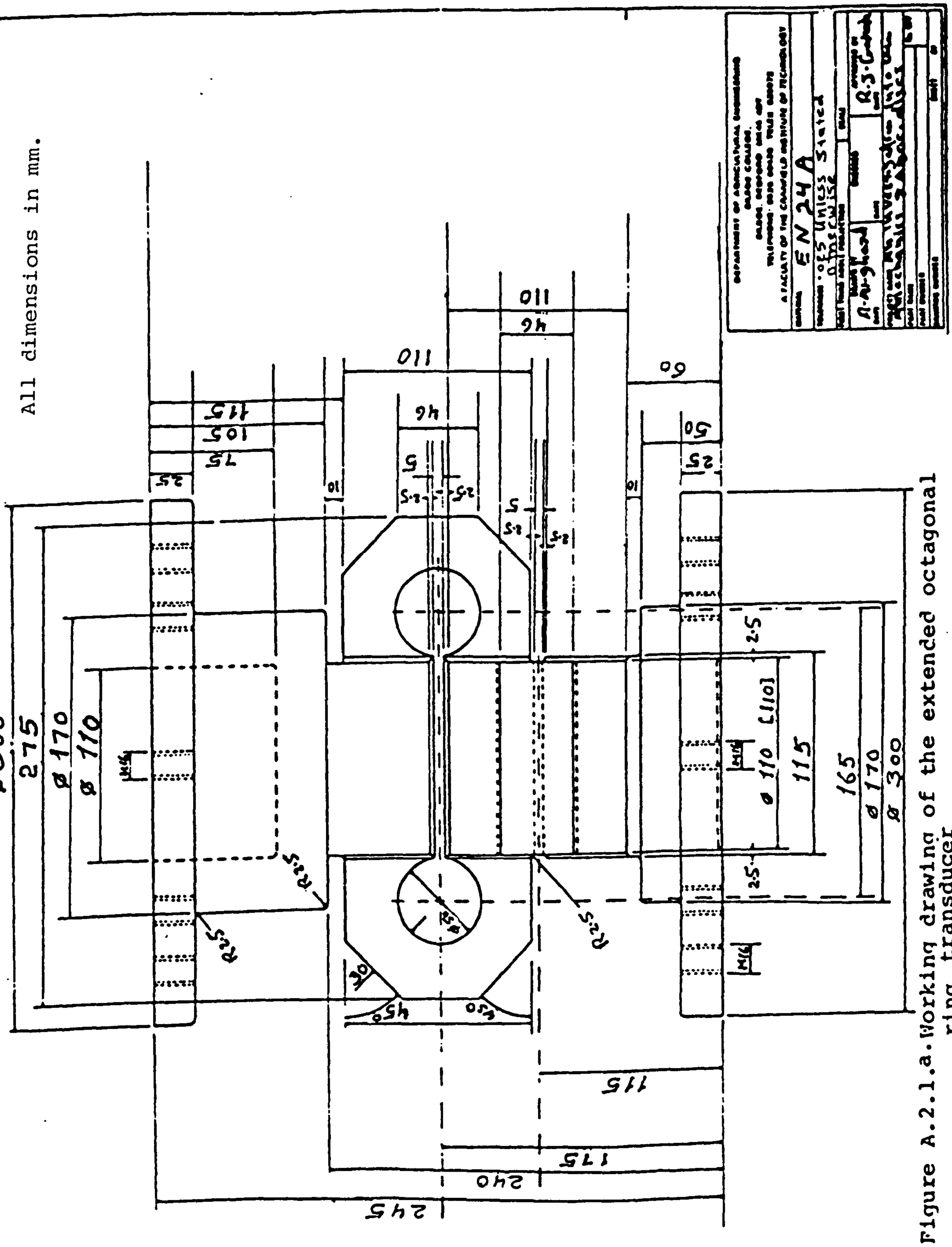

Figure A.2.1.a. Working drawing of the extended octagonal ring transducer

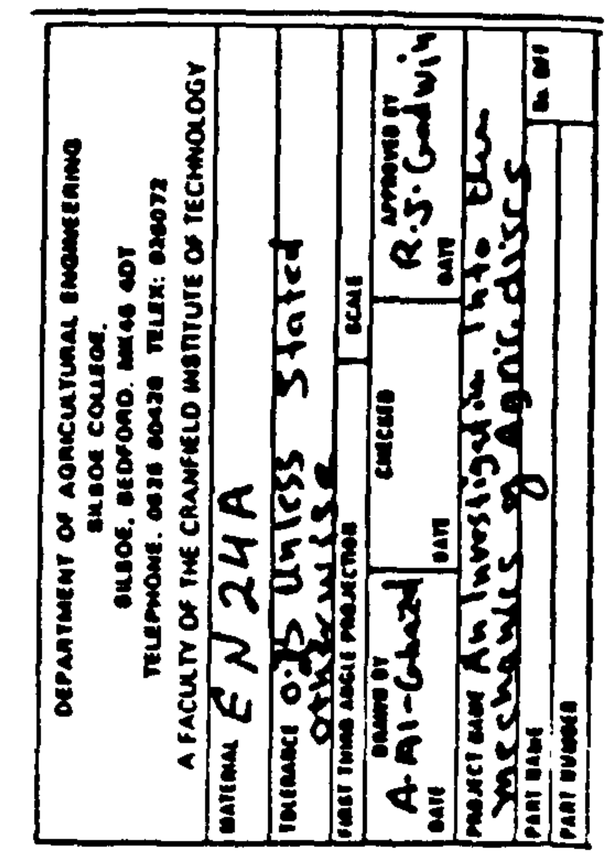

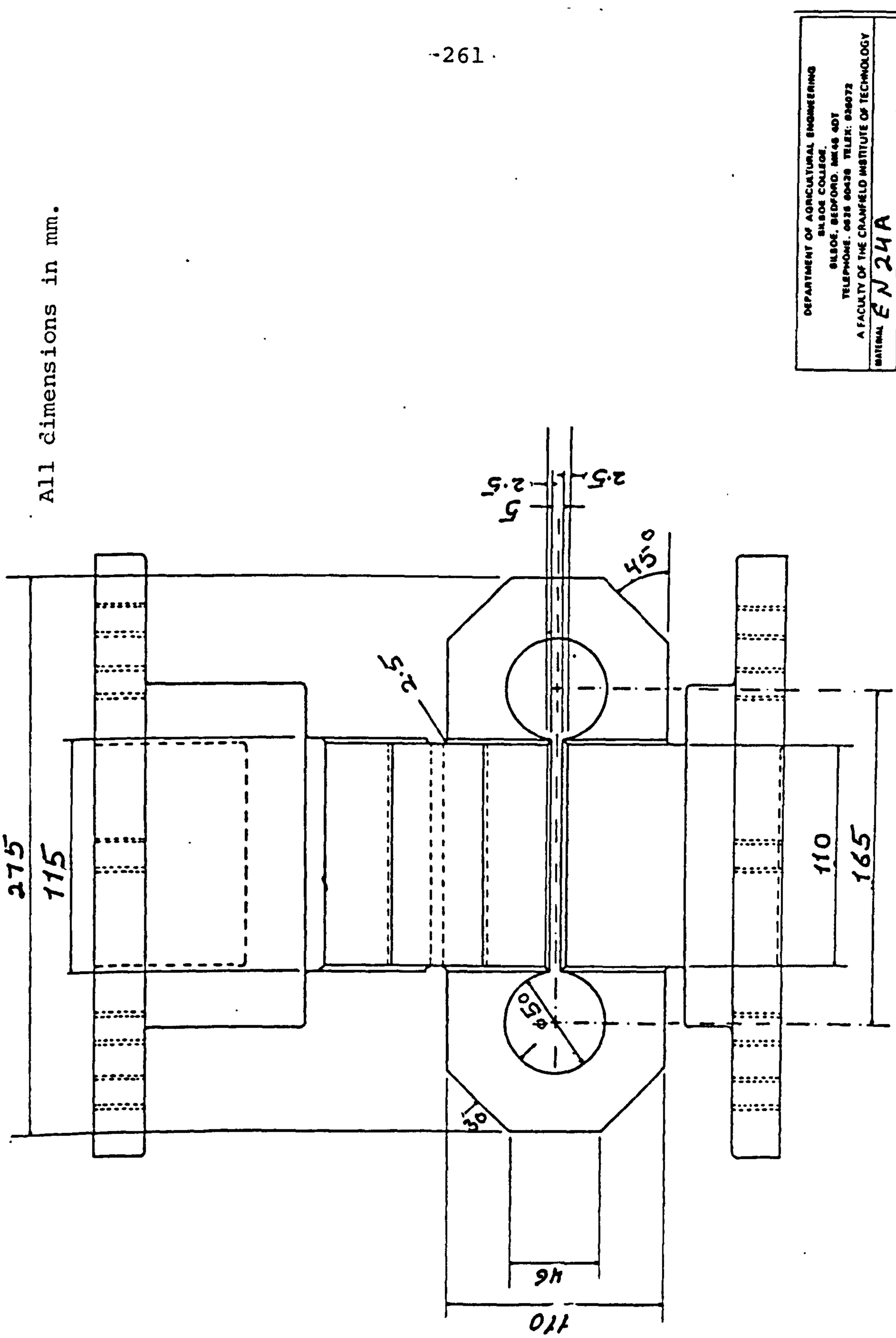

Figure A.2.1.b. Working drawing of the extended octagonal ring transducer

All dimensions in mm.

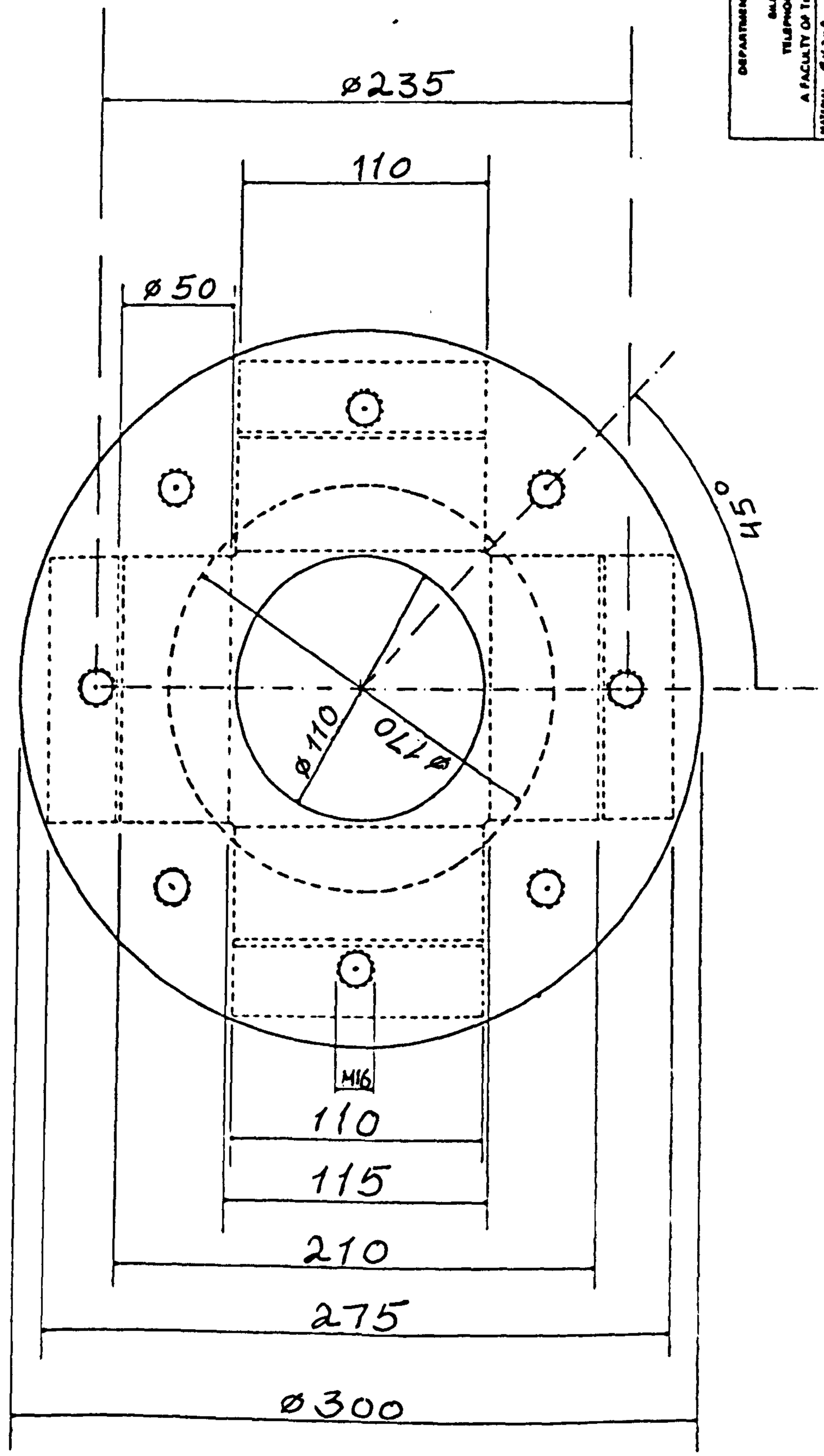

Figure A.2.1.c. Working drawing of the extended octagonal ring transducer

APPENDIX 3

CALCULATION OF NODES USING STRAIN ENERGY THEORY

a. Consider one-half of a ring, from Cook and Rabinowicz (1963)

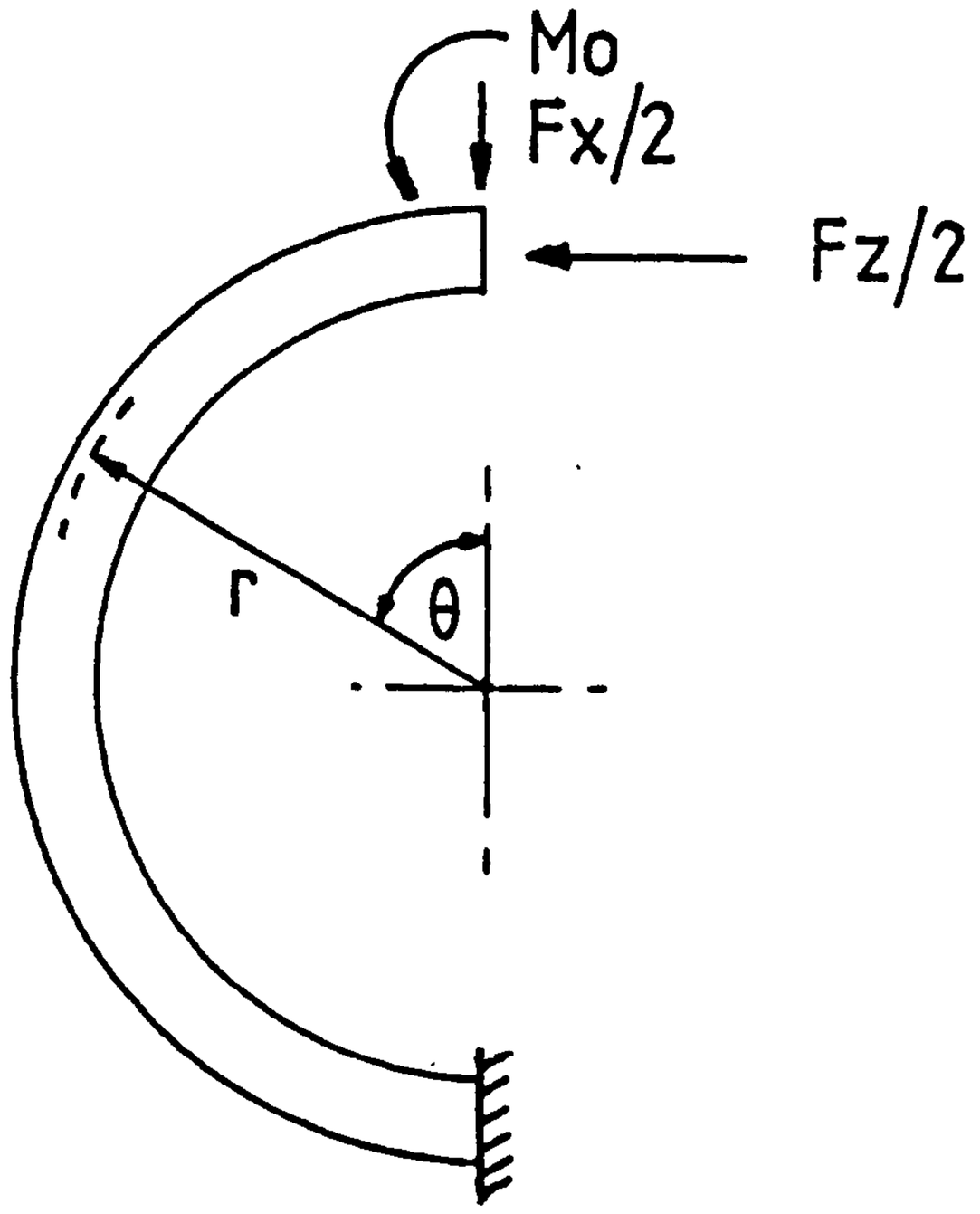

The bending moment MΘ at any point in the ring is

$$M\Theta = MO + \frac{Fxr}{2} \text{Sin}\Theta + \frac{Fzr}{2} (1 - \text{Cos}\Theta) \quad \ldots\ldots\ldots (A3.1)$$

The total strain energy in the ring is

$$U = \frac{1}{2EI} \int_0^{\pi} M\,\Theta^2 r d\Theta \quad \ldots\ldots\ldots (A3.2)$$

The angular rotation Ø of the ring at Θ = O is O thus

$$\left(\frac{\partial U}{\partial Mo}\right)\theta = o \quad = o \quad = \frac{1}{EI}\int_{o}^{\pi} M\theta \frac{\partial M}{\partial M} \quad \theta \text{ rd } \theta \qquad \ldots\ldots(A3.3)$$

From Equation A3.1.

$$o = \int_{o}^{\pi}\left[MO + \frac{Fxr \ Sin\theta}{2} + \frac{Fzr \ (1 - Cos \ \theta)}{2}\right].d\theta \ \ldots(A3.4)$$

When integrated this gives:

$$MO\pi + Fxr + \frac{Fzr\pi}{2} = o \qquad \ldots\ldots\ldots(A3.5)$$

$$MO = -\frac{Fxr}{\pi} - \frac{Fzr}{2} \qquad \ldots\ldots\ldots(A3.6)$$

Substituting into Equation A3.1. gives:

$$M\theta = \frac{Fxr}{2}(Sin \ \theta - \frac{2}{\pi}) - \frac{Fzr}{2} Cos\theta \qquad \ldots\ldots\ldots(A3.7)$$

The moment due to $\frac{Fx}{2}$ is zero when

$$Sin \ \theta = \frac{2}{\pi} \quad \theta = 39.6^{o}$$

and the moment due to $\frac{Fz}{2}$ is zero when

$$Cos \ \theta = o \quad \theta = 90^{o}$$

Hence the two positions $\theta = 39.6^{o}$ and $\theta = 90^{o}$ are the strain nodes for each force.

b. The limits of integration, for octagonal rings are less than 0 and greater than π, for example -0.133π to 1.333π, this being the limit of unsupported ring. Substituting into Equation A3.4. gives:

$$O = \int_{-0.133\pi}^{1.133\pi} \left[MO + \frac{Fxr \ Sin \ \Theta}{2} + \frac{Fzr \ (1 - Cos \ \Theta)}{2} \right] d\Theta \quad ...(A3.8)$$

Integrating gives

$$O = MO \ 1.266\pi + \frac{Fxr}{2} 1.828 + \frac{1.266\pi \ Fzr}{2} \quad .....(A3.9)$$

Therefore

$$MO = \frac{-Fxr}{2} 0.4598 - \frac{Fzr}{2} \quad ..... (A3.10)$$

Substituting into Equation A3.1. gives:

$$M\Theta = -Fxr \ 0.4598 - \frac{Fzr}{2} + \frac{Fxr \ Sin \ \Theta}{2} + \frac{Fzr \ (1 - Cos \ \Theta)}{2}$$

$$= \frac{Fxr}{2} (Sin \ \Theta - 0.4598) - \frac{Fzr}{2} Cos \ \Theta \quad .....(A3.11)$$

The moment due to $\frac{Fx}{2}$ is zero when

$$Sin \ \Theta = 0.4598$$

Therefore

$$\theta = 27.3^{o}$$

The moment due to $\frac{Fzr}{2}$ is zero when

$$\cos \theta = 0$$

Therefore

$$\theta = 90^{o}$$

Hence the positions of $\theta = 27.3^{o}$ and $\theta = 90^{o}$ are the positions of the strain nodes for each force.

APPENDIX 4

DETAIL OF THE STRAIN GAUGE BRIDGE NETWORKS

Strain gauges were attached in eight Wheatstone bridges, one for each of four forces, Fx1, Fx2, Fz and Fs and one for each of the moments, MDV, MSD, MSV1 and MSV2 as shown in Figure 3.4.

The Fx1 bridge consists of gauges 2, 4, 5 and 7 mounted at $\theta = 90^{o}$ when the moment due to Fz is zero (first ring).

The Fz bridge consists of 9, 10, 11, and 12 located at $\theta = 27.3^{o}$ where the moment due to Fx1 is zero (first ring).

The Fx2 bridge consists of gauges 14, 16, 17, and 19 wired at $\theta = 90^{o}$ when the moment due to Fz is zero (second ring).

The Fs bridge consists of gauges 21, 22, 23 and 24 located at $\theta = 90^{o}$ where the moments due to Fx1, Fx2 and Fz are zero (second ring).

The MDV bridge consists of gauges 1, 3, 6 and 8 located at $\theta = 90^{o}$ (first ring).

The MSD bridge consists of gauges 13, 15, 18 and 20 mounted at $\theta = 90^{o}$ (second ring).

The MSV1 bridge consists of gauges 25, 26, 29 and 30 mounted for torque across the vertical plane.

The MSV 2 bridge consists of gauges 27, 28, 31 and 32 mounted for torque across the horizontal plane.

The output from the channels is proportional to the sum of each individual strain gauge's output when the strain gauges have opposite outputs. The outputs from the MDV, MSD, MSV1 and MSV2 are proportional to the sum of each individual strain gauge output.

APPENDIX 5

DETERMINATION OF TRANSDUCER CHARACTERISTICS

A5.1. Introduction

The objective of the transducer characteristics was to determine the response of the ring to various hydraulic loads. Different hydraulic loads and a range of different positions were applied. The output from the force sensing bridges should be independent of the position of these forces within the working range.

The output from each of eight channels was recorded in Tables A5.1., A5.2, A5.3, A5.4, A5.5, A5.6, A5.7 and A5.8. The bridge output characteristics for the applied hydraulic load and the effect of cross-sensitivity were determined for the four forces and the moments in the plane of these forces.

A5.2. The results analysis

1. Force channel Fx1

Table A5.1. and Figure A5.1. show the following:

i. The linear response with a coefficient of determination for the regression analysis was $r^2 = 0.9997$.

For the range of applied hydraulic loads, the maximum percentage of deviation from the regression line was $\pm$ 2.1%

ii. The maximum deviation between the relative magnitude of the loading and unloading curves is $\pm$ (0.176 - 0.174/0.176 + 0.0174) x 100 = 0.57%. McFarland and Dimeff (1956) explained the relationship between the loading and unloading curves as resulting from the combination of the hysteresis of the strained member and the large but negative hysteresis of the material.

iii. The error between the output of the response curves for the load position of 1000 mm = 0.836 and 800 mm = 0.822 was 1.7% at a load of 16.92 kN

iv. The cross-sensitivity resulting from this channel which affected vertical and side forces was 5.43×10^{-4} and $1.1 \times 10^{-3} \mu v/N/v$ respectively.

2. <u>Force channel Fx2</u>

From Table A5.2. and Figure A5.2., the force channel Fx2 indicated that:

i. The coefficient of determination for the regression

analysis of r^2 = 0.9996.

ii. The maximum deviation between the loading and unloading curves is $\pm$ (0.207 - 0.205/0.207 + 0.205) x 100 = 0.49%.

iii. The error between the output of the response for the load position of 1000 mm = 0.980 and 800 mm = 0.96 was no greater than 1.8% at load of 16.92 kN.

iv. The cross-sensitivity resulting from this channel was the same cross-sensitivity resulting from Fx1 which affected vertical and side forces respectively.

3. <u>Force channel Fz</u>

Table A5.3 and Figure A5.3. indicated that:

i. The common coefficient of determination for the regression analysis was r^2 = 0.9998 and there was a linear response for both directions of hydraulic loads.

ii. The magnitude of the response was independent of the direction based on the identical regression coefficients.

iii. The error between the output of the load position 1000 mm = 0.162 and 800 mm = 0.160 was no greater than 1.2% at a load of 7.53 kN.

iv. The cross-sensitivity resulting from force Fz which affected draught and side forces was 1.85×10^{-4} and 1.59×10^{-4} μv/N/v respectively.

4. Force channel Fs

Table A5.4. and Figure A5.4. show the following results:

i. The coefficient of determination for the regression analysis was $r^2 = 0.9998$ and the response for both directions of load application was linear.

ii. The error between the output of the response curves for the load position 1000 mm = 0.247 and 800 mm = 0.242 was 2% for a load of 10.13 kN.

iii. The cross-sensitivity resulting from this channel which affected the draught and vertical forces was 3.94×10^{-4} and 1.77×10^{-4} μv/N/v.

5. The moment channels (MDV, MSD, MSV1 and MSV2)

From Tables A5.5., A5.6., A5.7., and A5.8 and Figures A5.5., A5.6., A5.7. and A5.8. the following were observed:

i. The coefficient of determination for the regression analysis r^2 was greater than 0.9998 for all the channels.

ii. The errors between the output of the load position 1000 mm and 800 mm were 1.54%, 1.59%, 1.9% and 1.5% for MDV, MSD, MSV1 and MSV2 respectively.

iii. The responses were independent of the origin of the eccentric forces. The arm moments were 0.345m, 0.33 m, 1 m and 1 m for MDV, MSD, MSV1 and MSV2 respectively

Table A5.1. Fxl Bridge and cross-sensitivity outputs, V

Load kN	1000mm		900 mm		800 mm		Vert.	Side
	Load	Unload	Load	Unload	Load	Unload		
1.87	0.098	0.098	0.098	0.098	0.098	0.098	0.003	0.01
3.76	0.176	0.174	0.175	0.174	0.175	0.174	0.007	0.019
5.64	0.299	0.298	0.298	0.297	0.297	0.296	0.013	0.032
7.52	0.364	0.364	0.362	0.361	0.361	0.361	0.019	0.052
9.39	0.475	0.474	0.473	0.471	0.471	0.470	0.025	0.052
11.28	0.572	0.571	0.569	0.568	0.566	0.566	0.03	0.065
13.16	0.642	0.641	0.639	0.639	0.635	0.634	0.035	0.074
15.04	0.759	0.759	0.753	0.753	0.747	0.747	0.041	0.083
16.92	0.836		0.826		0.822		0.046	0.096

Table A5.2. Fx2 Bridge and cross sensitivity outputs, V.

Load kN	1000 mm		900 mm		800 mm		Vert.	Side
	Load	Unload	Load	Unload	Load	Unload		
1.87	0.11	0.11	0.11	0.11	0.11	0.113	0.003	0.01
3.76	0.207	0.205	0.206	0.206	0.206	0.206	0.007	0.019
5.64	0.335	0.335	0.334	0.334	0.333	0.332	0.013	0.032
7.52	0.427	0.427	0.425	0.425	0.424	0.424	0.019	0.052
9.39	0.539	0.539	0.537	0.536	0.536	0.536	0.025	0.052
11.28	0.652	0.653	0.649	0.648	0.648	0.647	0.03	0.065
13.16	0.755	0.754	0.752	0.752	0.751	0.750	0.035	0.074
15.04	0.864	0.863	0.858	0.857	0.852	0.852	0.041	0.083
16.92	0.980		0.969		0.962		0.046	0.096

Table A5.3. Fz bridge and cross-sensitivity outputs, V

Load kN	1000mm Load	900mm Load	800mm Load	Draught Force	Side Force
0.44	0.009	0.009	0.009	0.001	0.001
0.76	0.016	0.016	0.016	0.002	0.001
1.17	0.025	0.025	0.025	0.003	0.001
1.64	0.035	0.035	0.035	0.003	0.002
1.98	0.043	0.043	0.043	0.003	0.002
2.29	0.05	0.05	0.05	0.004	0.002
2.73	0.058	0.058	0.058	0.004	0.003
3.18	0.068	0.068	0.068	0.004	0.003
3.8	0.081	0.081	0.081	0.005	0.003
4.27	0.091	0.091	0.091	0.005	0.004
4.82	0.103	0.103	0.103	0.006	0.004
5.28	0.113	0.113	0.113	0.006	0.004
5.98	0.128	0.128	0.128	0.006	0.005
6.75	0.144	0.144	0.143	0.007	0.006
7.53	0.162	0.161	0.160	0.007	0.006

Table A5.4. Fs bridge and cross-sensitivity outputs, V

Load kN	1000mm Load	900mm Load	800mm Load	Draught Force	Vertical Force
1.72	0.041	0.041	0.041	0.004	0.002
3.38	0.081	0.081	0.081	0.006	0.004
4.37	0.107	0.107	0.107	0.01	0.005
4.97	0.121	0.121	0.121	0.01	0.005
5.63	0.137	0.137	0.137	0.012	0.006
6.42	0.158	0.158	0.158	0.013	0.007
6.75	0.167	0.166	0.166	0.014	0.007
7.61	0.188	0.187	0.187	0.016	0.007
8.34	0.204	0.203	0.202	0.017	0.007
9.47	0.231	0.229	0.228	0.019	0.009
10.13	0.247	0.244	0.242	0.02	0.009

Table A5.5. MDV bridge output,V

Load kN.m	1000mm Load	900mm Load	800mm Load
0.162	0.042	0.042	0.042
0.286	0.068	0.068	0.068
0.421	0.097	0.097	0.097
0.655	0.145	0.145	0.145
0.797	0.179	0.179	0.179
0.931	0.204	0.204	0.204
1.1	0.247	0.246	0.245
1.28	0.286	0.286	0.286
1.48	0.337	0.336	0.336
1.63	0.368	0.366	0.365
1.89	0.428	0.425	0.424
2.07	0.467	0.464	0.463
2.2	0.499	0.495	0.494
2.39	0.540	0.536	0.532
2.58	0.584	0.579	0.575

Table A5.6. MSD bridge output, V

Load kN.m	1000mm Load	900mm Load	800mm Load
0.567	0.100	0.100	0.100
1.11	0.202	0.202	0.202
1.44	0.268	0.268	0.268
1.64	0.303	0.303	0.303
1.86	0.344	0.344	0.344
2.12	0.400	0.400	0.400
2.23	0.422	0.422	0.422
2.51	0.475	0.474	0.474
2.75	0.515	0.514	0.513
3.12	0.586	0.584	0.581
3.34	0.627	0.625	0.617

Table A5.7. MSV1 bridge output,V

Load kN.m	1000mm Load	900mm Load	800mm Load
1.92	0.135	0.135	0.135
3.24	0.230	0.229	0.228
3.97	0.282	0.281	0.280
5.3	0.382	0.380	0.379
5.96	0.430	0.429	0.428
6.69	0.482	0.480	0.478
7.48	0.531	0.529	0.528
7.95	0.571	0.568	0.566
8.61	0.615	0.611	0.610
9.14	0.650	0.644	0.643
10.00	0.712	0.706	0.698

Table A5.8. MSV2 bridge output, V

Load kN.m	1000mm Load	900mm Load	800mm Load
1.99	0.161	0.161	0.161
3.38	0.270	0.269	0.268
4.63	0.375	0.374	0.373
5.3	0.434	0.432	0.431
5.96	0.487	0.484	0.483
6.62	0.537	0.533	0.532
7.28	0.594	0.590	0.588
7.88	0.645	0.641	0.640
8.67	0.708	0.703	0.702
9.34	0.763	0.757	0.755
9.93	0.813	0.806	0.798

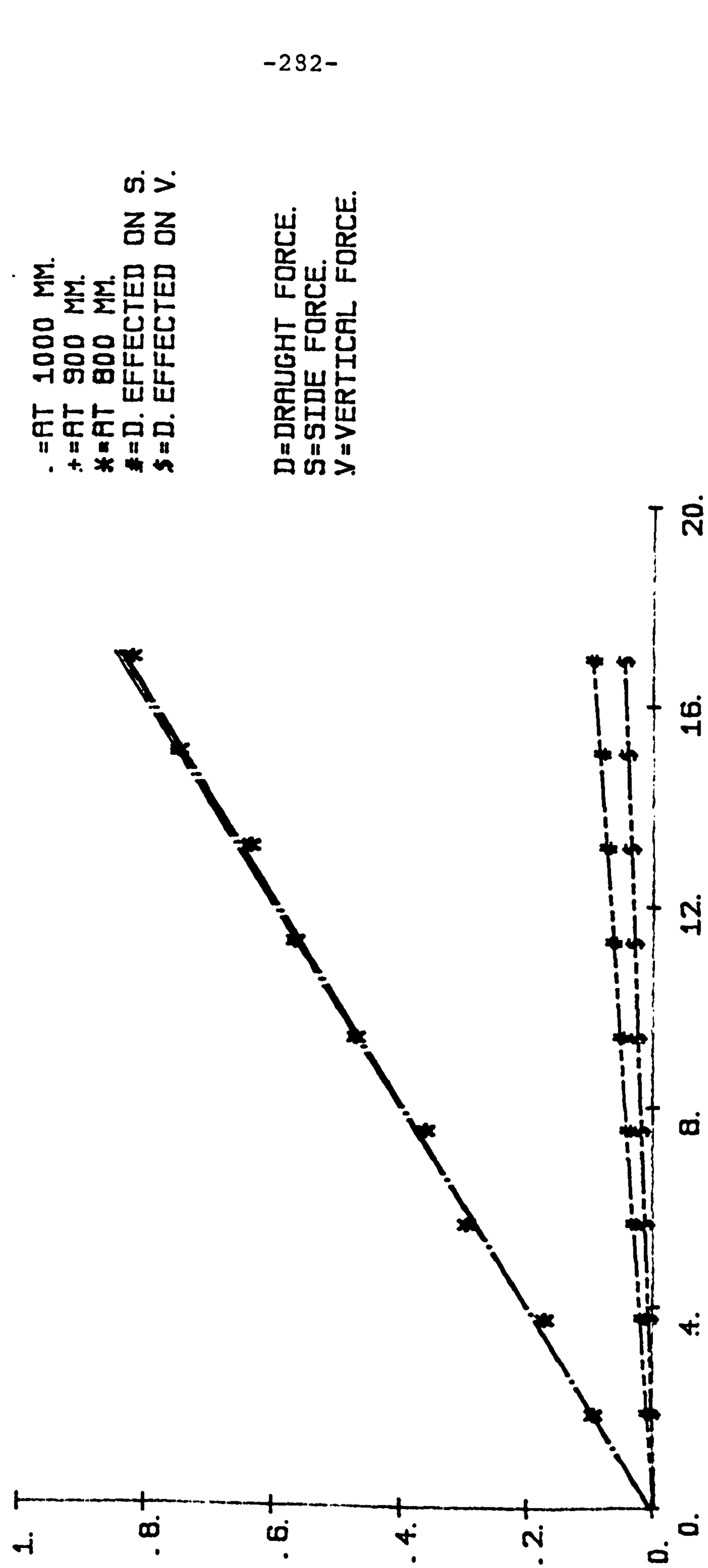

Figure A5.1. Fx1 bridge output characteristics

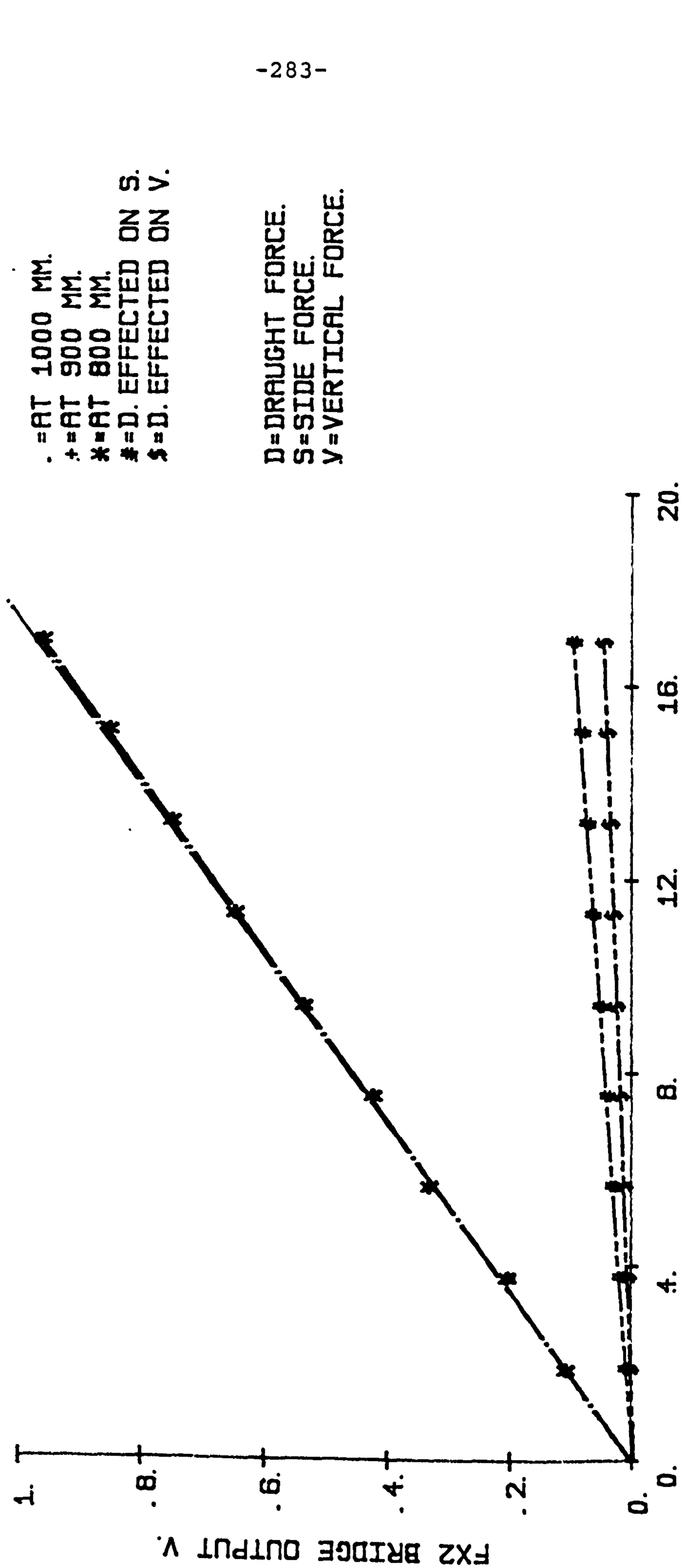

Figure A5.2. Fx2 bridge output characteristics

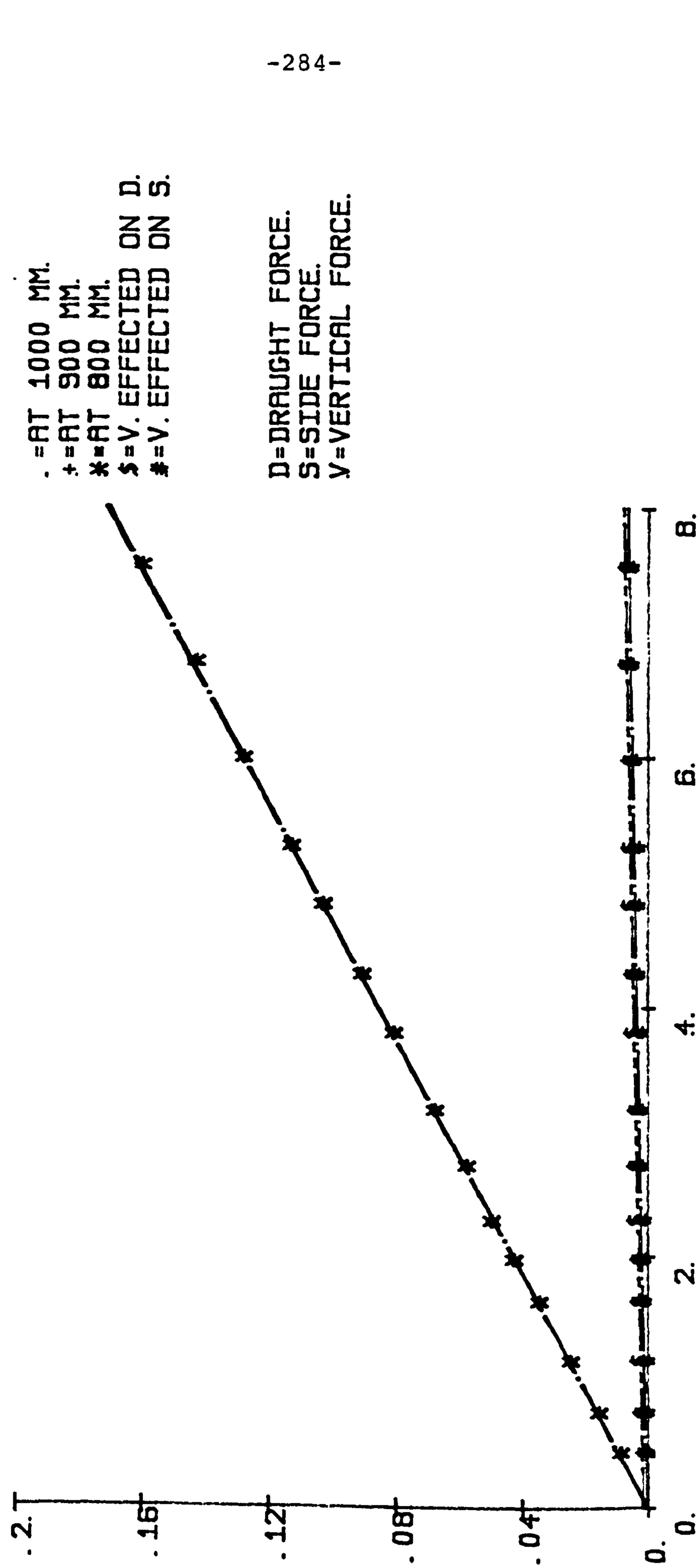

Figure A5.3. Fz bridge output characteristics

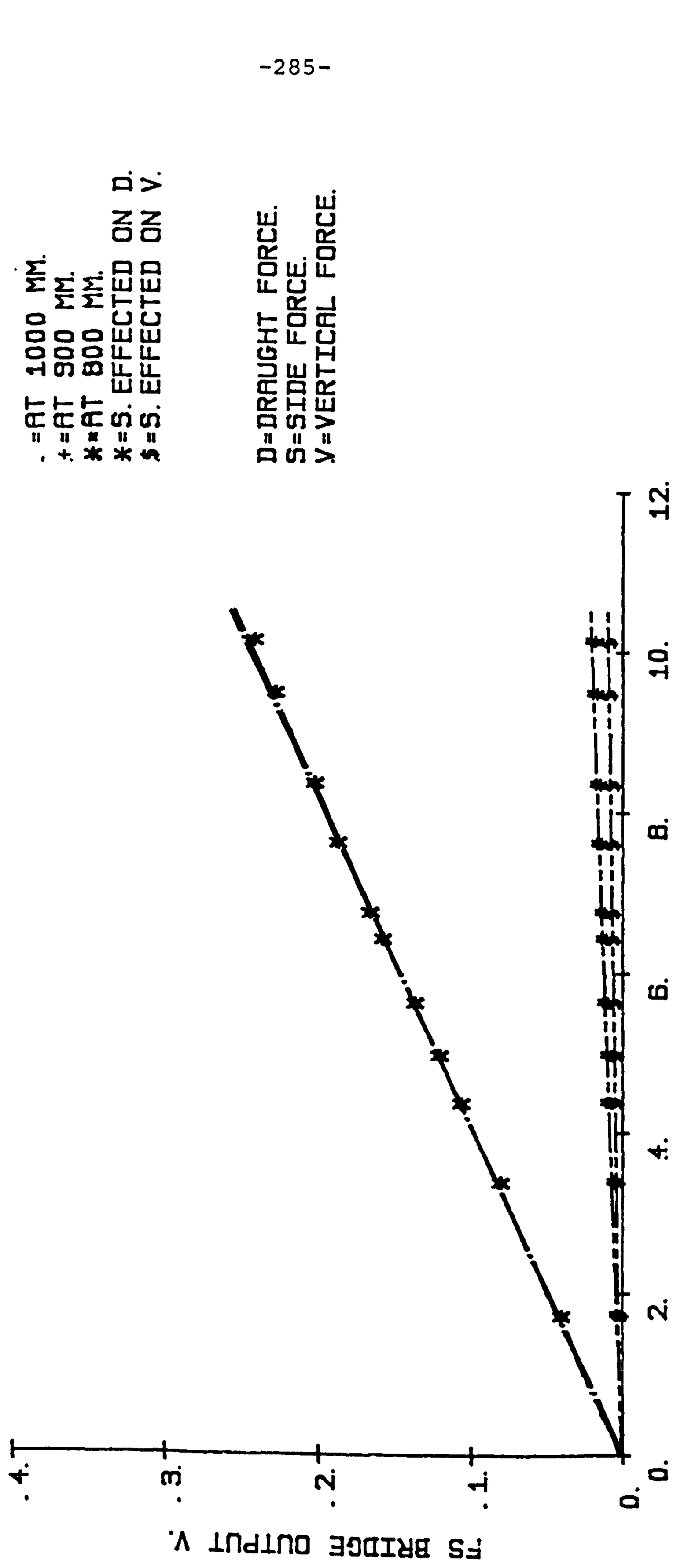

Figure A5.4. Fs bridge output characteristics

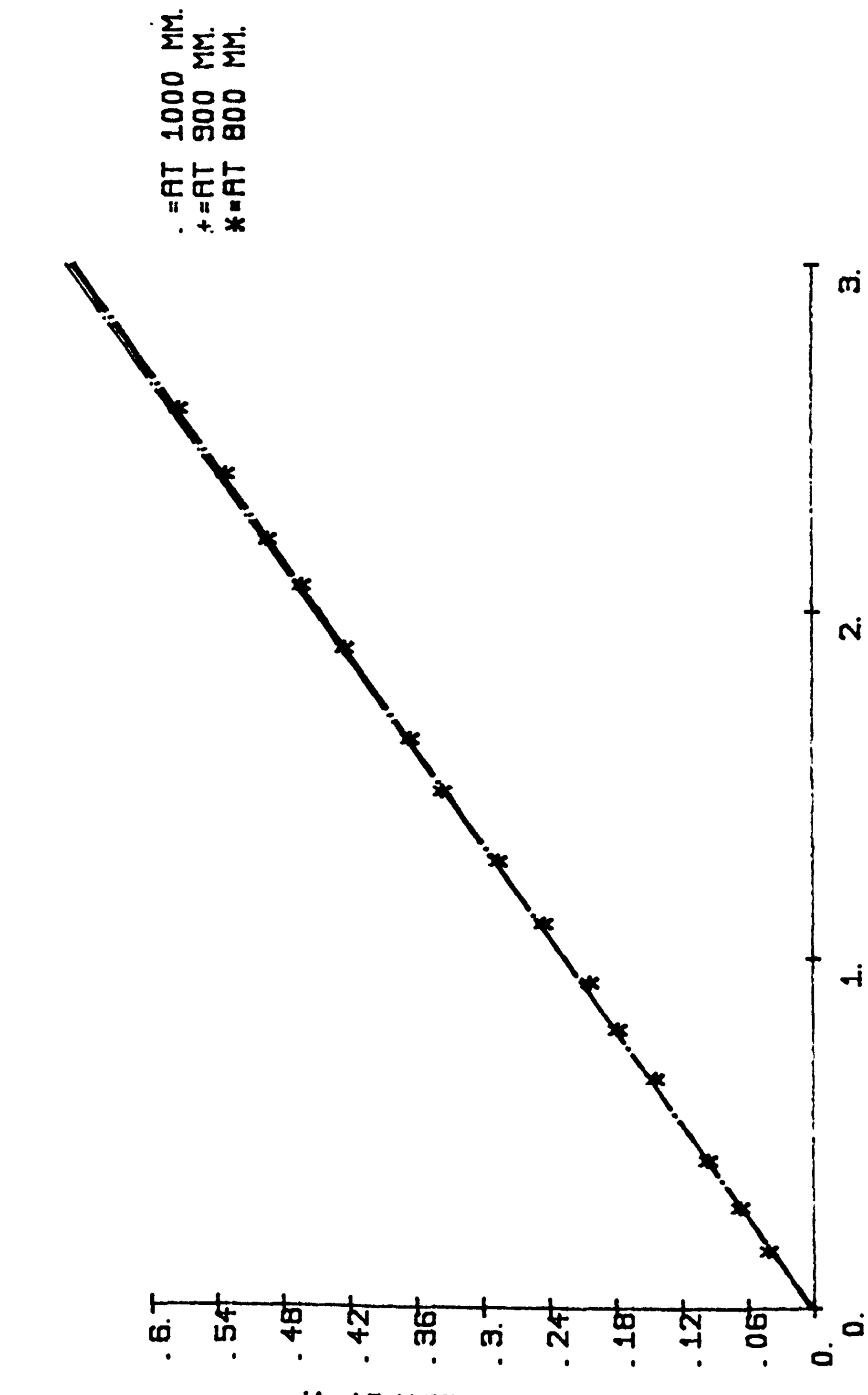
1000 MM.
900 MM.
800 MM.
.=AT
+=AT
*=AT
MDV BRIDGE OUTPUT V.
.6
.54
.48
.42
.36
.3
.24
.18
.12
.06
0.
0.
1.
2.
3.
LOAD KNM.
MDV bridge output characteristics

Figure A5.5.

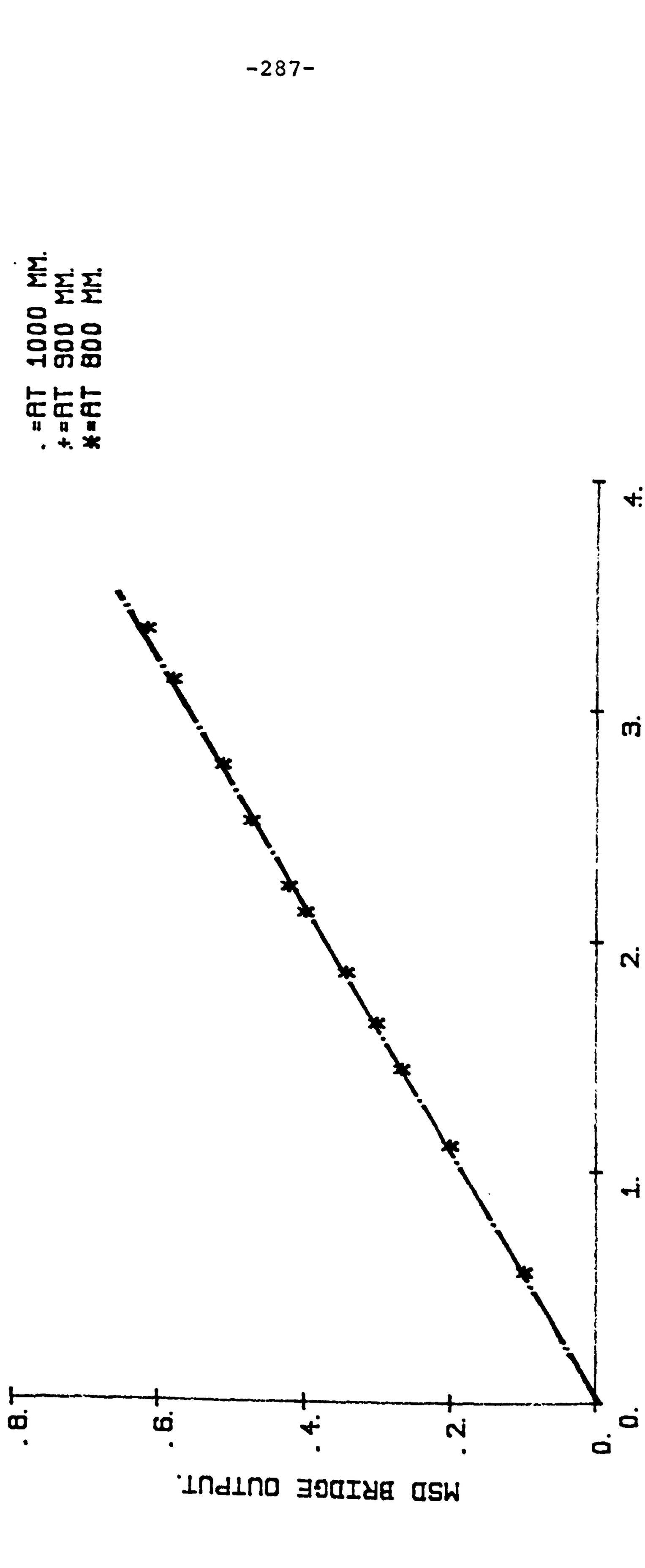

Figure A5.6. MSD bridge output characteristics

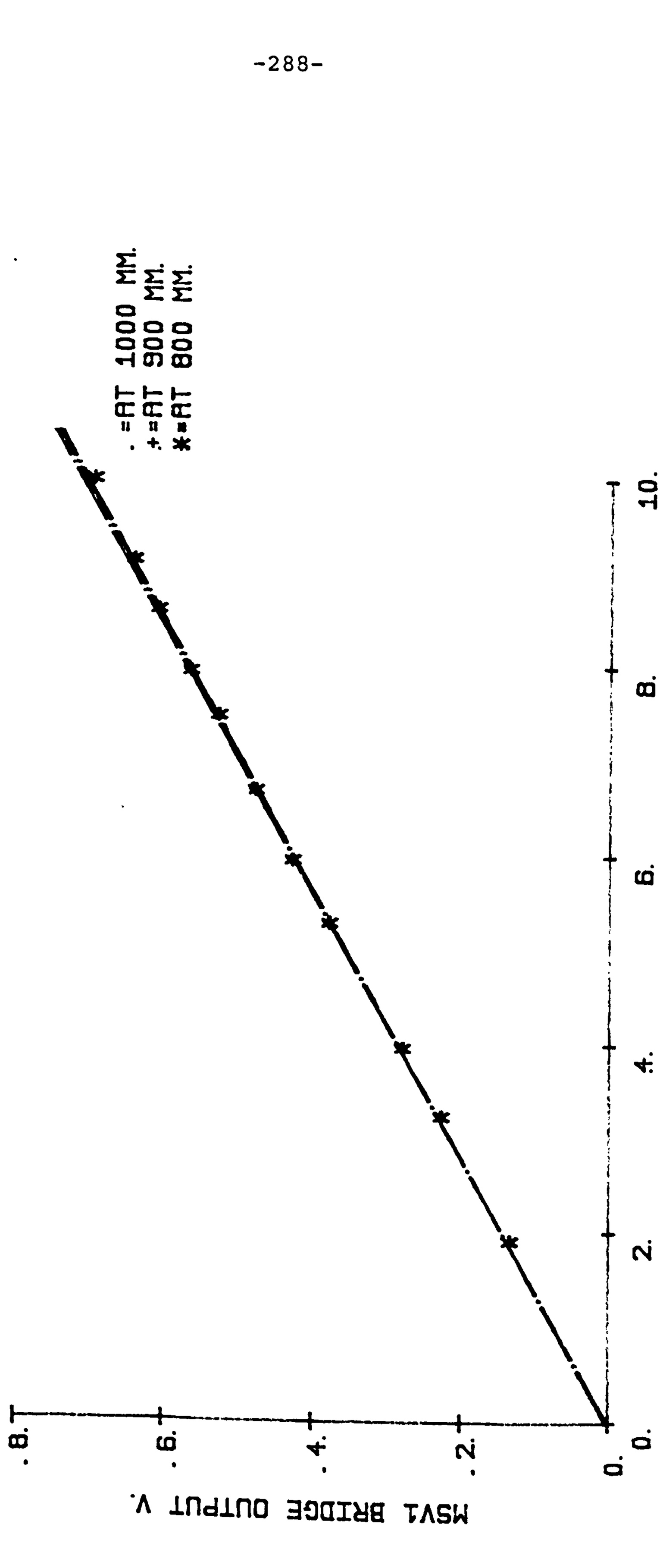

Figure A5.7. MSV1 bridge output characteristics

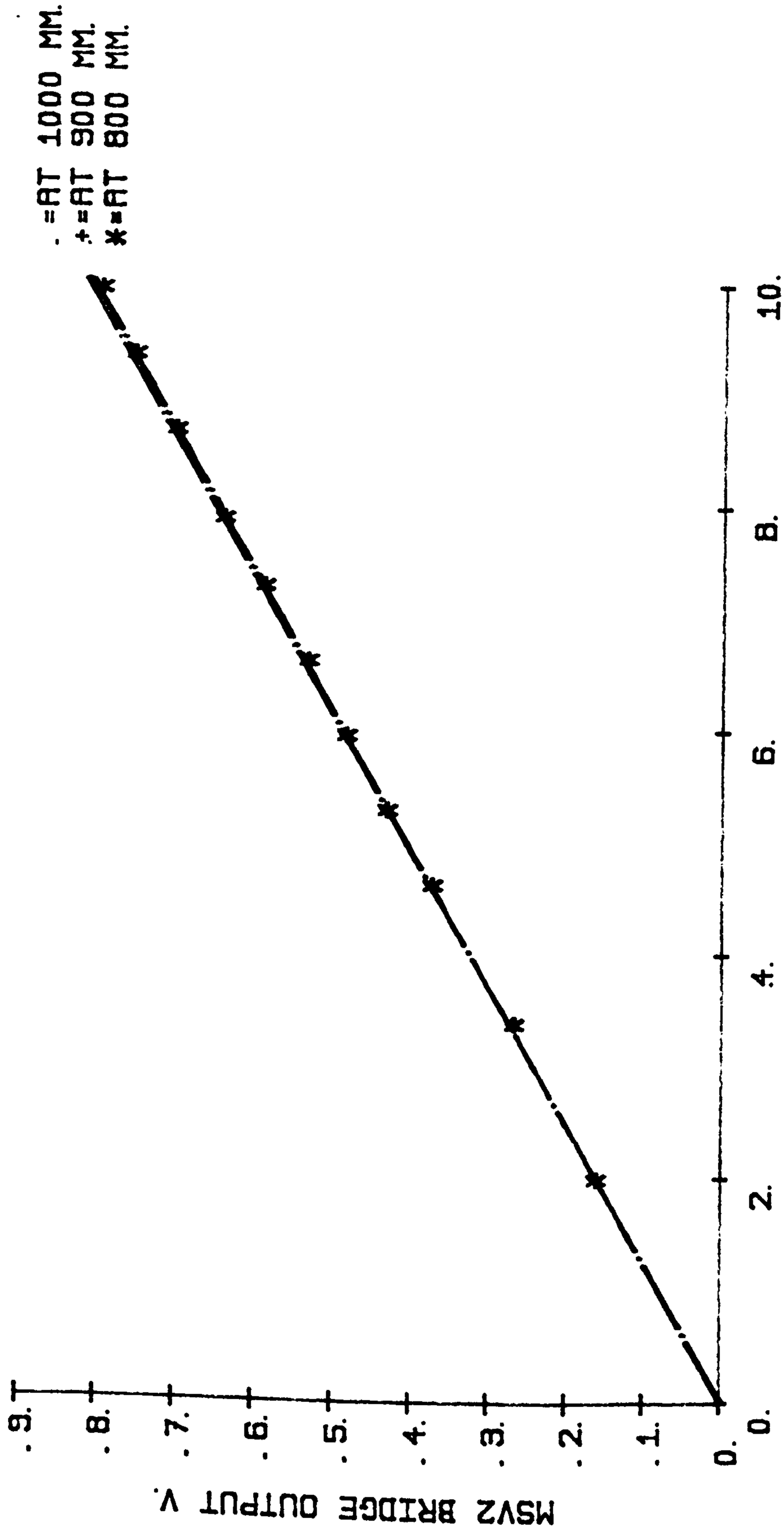

Figure A5.8. MSV2 bridge output characteristics

```
]LOAD DISCAL -GHAZAL7'S DISC GEOMETRY 1

FILE NOT FOUND

]LOAD AL-GHAZAL'S DISC GEOMETRY 1
]LIST

0  HOME : NORMAL
10  REM  8888888888888888888888888
      888
11  REM  A PROG TO CALCULATE THE
      CUT AREA OF A DISC
12  REM ************************
      ****
100  REM  VARIABLE ENTRY
105  PRINT "THIS PROGRAM IS TO CA
     LCULATE ": PRINT : PRINT "TH
     E AREA CUT BY ONE UNIT OF A
     GANG DISC"
110  PRINT "PLEASE ENTER THE FOLL
     OWING": PRINT
115  INPUT "ENTER DISC TYPE - ";A
     $
120  INPUT "ENTER THE DISC'SWEEP'
      ANGLE IN DEGREES - ";DA
121  PRINT
130  INPUT "ENTER THE DISC'TILT'A
     NGLE IN DEGREES - ";TA
131  PRINT
140  INPUT "ENTER THE DISC'CHORD'
     RADIUS IN MM - ";R
141  PRINT
150  INPUT "ENTER THE DISC 'DEPTH
     ' IN MM - ";DS
151  PRINT
160  INPUT "ENTER THE DISC 'STEPO
     VER' IN MM -";N
161  PRINT
163  PR# 1
165  PRINT "DISC ANGLE = "DA;" DE
     GREES"
166  PRINT "TILT ANGLE = "TA;" DE
     GREES"
167  PRINT "DISC RADIUS = "R;" MM
     "
168  PRINT "DEPTH IN SOIL = "DS;"
      MM"
169  PRINT "GANG SPACING = ";N;"M
     M"
170  PRINT "DISC TYPE = ";A$
175  PR# 0
190  IF N ( 1 THEN : PRINT "NO GA
     NG SPACING TO WORK ON ": FLASH
     : PRINT " TRY AGAIN THEN ": END

195  IF DA = 0 THEN  PRINT " ERRO
     R ": FLASH : PRINT "NO DISC
     ANGLE ": NORMAL : END
200  IF N ) (2 * R) THEN  PRINT :
     "THESE DISCS DO NOT INTERSEC
     T ": FLASH : PRINT :" TRY AG
     AIN  "
300  REM  FIRST DERIVATIVES
305  PR# 1
310 DR = DS / R
```

```
195  IF DA = 0 THEN  PRINT " ERRO
     R ": FLASH : PRINT "NO DISC
     ANGLE ": NORMAL : END
200  IF N ) (2 * R) THEN  PRINT :
     "THESE DISCS DO NOT INTERSEC
     T ": FLASH : PRINT :" TRY AG
     AIN  "
300  REM  FIRST DERIVATIVES
305  PR# 1
310 DR = DS / R
311  PRINT "DR = "DR
320 TA = (TA / 180) * 3.142
321  PRINT "TA = "TA;" RADIANS"
322 TA =  COS (TA)
323  PRINT " COS(TA) = ";TA
330 DA = (DA / 180) * 3.142
331  PRINT "DA = "DA;" RADIANS"
332 DA =  SIN (DA)
333  PRINT " SIN(DA) = ";DA
340 PA = (1 - DR)
341  PRINT "PA = "PA
350 PB = (2 - DR)
351  PRINT "PB = "PB
360 NR = ((N) * (( SQR ((DR) * (P
     B))) * (TA))) / ((R) * ( SQR
     ((DR) * ((2 * (TA)) - (DR)))
     ) * (DA))
361  PRINT "NR = ";NR
370 PC = (4 - ((NR) ^ 2))
371  PRINT "PC = ";PC
372  IF PC ( 1 THEN  PR# 0: PRINT
     : FLASH : PRINT " ERROR NO D
     ISC INTERSECTION ": NORMAL :
      END
375 CU = (1 - ((DR) * (TA)))
376  PRINT " CU = ";CU
385 RC = ((DR) * ((PB) * (PC)))
386  PRINT " RC  = ";RC
390 X =  -  ATN (CU /  SQR ( - CU
      * CU + 1)) + 1.5708
391  PRINT "COS-1 OF X = ";X
400 AP = ((R) ^ 2) * ((X) - ((CU)
      * ( SQR ((DR) * ((2 * (TA))
     - (DR))))) * (TA) * (DA)
401  PRINT "AP = ";AP
410 Y = (DR)
411  PRINT " Y = ";Y
420 YY =  -  ATN (Y /  SQR ( - Y *
     Y + 1)) + 1.5708
421  PRINT " COS-1 OF Y = ";YY
423 DC = (YY) - ((( SQR ((DR) * (
     PB)))) * (PA))
425  PRINT " DC = ";DC
430 A = (4 - ((2 * (NR)) * ( SQR
     ((DR) * (PB)))) - (( SQR (PC
     )) * (2 * (PA))))
431  PRINT "A = ";A
440 B = (((2 * ( SQR ((DR) * (PB)
     ))) * ( SQR (PC))) + (2 * ((
     NR) * (PA))))
441  PRINT " B = ";B
450 CC = ((( SQR ((DR) * (PB) * (
     PC))) - ((NR) * (PA))) / 2)
451  PRINT "CC = ";CC
460 C =  ATN (CC /  SQR ( - CC *
     CC + 1))
461  PRINT " C = ";C
464 D = (C) - (CC)
465  PRINT " D = ";D
466 M = ((D) / (DC))
467 L = ((A) * (B))
468  PRINT " D/DC = ";M
469  PRINT " A*B = ";L
470 Z = (((A) * (B)) / (16 * (DC)
     )) + ((D) / (DC))
```

```
464 D = (C) - (CC)
465  PRINT " D = ";D
466 M = ((D) / (DC))
467 L = ((A) * (B))
468  PRINT " D/DC = ";M
469  PRINT " A*B = ";L
470 Z = (((A) * (B)) / (16 * (DC)
    )) + ((D) / (DC))
471  PRINT " Z = ";Z
480 AG = (AP) * (1 - (Z))
481  PRINT " THE ANSWER ))))) = "
    ;AG;" SQ MM "
490 AR = AG / 100
500  PRINT "DISPLACMENT AREA OF"
501  PRINT : PRINT "THIS PASS = "
    AR;" SQ CM"
504 AM = AR / 10000
505  PRINT : PRINT " SPECIFIC ARE
    A OF CUT = ";AM;"SQ M"
590  PRINT : PRINT "**************
    *****"
600  PR# 0
605  END
1000  REM  SPLIT FOR DISC30/TILT0

1005  PR# 1
1010 DR = DS / R
1020  PRINT "DR = "DR
1030 TA = (TA / 180) * 3.142
1040  PRINT "TA = "TA;" RADIANS"
1050 TA =  COS (TA)
1060  PRINT " COS(TA) = ";TA
1070 DA = (DA / 180) * 3.142
1080  PRINT "DA = "DA;" RADIANS"
1090 DA =  SIN (DA)
1100  PRINT " SIN(DA) = ";DA
1110 PA = (1 - DR)
1120  PRINT "PA = "PA
1130 PB = (2 - DR)
1140  PRINT "PB = "PB
1130 NR = ((N) * (( SQR ((DR) * (
    PB))) * (TA))) / ((R) * ( SQR
    ((DR) * ((2 * (TA)) - (DR)))
    ) * (DA))
1160  PRINT "NR = ";NR
1170 PC = (4 - ((NR) ^ 2))
1180  PRINT "PC = ";PC
1190 CU = (1 - ((DR) * (TA)))
1200  PRINT " CU = ";CU
1210 RC = ((DR) * ((PB) * (PC)))
1220  PRINT " RC  = ";RC
1230 X =  -  ATN (CU /  SQR ( - C
    U * CU + 1)) + 1.5708
1240  PRINT "COS-1 OF X = ";X
1250 AP = ((R) ^ 2) * ((X) - ((CU
    ) * ( SQR ((DR) * ((2 * (TA)
    ) - (DR))))) * (TA) * (DA)
1260  PRINT "AP = ";AP
1270 Y = (DR)
1280  PRINT " Y = ";Y
1290 YY =  -  ATN (Y /  SQR ( - Y
    * Y + 1)) + 1.5708
1300  PRINT " COS-1 OF Y = ";YY
1310 DC = (YY) - ((( SQR ((DR) *
    (PB)))) * (PA))
1320  PRINT " DC = ";DC
1330 A = (4 - ((2 * (NR)) * ( SQR
    ((DR) * (PB)))) - (( SQR (PC
    )) * (2 * (PA))))
1340  PRINT "A = ";A
1350 B = (((2 * ( SQR ((DR) * (PB
    )))) * ( SQR (PC))) + (2 * (
    (NR) * (PA))))
1360  PRINT " B = ";B
```

```
1300  PRINT " COS-1 OF Y = ";YY
1310 DC = (YY) - ((( SQR ((DR) *
     (PB)))) * (PA))
1320  PRINT " DC = ";DC
1330 A = (4 - ((2 * (NR)) * ( SQR
     ((DR) * (PB)))) - (( SQR (PC
     )) * (2 * (PA))))
1340  PRINT "A = ";A
1350 B = (((2 * ( SQR ((DR) * (PB
     )))) * ( SQR (PC))) + (2 * (
     (NR) * (PA))))
1360  PRINT " B = ";B
1370 CC = ((( SQR ((DR) * (PB) *
     (PC))) - ((NR) * (PA))) / 2)

1380  PRINT "CC = ";CC
1390 C =  ATN (CC /  SQR ( - CC *
     CC + 1))
1400  PRINT " C = ";C
1410 D = (C) - (CC)
1420  PRINT " D = ";D
1430 M = ((D) / (DC))
1440 L = ((A) * (B))
1450  PRINT " D/DC = ";M
1460  PRINT " A*B = ";L
1470 Z = (((A) * (B)) / (16 * (DC
     ))) + ((D) / (DC))
1480  PRINT " Z = ";Z
1490 AG = (AP) * (1 - (Z))
1500  PRINT " THE ANSWER ))))) =
     ";AG;" SQ MM "
1510 AR = AG / 100
1520  PRINT "DISPLACMENT AREA OF"

1530  PRINT : PRINT "THIS PASS =
     "AR;" SQ CM"
1540 AM = AR / 10000
1550  PRINT : PRINT " SPECIFIC AR
     EA OF CUT = ";AM;"SQ M"
1560  PRINT : PRINT "**********
     ******"
1570  PR# 0
```

```
]LOAD AL-GHAZAL'S DISC GEOMETRY 2
]LIST

5 H = H * PI / 180:E = E * PI / 1
    80
10  REM  AL-GHAZAL'S DISC GEOMETR
    Y 2
15  CLEAR
20  INPUT "H=";H: INPUT "E=";E: INPUT
    "R=";R: INPUT "R1=";R1: INPUT
    "D=";D
23  PR# 1
25  PRINT "AL-GHAZAL'S DISC GEOME
    TRY 2"
26  PRINT "H=";H: PRINT "E=";E: PRINT
    "R=";R: PRINT "R1=";R1: PRINT
    "D=";D
29  PRINT
30 PI = 3.1415926
35 H = H * PI / 180:E = E * PI /
    180
40 R2 = R1 / R
50 B =  ATN (R2 /  SQR ( - R2 * R
    2 + 1))
60 C = PI / 2 - B
70 K =  SIN (E + B) * ( SIN (E +
    B) - D / R) +  SQR ( COS (2 *
    (E + B)) + ( SIN (E + B)) ^
    4 + (2 *  SIN (E + B) - D /
    R) * D / R * ( COS (E + B)) ^
    2)
75 A =  - ATN (K /  SQR ( - K *
    K + 1)) + 1.5708
80 F1 =  SQR (D * (2 * R1 *  COS
    (E) - D)) / (R *  COS (E + B
     - A) *  COS (E))
85 F =  ATN (F1 /  SQR ( - F1 * F
    1 + 1))
90 AB = (A *  COS (E) *  COS (B -
    A) -  SIN (A) *  COS (B) *  COS
    (E) -  SIN (E + B - A) * ( COS
    (B - A) -  COS (B)) ^ 2) * R
     ^ 2 / (2 *  COS (E) *  COS
    (B - A)) * ((F - H) / F) ^ 2
    .5
100 I = 2 *  SQR (D * (2 * R1 *  COS
    (E) - D)) /  COS (E)
110 J = I / (2 * R1)
120 AP = R1 ^ 2 * ( ATN (J /  SQR
    ( - J * J + 1)) - I / (4 * R
    1 ^ 2) *  SQR (4 * R1 ^ 2 -
    I ^ 2)) *  SIN (H) *  COS (E
    )
125 A1 = 1 / 2 * PI - E - B
130 AR = A1 + 1 / 2 * A
135 AR = AR * 180 / PI
140  PRINT "B=";B * 180 / PI
150  PRINT "C=";C * 180 / PI
155  PRINT "C1=";90 - (C * 180 /
    PI)
160  PRINT "COS(A)=";K
170  PRINT "A=";A * 180 / PI
180  PRINT "F=";F * 180 / PI
190  PRINT "AB=";AB
200  PRINT "AP=";AP
205  PRINT "RAKE ANGLE=";AR
210  PRINT : PRINT : PRINT : PRINT
    : PRINT : PRINT
215  PR# 0
220  GOTO 15
```

```
]LOAD AL-GHAZAL'S DISC GEOMETRY 3
]LIST

10  REM  AL -GHAZAL'S DISC GEOMET
     RY 3
15  CLEAR
20  INPUT "H=";H: INPUT "E=";E: INPUT
     "R=";R: INPUT "R1=";R1: INPUT
     "D=";D
30  PR# 1
40  PRINT "AL-GHAZAL'S DISC GEOME
     TRY 3"
45  PRINT
50  PRINT "H=";H: PRINT "E=";E: PRINT
     "R=";R: PRINT "R1=";R1: PRINT
     "D=";D
70 PI = 3.1415926
80 H = H * PI / 180:E = E * PI /
     180
90 R2 = R1 / R
100 B =  ATN (R2 /  SQR ( - R2 *
     R2 + 1))
110 K =  SIN (E + B) * ( SIN (E +
     B) - D / R) +  SQR ( COS (2 *
     (E + B)) + ( SIN (E + B)) ^
     4 + (2 *  SIN (E + B) - D /
     R) * D / R * ( COS (E + B)) ^
     2)
120 A =  - ATN (K /  SQR ( - K *
     K + 1)) + 1.5708
123 A1 = 1 / 2 * PI - E - B
126 AR = A1 + 1 / 2 * A
128 AR = AR * 180 / PI
130 S = R *  COS (E + B - A)
140 C = 2 *  SQR (D * (2 * R1 *  COS
     (E) - D)) /  COS (E)
150 S1 = 2 * R *  COS (E + B - A)

160 M1 = C / S1
170 M2 =  ATN (M1 /  SQR ( - M1 *
     M1 + 1))
175 M = M2 - H
180 S2 = S ^ 2
190 L1 = C / (2 * R1)
200 L =  ATN (L1 /  SQR ( - L1 *
     L1 + 1))
210 C1 = C ^ 2
215 N =  ATN (M1 /  SQR ( - M1 *
     M1 + 1))
220 AH = S2 * M2 - C / 2 *  SQR (
     S2 - C1 / 4)
230 AI = (R1 ^ 2 * L - 1 / 2 * C *
     SQR (R1 ^ 2 - 1 / 4 * C1)) *
     SIN (E)
235 AL = AH + AI
240 ABH = S2 * (M -  SIN (M) *  COS
     (M)) / 2
245 AABH = 2 * ABH
250 APH = S2 * (M2 - M +  SIN (M)
     *  COS (M) - C / (4 * S) *
     SQR (4 - C1 / S2))
260  PRINT "B=";B * 180 / PI
270  PRINT "COS (A)=";K
280  PRINT "A=";A * 180 / PI
290  PRINT "M=";M * 180 / PI
300  PRINT "AR=";AR * 180 / PI
310  PRINT "AL=";AL
320  PRINT "AH=";AH
330  PRINT "AI=";AI
335  PRINT "2ABH=";AABH
340  PRINT "ABH=";ABH
350  PRINT "APH=";APH
365  PRINT "RAKE=";AR
370  PRINT : PRINT : PRINT : PRINT
     : PRINT : PRINT
380  PR# 0
385  PRINT : PRINT : PRINT
390  GOTO 15
```

```
]LOAD DCX2
]LIST

5 H = H * PI / 180:E = E * PI / 1
   80
10  REM  AL-GHAZAL'S DISC GEOMETR
     Y 2
15  CLEAR
20  INPUT "H=";H: INPUT "E=";E: INPUT
     "R=";R: INPUT "R1=";R1: INPUT
     "D=";D
23  PR# 1
25  PRINT "AL-GHAZAL'S DISC GEOME
     TRY 2"
26  PRINT "H=";H: PRINT "E=";E: PRINT
     "R=";R: PRINT "R1=";R1: PRINT
     "D=";D
29  PRINT
30 PI = 3.1415926
35 H = H * PI / 180:E = E * PI /
     180
40 R2 = R1 / R
50 B =  ATN (R2 /  SQR ( - R2 * R
     2 + 1))
60 C = PI / 2 - B
70 K =  SIN (E + B) * ( SIN (E +
     B) - D / R) +  SQR ( COS (2 *
     (E + B)) + ( SIN (E + B)) ^
     4 + (2 *  SIN (E + B) - D /
     R) * D / R * ( COS (E + B)) ^
     2)
75 A =  -  ATN (K /  SQR ( - K *
     K + 1)) + 1.5708
80 F1 =  SQR (D * (2 * R1 *  COS
     (E) - D)) / (R *  COS (E + B
      - A) *  COS (E))
85 F =  ATN (F1 /  SQR ( - F1 * F
     1 + 1))
90 AB = (A *  COS (E) *  COS (B -
     A) -  SIN (A) *  COS (B) *  COS
     (E) -  SIN (E + B - A) * ( COS
     (B - A) -  COS (B)) ^ 2) * R
      ^ 2 / (2 *  COS (E) *  COS
     (B - A)) * ((F - H) / F)
100 I = 2 *  SQR (D * (2 * R1 *  COS
     (E) - D)) /  COS (E)
110 J = I / (2 * R1)
120 AP = R1 ^ 2 * ( ATN (J /  SQR
     ( - J * J + 1)) - I / (4 * R
     1 ^ 2) *  SQR (4 * R1 ^ 2 -
     I ^ 2)) *  SIN (H) *  COS (E
     )
125 A1 = 1 / 2 * PI - E - B
130 AR = A1 + 1 / 2 * A
135 AR = AR * 180 / PI
140  PRINT "B=";B * 180 / PI
150  PRINT "C=";C * 180 / PI
155  PRINT "C1=";90 - (C * 180 /
     PI)
160  PRINT "COS(A)=";K
170  PRINT "A=";A * 180 / PI
180  PRINT "F=";F * 180 / PI
190  PRINT "AB=";AB
200  PRINT "AP=";AP
205  PRINT "RAKE ANGLE=";AR
210  PRINT : PRINT : PRINT : PRINT
     : PRINT : PRINT
215  PR# 0
220  GOTO 15
```

```
JLOAD DC
JLIST

 5 H = H * PI / 180:E = E * PI / 1
    80
 10  REM  AL-GHAZAL'S DISC GEOMETR
    Y 2
 15  CLEAR
 20  INPUT "H=";H: INPUT "E=";E: INPUT
    "R=";R: INPUT "R1=";R1: INPUT
    "D=";D
 23  PR# 1
 25  PRINT "AL-GHAZAL'S DISC GEOME
    TRY 2"
 26  PRINT "H=";H: PRINT "E=";E: PRINT
    "R=";R: PRINT "R1=";R1: PRINT
    "D=";D
 29  PRINT
 30 PI = 3.1415926
 35 H = H * PI / 180:E = E * PI /
    180
 40 R2 = R1 / R
 50 B =  ATN (R2 /  SQR ( - R2 * R
    2 + 1))
 60 C = PI / 2 - B
 70 K =  SIN (E + B) * ( SIN (E +
    B) - D / R) +  SQR ( COS (2 *
    (E + B)) + ( SIN (E + B)) ^
    4 + (2 *  SIN (E + B) - D /
    R) * D / R * ( COS (E + B)) ^
    2)
 75 A =  - ATN (K /  SQR ( - K *
    K + 1)) + 1.5708
 80 F1 =  SQR (D * (2 * R1 *  COS
    (E) - D)) / (R *  COS (E + B
    - A) *  COS (E))
 85 F =  ATN (F1 /  SQR ( - F1 * F
    1 + 1))
 90 AB = (A *  COS (E) *  COS (B -
    A) -  SIN (A) *  COS (B) *  COS
    (E) -  SIN (E + B - A) * ( COS
    (B - A) -  COS (B)) ^ 2) * R
    ^ 2 / (2 *  COS (E) *  COS
    (B - A)) * ((F - H) / F) ^ 2
    .5
100 I = 2 *  SQR (D * (2 * R1 *  COS
    (E) - D)) /  COS (E)
110 J = I / (2 * R1)
120 AP = R1 ^ 2 * ( ATN (J /  SQR
    ( - J * J + 1)) - I / (4 * R
    1 ^ 2) *  SQR (4 * R1 ^ 2 -
    I ^ 2)) *  SIN (H) *  COS (E
    )
125 A1 = 1 / 2 * PI - E - B
130 AR = A1 + 1 / 2 * A
135 AR = AR * 180 / PI
136 X = R ^ 2 * ( SIN (H)) ^ 2 *
    ( COS (E)) ^ 2 * ( COS (E +
    B - A)) ^ 2
137 Y =  - 2 * R1 *  COS (E)
138 DC = ( - Y -  SQR (Y ^ 2 - 4 *
    X)) / 2
140  PRINT "B=";B * 180 / PI
150  PRINT "C=";C * 180 / PI
155  PRINT "C1=";90 - (C * 180 /
    PI)
160  PRINT "COS(A)=";K
170  PRINT "A=";A * 180 / PI
180  PRINT "F=";F * 180 / PI
190  PRINT "AB=";AB
200  PRINT "AP=";AP
205  PRINT "RAKE ANGLE=";AR
207  PRINT "DC=";DC
210  PRINT : PRINT : PRINT : PRINT
    : PRINT : PRINT
215  PR# 0
220  GOTO 15
```

```
JLOAD X1
JLIST

5 H = H * PI / 180:E = E * PI / 1
    80
10  REM  AL-GHAZAL'S DISC GEOMETR
    Y 2
15  CLEAR
20  INPUT "H=";H: INPUT "E=";E: INPUT
    "R=";R: INPUT "R1=";R1: INPUT
    "D=";D
23  PR# 1
25  PRINT "AL-GHAZAL'S DISC GEOME
    TRY 2"
26  PRINT "H=";H: PRINT "E=";E: PRINT
    "R=";R: PRINT "R1=";R1: PRINT
    "D=";D
29  PRINT
30 PI = 3.1415926
35 H = H * PI / 180:E = E * PI /
    180
40 R2 = R1 / R
50 B =  ATN (R2 /  SQR ( - R2 * R
    2 + 1))
60 C = PI / 2 - B
70 K =  SIN (E + B) * ( SIN (E +
    B) - D / R) +  SQR ( COS (2 *
    (E + B)) + ( SIN (E + B)) ^
    4 + (2 *  SIN (E + B) - D /
    R) * D / R * ( COS (E + B)) ^
    2)
75 A =  -  ATN (K /  SQR ( - K *
    K + 1)) + 1.5708
80 F1 =  SQR (D * (2 * R1 *  COS
    (E) - D)) / (R *  COS (E + B
     - A) *  COS (E))
85 F =  ATN (F1 /  SQR ( - F1 * F
    1 + 1))
90 AB = (A *  COS (E) *  COS (B -
    A) -  SIN (A) *  COS (B) *  COS
    (E) -  SIN (E + B - A) * ( COS
    (B - A) -  COS (B)) ^ 2) * R
     ^ 2 / (2 *  COS (E) *  COS
    (B - A))
100 I = 2 *  SQR (D * (2 * R1 *  COS
    (E) - D)) /  COS (E)
110 J = I / (2 * R1)
120 AP = R1 ^ 2 * ( ATN (J /  SQR
    ( - J * J + 1)) - I / (4 * R
    1 ^ 2) *  SQR (4 * R1 ^ 2 -
    I ^ 2)) *  SIN (H) *  COS (E
    )
125 A1 = 1 / 2 * PI - E - B
130 AR = A1 + 1 / 2 * A
133 AR = AR * 180 / PI
140  PRINT "B=";B * 180 / PI
150  PRINT "C=";C * 180 / PI
155  PRINT "C1=";90 - (C * 180 /
    PI)
160  PRINT "COS(A)=";K
170  PRINT "A=";A * 180 / PI
180  PRINT "F=";F * 180 / PI
190  PRINT "AB=";AB
200  PRINT "AP=";AP
205  PRINT "RAKE ANGLE=";AR
210  PRINT : PRINT : PRINT : PRINT
    : PRINT : PRINT
215  PR# 0
220  GOTO 15
```

```
]LOAD DISC 4
]LIST
5 H = H * PI / 180:E = E * PI / 1
    80
10  REM  AL-GHAZAL'S DISC GEOMETR
    Y 2
15  CLEAR
20  INPUT "H=";H: INPUT "E=";E: INPUT
    "R=";R: INPUT "R1=";R1: INPUT
    "D=";D
23  PR# 1
25  PRINT "AL-GHAZAL'S DISC GEOME
    TRY 2"
26  PRINT "H=";H: PRINT "E=";E: PRINT
    "R=";R: PRINT "R1=";R1: PRINT
    "D=";D
29  PRINT
30 PI = 3.1415926
35 H = H * PI / 180:E = E * PI /
    180
40 R2 = R1 / R
50 B =  ATN (R2 /  SQR ( - R2 * R
    2 + 1))
60 C = PI / 2 - B
70 K =  SIN (E + B) * ( SIN (E +
    B) - D / R) +  SQR ( COS (2 *
    (E + B)) + ( SIN (E + B)) ^
    4 + (2 *  SIN (E + B) - D /
    R) * D / R * ( COS (E + B)) ^
    2)
75 A =  - ATN (K /  SQR ( - K *
    K + 1)) + 1.5708
80 F1 =  SQR (D * (2 * R1 *  COS
    (E) - D)) / (R *  COS (E + B
    - A) *  COS (E))
85 F =  ATN (F1 /  SQR ( - F1 * F
    1 + 1))
90 AB = (A *  COS (E) *  COS (B -
    A) -  SIN (A) *  COS (B) *  COS
    (E) -  SIN (E + B - A) * ( COS
    (B - A) -  COS (B)) ^ 2) * R
    ^ 2 / (2 *  COS (E) *  COS
    (B - A)) * ((F - H) / F) ^ 2
    .5
100 I = 2 *  SQR (D * (2 * R1 *  COS
    (E) - D)) /  COS (E)
110 J = I / (2 * R1)
120 AP = R1 ^ 2 * ( ATN (J /  SQR
    ( - J * J + 1)) - I / (4 * R
    1 ^ 2) *  SQR (4 * R1 ^ 2 -
    I ^ 2)) *  SIN (H) *  COS (E
    )
125 A1 = 1 / 2 * PI - E - B
130 AR = A1 + 1 / 2 * A
135 AR = AR * 180 / PI
140  PRINT "B=";B * 180 / PI
150  PRINT "C=";C * 180 / PI
155  PRINT "C1=";90 - (C * 180 /
    PI)
160  PRINT "COS(A)=";K
170  PRINT "A=";A * 180 / PI
180  PRINT "F=";F * 180 / PI
190  PRINT "AB=";AB
200  PRINT "AP=";AP
205  PRINT "RAKE ANGLE=";AR
210  PRINT : PRINT : PRINT : PRINT
    : PRINT : PRINT
215  PR# 0
220  GOTO 15
```